UNIVERSITY OF LIVERPOOL

Characterization of high-κ dielectrics on Germanium

Thesis submitted in accordance with the requirements of the University of Liverpool for the degree of Doctor in Philosophy

By

Mohammed Ghazi Althobaiti

February 2016

Abstract

This study explores and describes the interface properties of various high-k materials deposited on the Ge substrate. Deposition/ growth of these material films has been achieved using multiple techniques such as atomic layer deposition (ALD), molecular beam epitaxy and thermal growth. High dielectrics (k) materials based on metal (4d and 5d) such as Y_2O_3, ZrO_2, HfO_2, Ta2O_5, and from the lanthanide series, La_2O_3 and Tm_2O_3 were deposited on germanium and characterized to find out interface quality and band offset between Ge substrate and the oxides. Additionally, Al_2O_3 was considered, both as an interface barrier layer and as a high –k layer. Material and interface characterization was done using atomic force microscopy (AFM), capacitance-voltage (C-V), current-voltage (I-V), Variable Angle Spectral Ellipsometry (VASE), X-Ray diffraction (XRD), and X-ray photoelectron Spectroscopy (XPS) including the post growth micro-structural and compositional analysis using high resolution transmission electron microscope (HRTEM). Various physical and electrical studies were performed based on the above mentioned characterization techniques. The high-k material / Ge interface has been studied systematically using XPS and VASE characterization, considering the effects of temperature and thickness during deposition.

Two germanium interface engineering methods were developed and discussed: (i) germanate formation using La_2O_3 and Y_2O_3, and (ii) using Al_2O_3 and Tm_2O_3 as barrier layers, and S passivation for Ta_2O_5 films. Based on the physical and electrical characterization carried out in this work, Ge interface engineering using rare-earth material inclusion happens to be a promising route to fabricate Ge CMOS devices with high performance. This statement is supported by the fact that these high-k materials provide a defect free interface and reduce the possibility of unstable GeO_x formation at the interface, hence improving the interface quality.

Post deposition annealing effects on Tm_2O_3 has been analysed using XPS and VUV-VASE. The stack prepared for the purpose was of EOT (equivalent oxide thickness) ~5 nm Tm_2O_3/epi-Ge/Si. Study with Tm_2O_3 presented 3 main findings, i) Valence band offset estimation using Kraut's method was consistent within the experimental error, and found to be 3.05 ± 0.2 eV, ii) the VBO for thermal GeO_2/Ge stack was found to be matching with the recently reported value by Toriumi's group. The value of conduction band offset was estimated to be higher than 1 eV,

indicating the favorability of GeO_2 as a passivation layer for Ge, iii) the reactivity of Tm_2O_3 on Ge was found to be even lower than that of Si, indicating the possibility of a desirable interface.

This thesis further explores the use of hafnia and alumina with Sulphur (S) passivated and un-passivated Ge samples. For this purpose HfO_2/Ge and Al_2O_3/Ge stacks were prepared using ALD technique. It was observed that using H_2O with O plasma, reduces the purge time and gives low carbon incorporation from metals. Hence O plasma and H_2O were used as oxidizing agents and the interface properties were studied systematically, which is a new contribution by this work. Further the effects of adding TiO_2 contents to HfO_2 layer on interface properties were studied, using Al_2O_3 (0.3 nm) as surface passivation.In this work the achieved EOT of HfO_2 with the controlled introduction of TiO_2 was ~ 1.3 nm, giving a leakage current as low as10^{-7} A/cm^{-2} at ±1 V, which is in the acceptable limits.

Finally, Ta_2O_5 films were characterized on Ge for band line up with respect to Ge. The deposition of the films was done by ALD technique at 250 °C. The analysis was done on both S passivated and un-passivated samples. The band line up parameters were estimated using XPS and it was observed that the valence band offset for S passivated sample was 2.67 eV whereas it was 2.84 eV for un-passivated Ge sample. Ta_2O_5 reflected a band gap of 4.44 eV (estimated from the energy loss spectrum of O1 s core level) for a 20 nm thick film deposited by ALD. Hence this thesis will cover the high-k materials and their application as a gate oxide and also the passivation layer for Ge substrates for Ge CMOS devices.

Acknowledgements

I would like to thank my supervisors Dr Vinod Dhanak and Dr Ivona Mitrovic, for their motivation, continuous interactions, valuable insights and guidance. They being humble at every twists and turns faced during my PhD helped a lot with their vast knowledge and expertise. I fell short of words thanking them for giving me the opportunity to work under their supervision and for their constant guidance and support throughout. Also, I would like to thank the Saudi government for funding my PhD study.

Many thanks to Prof. Steve Hall, Dr. Naser Sedghi and Ayndra Weerakkody from Electrical Engineering department at University of Liverpool for their support and help during my PhD work.

Special thanks to people from school of ICT, KTH Royal Institute of Technology, Sweden, Dr.C. Henkel, Dr.E. Dentoni Litta, Dr.P.-E. Hellström, Dr. M. Östling for their collaboration and their help and support when I visited Atomic layer Deposition lab at KTH.

Also, I would like to thank David Hesp, Ian Mcleod and Tom Whittles for their help and support in the lab.

Finally, I thank my family especially my mother and father for all their help and support.

Authors Contributions to Publications

Chapter 3

I.Z. Mitrovic, M. Althobaiti, A.D. Weerakkody, N. Sedghi, S. Hall, V.R. Dhanak, P.R. Chalker, C. Henkel, E. Dentoni Litta, P.-E. Hellström, and M. Östling, ECS Transactions, 61 (2), pp. 73-88, (2014). M. Althobaiti collected and analyzed XPS, XRD data, prepared the figures and discussed all the results. I.Z. Mitrovic wrote the paper. N. Sedghi collected the CV measurements and A.D. Weerakkody analyzed SE data. C. Henkel, E. Dentoni Litta, P.-E. Hellström and M. Östling made the samples. All authors, including S. Hall, V.R. Dhanak, P.R. Chalker, were involved in the discussion of the results.

Chapter 4

I.Z. Mitrovic, M. Althobaiti, A.D. Weerakkody, V.R. Dhanak, W.M. Linhart, T.D.Veal, N. Sedghi, S. Hall, and P.R. Chalker, Appl. Phys. 115 (11), pp. 114102 (2014). M. Althobaiti collected and analyzed XPS, XRD data, prepared the figures and discussed all the results. I.Z. Mitrovic wrote the paper. N. Sedghi collected the CV measurements and A.D. Weerakkody analyzed SE data. All authors, including S. Hall, V.R. Dhanak, P.R. Chalker, W.M. Linhart, T.D.Veal, were involved in the discussion of the results.

Chapter 5

I.Z. Mitrovic, M.Althobaiti, A.D.Weerakkody, N.Sedghi, S.Hall, V.R. Dhanak, P.R.Chalker, C.Henkel, E.Dentoni Litta, P.-E. Hellström, and M.Östling, Microelectron. Eng. 109, pp. 204 (2013).

M. Althobaiti worked on ALD at KTH, Sweden to fabricate the Tm_2O_3 thin films with C. Henkel, P. E. Hellström, and M.Östling and E.Dentoni Litta. M.

Althobaiti then collected and analyzed XPS, XRD and SE data. I.Z. Mitrovic authored the paper. N. Sedghi collected the CV measurements and A.D. Weerakkody analyzed SE data. All authors, including S. Hall, V.R. Dhanak, P.R. Chalker, were involved in the discussion of the results.

I.Z. Mitrovic, S. Hall, M. Althobaiti, D. Hesp, V.R. Dhanak, A. Santoni, A.D. Weerakkody, N. Sedghi, P.R. Chalker, C. Henkel, E. Dentoni Litta., P.-E. Hellström, M. Ostling, H. Tan, and S. Schamm-Chardon, J. Appl. Phys. 117, pp. 214104 (2015). M. Althobaiti worked on ALD at KTH, Sweden to fabricate the Tm_2O_3 thin films with C. Henkel, P.-E. Hellström, and M.Östling and E.Dentoni Litta. M.Althobaiti then collected and analyzed XPS, XRD, SE data back in Liverpool. I.Z. Mitrovic authored the paper. A. Santoni carried out depth profiling experiment. N. Sedghi collected the CV measurements and A.D. Weerakkody analyzed SE data. All authors, including S. Hall, V.R. Dhanak, P.R. Chalker, D. Hesp H. Tan, and S. Schamm-Chardon were involved in the discussion of the results.

Chapter 6

S. Mather, N. Sedghi, M. Althobaiti, I.Z. Mitrovic, V.R. Dhanak, P.R. Chalker, and S. Hall, Microelectron. Eng. 109, pp. 126 (2013).
M. Althobaiti collected and analyzed the XPS data. S. Mather wrote the paper and carried out CV measurements. All authors, including S. Hall, P.R. Chalker, N. Sedghi, V.R. Dhanak, P.R. Chalker, and I.Z. Mitrovic were involved in the discussion of the results.

Chapter 7

M. Althobaiti, S. Mather, N. Sedghi, V.R. Dhanak, I.Z. Mitrovic, S. Hall, and P.R. Chalker, Vacuum 122, pp. 306 (2015). M. Althobaiti fabricated the HfO_2 thin films by ALD with S. Mather collected and analysed the XPS and IPES data, and wrote the paper. N. Sedghi collected the CV measurements. All authors, including S. Hall, P.R. Chalker, N. Sedghi, V.R. Dhanak, and I.Z. Mitrovic were involved in the discussion of the results.

Chapter 8

Lu. Qifeng, Mu. Yifei, W. Joseph, M. Althobaiti, V.R. Dhanak, W. Jingjin, Z. Chun, C. Zhou, L. Yang, I.Z. Mitrovic, S. Taylor. P.R. Chalker, Materials, (2015). Awaiting Publication. M. Althobaiti collected and analysed the XPS data. Lu. Qifeng wrote the paper. All authors, including Mu. Yifei, W. Joseph, V.R. Dhanak, W. Jingjin, Z. Chun, C. Zhou, L. Yang, I.Z. Mitrovic, S. Taylor. P.R. Chalker, were involved in the discussion of the results.

Chapter 9

M. Althobaiti, J. Stoner, V.R. Dhanak,, R.J. Potter, and I.Z. Mitrovic, Proc. IEEE PRIME. 161, 2015. M. Althobaiti wrote the paper, fabricated the Ta_2O_5 by ALD with R. J. Potter, collected and analyzed XPS data. All authors, including J. Stoner, V.R. Dhanak, R.J. Potter, and I.Z. Mitrovic were involved in the discussion of the results.

Oral and poster presentations

1- Spectro-ellipsometric and X-ray photoelectron studies of thulium oxide on Ge, High-k dielectrics on Ge", 2012, Cambridge University. (Oral presentation).

2- Interface study of Y_2O_3, Al_2O_3 & GeO_2 on Ge by XPS and VASE, at "High-k dielectrics on Ge", 8 June 2012 Liverpool John Moores University, Liverpool. (Oral presentation).

3- Photoemission and ellipsometry measurements of GeO_2 and $Y2O_3$ films on Ge substrates. (For CMD-24, CMMP-12, ECOSS-29, ECSCD-11 3 -7 September 2012, Edinburgh International Convention Centre, and Edinburgh, UK. (Poster presentation)

4- Interface study of high k materials by XPS and VASE, Poster Day Central Teaching Laboratory on April 11 2013, University of Liverpool. (Poster presentation).

5- Low EOT $GeO_2/Al_2O_3/HfO_2$ on Ge substrate Using Ultrathin Al Deposition. INFOS. Elsevier, Cracow pp 2-Poland, 2013. (Oral presentation).

6- Interface engineering of Ge using thulium oxide: band line-up study. Microelectronic Engineering vol 109 pp 204-207 Poland. 2013. (Oral presentation).

7- Germanium Based High- K Oxide for Device Materials on 13th November 2012, Department of Physics, University of Liverpool. (Oral presentation).

8- Interface study of high k materials by XPS and VASE. Poster day Central Teaching Laboratory on April 11 2013, University of Liverpool.(Poster presentation)

9- Band alignment of Ta2O5 on sulphur passivated germanium by x-ray photoelectron spectroscopy 11th Conference on PhD Research in Microelectronics and Electronics (IEEE PRIME 2015), 29 June - 2 July 2015, University of Glasgow

Contents

Abstract

Acknowledgements

Authors Contributions to Publications

Chapter 1 Introduction 1

1.1 A brief history of Semiconductor Devices 2
1.2 Moore's law and MOS Device Scaling 3
1.3 Limits to SiO_2 Scaling 5
1.4 Replacement of SiO_2 with high-κ gate dielectric materials 5
1.5 Germanium-based MOSFET 9
1.6 Band offsets at the interfaces 11
1.7 Research Objectives and Scope of this Work 13
1.8 References 17

Chapter 2 Experimental Techniques 21
2.1 Atomic Layer deposition (ALD) 22
2.2 Molecular Beam Epitaxy (MBE) 23
2.3 Vacuum System 24
2.4 Photoelectron spectroscopy (PES) 25
2.4.1 Basic Principle 25
2.4.2 Analysis Depth 27
2.4.3 Photon source 28
2.4.4 Electron Energy Analyser 30
2.4.5 Resolution 34
2.4.6 Measurement of band offsets using Krauts method 35
2.5 Inverse Photoemission (IPES) 37
2.6 Spectroscopic Ellipsometry (SE) 38
2.7 X-Ray Diffraction 42
2.7.1 Principles of XRD 42
2.7.2 Experimental set-up for the study of XRD 43
2.8 C-V Measurement Technique 44
2.8.2 Basic Principles of MOS Capacitors 45
2.8.3 Modes of operation 46
2.8.3.1 Accumulation 46
2.8.3.2 Depletion 47
2.8.3.3 Inversion 47
2.9 Atomic Force Microscopy 48
2.9.1 Principles of AFM 48

2.9.2 AFM Operation Modes 49
2.9.2.1 Contact mode 49
2.9.2.2 Non-contact mode 50
2.9.2.3 Tapping mode 50
2.9.3 Extraction of surface roughness by AFM 51
2.10 Transmission electron Microscopy (TEM) 52
2.10.1 Operation 53
2.10.2 Sample Preparation 54
2.11 Conclusion 54
2.12 References 55

Chapter 3 Interface Engineering Routes for a Future CMOS Ge-based Technology 57

3.1 Introduction 58
3.2 Samples Fabrication and Characterization 58
3.3 Formation of Germanate Interfacial Layers using La_2O_3 and Y_2O_3 59
3.4 Band gap estimation from VUV-VASE 63
3.5 Band line-up correlation with electrical characterization data 65
3.6 Al_2O_3 and Tm_2O_3 as barrier interfacial layers on Ge 66
3.7 HfO_2 Deposition on Alumina and Sulfur Passivated Interface 70
3.8 Conclusion 72
3.9 References 74

Chapter 4 Ge interface engineering using ultra-thin La_2O_3 and Y_2O_3 films: A study into the effect of deposition temperature 79

4.1 Introduction 80
4.2 Experimental 83
4.3 Results and Discussion 85
4.3.1. La_2O_3/Ge gate stacks 85
4.3.2. Y_2O_3/Ge and Al_2O_3/Ge gate stacks 92
4.3.2.1 Thickness, band gap and sub-band gap absorption 92
4.3.2.2 Interfacial layer study for Y_2O_3/Ge 96
4.3.2.3 Estimation of VBO and derivation of a band diagram for Y_2O_3/Ge 101
4.3.2.4 Electrical characterization of Y_2O_3/Ge stacks 102
4.3.2.5The effect of an Al_2O_3 capping layer 104
4.4 Conclusion 106
4.5 References 109

Chapter 5 Atomic-layer deposited thulium oxide as a passivation layer on germanium 120

5.1 Introduction 121
5.2 Experimental 122

5.3 Results and Discussion 123
5.3.1 Valence Band offset and band gap estimation for Tm_2O_3/Ge 123
5.3.2 Sub-band gap absorption features, interface and EOT for Tm_2O_3/Ge 126
5.3.3 Estimation of VBO for Tm_2O_3/Ge gate stack 130
5.3.4 Estimation of VBO for GeO_2/Ge gate stack 133
5.3.5 Band gap evaluation and nature of Tm_2O_3/Ge interface 134
5.4 Conclusion 136
5.5 References 137

Chapter 6 Low EOT $GeO_2/Al_2O_3/HfO_2$ on Ge Substrate Using Ultrathin Al Deposition 143

6.1 Introduction 144
6.2 Sample Preparation 144
6.3 Results and Discussion 145
6.4 Conclusion 148
6.5 References 149

Chapter 7 Hafnia and Alumina on Sulphur Passivated Germanium 150

7.1 Introduction 151
7.2 Experimental 151
7.3 Results and Discussion 153
7.3.1 Interfacial Features of Hafnia on Sulphur Passivated Germanium 153
7.3.2 Interfacial Features of Al_2O_3 on Sulphur Passivated Germanium 156
7.3.3 The Effect of S and S/sub-nm Al_2O_3 passivation on CV characteristics of HfO_2/Ge stacks 157
7.3.4 Determination of Band Gap of HfO2 on Ge 160
7.4 Conclusion 161
7.5 References 162

Chapter 8 Electrical property and interfacial study of $Hf_xTi_{1-x}O_2$ high permittivity gate insulators deposited on germanium substrates 165

8.1 Introduction 166
8.2 Experimental Section 167
8.3 Results and Discussion 169
8.4 Conclusions 180
8.5 References 181

Chapter 9 Band Alignment of Ta_2O_5 on Sulphur Passivated Germanium by XPS 184

9.1 Introduction 185
9.2 Experimental 185
9.3 Results and Discussion 186

9.4 Conclusion 190
9.5 References 191

Chapter 10 Conclusion 192

Chapter 1

Introduction

Introduction

The development of effective semiconductor materials for electronic applications has undergone steady revolution since the vacuum tube was invented in 1900s. And over the years, researchers have faced and overcome several challenges to improve the performance and scaling down of electronic devices by developing high-κ materials which are stable, reliable, cost effective and can be scaled without any changes to their desirable properties. This chapter reviews high-κ dielectric materials, which are potential replacement for SiO_2 and the limitations faced to realise these goals. Also, this chapter considers some of the features which any high-κ materials must satisfy in order to be considered a better replacement for SiO_2 and examine problems such as structural defects which may either occur as a result of high gate leakage current or defects caused during the growth or treatment process. Moreover, the electronic properties such as large bandgap, band offset, valence band and conduction band of the semiconductors and high-κ materials are considered, and how these properties can determine performance of MOSFETs and evaluated to enhance the performance. Following this brief review, the germanium based channel devices and the requirement for high dielectric gate material are considered. Engineering a suitable interface between a dielectric gate material and the Ge channel, forms the main focus of this thesis.

1.1 A brief history of Semiconductor Devices

In 1906 the first vacuum tube was invented by L.D. Forest which was widely used to rectify, amplify and switch signals. Over the years the evolution of this device has continued to play significant role towards the development of electronics [1]. But due to their large size and their enormous power consumption vacuum tubes have limited use. Lillienfeld had proposed the development of field-effect transistor, this device is unipolar in nature and its operation only requires one type of charge carrier [2]. In 1948, W. Shockley proposed bipolar junction transistor, the device which operates through the flow of electrons and holes as the charge carriers [3]. By 1951, W. Shockley had invented the bipolar transistor and it was the revolutionary discovery of this solid state device that effectively replaced vacuum tube transistor [4].

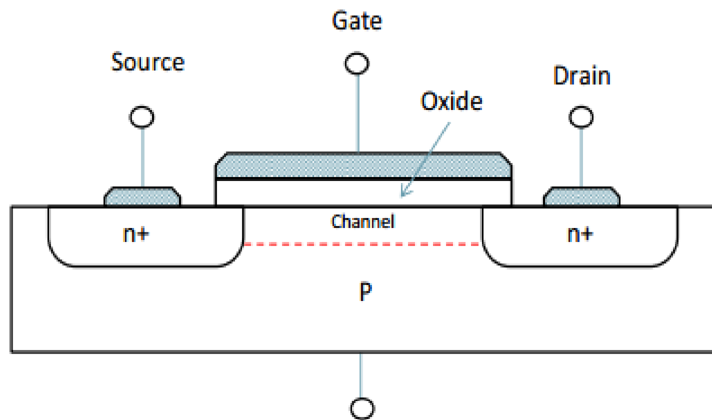

Figure 1.1 A schematic diagram of an FET. The current flow in the channel is controlled by applying voltage on the gate [5].

Transistors acting as switches are considered as the basic building blocks of computer electronics. The Field Effect Transistor (FET) typically is a three terminal device schematically shown in Figure 1.1. Transistor basically means transfer + resistor, which mean it is about change in conductance. This conductance change happens by applying some voltage at the gate terminal, change in conductance is usually termed as change of the transistor state, from being on to off [6]. In FETs, gate and channel are coupled using a capacitor layer. FETs can further be classified based on this coupling layer. First type is junction FETs, where a p-n junction works as the coupling layer, second type is metal-semiconductor FETs (MESFETs), where coupling layer is a Schottky (metal – semiconductor) junction and third is metal-oxide-semiconductor FETs (MOSFETs) with a dielectric oxide layer as capacitive coupling layer. Among these, the MOSFET is the mostly used type for transistors because of low cost, high yield, and dense packing for the microelectronics [7, 10, 11].

1.2 Moore's law and MOS Device Scaling

The significant success of semiconductor manufacturing can be attributed to steady and perpetual improvement of integrated circuit efficiency. The rise in the device performance is obtained by scaling down the dimensions of the MOSFET. Moore's law is a common tool used in the semiconductor industry roadmap for predicting the scaling of MOSFET, and interestingly, this year makes the 50th year that this law has guided the industry. One of the predictions of Moore's law is that the number of transistors that can be integrated on a chip

roughly doubles every year as shown in Figure 1.2. One of the benefits of reduction in the dimension is that it makes possible for large number of transistors to be integrated on a chip, which in return allows faster processing speed and improves economy by reducing the cost [8, 9]. As of 2015, the highest transistor count in a commercially available CPU (in one chip) was over 5.5 billion transistors, in Intel's 18-core Xeon Haswell-EP.

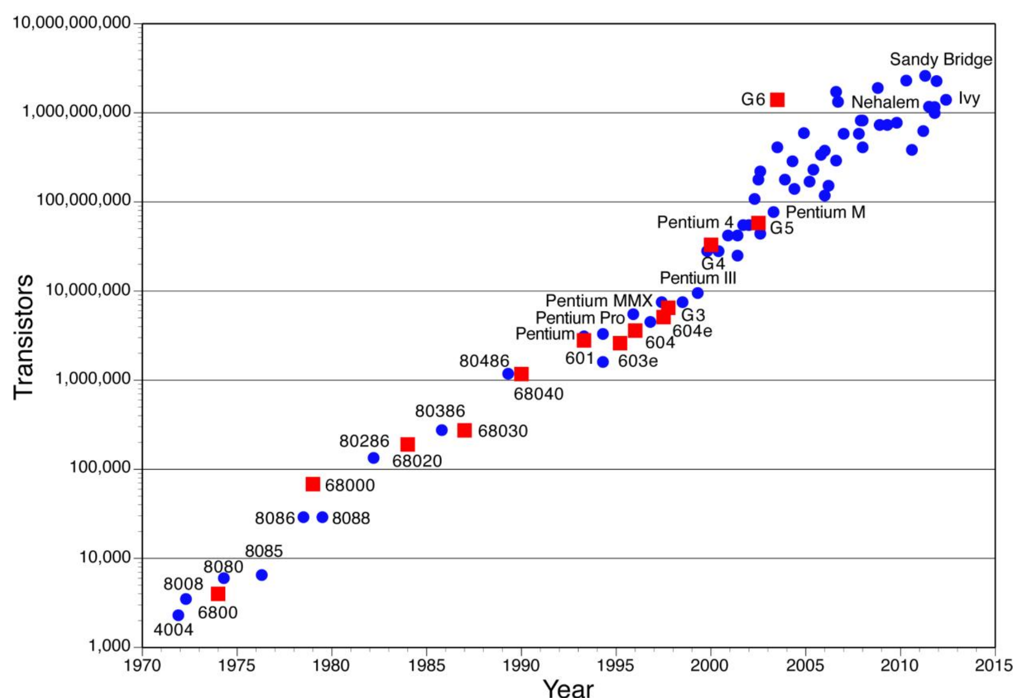

Figure 1.2 Plot of transistor counts against dates of introduction. The curve shows counts doubling every two years [13].

Silicon dioxide (SiO_2) used for the gate in MOSFETs has remained the most efficient material for the manufacturing of electronic devices. This can be attributed to the excellent material and electrical properties of SiO_2. SiO_2 possesses several characteristics that make it qualify as an effective gate insulator. One of these features is that SiO_2 can easily be grown thermally on silicon with controllable thickness and steady homogeneity. This allows SiO_2 to form a naturally stable interface with the silicon substrate, possessing low density and an almost defect free structure. Another important attribute of the SiO_2 that makes it a suitable material for MOSFET is its excellent chemical and thermal stability which are prerequisite for fabrication of transistors even at annealing treatments as high as 1000°C. The κ-value of SiO_2 is 3.9 and it is characterized with a large band gap (about 9 eV), which provides it with excellent electrical properties [14]. These features have enabled the fabrication of effective operating MOSFETs from thin (around 1.5nm) SiO_2 gate layer [14, 15]. The only setback of the SiO_2 gate is that further scaling below 1.5nm thickness, for applications such as high logic performance in

microprocessors, in personal computers and low operating logic performance in wireless applications is very challenging [15].

1.3 Limits to SiO_2 Scaling

There are several challenges that can limit SiO_2 scaling for MOSFET applications. One of the major problems is the SiO_2 layer thickness which is linked with current leakage through the metal-oxide-semiconductor. The current leakage in SiO_2 when scaling below the layer thickness of 3nm involves a process where charge carriers can pass through the dielectric layer by quantum tunneling mechanism [16]. Wetzel-Kramer's-Brillouin observed that the SiO_2 layer thickness decreases as tunneling probability increases exponentially [17]. The effect is that a large current leakage is observed flowing though the device when the SiO_2 thickness decreases. For instance, it was reported that a current density leakage exceeding $100A/m^2$ was observed when the SiO_2 gate was 1nm. Second to this setback is the problem arising from SiO_2 scaling thickness reliability. This is caused by the defects created when charge carriers flow through the SiO_2 gate layer and at Si/ SiO_2 interface during MOSFET operation. At a point a critical density of defects can result in the breakdown of the SiO_2 gate interface, hence, this can lead to device failure [18]. An added consequence and a challenge is that leakage current increases the thermal load in devices, which is unacceptable in view of the drive toward energy efficiency in developing high technology devices.

1.4 Replacement of SiO_2 with high-κ gate dielectric materials

The metal gate-oxide-semiconductor channel model shown in Figure 1.3 can be visualized as a parallel plate capacitor, in which the application of a gate voltage V_G induces charges of opposite sign in the top layer of the substrate. These charges form the channel that connects the source and the drain of the MOSFET device.

Clearly the gate insulator is an important part for a MOSFET device. A transistor is supposed to work stable only when a gate insulator of very high capacitance value is used. To understand this, consider the circuit model of the FET shown in Figure 1.3 considering small devices, the current between the gate and source terminal depends on the energy levels available in the channel. However, these levels are dependent on the applied channel voltage. If the source terminal is grounded (Vs = 0), the amount of charge (Q) in the channel is given by equation (1.1) [19].

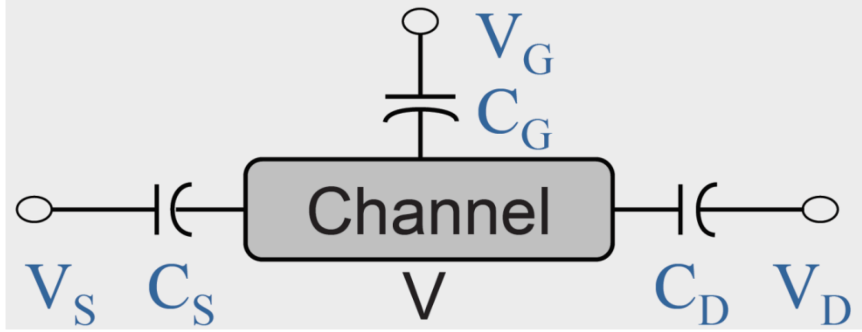

Figure 1.3 A circuit model for the transistor depicted in Figure 1.1.

$$Q = -q\Delta n = C_s V + C_G(V - V_G) + C_D(V - V_D) \qquad (1.1)$$

Where V_G and V_D are the gate and drain voltages

Solving for the voltage V in the channel,

$$V = V_L + V_{SEC} = \frac{C_G V_G + C_D V_D}{C_S + C_D + C_G} + \frac{-q\Delta n}{C_S + C_D + C_G} \qquad (1.2)$$

The first term in equation 1.2 shows the effect of the source, gate and drain voltages (V_S does not appear as it has been set to 0 as reference) and is termed the Laplace potential. The second term is due to the change in the number of electrons in the channel. Considering the Laplace term, the potential in the channel depends on how far the channel is from the gate and drain, and its effect is to change the density of states (DOS) in the channel. In an ideal transistor, the drain current saturates as a function of drain voltage for a given gate voltage. However, for small transistors, often the current continues to increase instead of saturating. The reason is that the DOS in the channel moves as the drain voltage is increased. To avoid this, a good transistor design requires a large gate capacitance C_G to make the effect of V_D negligible. This is why device designers like to have the gate as close as possible to the channel. As scaling down continues, the length of the channel gets smaller and the gate is then even closer to the channel. At the same time, leakage current through the oxide has to be avoided.

The capacitance of the parallel plate capacitor is given by

$$C = \frac{A\kappa\varepsilon_O}{t_{ox}} \qquad (1.3)$$

Where A is the capacitor area, κ is the relative dielectric constant (3.9 for SiO_2), ε_0 is the permittivity of free space (8.85×10^{-12} Fm^{-1}) and t_{ox} represents thickness of the gate oxide, or how close the gate is to the channel. Equation 1.3 depicts that a decrease in t_{ox} will lead to an increase in capacitance, which will in turn increase the number of charges in the channel (V_G

constant). Since leakage limitation constrains the reduction of SiO_2 layer thickness, an alternative way to increase the capacitance is by increasing the relative dielectric constant, i.e. replacing SiO_2 altogether with a higher-κ material [21,22]. The relation between equivalent oxide thickness (EOT) and the thickness of the higher-κ layer is expressed as follows:

$$EOT = \frac{k_{SiO2}}{k_{high-k}} T_{high-k} \tag{1.4}$$

Where K_{SiO2} and K_{high-K} are the dielectric constants of SiO_2 and high-κ dielectric, respectively. T_{high-K} is the physical thickness of the high-κ dielectric gate oxide. Figure 1.4 illustrates the advantage of using high-κ materials to reduce the leakage current of the device.

In the following, some of the challenges of replacing silicon dioxide by using a higher-κ dielectric oxide on silicon in the current MOSFET designs are considered. The overall effect of this replacement is to enhance the capacitance of the metal-oxide semiconductor structure. Using a higher-κ material to replace the SiO_2 means that a thicker material can be used, thereby reducing the risk of current leakage through the gate and the device, and achieving a reliable gate dielectric [23, 24]. The challenge then is to design or develop materials that can be used to engineer stable and reliable interfaces.

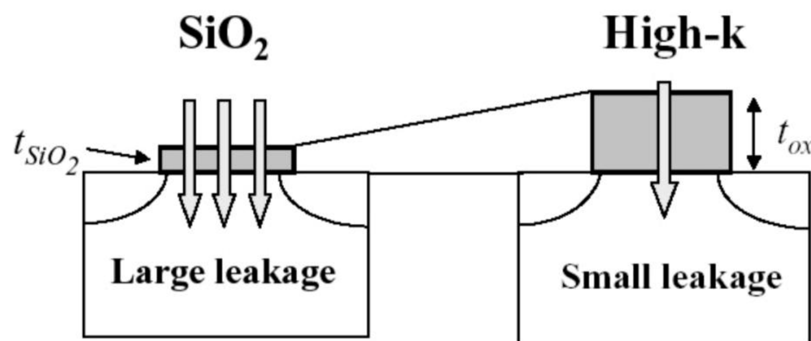

Figure 1.4 Advantage of replacement SiO_2 by a high-κ material [25].

Using high-κ dielectric materials should help in resolving the scaling issue and this was recognized early [26,27]. Several metal oxides were studied and shown to reveal a trend (Figure 1.5). The higher the κ-value, the lower the band gap in general, resulting in lower band offset

between the oxide and the silicon substrate. Hence, the further selection of high-κ materials gets limited, as it would lead to high band gap requirement to achieve necessary band offset with silicon.

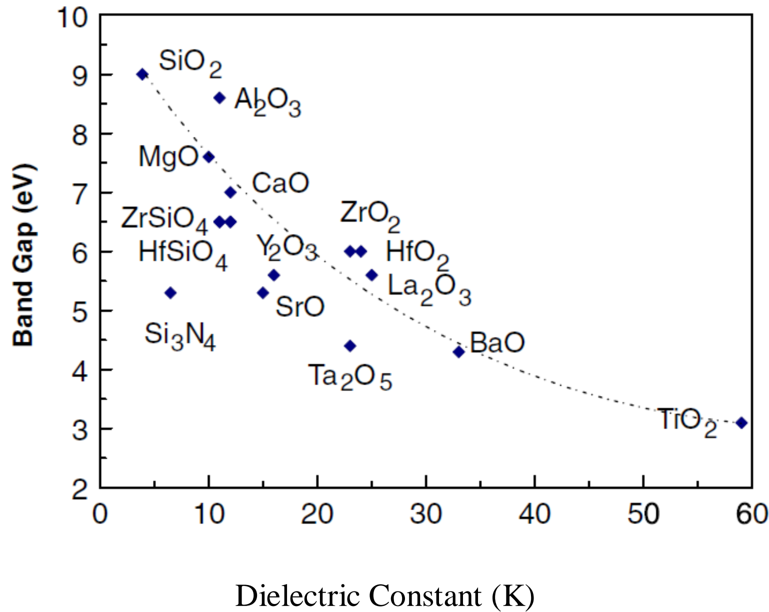

Figure 1.5 Observed relation between band gap of a dielectric and its dielectric constant [28].

Following several trials, in 2007 INTEL introduced Hafnium oxide (HfO_2) in their 45 nm node technology and following improvements to the surface quality, into the 32 nm node. However, the low interface quality was always a concern which limited the effective dielectric constant of HfO_2 to 15 [29]. That is, because of some reaction between HfO_2 and silicon at the interface, the relevant parameters' values lie between that of HfO_2 and SiO_2.

Besides low interface quality between HfO_2 and Si substrate, HfO_2 also has an issue of crystallization even at lower temperature (800 K), and this makes the manufacturing technology more difficult [30]. Hence, for future microelectronics technology, new materials are needed to be introduced. Relevant κ-value of the metal oxide is recommended to be over 10, preferably 20-40. However, as shown in Figure 1.5 the κ-value and band gap of the insulator are correlated. As κ-value of the gate material increases, the bandgap decreases, such that a very high-κ value dielectric will have a too low bandgap that maybe useful in ferroelectric applications but will not be suitable for use in MOSFETs [31].

The dielectric materials required for the fabrication of transistors must possess bandgap larger than 5eV. As part of the requirements, the band offsets with silicon CB and VB must exceed 1eV to prevent conduction by Schottky junction of electron or holes into the oxide.

There is usually instability at the interface between the high-κ oxide and silicon, which can be attributed to the formation of silicide or SiO_2 layer at an elevated temperature, with the oxygen for the silicon oxide formation possibly coming from the metal oxide high-κ dielectric layer. The gate oxides are either directly or indirectly exposed to high temperatures during the fabrication of the device. However, the effect of the thermal treatment on the gate dielectric can be categorised into four issues [33]. First, a thin layer of SiO_2 is formed at high-κ /silicon interface. The thin layer of SiO_2 at the interface reduces benefits of the high dielectric oxide. Second, high-temperature annealing is required to eliminate deep trap centers from the gate oxides. Thirdly, at elevated temperatures, high-κ materials tend to decompose and transform to a more stable silicide at the interface; it also promotes the formation of oxygen vacancies within the bulk oxide layer even in a nitrogen controlled environment during annealing. The fourth issue is the crystallization occurring in as-deposited amorphous metal oxide layers. It has been observed that the crystallization of a thin layer can increase the leakage current through extra leakage via the grain boundary. Therefore, the combination of these processes requires that a high-κ material, which is thermally stable, be highly recommended for CMOS applications in the future [34, 35]. The growth of crystalline high-κ oxide layer on silicon has been observed to be challenging in other ways also, especially if the silicon and oxide layer possess similar lattice constants. The high dielectric metallic oxides are more ionic in nature and coupled with their high coordination number the interface bonding with silicon is more unstable unlike SiO2, thus leading to higher charge trap density of states.

For effective high-performance, CMOS devices made from metal-oxide/silicon interface must be free of inter-boundary/interfacial imperfections since most carriers flow within the channels at the interface. In addition, the surface structure of the gate dielectric can also affect the performance of the device. For instance, polycrystalline material may have surface roughness and will have several defects around the grain boundaries of its nanocrystals. In contrast, amorphous film of dielectric gate may provide minimal surface defects, thereby improving electrical performance of the device [36].

1.5 Germanium-based MOSFET

It has been widely reported that semiconductors with high channel mobility can also improve the performance of MOSFETs by enhancing speed and lowering power dissipation. In recent times, germanium has remained a contending candidate to replace Si for the future generation of CMOS technology, and its application is being used in other higher performance devices. One

of the reasons that Ge is a potential replacement material for Si for future high-speed CMOS applications is due to the fact that bulk Ge is considered to possess higher electron and hole mobilities compared to Si at room temperature as shown in table 1.1 [40]. However its application has not been realised mainly because Ge surface has an ineffective passivation with Ge oxides. The effect of the unstable nature of Ge oxide is that it can affect interfacial point defects. Further investigation of Ge oxidation reveals that decomposition of GeO_2 by heating can form Ge suboxides (GeO_x). GeO, which is one of the suboxides, can thermally absorb Ge from its surface at a reduced temperature (~450°C) and at ordinary atmospheric pressure, this atomic diffusion can lead to the depletion of Ge channel, leading to defects [37]. Recently, attention has focused on developing a reliable gate oxide for Ge MOSFETs applications, and since Ge lattice constant is 5.6461Å, it offers certain advantages in making it suitable for several materials to be grown on its surfaces with little structural strain. Indeed, many Ge MOSFETs have been fabricated with high-κ gate oxides such as germanium oxynitride, Al_2O_3, ZrO_2, Y_2O_3 and HfO_2 [38].

Material	**Si**	**Ge**
Hole mobility (cm^{-1} v^{-1} s^{-1})	450	1900
Electron mobility(cm^{-1} v^{-1} s^{-1})	1500	3900

Table. 1.1 The hole and electron mobility for Ge and Si [39].

Scaling of Ge-based MOSFET is achievable due to germanium's smaller energy bandgap (about 0.66 eV compared to 1.2 eV for Si). In fact, the advantage of germanium was recognised early on, since the first transistor ever produced was with Ge in 1947, however, the rarity of a high quality native oxide was a significant setback for its application and adoption for the fabrication of electronic devices. The instability of the native germanium oxide comes about because it absorbs moisture from the atmosphere and become soluble, the hygroscopic nature of this oxide makes it almost impossible for fabrication of Ge CMOS components. For this reason, Si has been used as the major channel material in CMOS technology for over thirty years and only recently germanium appears to be making a comeback [41]. Germanium has become a viable channel material in MOS devices with the development of suitable dielectric oxides that can avoid the need for the unstable native oxide. Nevertheless challenges remain.

An important consideration for a stable dielectric oxide that does not react with the germanium substrate surface at the interface is passivation of the surface. The nature of the dangling bond

on the Ge surface in some way makes their substrates very reactive to oxygen and other species, a process also common with Si. Surface passivation is the process of terminating these bonds with elements such as H, N and S; in return this interaction helps to protect the surface by stabilising it. One of the major advantages of passivation Ge substrates is to reduce and prevent surface contamination. For instance, in the absence of surface passivation, Ge substrates can behave as gas ion-sputtered, hence it degrades the surface by inducing damage [42, 43]. Another significant importance of surface passivation is that it improves the dielectric/Ge interface which consequently enhances the performance of the device. Also, the application of high-κ materials as the gate dielectric on Ge can generate problems during the growth process. One of the most challenging of these problems is the formation of GeO_x interfacial layer between the high-κ gate dielectric and the Ge substrate, which can arise during high-κ dielectric depositions or post treatment such as annealing [42].

At elevated temperatures, dopants in the source and the drain are activated, hence during the growth and subsequently, there is a possibility of other unwanted reactions: (1) between the dielectric and Ge, (2) in the dielectric, (3) between the dielectric and the metal gate, and or (4) diffusion of metal through the gate dielectric and channel. The major effect of these side reactions makes it difficult to achieve EOT required for the fabrication of future electronic devices. Another negative implication of high temperatures is that it affects the morphology of the dielectric, making it into crystalline or polycrystalline materials. It is observed that increase in leakage current and the shift in the flatband and threshold voltages can be due to several reasons such as large grain boundaries, which acts as a channel for easy movement of carriers and dopants through the material [42].

In general, a very effective passivation treatment of material must be able to maintain chemical stability, provide protection for the substrate against unwanted oxidation and contamination with foreign elements and must effectively minimize the chance of interfacial or surface-induced carrier recombination. Elements such as H, N, C, S and other species have been used to achieve passivation of clean Ge surfaces.

1.6. Band offsets at the interfaces

When describing the high-κ dielectric applications, it is important that the band offset should be greater than 1 eV between the respective bands of the dielectric and substrate. However, in some high-κ dielectric materials with narrow band gap, as can be found in SrTiO3 (band gap of

only 3.2 eV), there must be symmetrical alignment in relation to both the conduction and valence-band edges of the semiconductor in order to achieve sufficient band offset (>1 eV). Hence, it is significant to effectively estimate the band offsets for high-κ dielectrics on semiconductor substrates and choose appropriate high-κ oxides [43]. As an example, figure 1.6 illustrates the band diagram of a $Si/SiO_2/HfO_2$ stack. It can be estimated from the figure that the barrier height of Si/HfO2 is 2.1 ± 0.2 eV. Barrier height is important for gate leakage current control and reliability, which is further required for HfO_2 integration in high-κ metal configurations. Valence band offset (VBO) and conduction band offset (CBO) for HfO_2/SiO_2 interface are 1.2 eV and 2.1 eV respectively.

Experimental methods can be used to estimate the band offsets of various dielectrics. In fact, several technical methods have been used to investigate the band offsets of thin interface, examples of such techniques include, X-ray photoemission spectroscopy, infrared absorption or photoluminescence excitation spectroscopy, transport methods and internal photoemission spectroscopy. Also first-principles simulations which can be modelled with density functional theory have recently received attention [48]. It has been widely observed that x-ray photoemission produces a more reliable band offsets for a variety of metal/high-κ /semiconductor systems when compared with other techniques. The reliability of photoemission spectroscopy methods can be attributed to the fact that the approach allows the valence-band offset to be estimated directly by measurement of valence-band maxima, which can be obtained by extrapolating the spectra of oxide and semiconductor substrate [44]. The prerequisite for an alternative high-κ gate oxide is that it must serve as an effective barrier to electrons and holes, and this requires that the band offsets for both conduction and valence-band must be greater than 1 eV to prevent the Schottky electrons or holes emission into their bands [45].

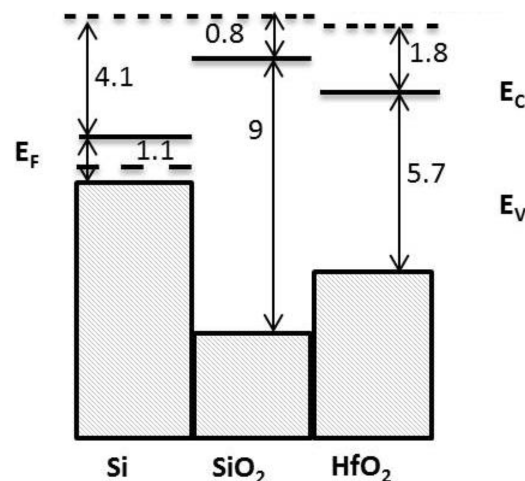

Figure 1.6 Band diagram of the $HfO_2/SiO_2/Si$ stack.

1.7 Research Objectives and Scope of this Work

The main aim of this thesis is to characterize the interfaces of various high-κ materials deposited on Ge substrates by Atomic Layer Deposition (ALD) and other deposition techniques for advanced MOSFET devices, with a view to determine the quality of the interface and band offsets. Physical and electrical device characterization included using techniques such as AFM (Atomic Force Microscopy), XRD (X-Ray diffraction), VASE (Variable Angle Spectral Ellipsometry), Capacitance Voltage (C-V), Current Voltage (I-V) and XPS (X-ray photoelectron microscopy), as well as post growth micro-structural and compositional analysis. As mentioned previously, some metal oxides, such as Y_2O_3, ZrO_2, HfO_2 and Al_2O_3 have been studied on germanium but generally these studies lack a systematic investigation at the interface and determination of the band alignment.

The X-ray photoemission (XPS) technique and Variable Angle Spectroscopic Ellipsometery (VASE) were used to systematically study the surface and interface of GeO_2, Y_2O_3, Al_2O_3, HfO_2, Ta_2O_5 and Tm_2O_3 thin film layers thermally grown on Ge substrates under differing conditions of temperature and thickness. Y_2O_3 was grown in-situ by co-deposition of Y and atomic oxygen, HfO_2 was deposited on Ge by ALD at University of Liverpool and Tm_2O_3 was deposited on Ge by ALD at KTH Sweden. Tm_2O_3 thin film layers on Si were also investigated.

The bulk of the work has been published in a series of publications, enabling the thesis to be presented as a series of published papers, and it is structured as follows:

Chapter 2 presents the fabrication techniques of the high-κ oxides on Ge, and briefly describes the physical principles of the various experimental techniques used.

Chapter 3 presents an overview study of two germanium interface engineering routes, firstly a germanate formation via La_2O_3 and Y_2O_3, and secondly a barrier layer approach using Al_2O_3 and Tm_2O_3. The interfacial composition, uniformity, thickness, band gap, crystallinity, absorption features and valence band offset are shown, as ascertained using X-ray photoelectron spectroscopy, ultra violet variable angle spectroscopic ellipsometry, and high resolution transmission electron microscopy. The correlation of these results with electrical characterization data make a case for Ge interface engineering with rare-earth inclusion as a viable route to achieve high performance Ge CMOS. This work has been published in ref [46]. The contributions of the authors are as follows: M. Althobaiti Collected and analyzed XPS, XRD data, prepared the figures and discussed all the results. I.Z. Mitrovic wrote the paper. N.

Sedghi collected the CV measurements and A.D. Weerakkody analyzed SE data. C. Henkel, E. Dentoni Litta, P.-E. Hellström and M. Östling made the samples. All authors, including S. Hall, V.R. Dhanak, P.R. Chalker, were involved in the discussion of the results.

Chapter 4 following the review of the rare-earth (RE) oxides La_2O_3 and Y_2O_3 on germanium presented in the previeus chapter, chapter 4 considers in details the effect of deposition temperature on molecular beam epitaxy fabricated La_2O_3/Ge and Y_2O_3/Ge gate stacks. This has been investigated using vacuum ultra-violet variable angle spectroscopic ellipsometry, X-ray photoelectron spectroscopy, medium energy ion scattering, Atomic Force Microscopy and X-ray diffraction. Moreover, this chapter focuses on the Ge interface engineering approach using La_2O_3 and Y_2O_3 RE-oxides. These high-κ oxides have moderate reactivity with Ge to form a germanate interface whose purpose is two-fold: firstly to reduce the interface defects and secondly to suppress the GeO_x desorption at the interface. This work has been published in ref [47]. The contributions of the authors are as follows: M. Althobaiti collected and analyzed XPS, XRD data, prepared the figures and discussed all the results. I.Z. Mitrovic wrote the paper. N. Sedghi collected the CV measurements and A.D. Weerakkody analyzed SE data. All authors, including S. Hall, V.R. Dhanak, P.R. Chalker, W.M. Linhart, T.D.Veal, were involved in the discussion of the results.

Chapter 5 while the rare-earth (RE) oxides La_2O_3 and Y_2O_3 show moderate reactivity with Ge, chapter 5 investigate the band line-up of Tm_2O_3 on Ge, sub-band gap absorption features, and interface properties of the thulium oxide deposited by atomic layer deposition (ALD) using angle resolved X-ray photoelectron spectroscopy (AR-XPS), and vacuum ultra violet variable angle spectroscopic ellipsometry. Furthermore, the effect of post-deposition annealing (PDA) on equivalent oxide thickness (EOT) of thin ~ 5 nm Tm_2O_3/epi Ge/Si gate stacks has been examined. This chapter conveys three important findings: (i) the valence band offset for Tm_2O_3/Ge of 3.05 ± 0.2 eV, determined by Kraut's method using a single sample consequently sputtered with core-level spectra taken at different sputtering times, shows consistency within experimental error with the offset result obtained using three distinctive samples (bulk, interfacial and substrate); (ii) the VBO for thermal GeO_2/Ge is in agreement with the most recent report from Toriumi's group substantiating a conduction band offset (CBO) higher than 1 eV and the appropriateness of GeO_2 use in passivation of Ge; (iii) Tm_2O_3 shows even lower reactivity on Ge than on Si, with an atomically sharp interface indicating possible barrier

properties. This work has been published in ref [48, 49]. The contributions of the authors is as follows*:* M.Althobaiti worked on ALD at KTH, Sweden to fabricate the Tm2O3 thin films with C. Henkel, P. E. Hellström, and M.Östling and E.Dentoni Litta. M. Althobaiti then collected and analyzed XPS, XRD and SE data**.** I.Z. Mitrovic authored the paper. N. Sedghi collected the CV measurements and A.D. Weerakkody analyzed SE data. All authors, including S. Hall, V.R. Dhanak, P.R. Chalker, were involved in the discussion of the results.

Chapter 6 having considered the rare-earth oxides in the previous chapters, the following three chapter's discuses HfO_2 on germanium. Chapter 6 considers the use of a passivation scheme combined with HfO_2 as a high-*κ* layer, to achieve an EOT as low as 1.3 nm with an acceptable leakage current of less than $10^{-7}Acm^{-2}$ at ±1 V .This work has been published in ref [50]. The contributions of the authors are as follows*:* M. Althobaiti collected and analyzed the XPS data. S. Mather wrote the paper and carried out CV measurements. All authors, including S. Hall, P.R. Chalker, N. Sedghi, V.R. Dhanak, P.R. Chalker, and I.Z. Mitrovic were involved in the discussion of the results.

Chapter 7 the use of a passivation scheme is explored in chapter 7 which considers hafnia and alumina thin films together with sulphur pre-passivation of germanium. HfO_2/Ge and Al_2O_3/Ge gate stacks were deposited by ALD using O-plasma and H_2O. Both O-plasma and O_3 as the co-reagents in ALD avoid the potential incorporation of hydrogen that is possible if using H_2O vapour. The hydroxyl incorporation has been reported for H_2O-based ALD. Oxygen-plasma and O_3 have more effective pumping speeds facilitating shorter purge times than H_2O. O_3 is effectively more reactive than O-plasma, which can lead to thicker interfacial oxides at the growth temperatures of 250°C used in this work, and also can lead to more carbon incorporation from the metal precursor ligands. Therefore, O-plasma and H_2O were used as oxidants during ALD and an assessment of their effect on the S passivated germanium is the main new contribution of this work. This work has been published in ref [51]. The contributions of the authors are as follows: M. Althobaiti fabricated the HfO_2 thin films by ALD with S. Mather, collected XPS, IPES, data and analyzed it and wrote the paper. N. Sedghi collected the CV measurements. All authors, including S. Hall, P.R. Chalker, N. Sedghi, V.R. Dhanak, and I.Z. Mitrovic were involved in the discussion of the results.

Chapter 8 continues the investigation of HfO_2 on germanium and considers the effect of mixing the HfO_2 with TiO_2. A 0.3 nm Al_2O_3 interfacial layer was deposited on the germanium substrate to passivate the surface. Then, the thin films with different content of the TiO_2 in HfO_2 were deposited by atomic layer deposition (ALD). The effect of TiO_2 content in hafnium oxide was explored in terms of physical and electrical properties. Furthermore, the interface quality and chemical structure between the oxides and substrate was investigated. The results provided a reference for the properties and the performance of TiO_2-HfO_2 thin films, which are presented and discussed in the chapter. This work has been published in ref [52]. The contributions of the authors are as follows*:* M. Althobaiti collected and analysed the XPS data. Lu. Qifeng wrote the paper. All authors, including Mu. Yifei, W. Joseph, V.R. Dhanak, W. Jingjin, Z. Chun, C. Zhou, L. Yang, I.Z. Mitrovic, S. Taylor. P.R. Chalker, were involved in the discussion of the results.

Chapter 9 presents measurements of Ta_2O_5 thin films on Ge. Ta_2O_5 films were deposited on germanium by atomic layer deposition (ALD) at 250°C with and without sulphur passivation. X-ray photoelectron spectroscopy (XPS) was carried out to investigate the band line-up of Ta_2O_5 films with respect to germanium. The results show that the valance band offsets of Ta_2O_5 with respect to sulphur-passivated and unpassivated germanium are 2.67 eV and 2.84 eV respectively. The band gap value of 20 nm thick Ta_2O_5 films was determined to be 4.44 eV from the electron energy loss spectrum of O1s core level [53].

Chapter 10 summarizes the work of the thesis and concludes with an outlook for future work.

1.8 References

[1] De Forest L, inventor. Oscillation-responsive device. United States patent US 824,637. 1906 Jun 26.

[2] Edgar LJ, inventor. Method and apparatus for controlling electric currents. United States patent US 1,745,175. 1930 Jan 28.

[3] William S, inventor; Bell Telephone Labor Inc, assignee. Semiconductor amplifier. United States patent US 2,502,488. 1950 Apr 4.

[4] Shockley W, Sparks M, Teal GK. p− n Junction Transistors. Physical Review. 1951 Jul 1;83(1):151.

[5] Sze SM, Ng KK. Physics of semiconductor devices. John Wiley & Sons; 2006 Nov 3.

[6] Sapoval B, Hermann C, Hermann C. Physics of semiconductors. Springer Science & Business Media; 2003 Oct 17.

[7] Balkanski M, Wallis RF. Semiconductor physics and applications. Oxford University Press; 2000 Aug 31.

[8] Nobelprize.org. The Nobel Prize in Physics 2000 [Internet]. 2016 [cited 8 January 2016]. Available from: http://www.nobelprize.org/nobel_prizes/physics/laureates/2000

[9] Kahng D, Atalla MM. Silicon-silicon dioxide field induced surface devices. InIRE Solid-State Device Research Conference 1960 Jun 13.

[10] Source: http://www.computerhistory.org/semiconductor/timeline/1960-MOS.html.

[11] He G, Sun Z, editors. High-k Gate Dielectrics for CMOS Technology. John Wiley & Sons; 2012 Aug 10.

[12] Moore G. Moore's law. Electronics Magazine. 1965 Apr.

[13] Is.umk.pl. [Internet]. 2016 [cited 8 January 2016]. Available from: http://www.is.umk.pl/~duch/Wyklady/komput/w03/Moores_Law.jpg

[14] Timp G, Bude J, Bourdelle KK, Garno J, Ghetti A, Gossmann H, Green M, Forsyth G, Kim Y, Kleiman R, Klemens F. The ballistic nano-transistor. InElectron Devices Meeting, 1999. IEDM'99. Technical Digest. International 1999 Dec 5 (pp. 55-58). IEEE.

[15] Chau R, Kavalieros J, Roberds B, Schenker R, Lionberger D, Barlage D, Doyle B, Arghavani R, Murthy A, Dewey G. 30 nm physical gate length CMOS transistors with 1.0 ps n-MOS and 1.7 ps p-MOS gate delays. InElectron Devices Meeting, 2000. IEDM'00. Technical Digest. International 2000 Dec 10 (pp. 45-48). IEEE.

[16] Depas M, Vermeire B, Mertens PW, Van Meirhaeghe RL, Heyns MM. Determination of tunnelling parameters in ultra-thin oxide layer poly-Si/SiO 2/Si structures. Solid-State Electronics. 1995 Aug 31;38(8):1465-71.

[17] Fromhold AT. Quantum Mechanics for Applied Physics and Engineering. Courier Corporation; 1981.

[18] Stathis JH. Percolation models for gate oxide breakdown. Journal of Applied Physics. 1999 Nov 15;86(10):5757-66.

[19] Nazarov YV, Blanter YM. Quantum transport: introduction to nanoscience. Cambridge University Press; 2009 May 28.

[20] Busani T, Devine RA. The importance of network structure in high-k dielectrics: LaAlO3, Pr2O3, and Ta2O5. AIR FORCE RESEARCH LAB KIRTLAND AFB NM SPACE VEHICLES DIRECTORATE; 2005 Aug 19.

[21] Zhu X, Zhu JM, Li A, Liu Z, Ming N. Challenges in atomic-scale characterization of high-k dielectrics and metal gate electrodes for advanced CMOS gate stacks. Journal of materials science & technology. 2009 May 1;25(3):289.

[22] Plummer JD, Griffin PB. Material and process limits in silicon VLSI technology. Proceedings of the IEEE. 2001 Mar;89(3):240-58.

[23] Buchanan DA, Lo SH. Reliability and integration of ultra-thin gate dielectrics for advanced CMOS. Microelectronic engineering. 1997 Jun 30;36(1):13-20.

[24] Robertson J. High dielectric constant gate oxides for metal oxide Si transistors. Reports on Progress in Physics. 2006 Feb 1;69(2):327.

[25] Coh S, Heeg T, Haeni JH, Biegalski MD, Lettieri J, Edge LF, O'Brien KE, Bernhagen M, Reiche P, Uecker R, Trolier-McKinstry S. Si-compatible candidates for high-κ dielectrics with the P b n m perovskite structure. Physical Review B. 2010 Aug 3;82(6):064101.

[26] Intel.com. High-k and Metal Gate Transistor Research [Internet]. 2016 [cited 8 January 2016]. Available from: http://www.intel.com/pressroom/kits/advancedtech/doodle/ref_HiK-MG/high-k.htm

[27] Robertson J. High dielectric constant oxides. The European Physical Journal Applied Physics. 2004 Dec 1;28(03):265-91.

[28] Wilk GD, Wallace RM, Anthony JM. High-κ gate dielectrics: Current status and materials properties considerations. Journal of applied physics. 2001 May 15;89(10):5243-75.

[29] Coh S, Heeg T, Haeni JH, Biegalski MD, Lettieri J, Edge LF, O'Brien KE, Bernhagen M, Reiche P, Uecker R, Trolier-McKinstry S. Si-compatible candidates for high-κ dielectrics with the P b n m perovskite structure. Physical Review B. 2010 Aug 3;82(6):064101.

[30] Zhan N, Poon MC, Kok CW, Ng KL, Wong H. XPS study of the thermal instability of HfO2 prepared by Hf sputtering in oxygen with RTA. Journal of The Electrochemical Society. 2003 Oct 1;150(10):F200-2.

[31] Peacock PW, Robertson J. Bonding, Energies, and Band Offsets of S i− Z r O 2 and H f O 2 Gate Oxide Interfaces. Physical review letters. 2004 Feb 6;92(5):057601.

[32] Surnev L, Tikhov M. Oxygen adsorption on a Ge (100) surface: I. Clean surfaces. Surface Science. 1982 Dec 2;123(2):505-18.

[33] Chen JJ, Bojarezuk N, Shang H, Copel M, Hannon JB, Karasinski J, Preisler E, Banerjee SK, Guha S. Ultrathin Al 2 O 3 and HfO 2 gate dielectrics on surface-nitrided Ge. Electron Devices, IEEE Transactions on. 2004 Sep;51(9):1441-7.

[34] Thayne I, Hill R, Holland M, Li X, Zhou H, Macintyre D, Thoms S, Kalna K, Stanley C, Asenov A, Droopad R. Review of Current Status of III-V MOSFETs. ECS transactions. 2009 May 15;19(5):275-86.

[35] Jackson TN, Ransom CM, DeGelormo JF. Gate-self-aligned p-channel germanium MISFETs. Electron Device Letters, IEEE. 1991 Nov;12(11):605-7.

[36] Dimoulas A, Mavrou G, Vellianitis G, Evangelou E, Boukos N, Houssa M, Caymax M. HfO2 high-kappa gate dielectrics on Ge (100) by atomic oxygen beam deposition. Applied Physics Letters. 2005 Jan;86(3):2908.

[37] Nelen LM, Fuller K, Greenlief CM. Adsorption and decomposition of H 2 S on the Ge (100) surface. Applied surface science. 1999 Aug 11;150(1):65-72.

[38] Krüger P, Pollmann J. First-principles theory of sulfur adsorption on semi-infinite Ge (001). Physical review letters. 1990 Apr 9;64(15):1808.

[39] Dalapati GK, Tong Y, Loh WY, Mun HK, Cho BJ. Electrical and interfacial characterization of atomic layer deposited high-κ gate dielectrics on GaAs for advanced CMOS devices. Electron Devices, IEEE Transactions on. 2007 Aug;54(8):1831-7.

[40] Weser T, Bogen A, Konrad B, Schnell RD, Schug CA, Steinmann AW. Photoemission surface core-level study of sulfur adsorption on Ge (100). Physical Review B. 1987 May 15;35(15):8184.

[41] Waldrop JR, Grant RW, Kowalczyk SP, Kraut EA. Measurement of semiconductor heterojunction band discontinuities by x-ray photoemission spectroscopy. Journal of Vacuum Science & Technology A. 1985 May 1;3(3):835-41.

[42] Franciosi A, Van de Walle CG. Heterojunction band offset engineering. Surface Science Reports. 1996 Dec 31;25(1):1-40.

[43] Sze SM. Physics of semiconductor devices. New York, Wiley-Interscience, 1981. 878 p.. 1981;1.

[44] Puthenkovilakam R, Chang JP. Valence band structure and band alignment at the ZrO2/Si interface. Applied physics letters. 2004;84(8):1353-5.

[45] Martinez E, Leroux C, Benedetto N, Gaumer C, Charbonnier M, Licitra C, Guedj C, Fillot F, Lhostis S. Electrical and chemical properties of the HfO2/SiO2/Si stack: Impact of HfO2 thickness and thermal budget. Journal of The Electrochemical Society. 2009 Aug 1;156(8):G120-4.

[46] Mitrovic IZ, Althobaiti M, Weerakkody AD, Sedghi N, Hall S, Dhanak VR, Mather S, Chalker PR, Tsoutsou D, Dimoulas A, Henkel C. (Invited) Interface Engineering Routes for a Future CMOS Ge-Based Technology. ECS Transactions. 2014 Mar 24;61(2):73-88.

[47] Mitrovic IZ, Althobaiti M, Weerakkody AD, Dhanak VR, Linhart WM, Veal TD, Sedghi N, Hall S, Chalker PR, Tsoutsou D, Dimoulas A. Ge interface engineering using ultra-thin La2O3 and Y2O3 films: A study into the effect of deposition temperature. Journal of Applied Physics. 2014 Mar 21;115(11):114102.

[48] Mitrovic IZ, Hall S, Althobaiti M, Hesp D, Dhanak VR, Santoni A, Weerakkody AD, Sedghi N, Chalker PR, Henkel C, Litta ED. Atomic-layer deposited thulium oxide as a passivation layer on germanium. Journal of Applied Physics. 2015 Jun 7;117(21):214104.

[49] Mitrovic IZ, Althobaiti M, Weerakkody AD, Sedghi N, Hall S, Dhanak VR, Chalker PR, Henkel C, Litta ED, Hellström PE, Östling M. Interface engineering of Ge using thulium oxide: Band line-up study. Microelectronic Engineering. 2013 Sep 30;109:204-7.

[50] Mather S, Sedghi N, Althobaiti M, Mitrovic IZ, Dhanak V, Chalker PR, Hall S. Low EOT GeO 2/Al 2 O 3/HfO 2 on Ge substrate using ultrathin Al deposition. Microelectronic Engineering. 2013 Sep 30;109:126-8.

[51] Althobaiti M, Mather S, Sedghi N, Dhanak VR, Mitrovic IZ, Hall S, Chalker PR. Hafnia and alumina on sulphur passivated germanium. Vacuum. 2015 Mar 28;122:306-309.

[52] Lu Q, Mu Y, Roberts JW, Althobaiti M, Dhanak VR, Wu J, Zhao C, Zhao CZ, Zhang Q, Yang L, Mitrovic IZ. Electrical Properties and Interfacial Studies of HfxTi1−xO2 High Permittivity Gate Insulators Deposited on Germanium Substrates. Materials. 2015 Dec 2;8(12):8169-82.

[53] Althobaiti MG, Stoner J, Dhanak VR, Potter RJ, Mitrovic IZ. Band alignment of Ta 2 O 5 on sulphur passivated Germanium by X-ray photoelectron spectroscopy. InPh. D. Research in Microelectronics and Electronics (PRIME), 2015 11th Conference on 2015 Jun 29 (pp. 161-163). IEEE.

Chapter 2

Experimental Techniques

2.1 Atomic layer deposition (ALD)

Atomic layer deposition (ALD) is an extremely powerful technology for various advanced nanotechnology research. It has variety of applications in microelectronics, biomedical, and quality control. It can be used to get very high quality gate dielectrics (including high-k dielectrics) for microelectronics applications. ALD is the state-of-art controlled technique of precise deposition ofatomically specified material layers. ALD is based on chain of, surface controlled and self-limiting gaseous phase chemical reactions with the capability of growing highly uniform atomically thick material films. Precursor gases are pulsed sequentially in the chamber where the substrate is kept. Precursors may be one or more chemical vapours or gases. Deposition process is designed as sequence of pulse and purge steps. After every pulse of vapour or gas a purge step is done to remove the byproducts formed during the pulse process. This is the reason why two pulse and purge steps are needed for a complete cycle [1].

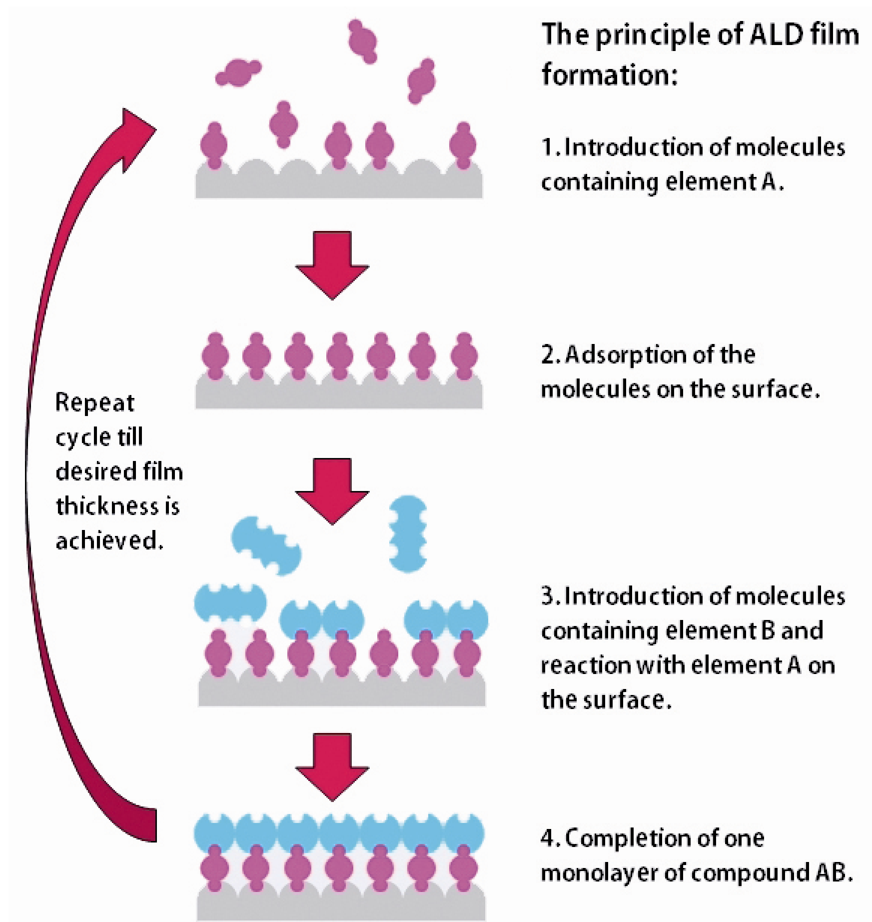

Figure 2.1 Cycle of the ALD process.

Figure 2.1 shows the individual introduction of reactants A and B to get the final product (film) AB. Molecule A is introduced in the first pulse, where it interacts with the surface of the

substrate and gets absorbed. Once this is done the substrate surface is purged during the following purge step, this removes the unabsorbed traces of molecule A. In the next step molecule B is pulsed to the chamber, where it reacts with absorbed molecule A and forms the desired product AB. Another purge step is done to remove the remaining by products from the chamber, which completes the process cycle. Number of cycles can be decided based on the required film thickness. It is also possible to create multilayer structures using atomic layer deposition. It is usually done at lower temperature which makes the use of biological and fragile substrates possible. The limitations of ALD technique are low deposition rate, limitations of substrates to be used as many precursors are sensitive to oxygen/ air, and volatile precursors [1].

2.2 Molecular Beam Epitaxy

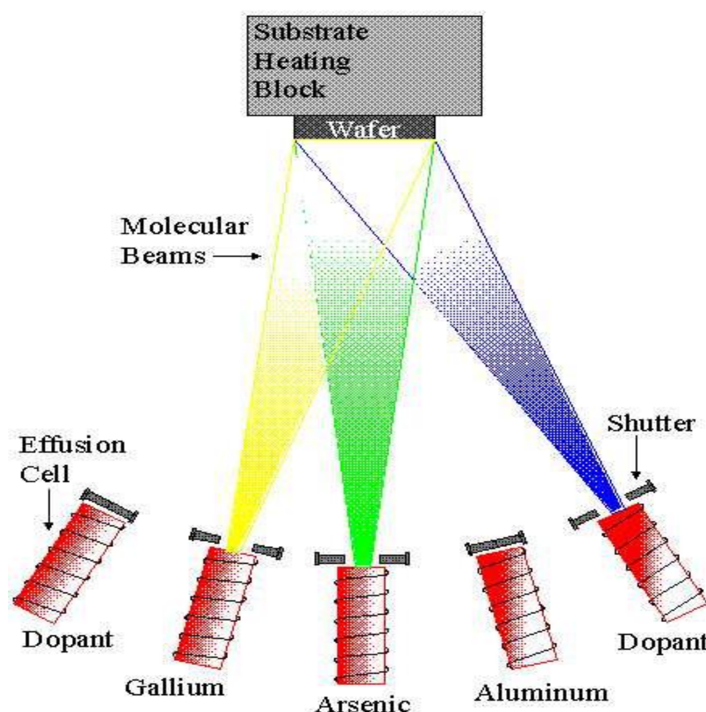

Fig. 2.2 Schematic drawing of a generic MBE system [25].

Molecular beam epitaxy (MBE) is a technique of producing high quality molecular layers of metals, insulator and superconductors. MBE is an UHV based technique providing monolayer deposition control. Films are deposited over a heated substrate by molecular beams produced by the sublimation of desired materials kept in high purity crucibles. A schematic of the apparatus is shown in Fig. 2.24, the beams produced by the sublimation of materials possess thermal energy and get absorbed on the substrate surface. These beams can also be produced by directly

using the gas sources such as PH_3, and AsH_3 [2]. Molecular beam epitaxy is considered to be a good technique for controlled deposition of thin films. Properties such as roughness, uniformity and interface quality can be controlled while using MBE for deposition. It also allows the use of electron diffraction probes for analysis during the growth. The MBE instrument has various sections, the important section or parts are vacuum system, pumping system, liquid N_2 cryopanels, effusion cells, substrate manipulators and analysis tools. The deposition technique selection depends on the application. For example if the film purity, surface roughness and interface quality are important features then MBE is the preferred choice whereas MBE is not suitable for mass production because of its low deposition rate and limited wafer holding capacity [2].

2.3 Vacuum System

Ultra High Vacuum X-ray phptoelectron spectroscopy (XPS) is a method for analysing the surface properties of materials; however it is a surface sensitive technique. Presence of impurities onto the surface may lead to significant interference with the observed spectra and in fact, almost all the procedures involved in the preparation of the sample are also expected to contribute to the problem. In order to overcome this major barrier, first, a good vacuum is required to create a perfect surface of high degree purity. As a rule, pressure as low as 10^{-5} torr would create the required passing medium to allow photoelectron to reach the detector without collision with other gas molecules. Whereas, pressure of 10^{-9}torr or lower (an ultra-high vacuum, UHV) is a prerequisite to keep an active surface clean for several minutes. However, where contamination is minimal, which is commonly needed for most work, pressures in the range of 10^{-8}-10^{-9} torr would be reasonable, although, UHV is an essential requirement for well-defined characteristics [3].

One of the major setbacks suffered by XPS developments is the inability to create the required vacuum condition that is needed for the construction of XPS instruments. A vacuum is created when molecules of gas or air is pumped out of a confined space relative to its surrounding. According to classical physics, it is the collisions between these molecules and its confined boundary that constitute the pressure. A highly efficient pumping system and a chamber capable of displaying the outgassing features, are required to create an ultra-high vacuum condition. Simply put, outgassing is defined as surface adsorbates' removal, these adsorbates are produced during exposure of a surface to atmospheric ambient [3].

The construction of vacuum chambers is commonly done with high quality stainless-steel with metal lining on it. The choice of this material is based on various factors such as lower corrosion rate (which can be further reduced in ultra-high vacuum condition), low outgassing rate, low vapour pressure (stainless-steel is characterised with high melting point), cost effectiveness, easy fabrication techniques such as machining and magnetic shielding.

In fact, during the construction the use of low vapour pressure materials such as borosilicate glass, adhesive tape, and rubber O-ring are considerably minimised. The structural efficiency of the pump is improved when the chambers aim to accommodate UHV conditions are designed in either spherical or cylindrical shapes. There is a specialised plumbing system in XPS instrument and this is made up of more than one pump, tubing, valves, and vacuum gauges [4].

2.4 Photoelectron spectroscopy (PES)

2.4.1 Basic Principle

Ionization energy in the form of radiation is imparted on the material surface, and if the energy is sufficient enough (work function of the material) it knocks out electron from the atom. Such electrons are called photo electrons. The energy of these photoelectrons is monitored and mapped with corresponding location in the material. The number of ejected electrons depends on the photon energy and based on this energy, photoelectron spectroscopy can be categorized intotwo groups: If the energy is lower the technique is Ultraviolet photoelectron spectroscopy (UPS) and XPS for the higher energy which involves X-Rays. XPS further can be split into two categories namely, s-XPS and XPS. s-XPS is termed for energy values below 2000eV, here's represents the soft X-rays. For the higher energy (hard X-rays) the technique is named just the XPS. The typical schematic setup of the XPS system is shown in Figure 2.3.

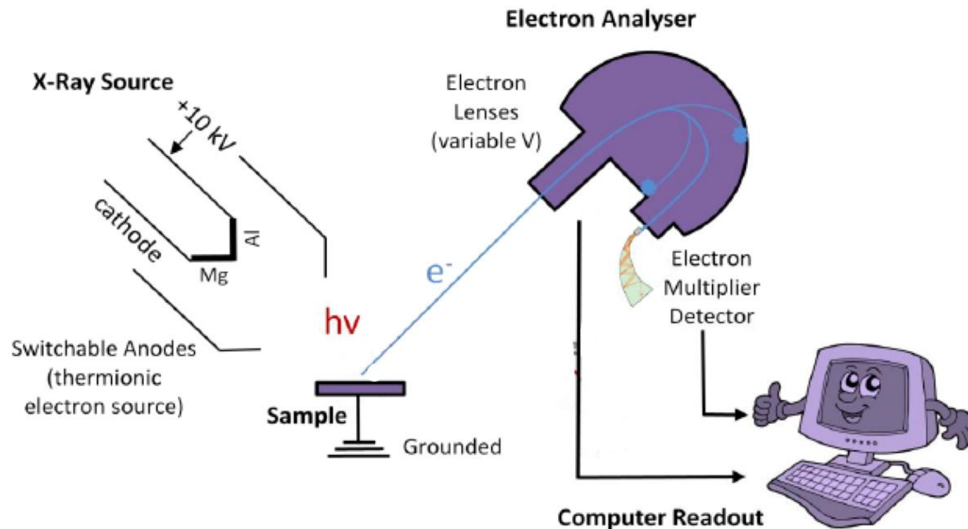

Figure 2.3 XPS system schematic, showing three main parts photon source, sample and analyzer.

XPS system chamber is kept at UHV for operation so that, the photoelectron scattering can be avoided, improving the analysis accuracy. Photoelectron's energy is the energy difference between the incident photon energy and the minimum energy required to take the electron out of the atom. More precisely the electron must have the energy which is the sum of binding energy and workfunction for the material surface. The relationship can be represented by the following expression:

$$K.E = hv - B.E - \varphi \tag{2.1}$$

In equation (2.1), K.E is photoelectron kinetic energy, is the material workfunction, B.E is the electron binding energy and is incident photon frequency. The photoelectron emission process has been described in Figure 2.2. Energy of the occupied energy levels in material can be estimated by the analysis of electron energy. This technique is very specific as each material exhibits the unique energy level sets. Thus a material and its composition can easily be mapped with its corresponding energy level set. This technique can be considered as "material fingerprinting".

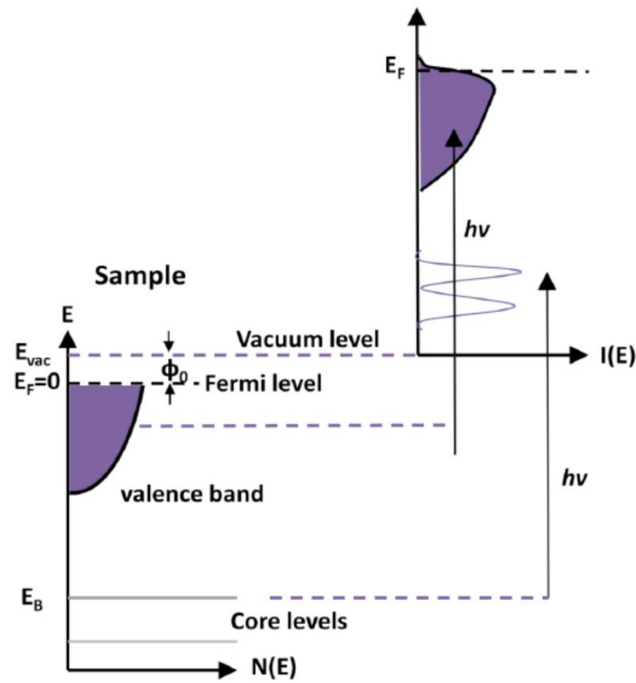

Figure 2.4 Energy level schematic, depicting the photoelectron emission process.

2.4.2 Analysis Depth

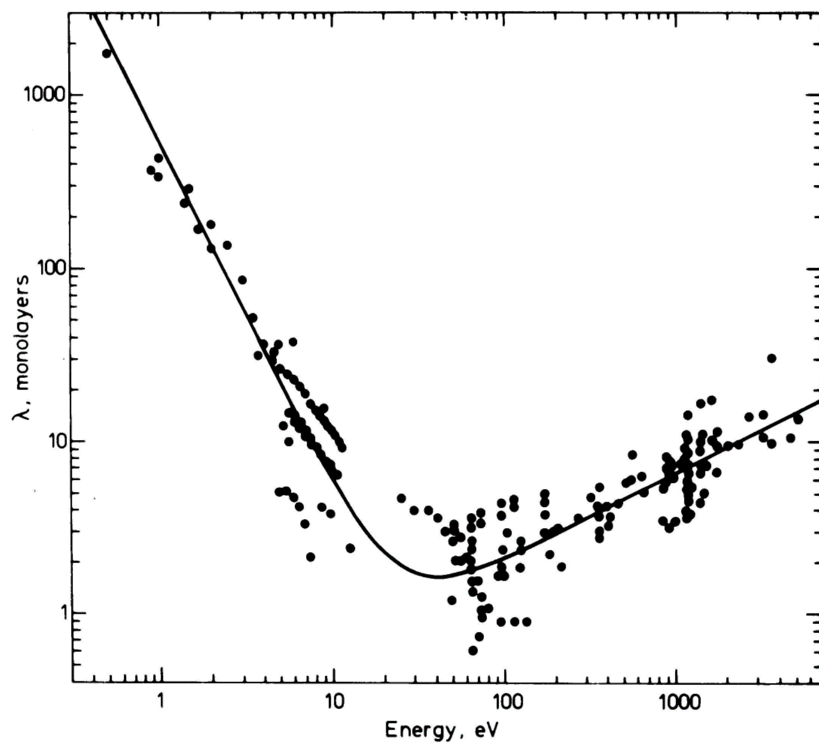

Figure 2.5 Variation in MFP as a function of electron kinetic energy.

Photoemission spectroscopy technique is basically surface sensitive; however we can also formulate the depth sensitivity as well. Figure 2.5 ahows that Depth sensitivity depends on the electron mean free path inside the materialwhich depends on kinetic energy of the electron.The interaction between photoelectrons and electrons makes it a complex process. Emitted electron intensity (I) gets affected by material depth through which an electron possibly travels (d) and the mean free path (λ). The escape depth is found to be proportional to e^{-1}. The relation can be represented as:

$$I \propto e^{-d/\lambda} \tag{2.2}$$

The 95% of the photoelectrons get emitted from the 3λ within the material, and 65% electron emit from λ inside the sample. The percentage can be related to the known values to know the analysis depth. For very complex structure, it is difficult to estimate the analysis depth because of the unavailability of empirical data.

2.4.3 Photon source

Typical size of the photon source consists of about half the complete system. It is observed that for accuracy in the measurement the use of narrow photon energy range is essential, and even better is to use monochromated source.

Energy required to eject electron depends upon the depth from where we are trying to liberate an electron. For example higer energy is required to liberate deeper core level electrons, however energies of less than 20 eV are sufficient for the valence electrons. It can be inferred that ultra violet light source is required electron liberation near the Fermi level, whereas it requires the use of X-rays to study the closed core shell electrons.These X-rays have energies upto several keV. On the other hand, surface sensitivity implies that electrons with energy near the Fermi level (i.e. valence band electrons) would have come from the surface layers of the materials when using UV radiation, and from more bulk regien when using harder X-rays.

The different energy levels can be accessed by different X-ray energy sources as shown in Figure 2.6 According to the physics of XPS, synchrotron based light sources give most accurate measurements. These sources require a big infrastructure and a dedicated facility for their operation. On the other hand lab based X-ray sources are easier to use, with reduced intensity

and resoluation.For example, XPS at generation synchtron facilty such as ELETTRA, can be performed with a resolution of 50 meV at the C1s level.In contrast, our laboratory based monochromated XPS system operates with a resolution of about 0.4 eV. Nevertheless, lab based source has advantges that they can be used routinely and cheaply, and for our purposes provide sufficient resolution. For X-ray generation, a filament forces with a current is kept very close to the metal target. Thermal electrons emitted from the filament get accelerated by the potential applied on the metal target. These electrons, if attain sufficient energy, remove core electrons from the atom. Creating vacancies which are then filled by the higher energy electron, thus releasing energy in the form of X-rays. Table 2.1 shows the common list of metals with their corresponding X-rays.

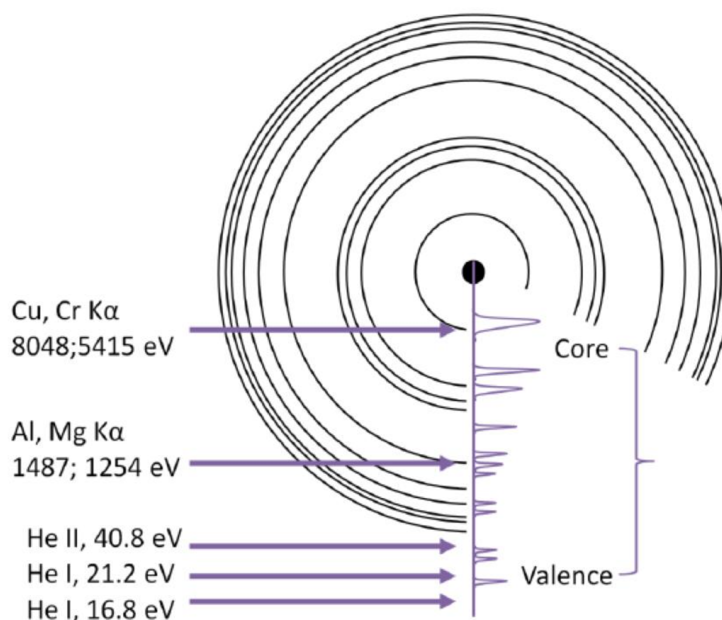

Figure 2.6 Energy levels in an imaginary atom, exited with a range of electromagnetic energies.

Table 2.1 Metal x-ray resonance emission [5].

Element	Energy (eV)	FWHM (eV)
Mg	1253.6	0.7
Al	1486.6	0.9
Si	1739.6	1.0
Cr	5417.0	2.1

2.4.4 Electron Energy Analyser

Energy of the photoelectrons is measured by an electron energy analyser. Electron energy can be measured by three methods which are electric field acceleration, time of flight and change of orbit in a magnetic field. The method using electric field acceleration is used in our lab.

Use of a hemispherical analyser (HAS) is the most popular setup while the cylindrical deflection analysers and cylindrical mirror were the precursors for this. Schematic of a typical hemispherical analyser is shown in Figure 2.7. HAS has a main advantage over other designs that it is having 180° geometry which permits accurate focusing of the electrons without any distortion which in turn allows a well defined angular and energy dispersion. The analyser's function can be divided into three parts which are the focusing by lens, dispersion and counting of the electrons [6, 7].

The desirable electrons to be counted are collected and focused to the entrance slit of the analyser. In the process, the lens operates to accelerate or retard the electrons. At the entrance slit, they have the energy set by the potentials on the lensphase.The lens also allows the sample to be placed at a working distance from the entrance.

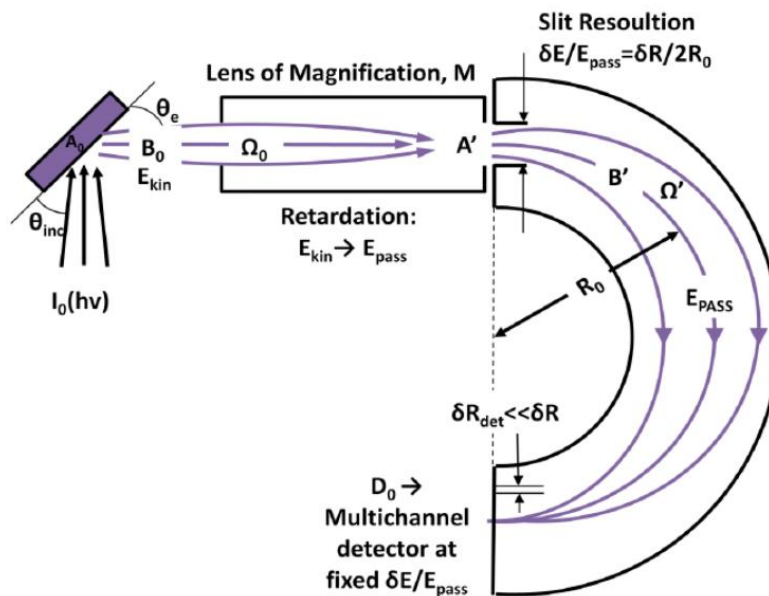

Figure 2.7 Schematic of hemispherical analyzer. Photoelectrons are produced by the sample (top left) and collected by a lens (top centre). Hemispheres are shown on the right and the exit plane with a multi-channel detector is shown on bottom right. At the end a single point detectoralong with an exit slit can also be used.

Complex arrangements of the lenses are used in modern analysers so that the area of the sample can be reduced and the data collected from this allow analysis of smaller samples or to gather more local information from various parts of the sample.

Two concentric and hemispherical metal plates are used to do electron dispersion in a hemispherical analyser. When potential is applied to each of the plates, only electrons which are having certain energies are allowed to pass through to the detector. In order to select the desirable electron energy certain variations in potential can be done on each plates which can be given by the following relationship [5]:

$$\Delta E = e\Delta V\ (R_{inner}R_{outer}/R_{outer}^{2}\text{-}R_{inner}^{2}) = ke\Delta V \qquad (2.3)$$

where, the range of electron energies which are able to pass through is given by ΔE, potential difference between outer and inner hemispherical plates is given by ΔV, plate radius is denoted by R and for a given analyser the particular geometrical constant is given by k. However, the situation is more complex as the resolution of the analyser also depends on the electron energy with improved resolution at lower energies. Due to this, before there is entry of electrons between the plates, a retarding field is applied which can be varied in order to adjust the optimal level electron energies depending on the desired energy. At the exit, there is natural dispersion of electron energy in one direction and angular dispersion in an orthogonal axis [8].

Detection generally involves the counting of electrons or macroscopically measuring of current. Generally, counts per second is used for measuring intensity and the number of voltage pulses in a specified time period is measured by detectors. At any given energy, generally there are very small number of electrons to the point of problematic detection. So, a channel electron multiplier or (CEM) is used to boost the count rate (Fig 2.8).

A channel electron multiplier increase the number of electrons by using a secondary electron emission. After an electron collision event, various electrons are emitted due to the coating of a material on them. CEM design includes a large opening (used to collect incoming electrons) connected to a curved tube. Curved tube of the CEM helps in increasing the feasibility of secondary electrons to collide with the tube in order to produce more and more electrons till the signal is sufficiently amplified.

Following Figure 2.8 illustrates the basic principle of CEM:

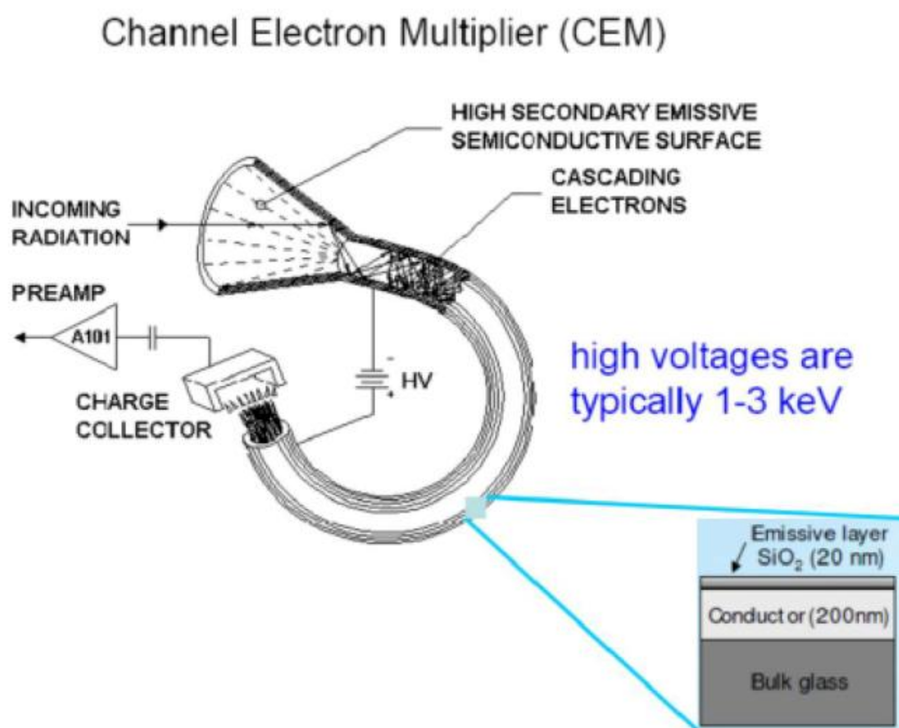

Figure 2.8 A typical channeltron configuration representation with a large opening for collecting incoming electrons and the connecting curved tube [9].

In the front of the collection device, a slit (termed as exit slit) is placed so that the area is selected over which electrons are collected. Energy resolution is defined by slit width which can be varied whereas the angular resolution is defined by the area of the CEM which is generally fixed. There is natural dispersion of the electron energy in the exit plane. When this whole energy window is measured it will markedly increase the count rate and in turn reduce collection time. Hence, the limitation of using a single collection device is shown by this. To tackle this, there is a possibility of using multi-channel devices and there are analysers which have arrays of 5, 9, or more channeltrons. Physical size of such devices is a significant limitation which results in taking up the exit plain by the inter-channeltron space.

In the detector, the entire energy window is measured by the use of a microchannel plate (MCP). A microchannel plate (MCP) is a plate having small CEMs of high density. Gained signal is not as high as a single channel device but it can be increased by using plates in series.

A multi-channel plate is shown in Fig.2.9. MCP's generally have a dense array of hole openings, each a small size of 0.5 mm with 12.5 µm spacing. Because of their small size, the gain is much less as compared to a channeltron unit and hence to produce similar final gains, multi-channel plates are often used in tandem. After amplification of the electron count, the electrons emerge on the other side of the MCP, and are accelerated away and proximity focused onto a phosphor screen. The scintillation of the phosphor is then detected by a CCD camera.

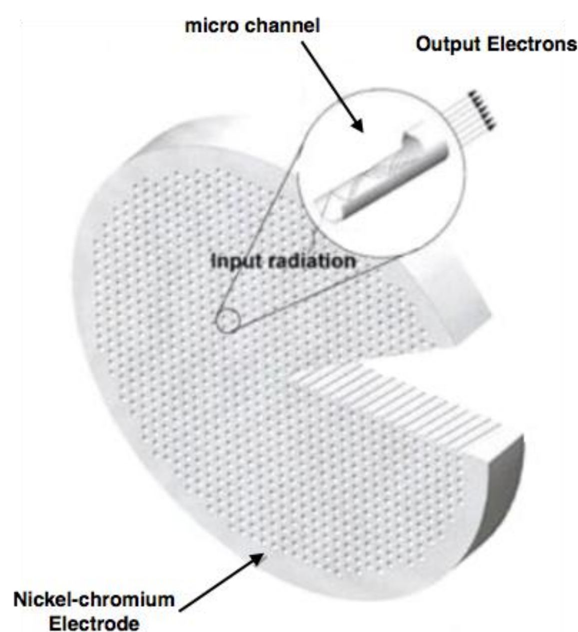

Figure 2.9 A multi-channel plate illustration.

In the current work, XPS was measured with both types of detectors; one containing an array of five CEM's and in another UHV system, an analyser containing a pair of MCP plates mounted in front of a phosphor screen. The main UHV systems used in this work are shown in Fig. 2.9.

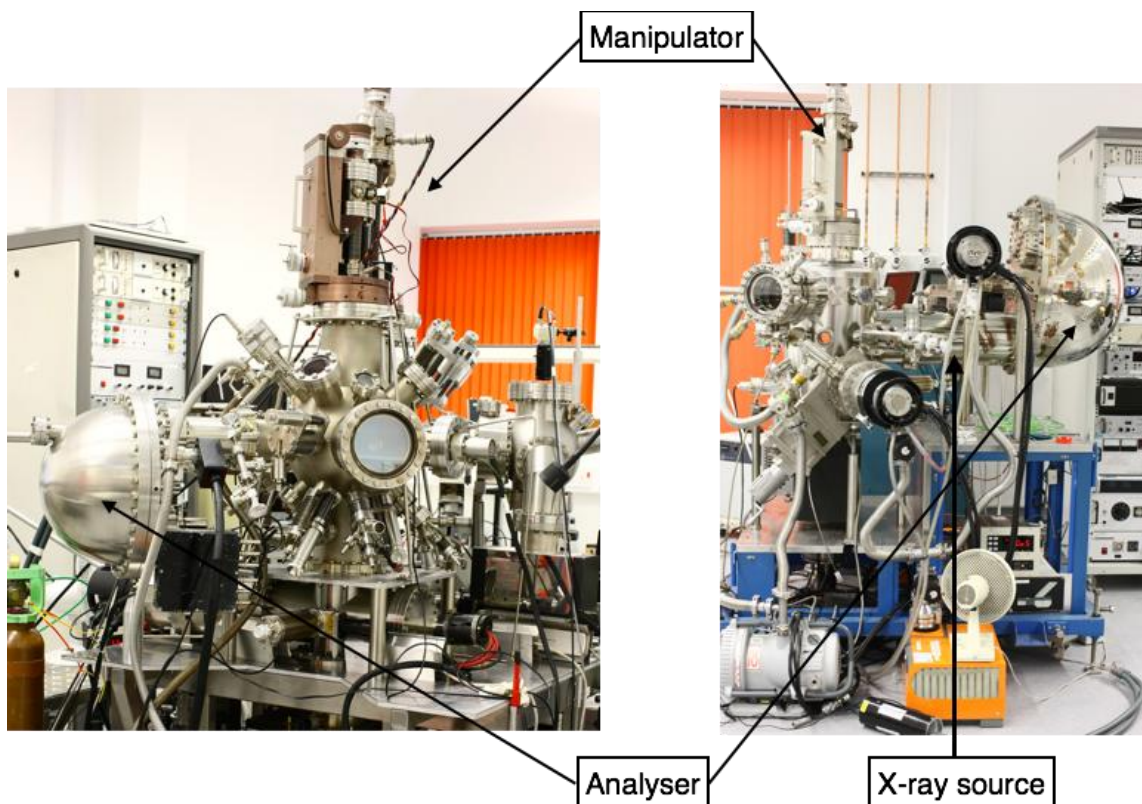

Figure 2.10 UHV systems used in this work at University of Liverpool.

2.4.5 Resolution

Resolution in XPS is affected by three factors such as source width, sample's inherent line width and analyser's resolution. Following expression relates the full width half maximum (FWHM) of the observed peak to the above three factors:

$$w_o^2 = w_s^2 + w_x^2 + w_a^2 \qquad (2.4)$$

where, w_o represents the measured full width half maximum of the XPS core line, w_s represents the intrinsic width of the sample's core level, w_x is the x-ray's FWHM, and w_a is the resolution of the analyser.

The w_s term is a physical property of the sample and represents the core electron hole lifetime, and as such is a constant. The lifetime varies depending on the core level. For example, for shallow core levels and valence levels, the hole lifetime is short, resulting in broad FWHM, while for deeper core levels, the hole lifetime is long, leading to sharp narrow FWHM.

Another physical constant of the X-ray source is the incoming X-ray's natural line width. For a given experiment, different characteristic X-rays are generated by different materials so as to select a good anode, which in turn will improve the resolution. The FWHM and energy values

of few general materials, which are used in X-ray sources is shown in table 2.1. A monochromator can also be used to improve the line width. As compared to a non-monochromatic X-ray, various features such as small X-ray line widths, X-ray satellite lines removal and Bremsstrahlung's reduction are generally offered by the monochromatic X-ray system which results in the reduced incident x-ray's line width and hence improvement in the energy resolution. Al k-α X-rays have 0.9 eV line width whereas the line width reduce by the monochromator for Al k-αis about 0.3 eV. On the other hand UV radiation, which is produced by He excitation in a discharge tube has a source linewidth of 10meV or less.

In accordance with the following expression (Eq. 2.5), the resolution for a hemispherical sphere generally depends both on the incoming photoelectrons angular divergence and the geometrical parameters:

$$\Delta E = E_o\left(\frac{\omega}{2R_O} + \frac{\alpha^2}{4}\right) \quad (2.5)$$

where the average width of two slits is given by , R_o represents the analyser's radius, and the incidence angle of the incoming photoelectrons. E_o is the pass energy of the HAS and is the central potential between the two concentric hemispheres. Generally the first term in equation 2.5 dominates the contribution of the analyser to the overall resolution in XPS. As such, although there are certain difficulties because of size which limits the actual possible sizes, increase in the analyser's radius improves the resolution. E_o can be selected to charge the resolution contribution of analyser.It is clear from the above discussion that when using UV radiation for valence band measurement, the overall resolution is dominated by the contribution of the analyser. On the other hand for XPS the overall resolution is dominated by the X-ray source.

2.4.6 Measurement of band offsets using Krauts method

The X-ray photoelectron spectroscopy has remained the prominent method of measuring the valence band offset (VBO)from the core levels of a system.The basic principle of the Krauts method is illustrated using Fig 2.11 which shows the band offset of Y_2O_3 with respect to germanium (the results is discussed in detail in chapter 4).The first step in this method is to measure the difference between the core level and thevalence band maximum (VBM) for both the high-k oxide ($(E_C - E_V)O_x$ term) and the bulk semiconductor sample. Secondly, a film of high-k oxide/Ge system is measured ($(E_C - E_C)_{int}$ term) using XPS to investigate the difference

in energy of the core levels for each material. Finally, from Kraut equation VBO can be calculated as [10]:

$$VBO = (E_C - E_V)_{Sub} - (E_C - E_V)_{Ox} + (E_C - E_C)_{int} \quad (2.6)$$

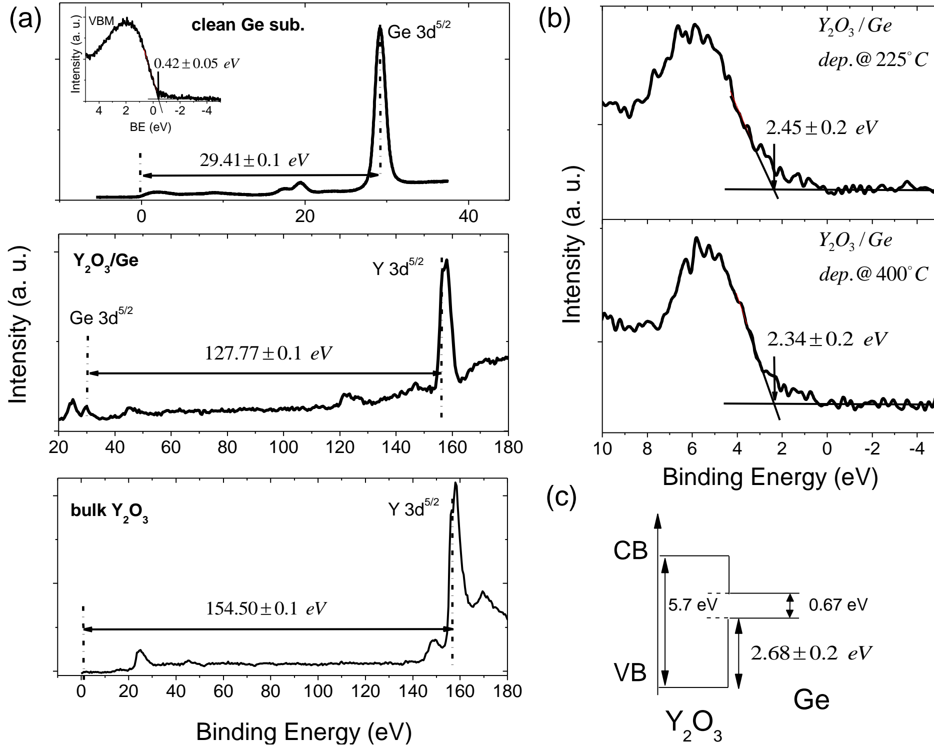

Fig 2.11 shows the band offset of Y_2O_3 with respect to germanium. (a) The XPS spectra for the calclation of VBO for Y_2O_3/Ge using Kraut's method. (b) Valence band spectra for Y_2O_3/Ge gate stacks showing VBO of 2.4 ± 0.20 eV; (c) Derived band diagram for the Y_2O_3/Ge stack.

XPS can be used to determine the oxide bandgap via the loss feature on the high binding energy side of a core level. Determining the band gap allows location of the conduction band offset (CBO). Although, the accuracy of bandgap obtained through this approach is restricted, notwithstanding, the gradient of the loss feature is not different from the background of the XPS spectrum. The oxide bandgap can be measured once the VBO is known, so an accepted value for semiconductor bandgap can be used together with these parameters to estimate the (CBO) between the semiconductor and oxide. Alternatively, a direct estimate of the oxide bandgap can be obtained from the literature. This procedure is subjected to several inconsistencies; this is because the oxide bandgap is known to vary with sample preparation. In this thesis, the band gap was measured by XPS and VASE for a reliable estimate of the band line-up.

2.5 Inverse Photoemission (IPES)

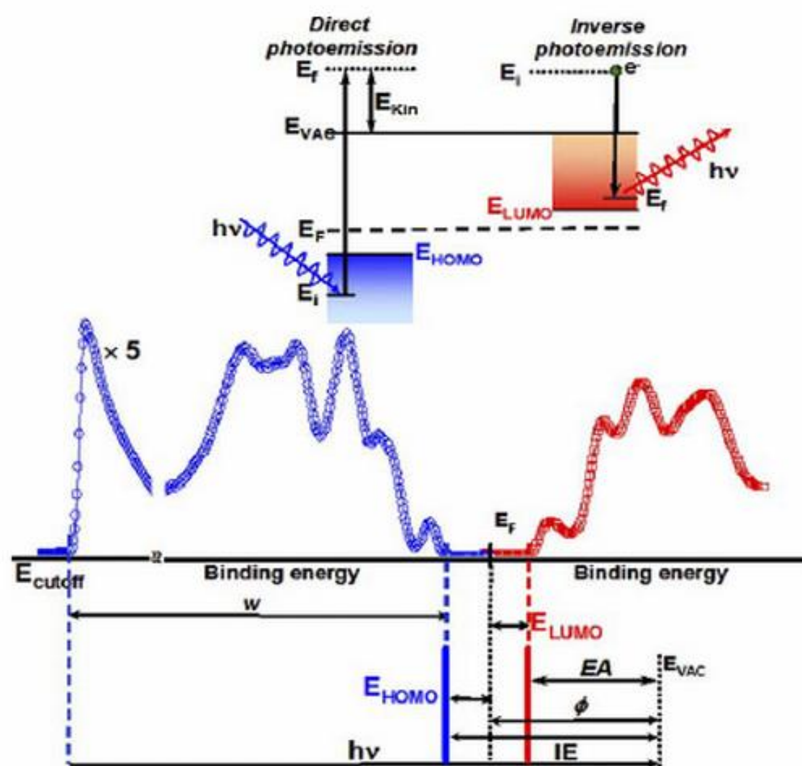

Figure 2.12 illustrates the principles of direct photoemission (blue) and its complementary technique inverse photoemission (red), along with the correspondingly acquired electronic DOS. The figure also presents the fundamental parameters directly probed by the photoemission characterization, such as Highest Occupied Molecular Orbital (HOMO), referring to an organic film or the equivalent VBM for a semiconductor, and Lowest Unoccupied Molecular Orbital (LUMO) or CBM, Electron Affinity (EA), Ionization Energy (IE), and work function (Φ) related to the Fermi level (E_F) and vacuum level (E_{VAC}).

Inverse photoelectron spectroscopy provides a direct way to determine the conduction band maxmuim (CBM). This technique is sometime called Bremsstrahlung Isochromat spectroscopy. It complements ultra-violet photoelectron spectroscopy (UPS) and is used to probe the empty density of states above the Fermi level. Thus a combination of UPS and inverse photoemission (IPES) can be used to determine the valance band maximum (VBM), conduction band maximum (CBM) and indeed the bandgap.

The principle of the technique is shown schematically in Fig. 2.12. A collimated beam of low energy electrons (<20eV) from Barium oxide (BaO) cathode is directed at the sample. These electrons occupy high lying empty electronic states from which they decay to lower states. The

decay process leads to the emission of a photon which is detected using a NaCl coated Ta core. The photon count vs kinetic energy of the incoming electrons is plotted to give a measure of the empty DOS. The system used in this work was a commercial one from PSP vacuum system who also supplies the XPS source and analyser. Thus, the operating software and procedure was complimentary.

2.6 Spectroscopic Ellipsometry (SE)

Spectroscopic ellipsometryis a characterization technique which is used to determine the thickness of the layers, their optical properties and composition. It is based on the polarization difference (incident vs. reflected) measurement over a spectral region from 235 nm to 10000 nm. A probe beam, whose polarization state is known, is launched on the sample under test and the reflected beam is analysed for its polarization state. The two important parameters measured for samples are the wave function (Ψ) and the phase (Δ). Probe beam is a linearly polarized which gets modified to an elliptically polarized beam (reflected), as depicted in Fig. 2.13 The polarization ellipse can be described using a typical p-s coordinate system, where the s-direction is parallel to the sample surface and perpendicular to the propagation direction. However the p-direction is considered to be contained in the plane of incidence and perpendicular to the propagation direction. The plain containing the output beam, the input beam, and the direction normal to the sample surface, is defined as the plane of incidence. The angle between the directions of input beam and normal to the sample surface is defined as the angle of incidence.
Light is a transverse electromagnetic wave which is made up of fluctuating magnetic and electric fields which are perpendicular to each other. Ordinary white light consist of waves fluctuating at possibly all angles. If the light contains waves fluctuating in only a specific plane, it is considered to be "linearly polarized" (Fig. 2.13).

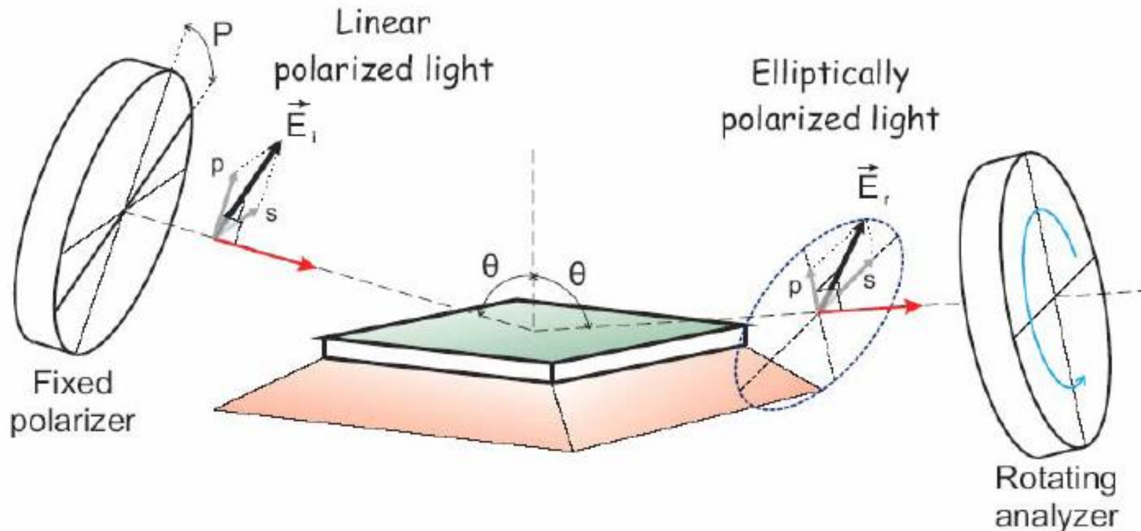

Fig. 2.13 Geometry of an ellispometric experiment showing the p- and s- directions.

It can generate light with a specific angle of vibration, by using polarization effect, which allow only light with a specific vibration angle [11].

Linear polarization can be understood as a special case of circular polarization. It can consider a case where we have one XY plane polarized wave and one YZ plane polarized wave. If the waves are in phase that means they reach their maximum and minimum points at the same time, then their vector sum will lead to a 45° linearly polarized wave (Fig. 2.14a). However, if the two waves are considered 180° out of phase, the resultant will be 45°linearly polarized in the opposite manner (Fig. 2.14b). Further, if the two waves are 90° degrees out of phase and of the same magnitude, the resultant will be circularly polarized (Fig. 2.14c). In general, the two field components E_x and E_y do not have to be equal in magnitude, and therecan be any phase relationship (not necessarily 90° or 180°). An ellipse as a function of time is traced by the tip of the total E-field vector for a general polarization state.As we know that a line segment and a circle are two special types of ellipse, therefore, linearly and circularly polarized light can be achieved by elliptically polarized light. In ellipsometry, Ψ and $\Delta$are measured by determining the polarization of ellipse of the probe beam, that's why this is called ellipsometry. The values Ψ and Δ are expressed using the ratio of Fresnel reflection coefficients $\tilde{R}_s$ and $\tilde{R}_p$ for polarized light s- and p- , respectively according to the relation:

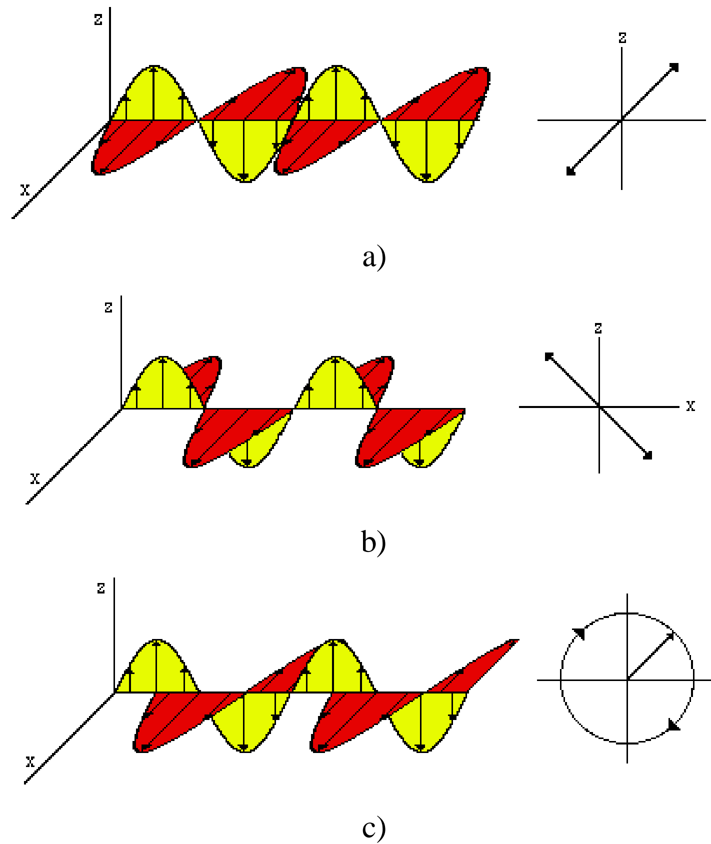

Fig. 2.14 The schematic representation for a)-b) linear and c) circular polarized light.

$$\tilde{\rho} \equiv \frac{\tilde{R}_p}{\tilde{R}_s} = \tan\Psi \exp(i\Delta) \qquad (2.7)$$

In ellipsometry the ratio of two values is estimated which makes it precisely accurate and highly reproducible. Furthermore, the ratio is complex number which contains the information about "phase" (Δ) making the measurement quite sensitive.

A J.A. Woollam Co., Inc. VASE (Variable Angle Spectroscopic Ellipsometry) which is based on the traditional rotating analyzer design canacquire data even at multiple angles of incidence. The basic reason of using a variable angle of incidence instrument is to gather data at angles of incidence around the pseudo-Brewster angle for each and every sample. When the incidence angle is close to pseudo-Brewster angle, the measured Δ values are found to be around 90°, and this range of Δ values gives the sample's most sensitive measurement. It is observed that for semiconductor samples, the pseudo-Brewster angle typically comes out to be around 75°. The ellipsometric system WVASE32^{TM} is used in the Electrical Engineering & Electronics Department; it has the possibility to cover the 245-1000 nm spectral range (470 wavelengths) at a

fixed incidence angle of 75° and also has fast acquisition time, ~ 390 wavelengths in less than 1 second. Within WVASE32^{TM}, optical constants can be represented as a complex refractive index, $\tilde{n} = n + ik = \sqrt{\tilde{\varepsilon}}$ or as a complex dielectric function, $\tilde{\varepsilon} = \varepsilon_1 + i\varepsilon_2$ WVASE32^{TM} considers any optical constants with a positive imaginary part to represent an absorbing material [11].

Using SE, we can determine thin film thicknesses as well as optical constants. To achieve best results with ellipsometry the film thickness should not vary too much in comparison to the wavelength of the light used. This is due the working principle of ellipsometry in which measurement is wavelength limited and also periodic, so if the variation in thickness is much the accurate thickness cannot be estimated. Ellipsometry is especially for dielectric films and limited to one layer analysis with single wavelength ellipsometry. Also, for a valid spectroscopy ellipsometry analysis, roughness of the sample surface or film interfaces should be smaller than ~ 10% of the input beam wavelength. Larger features have concerns of causing non-specular scattering of the incident beam and depolarization of the specularly reflected beam. Finally, the films thicknessunder study should not vary by more than ~ 10% over the spot width on the sample surface, else the assumption of parallel filminterfaces will not be valid, and the calculated data cannot be expected to be close to the experimental data.

SE is an optical technique which requires aprecisely formulated model of the measurement process to analyse the measured data. The main measurements/ parameters analysed by ellipsometric models are the thickness of the layers, andthe optical constants of the substrate and oxide layers. To get good model fits to the measured data we need highly accurate optical constants.It is evident that on the visible, near-UV, and near-IR wavelength ranges, the premier technique for measuring optical constants is ellipsometry.

Precise models are made in such a way that the calculated ellipsometric data matches closely with the experimental data (Ψ, Δ), which helps in determining the structure and composition of the samples.Maximum likelihood estimator defines the goodness of match between the data calculated using the model and the one acquired experimentally. The value of maximum likelihood estimator must be a smallest possible positive number approaching to zero, in the condition of a perfect match in the case of calculated and the experimental data. WVASE32^{TM} uses the mean-squared error (MSE) value as maximum likelihood estimator which is given as:

$$MSE = \frac{1}{2N-M}\sum_{=1}^{N}\left[\left(\frac{\Psi_i^{\mathrm{mod}} - \Psi_i^{\mathrm{exp}}}{\sigma_{\Psi,i}^{\mathrm{exp}}}\right)^2 + \left(\frac{\Delta_i^{\mathrm{mod}} - \Delta_i^{\mathrm{exp}}}{\sigma_{\Delta,i}^{\mathrm{exp}}}\right)^2\right] = \frac{1}{2N-M}\chi^2 \qquad (2.8)$$

where M is the total number of variable parameters used in the model, N is the number of (ψ, Δ) pairs, and σ are the standard deviations calculated on the experimentally calculated data points. Further to estimate the set of values for the variable model parameters which yields a single unique absolute minimum of the MSE fitting is required. This problem is a minimization problem where we need to estimate the minimum value of the MSE. The minimum value should happen at a small value of the MSE, and it should be fairly sharp as a function of the variables. Only one out of many sets of variable parameters will lead to the lowest MSE from the given model. To obtain calibration parameters, WVASE32^{TM} implements the Levenberg-Marquardt algorithm for all model minimizations and for analysis of the calibration data. The primary drawback or limitation of used algorithm is that sometimes it tends to freeze on local minima of the MSE surface, which leads to an incorrect result. Mentioned limitation can be addressed by fitting from widely separated initial guesses for the variables ensuring the best suitable-fit minimum located by the fitting algorithm is actually the true MSE surface's minimum[11].

2.7 X-Ray Diffraction

2.7.1 Principles of XRD

Figure 2.15 shows a beam of X-rays incident on a crystal surface and the beam reflected from the crystals planes at the same angle. The crystal lattice planes can be denoted by Miller indices h.k.l and the separation between the planes can be denoted as d_{hkl} Bragg's law of diffraction can be derived in the following manner. The constructive interference between the reflected and scattered X-rays occurs when the difference of the path lengths Δl of the incident and reflected beams inside the crystal (Fig. 2.15) equals an integer number of wavelengths λ [12-14]:

$$\Delta l = n\lambda \ , n \in \ N \qquad (2.9)$$

When n is na integer (1, 2, 3, etc.) constructive interference occurs.

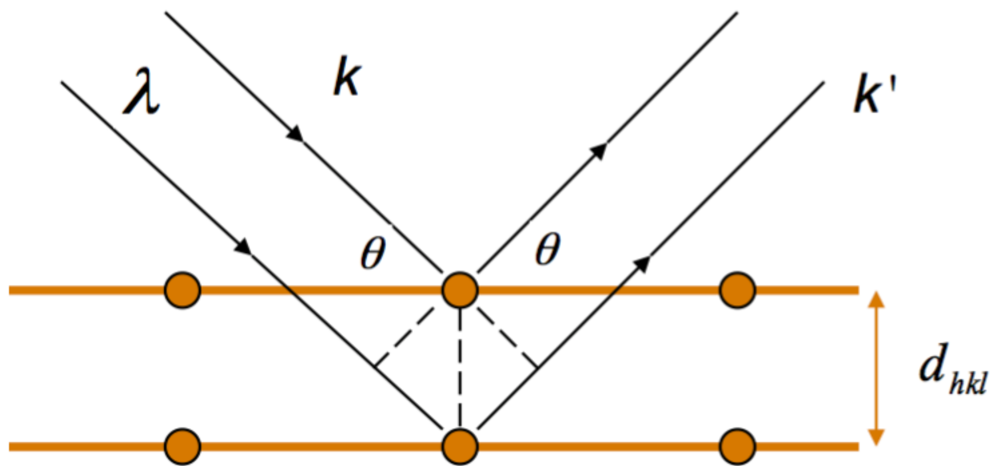

Figure 2.15 Schematic diagram illustrating the principle of X-ray diffraction.

By simple trigonometric geometry, the relationship between the path difference and the distance separating the reflecting planes d_{hkl}:

$$\Delta l = 2d_{hkl} \sin\theta \qquad (2.10)$$

Thus, Bragg's law of diffraction is:

$$n\lambda = 2d_{hkl} \sin\theta \qquad (2.11)$$

Bragg's law of X-ray diffraction relates to the spacing between the crystal planes, the wavelength of the incoming beams and the angle of the reflected beams. This simple relationship can give powerful insights into the structure of crystallographic materials.

2.7.2 Experimental set-up for the study of X-ray diffraction

The experimental set-up of an X-ray diffraction machine consists of three parts, as shown schematically in Figure 2.16, X-ray source, sample and X-ray detector. The X-ray beams from the source are incident on the sample surface. The crystal planes in the sample reflect X-ray beams. The reflected X-ray beams from the crystal planes undergo constructive interference

whenever the path length of the X-ray beam inside the crystal matches with an integer number of wavelengths. The reflected beam is detected on the X-ray detector. The sample is rotated so that the X-ray from the source is incident at different angles on the sample surface. By measuring the angle of the reflected beam at points of constructive interference, the spacing between the crystal planes can be determined using Eq. (2.11) and related to the miller indices (hkl) of the planes.

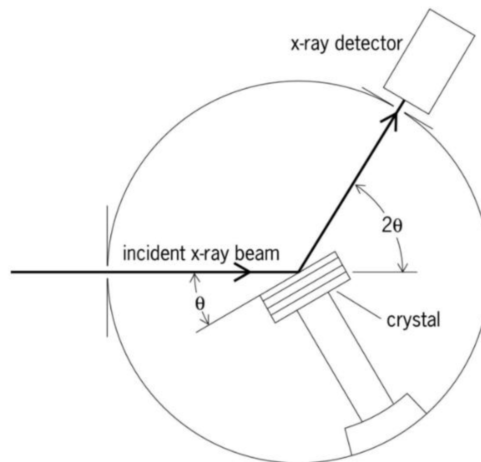

Figure 2.16 Schematic diagram of the experimental set-up of an X-ray diffractometer [15].

2.8 C-V Measurement Technique

2.8.1. Introduction

The most important task in a semiconductor lab is to maintain the quality and reliability of gate oxides of metal-oxide-semiconductor (MOS) structures. To check and examine this, Capacitance-Voltage (C-V) measurements are performed [16]. These C-V measurements are conducted on a two-terminal device called a MOS capacitor that is essentially a Metal-Oxide-Semiconductor-Field-Effect-Transistor (MOSFET). C-V measurement data provide a great amount of critical information about the device and processes like the formation of bulk and interface charges. Furthermore, C-V data can also be used to obtain additional information about many MOS device parameters, such as the oxide thickness, flatband voltage, and threshold voltage.

The Capacitance (C) of a device is defined as the change in charge (dq) per unit change in voltage (dV) across the device.

$$C = dq/dV \quad (2.12)$$

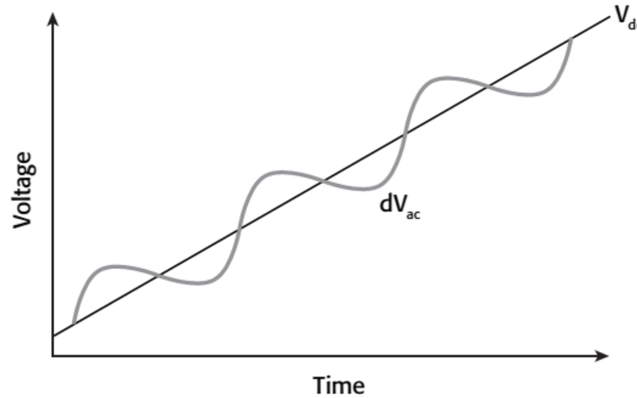

Figure 2.17 Schematic diagram showing the AC and DC voltage of a typical C-V sweep measurement [17].

Thus, the capacitance of a device can be easily calculated by applying a time-varying voltage signal to the device itself and measuring the current flowing through it. The charge accumulated in the device can be calculated by integrating the current over time. The ratio of the charge to the voltage applied then gives us the capacitance of the device under study.

To perform C-V measurements in a MOS device, two voltage sources are needed: an applied AC voltage signal (dV_{ac}) and a DC voltage (V_{dc}), simultaneously swept in time. This is schematically shown in Fig. 2.17, the two voltage sources serve two different functions. V_{dc} allows the sampling of material at different depths whereas dV_{ac} gives the small signal bias to perform the C-V measurement at a given depth in the MOS device. This is accomplished by sweeping the magnitude of V_{dc} is in time and keeping the magnitude and frequency of dV_{ac} fixed.

2.8.2 Basic Principles of MOS Capacitors

Schematic diagram of a p-type MOS capacitor is shown in Fig. 2.18. MOS capacitors basically consist of an oxide sandwiched between an n-type or p-type semiconductor and a metal gate.

The semiconductor and the metal gate constitute the two plates of the capacitor and the oxide layer acts as the dielectric. The area of the capacitor is defined by the area of the metal gate.

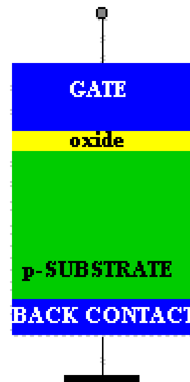

Figure 2.18 Schematic diagram of an MOS capacitor.

The most important characteristic of a MOS capacitor is that its capacitance undergoes a change when a DC voltage is applied across it. This allows the modes of operation of the MOS capacitor to be manipulated by changing the applied voltage. In aahigh frequency C-V curve for a p-type MOS capacitor it can be observed that when a DC sweep voltage is applied to the gate, the device pass through accumulation, depletion, and inversion regions successively.

2.8.3 Modes of operation

The modes of operation of a p-type MOS capacitor are discussed below:

2.8.3.1 Accumulation

When no voltage is applied across the device, a p-type semiconductor has holes, or majority carriers, in the valence band. However, the application of a negative voltage in between the metal gate and the p-type semiconductor leads to the appearance of more holes in the valence band at the oxide-semiconductor interface (Fig. 2.19a). This happens because the negative charge of the metal causes an equal amount of net positive charge to accumulate at the interface between the semiconductor and the oxide. This state of the p-type MOS is called accumulation. In the strong accumulation region, the C-V curve is almost flat and can be used to measure the capacitance of the oxide layer. Oxide thickness can then be calculated from the measurement of the oxide capacitance [17, 18].

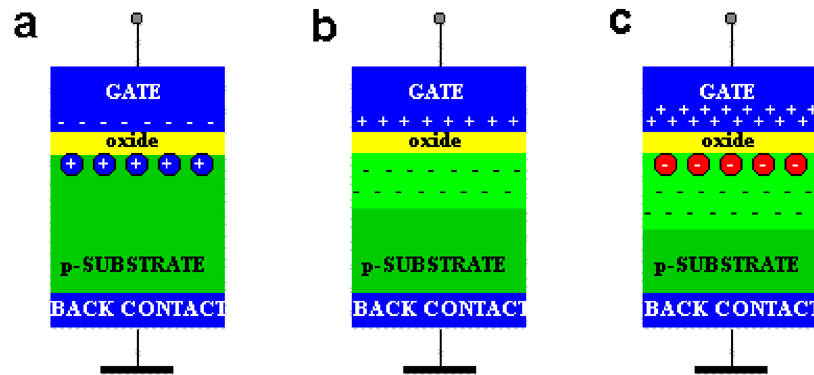

Figure 2.19 Schematic diagram showing the three different modes of operation of a p-type MOS device: (a) Accumulation, (b) Depletion and (c) Inversion [15].

2.8.3.2 Depletion

The state of depletion is achieved when a positive voltage is applied between the metal gate and the p-type semiconductor. Applying a small positive voltage will force holes away from the surface leaving a depletion region (Fig. 2.19b). That is to say, the semiconductor provides the necessary negative charge, with negative fixed ionized dopants. As the depleted area of the semiconductor no longer contains mobile free charges (holes or electrons), it acts as a dielectric or insulator. The measured capacitance in this state decreases as compared to the state of accumulation because the total measured capacitance now becomes the oxide capacitance and the depletion layer capacitance in series. The increase in the gate voltage causes the depletion region to move away from the gate. Therefore, the effective thickness of the dielectric between the gate and the substrate is increased, thus decreasing the capacitance of the MOS device [18].

2.8.3.3 Inversion

When the gate voltage of the p-type MOS capacitor is increased beyond the threshold voltage, electron-hole pairs are generated by the positive gate voltage, and electrons (the minority carriers) are attracted toward the metal gate. If a sufficiently large positive voltage is applied, the energy bands are bent sufficiently to approach the Fermi level and this predicts that the electron concentration is increasing. The surface thus "looks" n-type and is said to be inverted. This inversion condition is shown in Fig. 219c). Note that in inversion, the negative charge on that plate of the capacitor is made up of two components: inversion (electrons) and

depletion (acceptors) charge. Further increase of voltage, will be satisfied by an increase in the inversion component and the depletion width remains about constant in width. The inversion commences when the bands are bent by twice the Fermi potential, that is to say the surface potential is equal to twice the Fermi potential. For this condition, the minority carrier (electron) concentration at the surface is equal to the majority carrier (hole) concentration in the semiconductor bulk. These electrons are accumulated at the p-type semiconductor substrate-oxide interface (Fig. 2.19c). This state of minority-carrier accumulation is called the inversion, as the carrier polarity is now inverted with respect to the state of accumulation. The depletion layer reaches a maximum depth beyond a certain positive gate voltage. In this state, the total capacitance is the oxide capacitance in series with the maximum depletion capacitance and then assumes its minimum value [18].

2.9 Atomic Force Microscopy

2.9.1 Principles of AFM

AFM works on the principle of moving a sharp tip over a surface in such a way that the force of interaction between the surface and the tip remains constant [19-22]. As the tip encounters various high and low features (peaks and valleys) on the surface, this interaction force changes and the tip moves up or down via a feedback mechanism to keep it at a constant value.

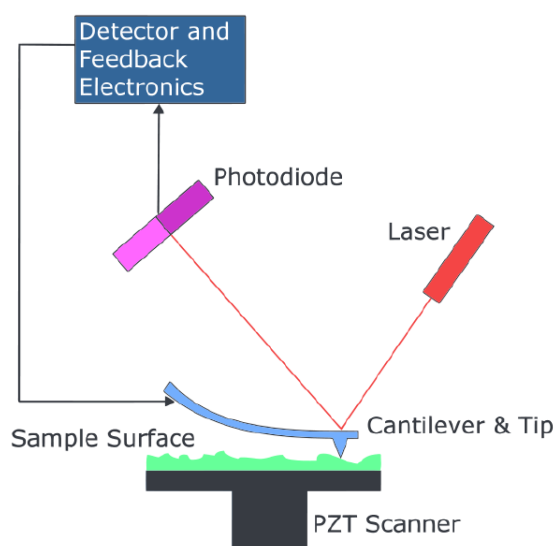

Figure 2.20 Schematic diagram showing the working principle of an atomic force microscope.

The vertical movement of the sharp tip is tracked by an optical lever mechanism that uses a laser [22] focused on the back side of the cantilever and reflected onto a photodetector (Fig. 2.20). This setting makes it possible to track the vertical movement of the tip which in turn, due to the feedback mechanism, can be used to extract topological information about the sample. The raster-scanning movement in the x and y directions is achieved through x and y scanners that allow very accurate control of the position and movement of the tip.

2.9.2 AFM Operation Modes

AFM modes can be divided into two broad classes: topographic and non-topographic. Only topographic modes are discussed in this thesis. Before moving onto the description of these modes though, a quick overview of how the interaction force between tip and surface changes as a function of the distance from each other.

When the tip is far away from the surface (i.e. the distance between the tip and the surface is grater than b in Fig. 2.21, the interaction force between the surface and the AFM tip is effectively zero. As the tip approaches the surface, the interaction force becomes attractive, until it reaches a minimum at point a in Fig. 2.21 It then starts to grow again for distances smaller than a and thus quickly turns positive (repulsive) again. Finally, the interaction force keeps increasing as the distance decreases [23].

2.9.2.1 Contact mode

In contact mode, the AFM tip is constantly touching the surface. Contact mode then operates in the repulsive regime of the tip-surface interaction. It is the fastest mode of AFM.

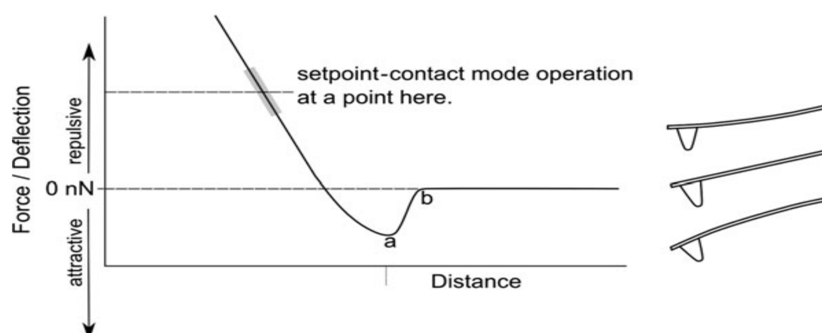

Figure 2.21 Force-distance curve showing contact mode regime [19].

2.9.2.2 Non-contact mode

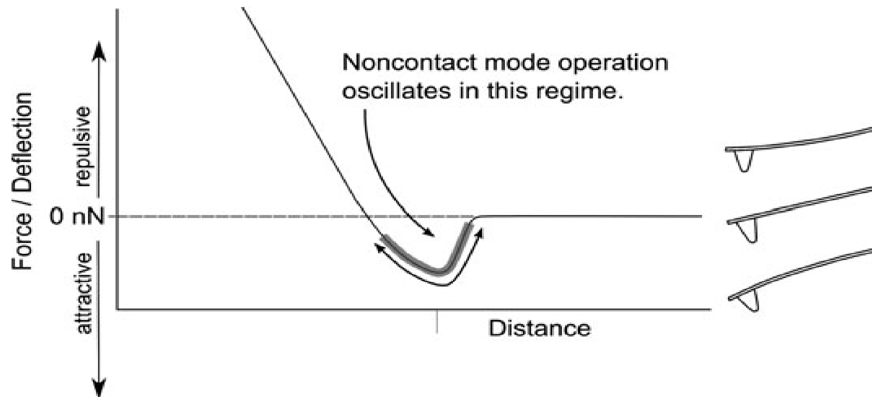

Figure 2.22 Force-distance curve showing non-contact mode regime [19].

In non-contact mode, the AFM tip does not touch the surface but oscillates with a constant amplitude slightly above the surface, in the attractive regime of the tip-surface interaction Fig. 2.22. When the tip encounters various features (peaks and valleys) on the surface the oscillation amplitude of the tip changes. The AFM feedback mechanism then moves the tip up or down to keep the amplitude constant. This up and down movement of the tip gives the topography of the sample.

2.9.2.3 Tapping mode

Tapping mode or intermittent contact mode is quite similar to non-contact mode, the only difference being that in tapping mode the AFM tip oscillates with a large amplitude over the surface in such a way that the tip experiences both the repulsive and attractive regimes of the force-distance curve in each cycle [24], as shown in Fig. 2.23.

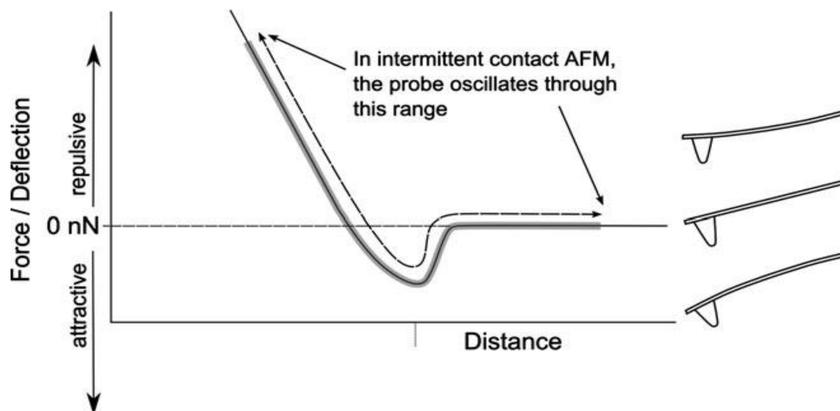

Figure 2.23 Force-distance curve showing tapping mode regime [19].

2.9.3 Extraction of surface roughness by AFM

The functional properties of many nanoscale devices critically depend on their surface roughness. Measurements of the surface property are then essential to predicting and optimising the performance of devices.

Two parameters are commonly used to characterise the roughness of a surface: average roughness and Root Mean Square (RMS) roughness [25]. The average roughness (R_a) of a surface is simply the arithmetic mean of the absolute deviations from the average height of features (peaks and valleys) of a surface. Its mathematical expression is

$$R_a = \frac{1}{L}\int_0^L |Z(x)|\,dx \tag{2.13}$$

Where Z(x) is the function that describes the height profile of the surface as a function of the position x over the evaluation length L. Even though roughness average is relatively easy to calculate, it can be misleading at times: two surfaces with totally different kinds of roughnesses can still be characterised by the same average roughness. Then, these two different surfaces can not be distinguished from each other by this parameter.

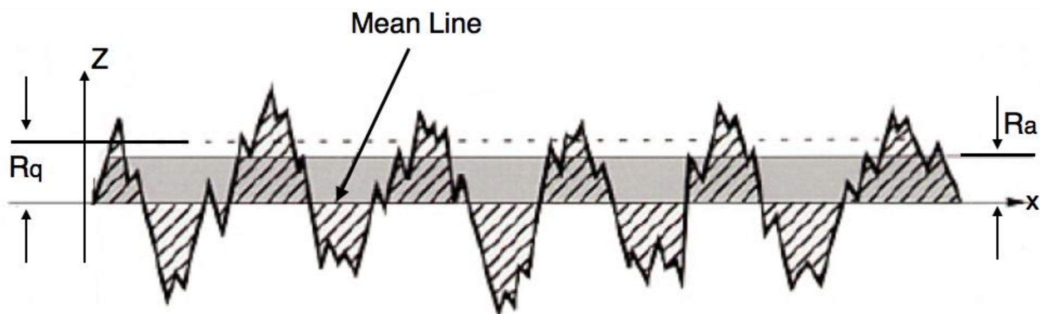

Figure 2.24 Schematic diagram showing the surface roughness (R_a) and the roughness average (R_q) and RMS roughness of a surface Z [25].

The second and more useful measure of surface roughness is the RMS roughness. It is the square root of the mean of squared deviations from the mean value of the local height of the sample. Mathematically we can write this as:

$$R_q = \sqrt{\frac{1}{L}\int_0^L |Z^2(x)|\, dx}$$

(2.14)

Where the symbols have the same meaning as in the previous paragraph. RMS roughness gives a more accurate idea of the surface roughness as it is more sensitive to peaks and valleys due to squaring the amplitude in its definition [25].

2.10 Transmission electron Microscopy (TEM)

Transmission Electron Microscopy (TEM) is a technique in which an electron beam is used for sample analysis. Electron beam interaction with the sample gives multiple information based on the group of electrons observed after interaction. Electrons emitted from the source pass through an electron optics, which focuses and magnifies the electron beam. A typical TEM geometry is shown in Fig. 2.25. Two condensers are used to confine the electron beam and also for brightness control, then beam passes through the condenser aperture and strikes the surface of the sample. The scattered electrons make the transmitted beams, passing through the objective lens. The image display as well as the following apertures is formed by the objective lens. Image forming elastically scattered electrons are chosen by the object and selected area aperture. At the end electron beam passes through a magnifying system, which has three lenses: two intermediate lenses for controlling magnification of the image and one project lens. The image thus formed can be viewed on a monitor of fluorescent screen and also printed [26, 27].

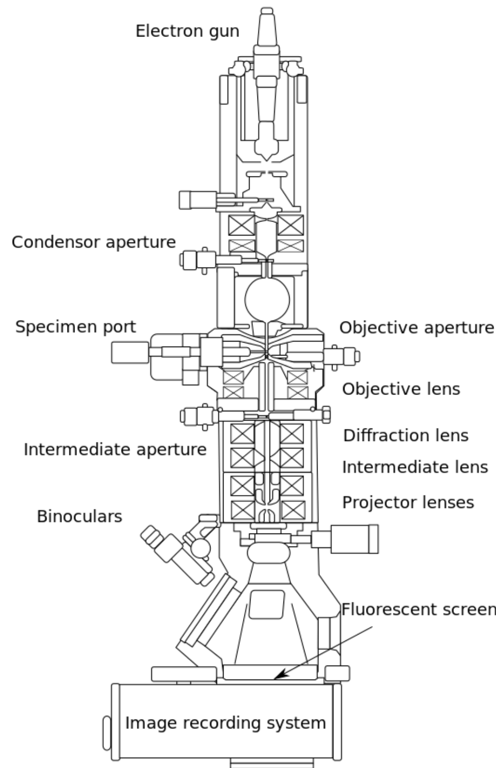

Figure 2.25 Transmission electron microscope schematic, depicting all components [27].

2.10.1 Operation

TEM operation takes place in ultrahigh vacuum (UHV) and requires high voltage. First recommended step is to turn the room lights off, so that the electron beam can be seen. The electron beam's brightness and focus is tunes using available buttons and controls. By adjusting and shifting the sample holder, thin area of the sample is located for the further analysis. The sample holder can be tilted to get more information from the sample. By properly using apertures and various electrons, different types of images can be obtained. By properly collecting and observing the scattered electrons, diffraction patterns can be achieved. A bright field can be obtained by selecting the unscattered electron beam, whereas if a diffracted beam is selected a dark field image is formed. For further analysis in TEM, EELS (Electron energy loss spectroscopy), EDX (Energy dispersive X-Ray spectroscopy), and EFTEM (Energy filtered transmission electron microscopy) are also used [28].

Transmission electron microscopy gives the crystallographic as well as compositional information, as the structure and atomic columns of sample under test can be observed. It is worth noting that TEM is a quite expensive characterization technique, needs good expertise

and preparing sample for analysis is very difficult mainly, because of the thin sample requirement.

2.10.2 Sample Preparation

As mentioned, sample preparation for TEM is quite cumbersome task and needs expertise. First it should be decided which view of sample should be observed: planar or cross-section. There is always a strong interaction between electrons and sample surface. Hence the sample needs to be as thin as possible (preferably less than 100nm). Based on the sample material, thinning can be done by several methods. Most common method is the mechanical thinning and polishing. Thin sample after polishing is glued on a small and round holder using the glue epoxy. During sample preparation a hole is created in the centre of the specimen using ion thinning, the data is collected from the edges of this hole at the centre. In ion thinning sample is irradiated by Ar (commonly) ion beams, leading to a hole at the centre. The damage during ion milling can be reduced by metal deposition on a sample [29]. Hence, sample preparation needs lot of care as it may affect the analysis and study.

2.11 Conclusion

This chapter covers various technologies which cover deposition techniques and characterization techniques. Based on the application the selection of deposition technique is done similarly the characterization technique is chosen based on the analysis requirement. ALD and MBE are important deposition technique with the capability of atomic thick layer deposition with precise control. XPS is used for elemental analysis and ellipsometry spectroscopy for the estimation of optical parameters such as refractive index and thickness. Surface analysis of the films can be done using atomic force microscopy (AFM). Hence film deposition and film characterization techniques are explained in this chapter.

2.12 References

[1] Kääriäinen T, Cameron D, Kääriäinen ML, Sherman A. Atomic Layer Deposition: Principles, Characteristics, and Nanotechnology Applications. John Wiley & Sons; 2013 May 17.

[2] Farrow RF. Molecular beam epitaxy: applications to key materials. Elsevier; 1995 Dec 31.

[3] Winograd N, Gaarenstroom SW. X-Ray Photoelectron Spectroscopy. Physical Methods in Modern Chemical Analysis. 1980;2:115-69.

[4] Van der Heide P. X-ray photoelectron spectroscopy: an introduction to principles and practices. John Wiley & Sons; 2011 Nov 1.

[5] Watts JF, Wolstenholme J. An introduction to surface analysis by XPS and AES. An Introduction to Surface Analysis by XPS and AES, by John F. Watts, John Wolstenholme, pp. 224. ISBN 0-470-84713-1. Wiley-VCH, May 2003.. 2003 May;1.

[6] Hüfner S. Photoelectron spectroscopy: principles and applications. Springer Science & Business Media; 2013 Jun 29.

[7] Kevan SD. Design of a high-resolution angle-resolving electron energy analyzer. Review of scientific instruments. 1983 Nov 1;54(11):1441-5.

[8] Helmer JC, Weichert NH. Enhancement of sensitivity in ESCA spectrometers. Applied Physics Letters. 1968 Oct 15;13(8):266-8.

[9] Docsto.com. docsto.com [Internet]. 2016 [cited 8 January 2016]. Available from: http://www.docsto.com/docs/95306562/the-channeltron

[10] Kraut EA, Grant RW, Waldrop JR, Kowalczyk SP. Precise determination of the valence-band edge in x-ray photoemission spectra: Application to measurement of semiconductor interface potentials. Physical Review Letters. 1980 Jun 16;44(24):1620.

[11] Johs BD, Woollam JA, Herzinger CM, Hilfiker JN, Synowicki RA, Bungay CL. Overview of variable-angle spectroscopic ellipsometry (VASE): II. Advanced applications. InOptical Metrology 1999 Jul (Vol. 1, pp. 29-58).

[12] Moore DM, Reynolds RC. X-ray Diffraction and the Identification and Analysis of Clay Minerals. Oxford: Oxford university press; 1989 Oct.

[13] Guinier A. X-Ray Diffraction: In Crystals, Imperfect Crystals, and Amorphous Bodies. Courier Corporation; 2013 Jan 17.

[14] Yasaka M. X-ray thin film measurement techniques. The Rigaku Journal. 2010;26:2.

[15] Kiessig H. Untersuchungen zur totalreflexion von röntgenstrahlen. Annalen der Physik. 1931 Jan 1;402(6):715-68.

[16] Schroder DK. Semiconductor material and device characterization 2nd, ed. by John Wiley and Sons.

[17] C-V Characterization of MOS Capacitors Using the Model 4200-SCS Semiconductor Characterization System, KEITHLEY Application Note Series, No. 2896, www.keithley.co.uk/data?asset=50977

[18] Anderson B, Anderson R. Fundamentals of Semiconductor devices. McGraw-Hill, Inc.;2004 Mar 12.

[19] Binnig G, Quate CF, Gerber C. Atomic force microscope. Physical review letters. 1986 Mar 3;56(9):930.

[20] Eaton P, West P. Atomic force microscopy. Oxford Univ. Press; 2010.

[21] Jagtap RN, Ambre AH. Overview literature on atomic force microscopy (AFM): Basics and its important applications for polymer characterization. Indian Journal of Engineering and Materials Sciences. 2006 Aug 1;13(4):368.

[22] Chatterjee S, Gadad SS, Kundu TK. Atomic force microscopy. Resonance. 2010 Jul 1;15(7):622-42.

[23] Johnson D, Hilal N, Bowen WR. Basic principles of atomic force microscopy. Atomic force microscopy in process engineering: An introduction to AFM for improved processes and product, UK, IChemE. 2009.

[24] Vilalta-Clemente A, Gloystein K. Principles of Atomic Principles Force Microscopy (AFM). Physics of Advanced Materials Winter School. 2008.

[25] De Oliveira RR, Albuquerque DA, Leite FL, Yamaji FM, Cruz TG. Measurement of the nanoscale roughness by atomic force microscopy: basic principles and applications. INTECH Open Access Publisher; 2012.

[26] Herguth WR, Nadeau G. Applications of scanning electron microscopy and energy dispersive spectroscopy (SEM/EDS) to practical tribology problems. Herguth Lab Inc CA. 2004;94590.

[27] Rose HH. Optics of high-performance electron microscopes. Science and Technology of Advanced Materials. 2008 Apr 1;9(1):014107.

[28] Wilson S, Brundle CR, Evans CA, editors. Encyclopedia of Materials Characterization [: Surfaces, Interfaces, Thin Films. Butterworth-Heinemann; 1992.

[29] Mayer J, Giannuzzi LA, Kamino T, Michael J. TEM sample preparation and FIB-induced damage. Mrs Bulletin. 2007 May 1;32(05):400-7.

Chapter 3

Interface Engineering Routes for a Future CMOS Ge-based Technology

3.1 Introduction

This chapter will discuss two possible routes for Ge interface engineering: (i) using high-κ materials that have a good interface with Ge, such as La_2O_3 and Y_2O_3, and (ii) introducing a robust ultra-thin high-κ interfacial layer (IL) barrier, such as Al_2O_3 or Tm_2O_3. Concerning the first route, the high reactivity of Ge with high-κ allows for germanate IL formation, which role is two-fold: to reduce the interface states and to suppress the GeO desorption at the interface [1, 2, 3]. The second route involves the use of ultra-thin barrier layers, Al_2O_3 and Tm_2O_3, as oxides highly resistant to oxygen diffusion and to reaction with Ge. The rare-earth metals (La, Y, Tm) tend to possess multiple valencies, such as + 2 and + 3 oxidation states, that can provide effective passivation of electrically active defects [4, 5, 6, 7]. The purpose is achieving a GeO_x-free gate stack with effective Ge surface passivation.

3.2 Samples Fabrication and Characterization

The 2 nm (nominal) La_2O_3/Ge and 5 nm (nominal) Y_2O_3/Ge gate stacks were deposited by Molecular Beam Epitaxy (MBE) at 400°C on n- and p-type Ge substrates. Prior to deposition, the Ge surface was cleaned by a mild degreasing with trichloroethylene, acetone and methanol for 5 minutes in each solvent to remove the organics. Then the GeO_x native oxide was thermally desorbed in-situ, by annealing at 450–500°C for 30 minutes. Y_2O_3 films were prepared by co-deposition of Y and atomic oxygen. The reference GeO_2 film of a nominal thickness of 5 nm was prepared by ex-situ furnace anneal at 450°C for 5 minutes. The Al_2O_3 layers were prepared in-situ by co-deposition of Al and atomic oxygen. It is worth mentioning that we have studied the effect of deposition temperature on La_2O_3/Ge and Y_2O_3/Ge stacks [8] and found that 400°C is optimal in terms of Ge interface passivation; hence, the stacks deposited at 400°C will only be considered in this chapter.

The Tm_2O_3 films were prepared by Atomic Layer Deposition (ALD) on Ge epitaxial layer (35 nm nominal) grown on Si (100). Prior to the gate oxide deposition on epi Ge/Si (100), samples were cleaned in a HF 0.5%/Isopropanol 1% /H_2O mixture to remove the native Ge oxide layer. The ALD was performed using a Beneq TFS 200 deposition system, heated to 250°C to deposit Tm_2O_3 layers of nominal thicknesses 5 and 10 nm. The layers were deposited using Tris(cyclopentadienyl)thulium, heated to 140°C, and water vapor (H_2O) as precursor gases. After the oxide deposition, a post-deposition annealing (PDA) treatment was used in order to

investigate the influence of post-processing temperatures of 350°C to 450°C and annealing atmospheres of O_2 and N_2/H_2 (10% H_2 in N_2) to as-deposited gate stacks.

The X-ray photoelectron (XPS) spectra for La_2O_3/Ge stacks were recorded at the Daresbury NCESS facility using an ESCA300 spectrometer with monochromated Al Kα X-rays of energy 1486.6 eV and electron take-off angles (TOA) of 15-90°. The spectrometer was calibrated so that the Ag $3d_{5/2}$ photoelectron line had a binding energy (BE) of 368.35 eV, and a full width at half maximum (FWHM) of 0.5 eV. The X-ray source power was 2.8 kW and the spectrometer pass energy was 150 eV with the entrance-slit width of the hemispherical analyzer set to 1.9 mm. Under these conditions, the overall spectrometer resolution was ~ 0.5 eV [9]. Charge compensation was achieved using a VG Scienta FG300 low energy electron flood gun, with the gun settings adjusted for optimal spectral resolution. The electron BEs were then corrected by setting the C1s peak in the spectra (due to stray carbon impurities) at 284.6 eV for all samples [10]. The core-level positions are defined as the FWHM and determined to be within 0.05 eV by fitting a Voigt curve to the measured peaks. A Shirley-type background [11] is used during the fitting of all the spectra. The angle resolved (AR)-XPS and measurements of Y_2O_3/Ge, Al_2O_3/Ge and Tm_2O_3/Ge stacks were made in a separate ultra-high vacuum system consisting of an Al Kα X-ray source and a PSP Vacuum Technology electron energy analyzer. This spectrometer was operated with an overall resolution of about 0.8 eV. The VUV-VASE measurements were performed using a spectral range from 0.5 – 8.8 eV (referring to wavelength range λ = 140-2500 nm), and angles of incidence of 55-75°, by 10° as a step, to maximize the accuracy. The XRD measurements were done using the Philips Xpert XRD system. The high-resolution transmission electron microscopy (HRTEM) was performed on a field emission TEM, FEI TecnaiTM F20, and on a JEOL 2100F TEM operating in STEM mode, with an operating voltage of 200 kV.

3.3 Formation of Germanate Interfacial Layers using La_2O_3 and Y_2O_3

Fig. 3.1 shows the Ge 3d core level spectra for the La_2O_3/Ge and Y_2O_3/Ge gate stacks. The data were fitted using a doublet of Voigt functions corresponding to Ge $3d_{5/2}$ and Ge $3d_{3/2}$ components. The spin-orbit splitting and area ratio values of 0.6 eV and 2:3 were fixed for the fit. The spin-orbital splitting for Ge 3d substrate peak (Ge $3d^0$) can be seen in Fig. 3.1 at energies of 28.6 and 29.2 eV. A high BE shoulder to the Ge $3d^0$ substrate peak can be seen for both La_2O_3 and Y_2O_3 samples. The rising edge in Fig. 3.1 (top) at a BE lower than ~ 28 eV originates from Y 4p to O 2s peaks at ~ 25 eV. The formation of the interfacial layer will be

reflected in the Ge 3d spectra as positive shifts (with respect to the substrate Ge $3d^0$ peak) when Ge reacts to form germanate layer.

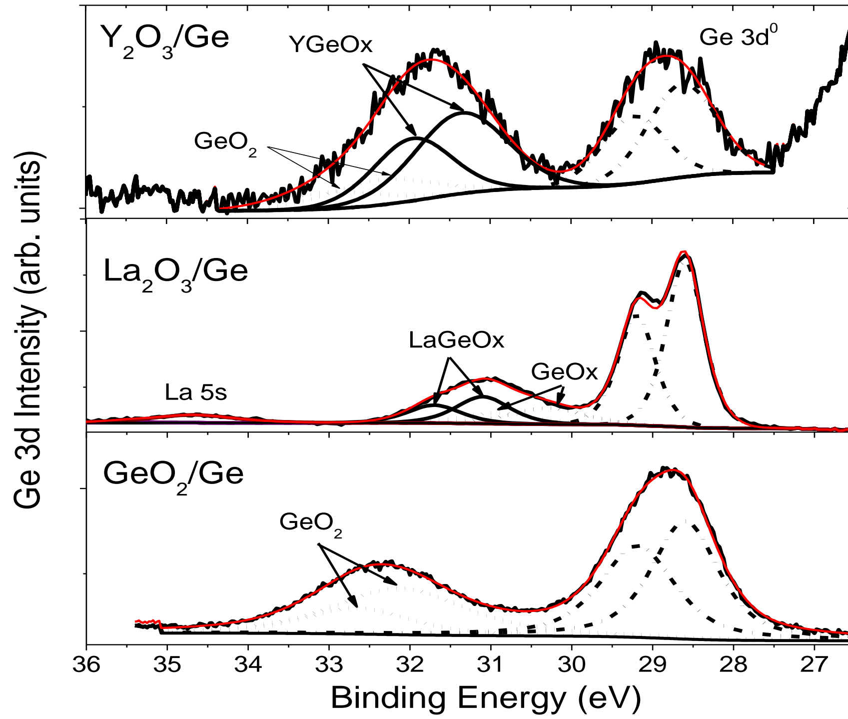

Fig. 3.1 Ge 3d XPS core level for La_2O_3/Ge and Y_2O_3/Ge stacks. The GeO_2/Ge is shown at the bottom as a reference. The spin-orbit splitting is visible for Ge substrate peak for the middle spectrum since the data were taken on higher resolution instrument.

No presence of GeO_2 at the interface for La_2O_3/Ge stack is evident (see the reference GeO_2/Ge spectrum at the bottom of Fig. 3.1 for comparison); the Ge +4 oxidation state has been reported to occur above 3 eV; @ 3.2 eV [7, 12] and 3.4 eV [13, 14] from the Ge $3d^0$. Considering the Gibbs free energy of formation of GeO_2 (–387 kJ/mol at 1000°K), the GeO_2 is thermodynamically unstable so that a GeO_2 layer is unlikely to form at the La_2O_3/Ge interface. Taking into account the electronegativity of Ge (2.01 using Pauling's scale), $LaGeO_x$ is expected to appear between the chemical shifts of GeO (Ge^{+2}) and Ge_2O_3 (Ge^{+3}), i.e. between 1.7 eV and 2.8 eV [13, 15]. The energy shift of 2.2 eV for $LaGeO_x$ has been reported [7, 16]. In our work, the presence of $LaGeO_x$ (3/2 and 5/2) can be de-convoluted at the chemical shift of +2.5 eV. Further evidence of $LaGeO_x$ formation comes from the observed shift of O 1s peak towards higher BE in Fig. 3.2(a) in comparison to the pure La_2O_3 at ~528.7 eV [17].

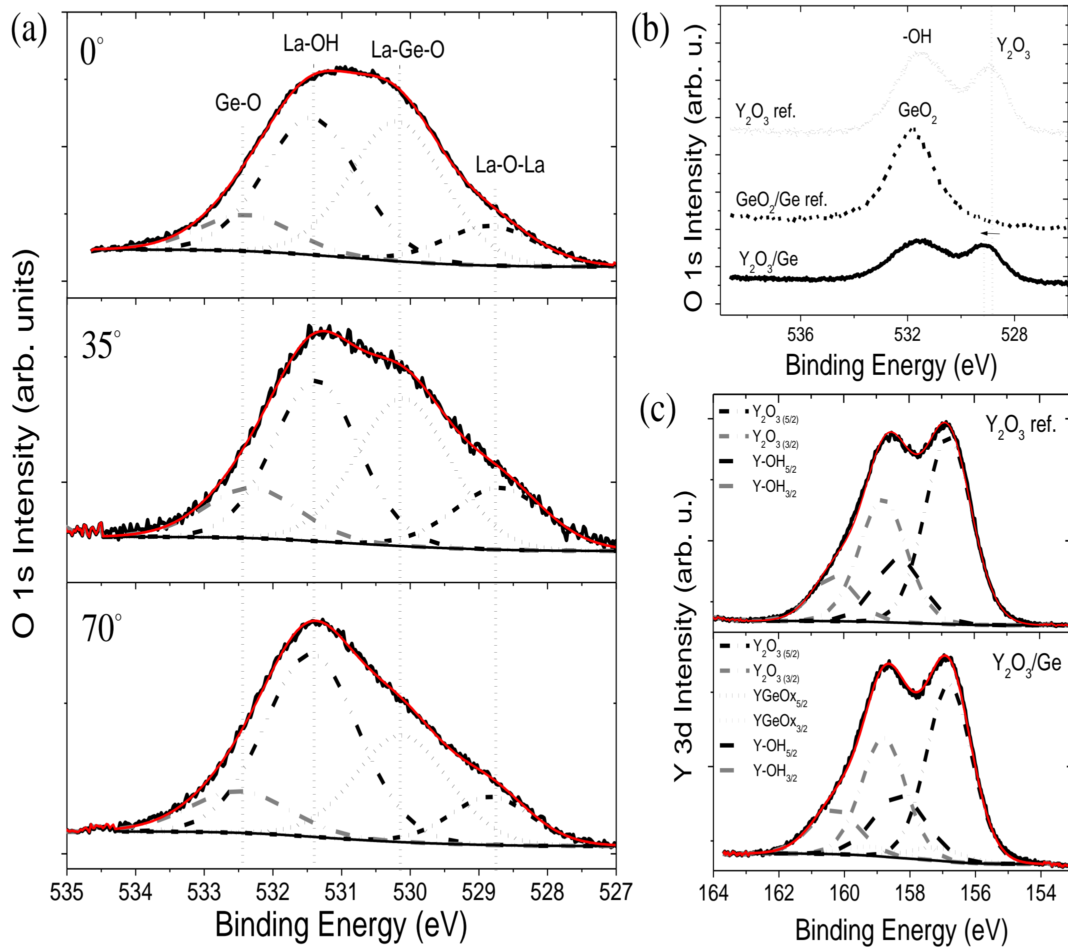

Fig. 3.2 (a)-(b) O 1s and (c) Y 3d XPS core levels for La_2O_3/Ge and Y_2O_3/Ge stacks with pure Y_2O_3 and GeO_2/Ge reference spectra. The spectra in (a) refer to take off angles 0 – 70°; the ones in (b)-(c) were taken at normal incidence angle of 0°.

In case of Y_2O_3/Ge, it has been reported that the Y-Ge-O bonding configuration gives rise to a BE shift within the range of + 2.2 to 2.5 eV due to a second nearest-neighbor effect, which is distinctly different from an O-Ge-O type bonding (+3.4 eV shift) [13,18]. In our data in Fig. 3.1 (top), the chemical shift for $YGeO_x$ layer is visible at + 2.7 eV from the substrate peak. Note the difference in the interfacial layer between the two samples. The La_2O_3/Ge stack features GeO_x layer at the interface, with a chemical shift of 1.7 eV consistent with +2 Ge oxidation state [14]. The Y_2O_3/Ge stack has sub-oxide fully eliminated, and GeO_2 appears at the interface. The angle-resolved XPS of O 1s core level is shown in Fig. 3.2(a). As the angle is increased, the broad centroid peak is transformed, showing sub-peaks as a signature of La-O-La, La-O-Ge, La-OH and the Ge-O-Ge bonds. The O 1s and Y 3d core level spectra for Y_2O_3/Ge were also measured to study the additional bonding and are shown in Figs. 3.2(b)-(c). A positive shift

from a reference Y_2O_3 bulk value can be seen from the O 1s shown in Fig. 3.2(b), and this provides firm evidence of charge transfer and formation of $YGeO_x$ at the interface. Furthermore, the peak appearing at ~156.95 eV for Y_2O_3/Ge samples represents the co-existence of Y_2O_3at 156.86 eV (Fig. 3.2(c), top) and Ge–O–Y bonding at 157.28 eV (Fig. 3.2(c), bottom). Note also that both the Y 3d and O 1s spectra show that -OH bond from moisture absorption is present, as in the case of La_2O_3/Ge stacks. The surface and even bulk hydration have been found to take place for all binary lanthanide oxides [17, 19, 20], and its strong presence is visible for these samples too. It has been shown that La is strongly electropositive and tends to strongly attract the neighboring O atoms [7]. The influence of La is considered to regulate the distribution of O in such a way that oxygen density is maximized in the final compound [16]. Furthermore, La on Ge in the presence of oxygen has been found to produce only La–O bonds [21], with no gap states, and the formation of stable $LaGeO_x$ layers [5, 7, 16, 22]. A penetration of Ge into the La_2O_3 layer, observed in this work and from the Medium Energy Ion Scattering (MEIS) experiments [8], is in agreement with the previous study [5] by energy dispersive X-ray spectroscopy where $LaGeO_x$ layer has been formed across the entire film at the temperature of 360°C. The thickness of the La_2O_3 has been found to be 2.6 nm from the MEIS calculated La and Ge depth profiles [8].

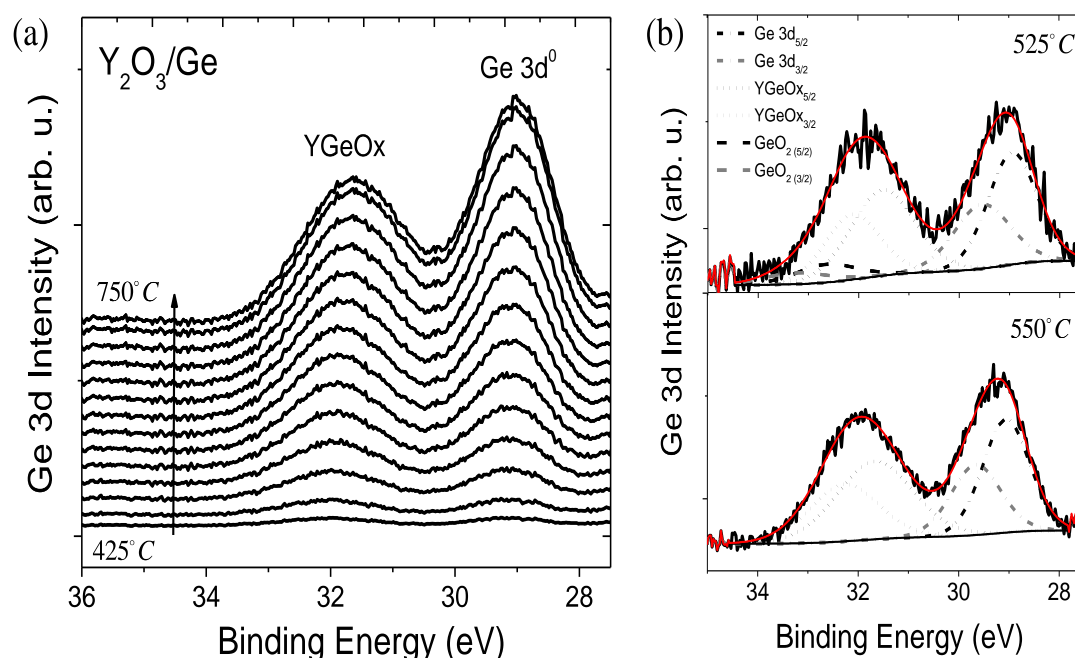

Fig. 3.3 (a) Ge 3d XPS core-levels taken after in-situ annealing from 425-750°C and (b) the fitting shown for two characteristic temperatures. The interfacial GeO_2 layer is not present after the annealing at 550°C.

The effect of temperature on the interfacial layer characteristics of Y_2O_3/Ge stack was studied by performing XPS in-situ annealing in the temperature range of 425°C to 750°C, with a step of 25°C. The referring Ge 3d core-level spectra are shown in Fig. 3.3. A presence of GeO_2 IL layer is apparent until the annealing temperature of 525°C. After the annealing at 550°C, the interface is pristine $YGeO_x$ layer. The results for Y_2O_3/Ge imply that Y–O–Y bonding configuration near the surface transforms to a Y–O–Ge configuration near the interface due to the incorporation of Ge atoms into the Y_2O_3 matrix. It has been inferred that Y and Ge atoms intermix more significantly at a higher process temperature [23]. The out-diffusion of Ge signifies the breaking of the strong covalent Ge-Ge bonds even at room temperature. The chemical bonding model proposes possible bond weakening via charge transfer during the formation of chemical bonds [24]. Since the electronegativity difference between Y and Ge (1.22 and 2.01 using Pauling's scale) is large, charge transfer and hence the bond weakening can be significant.

The band diagram of the La_2O_3/Ge stack has been derived using the valence [25, 26] and O1s energy loss XPS spectra [27, 28] and is fully described in Ref. 8. A VBO value of 2.75 ± 0.15 eV and band gap of 5.45 ± 0.2 eV were determined for the $LaGeO_x$ film in reasonable agreement with the theoretically predicted value of 3.0 eV and 5 eV for lanthanum germanate compounds [29]. By taking into account the band gap of Ge of 0.67 eV, the conduction band offset (CBO) for $LaGeO_x$/Ge is about 2 eV. This is in agreement with the internal photoemission study on ZrO_2/La_2O_3/Ge film, which indicates CBO of interfacial $LaGeO_x$ film of > 2.0 eV [30]. Interface state density (D_{it}) and leakage current density for La_2O_3/Ge stacks deposited at 360°C has been reported to be $< 9\times10^{11} eV^{-1}cm^{-2}$and ~ 10^{-1} A/cm^2 at 1 V [5] respectively.

3.4 Band gap estimation from VUV-VASE

The modelling and fitting procedure in this study consisted of firstly, determining the thickness and optical constants in the non-absorbing (transparent) region of spectra from 0.5–6 eV using a Cauchy layer representative of a dielectric film. Then, a Kramers-Kronig (KK) consistent B-spline layer [31] was used to extend the optical constants into the higher energy range, up to 8.5 eV. This method is consistent with the point-by-point fit method [32] used in WVASE32, but with two added advantages: firstly, the layer maintains KK consistency which forces the optical constants to keep a physical shape and secondly, the optical constants remain smooth and

continuous over the full spectrum, with a controllable parameter to decide the resolution of points. Additionally, the B-spline layer was replaced with the general oscillator model with a possibility of using Cody-Lorentz and Tauc-Lorentz oscillators to discern possible sub-band gap absorption features in the gate stacks and to determine the band gap.

Optical constants of germanium are available in the literature upto 6 eV photon energy. We used this spectral range to fit the surface layer thickness of native GeO_2 for the reference Ge substrate. Initial measurements (upon opening the container in N_2 purged environment) on a Ge substrate gave a GeO_2 native oxide thickness of 2.93 nm. Then the germanium optical constants (refractive index, n, and extinction coefficient, k) and dielectric function were fitted using a Kramers-Kronig consistent B-spline layer over the entire spectral range. This sample was used as a reference Ge substrate layer to determine the optical constants of high-κ oxide films using methodology explained above. The absorption coefficient (α) can be found from the extinction coefficient as,

$$\alpha = \frac{4\pi k(E)E}{hc} \tag{3.1}$$

where, *h* is the Planck's constant, *c* is the speed of light and *E* is the photon energy. The band gap in this work is extracted from the Tauc-Lorentz model [33, 35] and α-method. The plots of α vs E and the associated Tauc-Lorentz plots for Y_2O_3/Ge are shown in Fig. 3.4. In the inset of Fig. 3.4, the corresponding $(\alpha E)^2$ vs E graphs are added (valid for direct band gap transitions) [36]. Note that there is no band-edge tailing for the Y_2O_3/Ge stack. The linear extrapolation of the segments on the curves in the non-absorbing regions gives the band gap values of 5.99 eV from α-method and 5.7 eV from Tauc plots. It is apparent that the associated band gap values from the Tauc-Lorentz plots are ~ 0.3 eV lower than those derived from the α-method. The result is in agreement with the observations in Ref. [37] that the band gap values obtained from the α-method can be ~ 0.7 eV larger than the ones determined using the Tauc- or Cody-Lorentz methods.

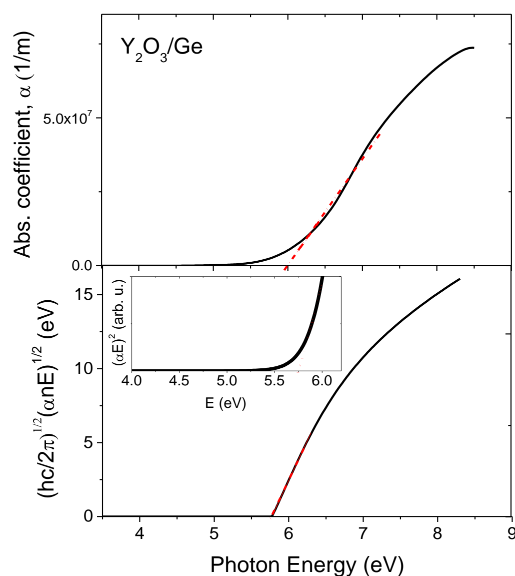

Fig. 3.4 The absorption coefficient and Tauc plots for Y_2O_3/Ge stack, as derived from VUV-VASE experimental data.

The VBO of Y_2O_3/Ge stack has been estimated by Kraut's method [8] and was found to be 2.68 ± 0.2 eV. It compares to the VBO of 2.78 eV reported for Y_2O_3/Ge prepared by rf sputtering [38]. By taking into account the band gap value of Ge of 0.67 eV and the band gap of 5.7 eV from the Tauc method, the CBO value from this work is 2.35 eV. The latter value compares to the theoretically predicted value of 2.56 eV [39].

3.5 Band line-up correlation with electrical characterization data

Electrical characterization was carried out at room temperature on metal insulator semiconductor (MIS) capacitors patterned by Pt e-beam evaporation on the dielectric surface through a shadow mask consisting of circular dots 300 μm in diameter. The back Ohmic contact was made using eutectic In-Ga alloy. The high-frequency capacitance voltage and the leakage current density characteristics for the Y_2O_3/Ge are shown in Fig. 3.5. The CV curves in Fig. 3.5(a) are well behaved and correlate with the Ge 3d XPS data presented in Fig. 3.1, where full elimination of GeO_x sub-oxide and $YGeO_x$ formation at the interface have been demonstrated. The full electrical characterization of La_2O_3/Ge stacks have been reported in Ref. 5. It can be seen from Fig. 3.5(b) that the leakage current is ~ 10^{-7} A/cm^2 at 1 V, as opposed to La_2O_3 that suffers from a high leakage current of ~ 10^{-1} A/cm^2 at 1 V for samples deposited at 360°C [5]. This observation substantiates the observed band line-up (see Table I), where the Y_2O_3/Ge stack

exhibits a higher conduction band offset (> 2.3 eV), than the respective La_2O_3/Ge (~ 2 eV). Furthermore, this behaviour is in good agreement with the reported XPS (Fig. 3.1) and VASE (Fig. 3.4) data of the La_2O_3/Ge and Y_2O_3/Ge stacks, where no defective GeO_x species have been observed for the latter. It is worth mentioning that a full elimination of GeO_2 for the former stack could lead to an abrupt $LaGeO_x$/Ge interface, introducing remote phonon and Coulomb scattering centers directly on the channel and so could reduce carrier mobility [29].

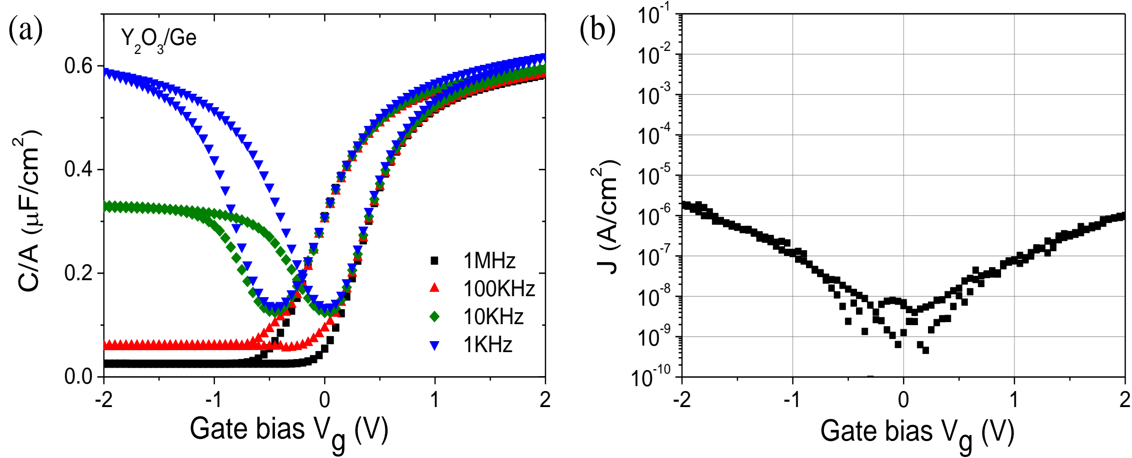

Fig. 3.5 Voltage characteristics for Y_2O_3/Ge.

(a) Capacitance voltage and (b) leakage current density

3.6 Al_2O_3 and Tm_2O_3 as barrier interfacial layers on Ge

The referring absorption coefficient and Tauc plots vs photon energy for Al_2O_3/Ge and Tm_2O_3/Ge stacks are shown in Figs. 3.6-3.7. The band gap value of Al_2O_3 is found to be 6.1-6.4 (see Table I and Fig. 3.6(a)-(b)). The ALD-deposited Al_2O_3 has been reported to have a much lower density (3.1-3.3 g/cm^3) than sapphire, and a lower band gap of ~ 6.2 eV (from photoconductivity measurements) [40,41] and 6.5 eV (from XPS) [42]; for sapphire the band gap is 8.8 eV [39,43]. For Tm_2O_3/Ge, the band gap value from Tauc plot is 5.3 ± 0.1 eV (Fig. 3.7(a), [44]), while from the α-method is ~ 5.8 eV (Fig. 3.7(c)). The former value is in close agreement with the theoretical prediction of Iwai [45] while the latter compares to a value of 5.76 eV reported recently for Tm_2O_3/Si using optical absorbance [46] and the direct band gap law. Our work as shown in reference [44] points to indirect band gap for Tm_2O_3.

No Urbach tail is evident for the Al_2O_3/Ge in this work (Fig. 3.6(a)), suggesting a negligible sub-band gap absorption. The sub-band gap features are evident for GeO_2/Ge sample in the energy range 4.8 – 5.5 eV in Fig. 3.7(b). Toriumi et al. [47] have reported a peak at 5.1 eV for the GeO_2/Ge sample, thought to be associated with neutral O vacancies or Ge^{+2} in oxygen deficient GeO_2[48]. The high-level ab-initio calculations [49, 50] have shown that E′ center at 5.06 eV and E′-oxygen vacancy at 5.16 eV, defects [48] are able to form a broad absorption band near 5 eV.

The interfacial features for the GeO_2/Ge and Al_2O_3/Ge stacks can be further discerned from inspecting the Ge 3d core levels, which are shown in Figs. 3.6(c)-(d). For the 4.4 nm GeO_2/Ge layer, a strong presence of Ge^{+4} oxidation state is evident from the chemical shift to the Ge $3d^0$ peak of > 3 eV [7,13,14] (Fig. 3.6(c)). Also, note that the GeO_x presence at ~ +1.4 eV chemical shift in Fig. 3.6(c), which correlates to the observed sub-band absorption in Fig. 3.7(b), indicates the existence of defective GeO_2 layer. In the case of Al_2O_3/Ge, no high BE shoulder is apparent in Fig. 3.6(d), rather just a peak referring to the Ge $3d^0$ substrate suggesting no interfacial layer (IL), and that Al_2O_3 acts indeed as a barrier layer.

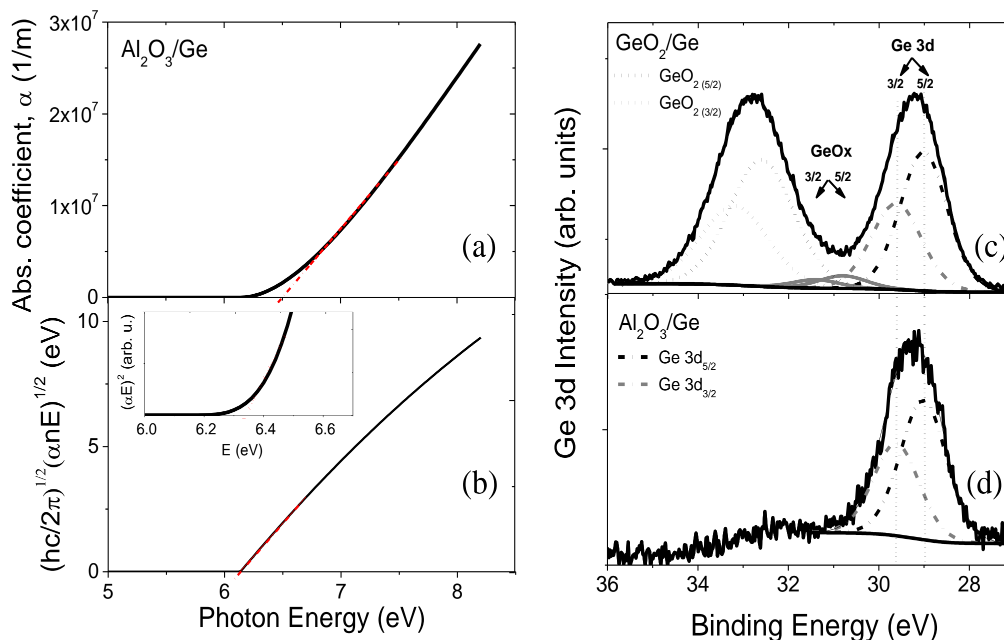

Fig. 3.6 (a) Absorption coefficient vs photon energy; (b) Tauc plots for Al_2O_3/Ge gate stack of 9.4 nm (estimated by VUV-VASE). Ge 3d XPS core level spectra for (c) reference GeO_2/Ge, and (d) Al_2O_3/Ge gate stacks.

It has been argued recently that Al_2O_3 is a good oxygen diffusion barrier and, therefore, blocks the O vacancy diffusion that allows the volatilization of GeO and the creation of sub-stoichiometric GeO_x interface states [29]. Calculations of electronic structures of interfaces and interface defects and of oxide reactions and considerations of diffusion barrier properties by Robertson's group [29, 51] suggest that a thin Al_2O_3layer in the overall dielectric might be a preferred passivation scheme for Ge channels [52]. The difference in the O density between La_2O_3, Y_2O_3 and Al_2O_3 allows for the different behavior of these oxides on Ge [7]. As seen in the previous section, both La_2O_3 and Y_2O_3 belong to a group of intimate dielectrics on Ge, i.e. they form stable germanate layers in contact with Ge. On the contrary, Al_2O_3 acts as a barrier on Ge. This has further been associated with the cation radius of the corresponding oxides [7]. In particular, the large ionic radius of La^{+3} (117 pm) compared to Al^{+3} (67.5 pm), implies large M–O bond length (M - metal ion), and consequently a less dense O structure.

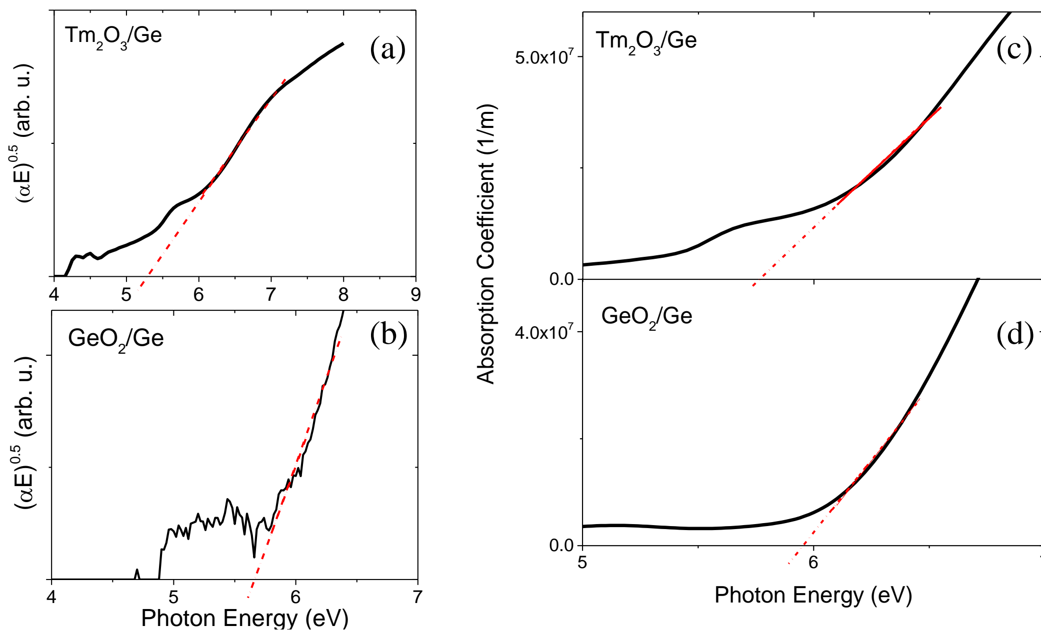

Fig. 3.7 (a)-(b) Tauc plots, and (c-d) absorption coefficient vs photon energy spectra derived from modeling VUV-VASE experimental data for Tm_2O_3/Ge and GeO_2/Ge.

The band gap of GeO_2 from the Tauc plot is found to be 5.65 ± 0.1 eV (Fig. 3.7(b), [44]), while from α-method ~ 5.95 eV (Fig. 3.7(d)). Note the sub-band gap absorption features for Tm_2O_3/Ge gate stack in Figs. 3.7(a) and (c). It has been argued that the Tauc plot is related to the degree of order in the structure [53], i.e. disorder generates defects and hence removes states

from the bands and generates band tails of localized states. A decrease in band tailing for the HfO_2 samples annealed at higher temperatures has been reported and attributed to defect reduction and temperature induced crystallization [54, 55]. The amorphous samples have been proposed to have a continuous and more dense bond network and hence a lower density of defects, which is substantiated by the lower trapped charge density [53]. In this work, a pronounced sub-band gap absorption correlates with the polycrystalline structure of Tm_2O_3 films, as inferred from XRD (not shown) and HRTEM (see Fig. 3.8(a)). We see atomic contact between Tm_2O_3 and Ge in Fig. 3.8(a), and structurally zero IL. This indicates low reactivity of Tm_2O_3 to Ge, and a possibility to act, like Al_2O_3, as a barrier layer.

From the Kraut's method, the VBO for Tm_2O_3/Ge [44] and GeO_2/Ge [56] have been estimated to be 5.95 ± 0.08 eV and 3.45 ± 0.20 eV respectively. For the 5 nm as-deposited Tm_2O_3/Ge stacks, well behaved CV characteristics have been reported [44], with the EOT of1.28-1.43 nm and relative permittivity of 14-15. No significant effects on the electrical properties have been observed regarding the chosen PDA temperatures and atmosphere of O_2 or N_2/H_2.

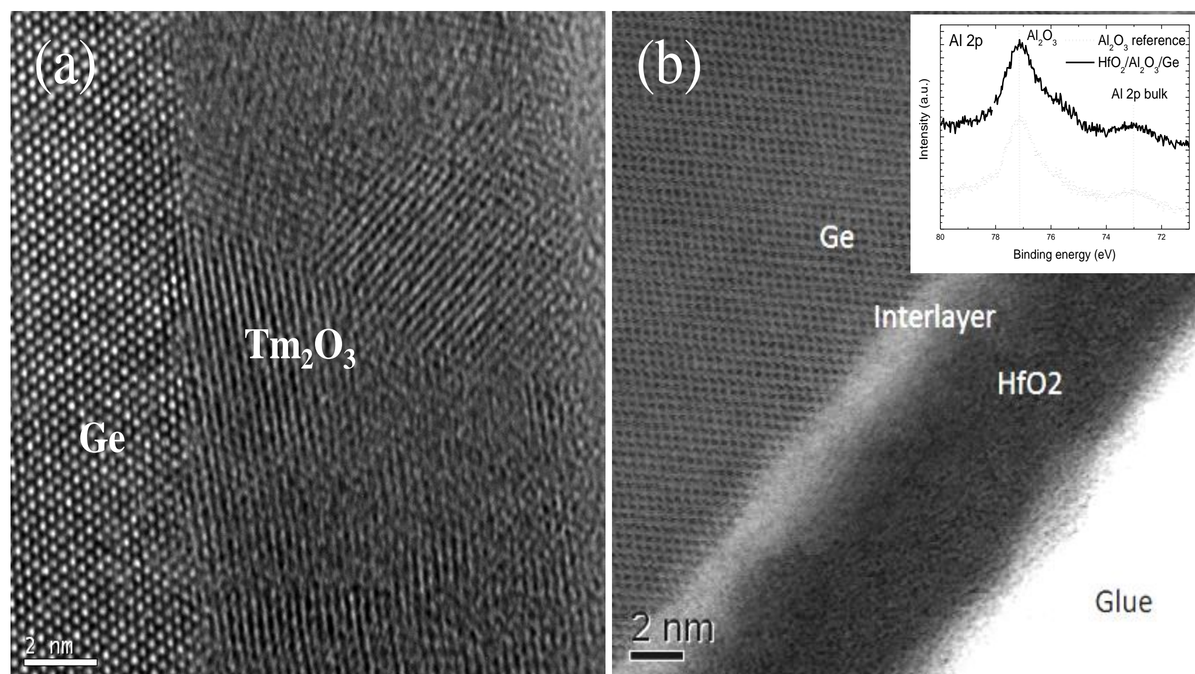

Fig. 3.8 The HRTEM images of (a) Tm_2O_3/Ge and (b) HfO_2/Ge with alumina interface passivation. The inset in (b) refers to Al 2p XPS core level scans showing presence of alumina layer at the interface from 10 s Al MBE exposure and 30 ALD cycles of HfO_2.

In summary, the experimental valence band offset and band gap data obtained from this work are shown in Table 3.1.

TABLE 3.1. A Summary of Valence Band Offset and Band Gap for La_2O_3, Y_2O_3, Al_2O_3, Tm_2O_3 and GeO_2 on Ge determined by VUV-VASE and XPS**.**

Gate Stack	VBO (eV)	Band gap (eV)
2.6 nm La_2O_3/Ge	2.75 ± 0.15	5.45 ± 0.20
7.9 nm Y_2O_3/Ge	2.68 ± 0.20	5.70 – 5.99
10.4 nm Tm_2O_3/Ge	2.95 ± 0.08	5.30 – 5.78
9.4 nm Al_2O_3/Ge	--	6.12 – 6.43
4.4 nm GeO_2/Ge	3.45 ± 0.20	5.65 – 5.95

3.7 HfO_2 Deposition on Alumina and Sulphur Passivated Interface

Ge (100) n- and p- wafers were cleaned in an ultra-high vacuum (< 10^{-6} mbar) at 500°C and 600°C for 10 minutes to evaporate any native oxide and achieve an oxide free surface. Subsequently, wafers were exposed to an Al flux for a range of times to deposit ultra-thin Al layers. The samples were then oxidized at ambient temperatures in the MBE load lock to produce Al_2O_3 layers. The samples were transferred within one minute to an Oxford Instruments OpAL reactor and thin films of HfO_2 were deposited on the Al_2O_3 by ALD. The HfO_2 depositions used a [$(CpMe)_2$HfOMeMe] precursor coupled with an O_2 plasma as the oxidizing species. Between 30 and 130 ALD cycles were used to grow HfO_2 thicknesses from 1.6 nm to 7 nm at 250°C. For electrical measurements, gold contacts were deposited on the films to form MIS gate electrodes and Al was deposited on the back of the Ge wafers to provide an Ohmic contact. After preliminary measurements, the samples underwent two different annealing treatments for 30 minutes: in forming gas (FGA) at 350°C, and in nitrogen at 400°C.

In Sulphur passivation, the few monolayers of S are incorporated on the surface of Ge, resulting in the reduction of dangling bonds. After cleaning and removal of native oxide as described above, the samples were dipped in a 20% ammonium sulphide ($(NH_4)_2S$) solution in water for 10 minutes and were dried in the nitrogen flow. They were immediately transferred into the ALD reactor where 130 cycles [$(CpMe)_2$HfOMeMe] precursor and oxygen plasma were used to grow a 7 nm thick HfO_2 layer.

Fig. 3.8 (b) shows a HRTEM image of a sample with 10 s exposures to the MBE Al source with 130 ALD cycles to deposit HfO_2. The image indicates a 2 nm thick layer of GeO_2/Al_2O_3 with a 7 nm layer of HfO_2 on top. The inset in Fig. 3.8(b) shows Al 2p XPS spectra, which confirm that Al_2O_3 is formed when compared to a reference Al foil. The small peak at 73 eV is attributed to differential charging across the thin alumina layer. The Ge 3d XPS core level data indicate that a layer of GeO_2 is present at the interface [57]. A very thin alumina interlayer acts as a desorption barrier to GeO and prevents formation of hafnium germanate.

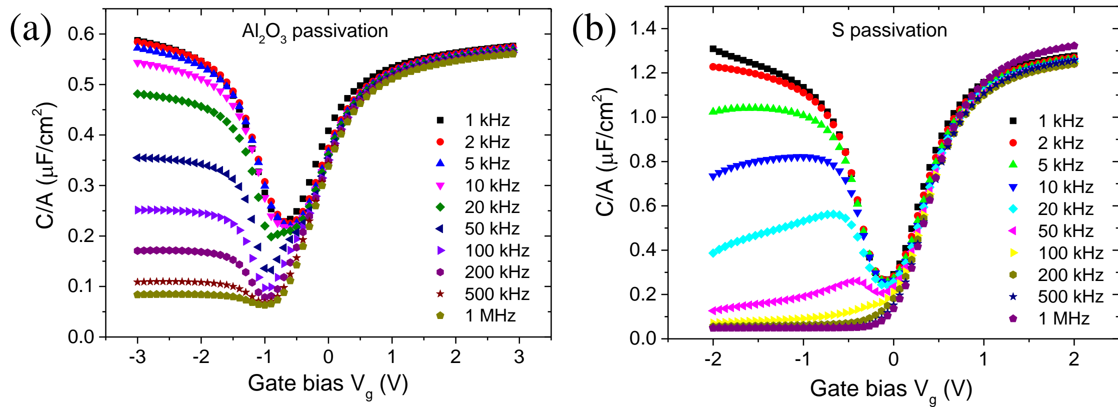

Fig. 3.9 Capacitance voltage characteristics for HfO_2 ALD stacks on Ge surface passivated with: (a) alumina and (b) Sulphur. The area, A, of the devices is 0.7×10^{-7} m^2.

Fig. 3.9 (a) shows the typical CV characteristics of the sample with 20 nm HfO_2, which exhibit small frequency dispersion in accumulation and well behaved inversion region. The CV hysteresis has been found to be low ~ 10 mV [57]. The capacitance equivalent thickness (CET) of the interfacial layer (GeO_2 and alumina) of 2.2 nm and relative permittivity of 21.3 were estimated from the variation of CET vs HfO_2 thickness. The CV characteristics of the S-passivated sample are shown in Fig. 3.9(b). Assuming dielectric constant of 21.3 for HfO_2, the CET of IL is estimated to be 1.3 nm, being considerably smaller than the value extracted from the samples with alumina capping.

The leakage current density (not shown) has been found to be less than 1×10^{-7} Acm^{-2} at ± 1 V for the sample thermally cleaned at 500°C with 3.5 nm of HfO_2. Fig. 3.10 shows the relationship between the CET and the physical thickness of HfO_2 layers on a Ge sample cleaned at 500°C for two different Al deposition times. The thickness of the alumina layer is estimated to be 0.6 nm per 5 s, and the thickness of GeO_2 is calculated to be ~ 1.6 nm. For the sample

cleaned at 600°C, the thickness of GeO_2 reduces to 1nm. The EOT of the gate stack can be further reduced from 1.7 nm (see Fig. 10) to 1.3 nm by FGA for a sample with 10 s Al MBE exposure and 30 ALD cycles of HfO_2. The latter result suggests a reduction of IL thickness, and a favorable effect of the forming gas anneal.

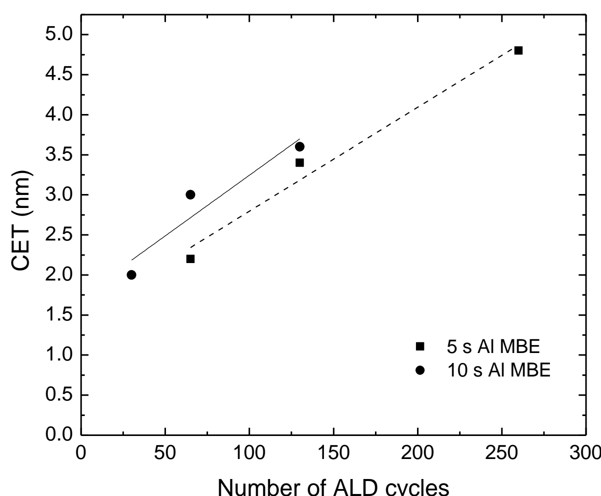

Fig. 3.10 CET vs number of ALD cycles (referring to various HfO_2 thickness data) for two MBE exposure times of Al: 5 s and 10 s. All data points refer to as-deposited stacks.

3.8 Conclusion

A comprehensive study of La_2O_3/Ge, Y_2O_3/Ge, Al_2O_3/Ge and Tm_2O_3/Ge gate stacks has been conducted in this chapter for consideration as interfacial layers for Ge surface passivation. Both La_2O_3 and Y_2O_3 show reactivity to germanium. A strong presence of germanate layers was found from the high binding energy shoulders to the Ge 3d substrate XPS core level peak, with a chemical shifts of +2.5 eV for $LaGeO_x$, and +2.7 eV for $YGeO_x$. The interface structure was found to be somewhat different. In case of La_2O_3/Ge, germanium sub-oxide species dominate the interface and are likely to be a cause of observed high leakage current of ~ 10^{-1} A/cm^2 at 1 V. The Y_2O_3/Ge stack has GeO_2 interfacial layer, which after the annealing above 525°C, transforms into pristine $YGeO_x$/Ge layer. This stack shows five orders of magnitude lower leakage current than the respective La_2O_3/Ge. The VUV-VASE data have enabled determination of band gap for Y_2O_3, Al_2O_3 and Tm_2O_3 films. The band line-ups have been derived from the XPS and VUV-VASE data for La_2O_3/Ge, Y_2O_3/Ge, Tm_2O_3/Ge, and GeO_2/Ge.

For both, Al_2O_3 and Tm_2O_3, barrier properties on Ge have been inferred from HRTEM and XPS study. Furthermore, ALD hafnia high-κ dielectric gate stacks have been fabricated on Ge with alumina as the barrier layer using a combined MBE and ALD techniques. The devices show low EOT down to 1.3 nm after forming gas anneal. An improved interfacial layer thickness has been observed for the S-passivated samples.

In summary, the results of this study points to Y_2O_3/Ge as a serious contender for Ge interface engineering with more attractive features than La_2O_3/Ge stacks - moderate reactivity to Ge, GeO_x-free interface, higher conduction band offset (~ 2.3 eV), larger band gap (~ 5.7 eV), and lower leakage current ($< 10^{-6}$ A/cm^2 at 1 V). Another central finding from this work is an observation that Tm_2O_3 could act as an interfacial barrier layer, in a similar way to an ultra-thin Al_2O_3 layer used in high-performance Ge CMOS gate stacks. This chapter considered La_2O_3 and Y_2O_3 as viable thin films on Ge and in next chapter the effect of temperature on the interface is considered.

3.9 References

[1] Takagi S, Zhang R, Takenaka M. Ge gate stacks based on Ge oxide interfacial layers and the impact on MOS device properties. Microelectronic Engineering. 2013 Sep 30;109:389-95.

[2] Toriumi A, Lee CH, Wang SK, Tabata T, Yoshida M, Zhao DD, Nishimura T, Kita K, Nagashio K. Material potential and scalability challenges of germanium CMOS. InElectron Devices Meeting (IEDM), 2011 IEEE International 2011 Dec 5 (pp. 646). IEEE.

[3] Caymax M, Eneman G, Bellenger F, Merckling C, Delabie A, Wang G, Loo R, Simoen E, Mitard J, De Jaeger B, Hellings G. Germanium for advanced CMOS anno 2009: a SWOT analysis. InProceedings of the IEEE International Electron Devices Meeting-IEDM 2009 (pp. 461-464).

[4] Nishimura T, Lee CH, Wang SK, Tabata T, Kita K, Nagashio K, Toriumi A. Electron mobility in high-k Ge-MISFETs goes up to higher. InVLSI Technology (VLSIT), 2010 Symposium on 2010 Jun 15 (pp. 209-210). IEEE.

[5] Mavrou G, Galata S, Tsipas P, Sotiropoulos A, Panayiotatos Y, Dimoulas A, Evangelou EK, Seo JW, Dieker C. Electrical properties of La2O3 and HfO2/La2O3 gate dielectrics for germanium metal-oxide-semiconductor devices. Journal of Applied Physics. 2008 Jan;103(1):4506.

[6] Dentoni Litta E, Hellstrom PE, Henkel C, Ostling M. Thulium silicate interfacial layer for scalable high-k/metal gate stacks. Electron Devices, IEEE Transactions on. 2013 Oct;60(10):3271-6.

[7] Dimoulas A, Tsoutsou D, Panayiotatos Y, Sotiropoulos A, Mavrou G, Galata SF, Golias E. The role of La surface chemistry in the passivation of Ge. Applied Physics Letters. 2010 Jan 4;96(1):012902.

[8] Mitrovic IZ, Althobaiti M, Weerakkody AD, Dhanak VR, Linhart WM, Veal TD, Sedghi N, Hall S, Chalker PR, Tsoutsou D, Dimoulas A. Ge interface engineering using ultra-thin La2O3 and Y2O3 films: A study into the effect of deposition temperature. Journal of Applied Physics. 2014 Mar 21;115(11):114102.

[9] Beamson G, Briggs D, Davies SF, Fletcher IW, Clark DT, Howard J, Gelius U, Wannberg B, Balzer P. Performance and application of the Scienta ESCA300 spectrometer. Surface and Interface Analysis. 1990 Sep 1;15(9):541-9.

[10] Vickerman JC. Surface analysis: the principal techniques.

[11] Shirley DA. High-resolution X-ray photoemission spectrum of the valence bands of gold. Physical Review B. 1972 Jun 15;5(12):4709.

[12] Baldovino S, Molle A, Fanciulli M. Evidence of dangling bond electrical activity at the Ge/oxide interface. Applied Physics Letters. 2008 Dec 15;93(24):242105.

[13] Schmeisser D, Schnell RD, Bogen A, Himpsel FJ, Rieger D, Landgren G, Morar JF. Surface oxidation states of germanium. Surface science. 1986 Jul 1;172(2):455-65.

[14] Sasada T, Nakakita Y, Takenaka M, Takagi S. Surface orientation dependence of interface properties of GeO2/Ge metal-oxide-semiconductor structures fabricated by thermal oxidation. Journal of Applied Physics. 2009 Oct;106(7):3716.

[15] Molle A, Bhuiyan MN, Tallarida G, Fanciulli M. In situ chemical and structural investigations of the oxidation of Ge (001) substrates by atomic oxygen. Applied physics letters. 2006 Aug 21;89(8):083504.

[16] Tsoutsou D, Panayiotatos Y, Sotiropoulos A, Mavrou G, Golias E, Galata SF, Dimoulas A. Chemical stability of lanthanum germanate passivating layer on Ge upon high-k deposition: A photoemission study on the role of La in the interface chemistry. Journal of Applied Physics. 2010 Sep 15;108(6):064115.

[17] Mitrovic IZ, Hall S, Sedghi N, Simutis G, Dhanak VR, Bailey P, Noakes TC, Alexandrou I, Engstrom O, Lopes JM, Schubert J. On the nature of the interfacial layer in ultra-thin TiN/LaLuO3 gate stacks. Journal of Applied Physics. 2012 Aug 15;112(4):044102.

[18] Opila RL, Wilk GD, Alam MA, Van Dover RB, Busch BW. Photoemission study of Zr- and Hf-silicates for use as high-κ oxides: Role of second nearest neighbors and interface charge. Applied physics letters. 2002 Sep 2;81(10):1788-90.

[19] Song J, Kakushima K, Ahmet P, Tsutsui KA, Sugii N, Hattori T, Iwai H. Improvement of interfacial properties with interfacial layer in La 2 O 3/Ge structure. Microelectronic engineering. 2007 Oct 31;84(9):2336-9.

[20] Lopes JM, Roeckerath M, Heeg T, Schubert J, Littmark U, Mantl S, Besmehn A, Myllymaki P, Niinistö L, Adamo C, Schlom DG. Amorphous lanthanum lutetium oxide thin films as an alternative high-k material. ECS Transactions. 2007 Sep 28;11(4):311-8.

[21] Houssa M, Pourtois G, Caymax M, Meuris M, Heyns MM. First-principles study of the structural and electronic properties of (100) Ge/Ge (M) O2 interfaces (M= Al, La, or Hf). Applied Physics Letters. 2008 Jun;92(24):2101.

[22] Mavrou G, Tsipas P, Sotiropoulos A, Galata S, Panayiotatos Y, Dimoulas A, Marchiori C, Fompeyrine J. Very high-kappa ZrO2 with La2O3 (LaGeOx) passivating interfacial layers on germanium substrates. Applied Physics Letters. 2008 Nov;93(21):2904.

[23] Wu ML, Wu YH, Lyu RJ, Chao CY, Wu CY, Lin CC, Chen LL. High quality Ge surface passivation layer formed by thermal oxidation of Y/Ge structure. Microelectronic Engineering. 2013 Sep 30;109:216-9.

[24] Nakayama T, Itaya S, Murayama D. Nano-scale view of atom intermixing at metal/semiconductor interfaces. InJournal of Physics: Conference Series 2006 May 10 (Vol. 38, No. 1, p. 216). IOP Publishing.

[25] Schmeißer D, Henkel K, Bergholz M, Tallarida M. The band gap and band offset in ultrathin oxide–semiconductor heterostructures. Superlattices and Microstructures. 2010 Mar 31;47(3):369-76.

[26] Perego M, Scarel G, Fanciulli M, Fedushkin IL, Skatova AA. Fabrication of GeO2 layers using a divalent Ge precursor. Applied physics letters. 2007 Apr;90(16):2115.

[27] Bell FG, Ley L. Photoemission study of SiO x (0≤ x≤ 2) alloys. Physical Review B. 1988 May 15;37(14):8383.

[28] Ohta A, Nakagawa H, Murakami H, Higashi S, Miyazaki S. Photoemission study of ultrathin GeO2/Ge heterostructures formed by UV-O3 oxidation. e-Journal of Surface Science and Nanotechnology. 2006;4:174-9.

[29] Li H, Lin L, Robertson J. Identifying a suitable passivation route for Ge interfaces. Applied Physics Letters. 2012 Jul 30;101(5):052903.

[30] Afanas' ev VV, Stesmans A, Mavrou G, Dimoulas A. Beneficial effect of La on band offsets in Ge/high-kappa insulator structures with GeO2 and La2O3 interlayers. Applied Physics Letters. 2008 Sep;93(10):2115.

[31] Johs B, Hale JS. Dielectric function representation by B-splines. physica status solidi (a). 2008 Apr 1;205(4):715-9.

[32] Price J, Lysaght PS, Song SC, Li HJ, Diebold AC. Identification of sub-band-gap absorption features at the HfO2/Si (100) interface via spectroscopic ellipsometry. Applied Physics Letters. 2007 Aug;91(6):1925.

[33] Jellison Jr GE, Modine FA. Erratum:‘‘Parameterization of the optical functions of amorphous materials in the interband region’’[Appl. Phys. Lett. 69, 371 (1996)]. Applied Physics Letters. 1996 Sep 30;69(14):2137-.

[34] Nguyen NV, Davydov AV, Chandler-Horowitz D, Frank MM. Sub-bandgap defect states in polycrystalline hafnium oxide and their suppression by admixture of silicon. Applied Physics Letters. 2005 Nov 7;87(19):192903.

[35] Nguyen NV, Sayan S, Levin I, Ehrstein JR, Baumvol IJ, Driemeier C, Krug C, Wielunski L, Hung PY, Diebold A. Optical band gaps and composition dependence of hafnium–

aluminate thin films grown by atomic layer chemical vapor deposition. Journal of Vacuum Science & Technology A. 2005 Nov 1;23(6):1706-13.

[36] Demkov AA, Navrotsky A, editors. Materials fundamentals of gate dielectrics. Amsterdam: Springer; 2005 Jul 14.

[37] Di M, Bersch E, Diebold AC, Consiglio S, Clark RD, Leusink GJ, Kaack T. Comparison of methods to determine bandgaps of ultrathin HfO2 films using spectroscopic ellipsometry. Journal of Vacuum Science & Technology A. 2011 Jul 1;29(4):041001.

[38] Chiam SY, Chim WK, Pi C, Huan AC, Wang SJ, Pan JS, Turner S, Zhang J. Band alignment of yttrium oxide on various relaxed and strained semiconductor substrates. Journal of Applied Physics. 2008 Apr;103(8):3702.

[39] Robertson J, Falabretti B. Band offsets of high K gate oxides on III-V semiconductors. Journal of Applied Physics. 2006 Jul;100(1):4111.

[40] Afanas' ev VV, Houssa M, Stesmans A, Heyns MM. Band alignments in metal-oxide-silicon structures with atomic-layer deposited Al2O3 and ZrO2. Journal of applied physics. 2002 Mar;91:3079-84.

[41] Afanas'ev VV, Stesmans A. Internal photoemission at interfaces of high-κ insulators with semiconductors and metals. Journal of applied physics. 2007 Oct 15;102(8):081301.

[42] Yu HY, Li MF, Cho BJ, Yeo CC, Joo MS, Kwong DL, Pan JS, Ang CH, Zheng JZ, Ramanathan S. Energy gap and band alignment for (HfO2) x (Al2O3) 1-x on (100) Si. Applied physics letters. 2002 Jul 8;81(2):376-8.

[43] Norton DP. Synthesis and properties of epitaxial electronic oxide thin-film materials. Materials Science and Engineering: R: Reports. 2004 Mar 15;43(5):139-247.

[44] Mitrovic IZ, Althobaiti M, Weerakkody AD, Sedghi N, Hall S, Dhanak VR, Chalker PR, Henkel C, Litta ED, Hellström PE, Östling M. Interface engineering of Ge using thulium oxide: Band line-up study. Microelectronic Engineering. 2013 Sep 30;109:204-7.

[45] Iwai H, Ohmi S, Akama S, Ohshima C, Kikuchi A, Kashiwagi I, Taguchi J, Yamamoto H, Tonotani J, Kim Y, Ueda I. Advanced gate dielectric materials for sub-100 nm CMOS. InElectron Devices Meeting, 2002. IEDM'02. International 2002 Dec 8 (pp. 625-628). IEEE.

[46] Jianjun WA, Ting JI, Yanyan ZH, Zebo FA, Weiyi RE. Band gap and structure characterization of Tm 2 O 3 films. Journal of Rare Earths. 2012 Mar 31;30(3):233-5.

[47] Toriumi A, Wang S, Lee CH, Yoshida M, Kita K, Nishimura T, Nagashio K. (Invited) Oxidation, Diffusion and Desorption in a Ge/GeO2 System. ECS Transactions. 2010 Apr 16;28(2):171-80.

[48] Hosono H, Abe Y, Kinser DL, Weeks RA, Muta K, Kawazoe H. Nature and origin of the 5-eV band in SiO 2: GeO 2 glasses. Physical Review B. 1992 Nov 1;46(18):11445.

[49] Zyubin AS, Mebel AM, Lin SH. Photoluminescence of oxygen-containing surface defects in germanium oxides: A theoretical study. The Journal of chemical physics. 2005 Jul 22;123(4):044701.

[50] Zyubin AS, Mebel AM, Lin SH. Photoluminescence of oxygen-deficient defects in germanium oxides: A quantum chemical study. The Journal of chemical physics. 2006 Aug 14;125(6):064701.

[51] Li H, Robertson J. Defects at Ge: GeO 2 and Ge: MeOx interfaces. Microelectronic Engineering. 2013 Sep 30;109:244-9.

[52] Zhang R, Iwasaki T, Taoka N, Takenaka M, Takagi S. High-Mobility Ge pMOSFET With 1-nm EOT Gate Stack Fabricated by Plasma Post Oxidation. Electron Devices, IEEE Transactions on. 2012 Feb;59(2):335-41.

[53] Martinez FL, Toledano-Luque M, Gandia JJ, Cárabe J, Bohne W, Röhrich J, Strub E, Mártil I. Optical properties and structure of HfO2 thin films grown by high pressure reactive sputtering. Journal of Physics D: Applied Physics. 2007 Sep 7;40(17):5256.

[54] Cho YJ, Nguyen NV, Richter CA, Ehrstein JR, Lee BH, Lee JC. Spectroscopic ellipsometry characterization of high-k dielectric HfO2 thin films and the high-temperature annealing effects on their optical properties. Applied physics letters. 2002 Feb 18;80(7):1249-51.

[55] Takeuchi H, Ha D, King TJ. Observation of bulk HfO2 defects by spectroscopic ellipsometry. Journal of Vacuum Science & Technology A. 2004 Jul 1;22(4):1337-41.

[56] I.Z. Mitrovic, S. Hall, A.D. Weerakkody, N. Sedghi, M. Althobaiti, D. Hesp, V.R. Dhanak, P.R. Chalker, C. Henkel, E. Dentoni Litta, P.-E. Hellström, M. Östling, S. Schamm-Shardon, Appl. Phys. Lett. 2014.

[57] Mather S, Sedghi N, Althobaiti M, Mitrovic IZ, Dhanak V, Chalker PR, Hall S. Low EOT GeO 2/Al 2 O 3/HfO 2 on Ge substrate using ultrathin Al deposition. Microelectronic Engineering. 2013 Sep 30;109:126-8.

Chapter 4

Ge interface engineering using ultra-thin La_2O_3 and Y_2O_3 films: A study into the effect of deposition temperature

4.1 Introduction

Last chapter discussed different routes to interface engineering and characterisation of La_2O_3 and Y_2O_3 thin films and their interface with Ge. This will be extended by considering the effect on the interface at deposition temperature. The most recent studies [1, 2] strongly advocate that high-performance Ge CMOS (Complementary Metal Oxide Semiconductor) technology is feasible. This technology is attractive due to the Ge intrinsic high mobilities for electrons (3900 cm^2/Vs) and holes (1900 cm^2/Vs) as well as the CMOS compactness (Ge-based n- and p-channel MOSFETs). The smaller band gap of Ge (0.67 eV) has the potential for lower contact resistances compared to Si and is consequently more suitable for voltage scaling [3]. Sub-nm equivalent oxide thickness (EOT) gate stacks are required to keep the intrinsically high performance of Ge. The focus is on finding suitable high permittivity κdielectric ($\kappa > 20$) to form a gate stack with low interface state density and EOT. The most perilous issue is engineering a high-quality interface between Ge and the high-κdielectric, that is, passivation of the Ge surface. An interfacial layer (IL) either intentionally or unintentionally formed during the high-κdielectrics deposition process is usually necessary for achieving high electrical performance of Ge-based MOS devices[4,5,6,7] but its presence has a significant effect on achieving the desired EOT; it must be as thin as possible and preferably with as high a permittivity as can be achieved. The four most commonly used approaches [7] for forming thin ILs for Ge passivation are: (i) nitridation, (ii) Si-based schemes, (iii) S-based passivation and (iv) GeO_x ($x < 2$) grown through thermal, ozone- or plasma-assisted oxidation. The peak electron mobility has been dramatically improved in Ge n-channel MOSFETs over recent years [2, 8, 10, 12]. The highest reported electron mobility is now approaching 2000 cm^2/Vs [8, 9, 12]. The key to this achievement has been mainly in interface state reduction at the GeO_2/Ge interface. Thermally grown GeO_2 is the most natural choice [13, 18]. A high-quality GeO_2 IL provides a possibility for both p- and n-type Ge channel FETs. However, it is worth recalling that GeO_2 has high water solubility, low desorption temperature (~ 430°C) and low dielectric constant of ~ 6. A detrimental Ge sub-oxide transition layer at a GeO_2/Ge interface can be expected [19, 20]. Toriumi's group has systematically investigated [8, 11, 21, 22] the GeO_2/Ge interface in terms of both thermodynamics and kinetics of the Ge oxidation process. An extremely low density of interface states ($D_{it} = 6 \times 10^{10}$ $eV^{-1}cm^{-2}$) has been reported for relatively thick (~ 20 nm) GeO_2/Ge[23] allowing for high performance Ge n-MOSFETs [21]. However, apparent degradation of drive current has been observed when the GeO_2 thickness has been further reduced [3]. A reduction in electron mobility to 265 $cm^2V^{-1}s^{-1}$ has been reported

when the GeO_2 IL is ~ 1.2 nm [24]. Oxygen plasma treatment has been proposed to form good quality ~ 5 nm GeO_2/Ge interface at low substrate temperatures, due to the highly reactive O radicals [25,26], leading to demonstration of an extremely low midgap D_{it} of 4.5×10^{10} $eV^{-1}cm^{-2}$. High-pressure oxidation and low temperature oxygen annealing have recently been suggested as the process recipes for nearly ideal GeO_2/Ge system [8]. It seems that low temperature oxygen annealing can work for mending the dangling bonds in GeO_2/Ge, while high-pressure oxidation suppresses the GeO_x desorption at higher temperature [27], resulting in robust and dense GeO_2on Ge.

For aggressive oxide scaling with EOT well below 1 nm, the combination of higher-κ oxide and ultra-thin GeO_2 is required. A small amount of rare-earth (RE) metal introduction into the GeO_2interface layer has been shown to dramatically improve the interface [8]. Rare earth metal ions in oxides generally have large polarizability [28]; among them, La^{+3} has one of the largest values, in excess of 6 Å. This significantly modifies the chemical bonding at the interface with Ge, redistributing the electronic charge and reducing the electrical activity of the interface states to produce good passivating properties [29]. Rare earth oxides (La_2O_3, Y_2O_3, $LaLuO_3$, Dy_2O_3, Gd_2O_3, and CeO_2) react strongly with the substrate resulting in catalytic oxidation of Ge and the spontaneous formation of stable interfacial layers [29, 32]. This high reactivity of Ge with high-κ oxide suggests the possibility of GeO_x-free gate stacks. Another passivation route is to introduce a robust, ultra-thin high-k IL barrier, such as Al_2O_3 [1, 33, 37] or Tm_2O_3 [38, 39]. It is worth noting here that the Ge surface passivated with Al_2O_3 is slowly oxidized without causing GeO_x diffusion or desorption. As a result, all the Ge atoms near the interface are terminated with oxygen atoms or Ge atoms without any dangling bonds under the oxidation condition lower than 4+, leading to low D_{it} even with GeO_x IL. Peak electron and hole mobilities of 689 cm^2/Vs and 546 cm^2/Vs respectively at EOT = 0.76 nm have been achieved by this approach for $HfO_2/Al_2O_3/GeO_x$/Ge gate stack[1].

This chapter focuses on the former Ge interface engineering approach using La_2O_3 and Y_2O_3 RE-oxides. These high-k oxides have moderate reactivity with Ge [40] to form a germanate interface whose purpose is two-fold: firstly to reduce the interface defects and secondly to suppress the GeO_x desorption at the interface. GeO_x-free gate stacks constitute another advantage of this approach by choosing appropriate deposition conditions and annealing procedures [2]. La_2O_3/Ge gate stacks have been investigated by a number of research groups [41, 49]. It has been shown [48] that La changes the surface chemistry so that a stable $LaGeO_x$

compound is favoured against the competing reaction of GeO_2 with Ge, resulting in suppression of GeO_x [49]. The stable La–O–Ge bond at the Ge interface provides a surface-state "free" Ge band gap due to the fourfold coordination of La in the GeO_x matrix as predicted theoretically by Houssa et al [19]. This allows for a gate stack with a low density of interface states (~ 10^{11} $eV^{-1}cm^{-2}$) with nearly ideal electrical characteristics [44, 47]. Moreover, internal photoemission experiments on ZrO_2/La_2O_3/Ge MIS structures [50] have indicated a sufficiently large conduction band offset (CBO > 2 eV). Theoretical calculations using charge neutrality levels predict a $LaGeO_x$ band gap of 5 eV, VBO of 3 eV [51], and CBO of La_2O_3 and Y_2O_3 on Ge of 2.56 eV[52,53]. The permittivity ranges from 9-12 [44, 54]. It is worth mentioning that only La_2O_3 is reactive to water due to its electropositive nature [55, 56] and may thus pose a challenge to the integration into a CMOS process flow. Moreover, LaO_x ($x < 1.5$) is only suitable for nFETs because LaO_x leads to an interfacial dipole in the gate stack and this could leads to increase the leakage current [57]. Passivation of Ge by La_2O_3 subsequently capped with ZrO_2 results in stabilization of the tetragonal crystalline ZrO_2phase [47, 58]. The scaling potential of ZrO_2/La_2O_3/Ge stacks to EOT values as low as 0.5 nm [59] and 0.96 nm[60] has been reported. The La_2O_3 deposition temperature has been found to have a noticeable effect on the capacitance voltage (CV) characteristics [44]. It is apparent that improved La_2O_3 electrical behaviour is obtained either by depositing the material at higher temperature or by applying post-deposition annealing independent of ambient (H_2, N_2, O_2). The best characteristics (especially low D_{it}) have been obtained when these two conditions are combined, although an increase in both leakage current and EOT has been observed [44]. There has been no explanation of these observations from the structural and band line-up studies and we have addressed these issues in this chapter.

By contrast, Y_2O_3 is Ge-friendly and robust against water. An amorphous Y_2O_3 layer provides a wide bandgap (~ 5.5-5.7 eV) [56], high crystallization temperature (~ 2325°C), relatively high dielectric constant (~ 11–18) [8, 61, 62] and can effectively passivate the Ge surface without the presence of GeO_x [62, 63]. The absence of GeO_x has been attributed to the stability of the Y_2O_3interlayer in contact with the Ge substrate [64]. The mechanism for this stability lies in the barrier role of the Y_2O_3 interlayer, which effectively blocks the inter-diffusion of Ge, thus suppressing the growth of unstable GeO_x and so improving the interface quality. Moreover, yttrium can also be used to tune the overall effective work function of the gate stack through the formation of interface dipoles [65]. An electron mobility of 1480 cm^2/Vs for Y_2O_3/Ge n-MISFET has been demonstrated recently [8]. From XPS measurements, the VBO offset of

Y_2O_3/Ge has been found to be 2.78 eV and the band gap, 5.7 eV [66]. Formation of the $YGeO_x$ affects leakage current, hysteresis, interface trap density, and other reliability issues that are important for device operation [9, 40, 61, 62, 66, 67]. The passivation effect of a $YGeO_x$ IL has been explained by so-called "valency passivation" [9]; the introduction of yttrium atoms effectively suppresses the dangling bonds in the interfacial region and consequently improves D_{it} in the range of 10^{11} $cm^{-2}eV^{-1}$ due to the trivalent RE nature of Y [68, 69].

Less is known, however, about the band line-up and structure of bulk and interfacial $LaGeO_x$ and $YGeO_x$ as a function of deposition temperature, which is the main focus of this chapter. A systematic study of the structural properties of La_2O_3/Ge and Y_2O_3/Ge gate stacks as a function of deposition temperature has been conducted by Medium Energy Ion Scattering (MEIS), X-ray Photoemission Spectroscopy (XPS), Vacuum Ultra Violet Variable Angle Spectroscopic Ellipsometry (VUV-VASE), and X-ray diffraction (XRD). The most significant findings from the results which will be presented here are two-fold: firstly, evidence for the optimal deposition temperature to tailor the interfacial layer for effective passivation of Ge interface; secondly, a comprehensive comparison between the two lanthanide oxides (La_2O_3 and Y_2O_3) in terms of band line-up, interfacial features and reactivity to Ge which points to the superiority of the gate stack for adoption in CMOS engineering.

4.2 Experimental

The 2 nm (nominal) La_2O_3/Ge and 5 nm (nominal) Y_2O_3/Ge gate stacks were deposited by Molecular Beam Epitaxy (MBE) at temperatures ranging from 44°C to 400°C on n- and p-type Ge substrates. Prior to deposition, the Ge surface was cleaned by a mild degreasing with TCE, acetone and methanol for 5 minutes in each solvent to remove the organics. Then the GeO_x native oxide was thermally desorbed in-situ, by annealing at 450 – 500°C for 30 minutes. The La_2O_3 films deposited at 44°C and 250°C were subjected to post-deposition oxygen (O_2) anneal at 300°C for 15 minutes. Y_2O_3 films were prepared by co-deposition of Y and atomic oxygen at temperatures 225°C and 400°C. The reference samples for spectroscopic ellipsometry and XPS studies entailed a selection of thermally grown GeO_2/Ge with/without capping Al_2O_3 layers, Al_2O_3/Ge as well as oxidized La and Y foils. The GeO_2 films of two nominal thicknesses 4.5 and 12 nm were prepared by ex-situ furnace anneal at 450°C for 5 min and 60 minutes respectively. The capping Al_2O_3 layers with 4 nm nominal thickness were prepared in-situ by co-deposition of Al and atomic oxygen.

The X-ray photoelectron spectra for La_2O_3/Ge stacks were recorded at the Daresbury NCESS facility using an ESCA300 spectrometer with monochromated Al Kα X-rays of energy 1486.6 eV and electron take-off angles (TOA) of 15-90°. The spectrometer was calibrated so that the Ag $3d_{5/2}$ photoelectron line had a binding energy (BE) of 368.35 eV, and a full width at half maximum (FWHM) of 0.5 eV. The X-ray source power was 2.8 kW and the spectrometer pass energy was 150 eV with the entrance-slit width of the hemispherical analyzer set to 1.9 mm. Under these conditions, the overall spectrometer resolution was ~ 0.5 eV [70]. Charge compensation was achieved using a VG Scienta FG300 low energy electron flood gun with the gun settings adjusted for optimal spectral resolution. The electrons BEs were then corrected by setting the C 1s peak in the spectra (due to stray carbon impurities) at 284.6 eV for all samples [71]. Wide scans were recorded in the 0-1250 eV energy range to determine the elements present in the samples and to check for surface contamination. Then the O 1s, Ge 3d, La 4d, and valence photoelectron lines were recorded separately. The core-level positions are defined as the FWHM and determined to within 0.05 eV by fitting a Voigt curve to the measured peaks. A Shirley-type background [72] is used during the fitting of all the spectra. The angle resolved (AR)-XPS and measurements of Y_2O_3/Ge stacks were made in a separate ultra high vacuum system consisting of an Al Kα X-ray source and a PSP Vacuum Technology electron energy analyser. This spectrometer was operated with an overall resolution of about 0.8 eV. To diminish the effect of differential charging on evaluating valence band offset (VBO) [73, 75], during the XPS measurements the X-ray beam exposure was across the whole sample. The individual core level scans were performed for the duration of at least an hour until the point they reached constant binding energies, and the samples could be considered as charge saturated. Medium energy ion scattering was carried out at the STFC Daresbury Laboratory, with a 100 keV He^+ beam and a double alignment scattering configuration with a scattering angle of 90° and 135°.

The VUV-VASE measurements were performed using a spectral range from 0.5 – 8.8 eV (referring to wavelength range λ = 140-2500 nm), and angles of incidence of 55-75°, by 10° as a step, to maximize the accuracy. The entire optical path was enclosed inside a dry nitrogen purge to eliminate absorption from ambient water vapour and oxygen. The XRD measurements were done using the Philips Xpert XRD system. Electrical characterization was carried out at room temperature on metal insulator semiconductor (MIS) capacitors patterned by Pt e-beam evaporation on the dielectric surface through a shadow mask consisted of circular dots 300 μm

in diameter. The back ohmic contact was made using eutectic In-Ga alloy. The high frequency capacitance voltage data were obtained with a HP4284 precision LCR meter.

4.3 Results and Discussion

4.3.1. La_2O_3/Ge gate stacks

MEIS and XPS measurements were performed to assess the thickness, distribution of elements and interfacial composition of the ultra-thin La_2O_3/Ge gate stacks. The key findings are outlined in this section. Note that as the thicknesses were less than 5 nm, the results from spectro-ellipsometry on these stacks were not conclusive, hence, Medium Energy Ion Scattering (MEIS) results were used. The MEIS energy spectra for the La_2O_3/Ge deposited at 44°C and 400°C are shown in Fig. 4.1(a). There is a small high energy tail on the Ge signal for sample deposited at 400°C that indicates an inclusion of Ge in the La_2O_3 film. The elemental depth profiles were calculated assuming the lanthanum signal is La_2O_3 with a stopping power density of 6.5 g/cm^3. The calculated La and Ge depth profiles are shown in Fig. 4.1(b), and reveal the structures of 3 nm La_2O_3/2.2 nm IL/Ge and 2.6 nm La_2O_3/1.7 nm IL/Ge for the stacks deposited at 44°C and 400°C respectively (Table 4.1). A reduction of the overall dielectric thickness of ~ 9 Å for the gate stack deposited at higher temperature is evident. Also, note that there is a significantly broader edge to the Ge substrate for the layer deposited at 44°C, however, a slightly narrower La_2O_3/Ge interface in comparison to the sample deposited at 400°C. The concentration of Ge (10-20%) in La_2O_3 sample deposited at 400°C drops off towards the surface. The results strongly point to the formation of Ge-rich interfacial layers. In case of 44°C deposited sample, the top layer is La_2O_3, while strong intermixing (penetration of Ge) is visible for sample deposited at higher temperature. It seems that bi-layer structure exists for the 44°C deposited sample, with germanate likely to be present at the interface. This observation is further underpinned by findings from the XPS data.

TABLE 4.1 Summary of thickness and band gap data determined by MEIS and VUV-VASE. The literature data [39, 56, 66, 97, 102] for the band gap of various La_2O_3 and Y_2O_3 films deposited on Ge and Si are added for comparison. (PLD refers to Pulsed Laser Deposition, ALD to Atomic Layer Deposition, and PC to photoconductivity measurement method.)

Sample	Deposition	Thickness (nm)		Band gap (eV)			
		MEIS	VASE	Tauc		α-method	XPS/PC
				$(\alpha nE)^{1/2}$	$(\alpha E)^2$		
La_2O_3/Ge dep. @ 44°C	MBE	2.6	…	…	…	…	…
La_2O_3/Ge dep. @ 250°C	MBE	…	…	…	…	…	…
La_2O_3/Ge dep. @ 400°C	MBE	3.0	…	…	…	…	5.45
Y_2O_3/Ge dep. @ 225°C	MBE	…	6.3	5.65	5.70	5.99	…
Y_2O_3/Ge dep. @ 400°C	MBE	…	7.9	5.77	5.77	5.99	…
Y_2O_3/Ge[a]	rf sputtering	…	…	…	…	5.7[a]	…
Y_2O_3/Ge[b]	rf sputtering	…	…	…	…	…	5.7[b]
Y_2O_3[e]	single crystal	…	…	…	…	6.08	…
GeO_2/Ge	thermal oxidation	…	4.4	5.65[f]	…	5.95[f]	…
Al_2O_3/Ge	MBE	…	9.4	6.12	6.33	6.43	…
Al_2O_3/GeO_2/Ge	MBE	…	7.8/3.2	…	…	…	…
		…	8.9/7.2	…	…	…	…

[a]Ref. [56][e] Ref. [99]
[b] Ref. [66][f] Ref. [39]
[c] Ref. [97][d] Ref. [98]

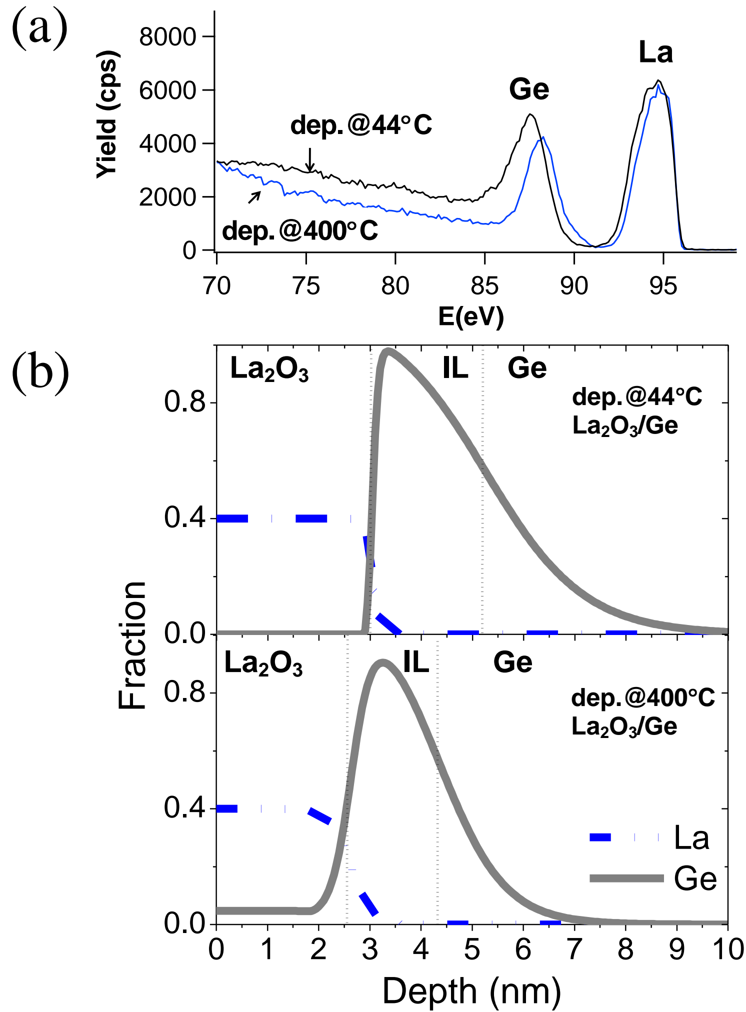

Fig. 4.1 (a) The MEIS yield vs. photon energy for the La_2O_3/Ge stacks deposited at 44°C and 400°C. (b) La and Ge depth profiles derived from the experimental data shown in (a).

It has been shown that La is strongly electropositive and tends to strongly attract neighbouring O atoms [49]. The influence of La is considered to regulate the distribution of O in such a way that oxygen density is maximized in the final compound [48]. Furthermore, La on Ge in the presence of oxygen has been found to produce only La–O bonds [19], with no gap states, and the formation of stable $LaGeO_x$ layers[44,47,49]. A penetration of Ge into the La_2O_3 layer observed in this work for the highest deposition temperature is in agreement with the previous study [44] by energy dispersive X-ray spectroscopy where $LaGeO_x$ layer has been formed across the entire film at the temperature of 360°C.

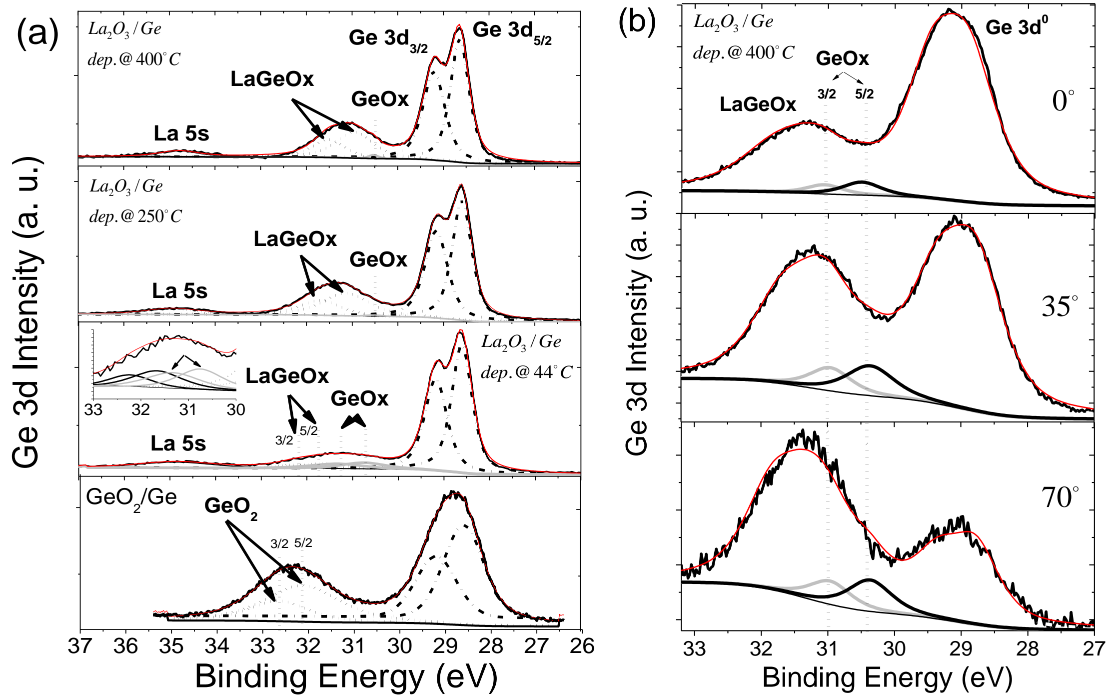

Fig. 4.2. (a) Ge 3d XPS core level spectra for La_2O_3/Ge stacks deposited at 44°C, 250°C and 400°C. (b) Angle Resolved-XPS Ge 3d core levels for the stack deposited at 400°C. The fitting shown refers to the doublet of Voigt peaks for GeO_x. Note that the spectra shown in (b) are acquired on a lower resolution instrument; hence the spin-orbit splitting for the $Ge3d^0$ substrate peak cannot be seen. There is evidence of GeO_x presence not only at the interface.

Fig. 4.2(a) shows the Ge 3d core level spectra for the 44°C, 250°C and 400°C deposited stacks. The data were fitted using a doublet of Voigt functions corresponding to Ge $3d_{5/2}$ and Ge $3d_{3/2}$ components. The spin-orbit splitting and area ratio values of 0.6 eV and 2:3 were fixed for the fit. The spin-orbital splitting for Ge 3d substrate peak (Gd^0) can be seen in Fig. 4.1(a) at energies of 28.6 and 29.2 eV. No presence of GeO_2 at the interface for La_2O_3/Ge stacks is evident from the Ge 3d core level spectra (see the reference GeO_2/Ge spectrum at the bottom of Fig. 4.2(a) for comparison); the Ge 4+ oxidation state has been reported to occur above 3 eV; @ 3.2 eV[49,76]and 3.4 eV[77,78]from the Gd^0. Considering that the Gibbs free energies of formation of GeO_2 (-387 kJ/mol at 1000°K), the GeO_2 is thermodynamically unstable so that a GeO_2 layer is unlikely to form at the La_2O_3/Ge interface. Taking into account the electronegativity of Ge ($\chi_{Ge} = 2.0$), $LaGeO_x$ is expected to appear between the chemical shifts of GeO (Ge^{+2}) and Ge_2O_3 (Ge^{+3}), i.e. between 1.7 eV and 2.8 eV [17, 77]. The energy shift of 2.2 eV for $LaGeO_x$ has been reported [48, 49]. In our work, the presence of $LaGeO_x$ (3/2 and 5/2) can be de-convoluted from the spectra at the chemical shift of +2.4 to +2.6 eV. Further

evidence of $LaGeO_x$ formation comes from the observed shift of La $4d_{5/2}$ doublet peak in Fig. 4.3(a) towards the higher BE (~ 0.1-0.2 eV) in comparison to the pure La_2O_3 at 102.2 eV [79]. Note that the BE of La $4d_{5/2}$ for the 44°C deposited sample shows no shift in comparison to the pure La_2O_3, substantiating the MEIS result in Fig. 4.1(b) that this layer constitutes mainly of lanthanum oxide. The O 1s spectrum shows further evidence of a clear La-O bond at 528.6 eV[79] (see top graph in Fig. 4.3(b)), which flattens out as the deposition temperature increases, and the centroid peak shifts towards lower binding energies for the 400°C deposited sample consistent with a formation of $LaGeO_x$ film[44].

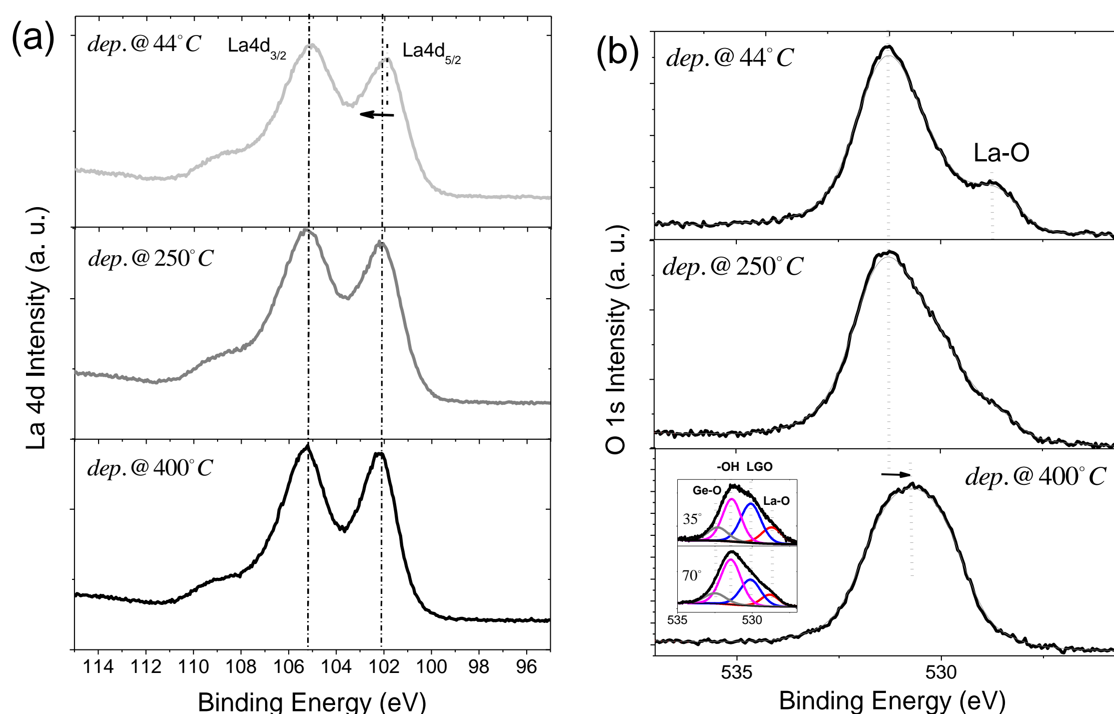

Fig. 4.3 (a) La 4d and (b) O 1s XPS core level spectra for La_2O_3/Ge stacks deposited at 44°C, 250°C and 400°C. The spectra are taken at the normal incidence angle, TOA = 0°. The inset in bottom part of (b) refers to the TOAs of 35° and 70° revealing the surface and bulk features for the 400°C deposited stack. The deconvolution of the main peak in the inset includes sub-peaks of: La-O-La, La-O-Ge (LGO), La-OH, and Ge-O-Ge from low to high BEs of O 1s peak.

The Ge 3d spectra in Fig 4.2(a) confirm the existence of an interfacial layer ascribed to GeO_x as the binding energy shift lies at ~ 1.4 eV from the Ge $3d^0$. The reported values of Ge^{+1} and Ge^{+2} are at ~ 1 eV and 1.8 eV shifts respectively [77, 78]. The spin-orbit splitting for GeO_x could only be resolved in the 44°C sample (see inset in Fig. 4.2 (a)), while for higher deposition temperatures, the fitting shows only a very small single peak. The angle-resolved XPS of this

region for the 400°C deposited La_2O_3/Ge is shown in Fig. 4.2 (b); the peak is more pronounced as the angle is increased indicating that GeO_x is present at the interface but surprisingly also in the oxide bulk. The same finding can be deduced from the AR-XPS spectra of O 1s core level shown in the inset of Fig. 4.3 (b). As the angle is increased, the broad centroid peak is transformed, showing sub-peaks as a signature of La-O-La, La-O-Ge, La-OH and the Ge-O-Ge bonds. The surface and even bulk hydration have been found to take place for all binary lanthanide oxides [41, 79, 80], and its strong presence is visible for these samples too.

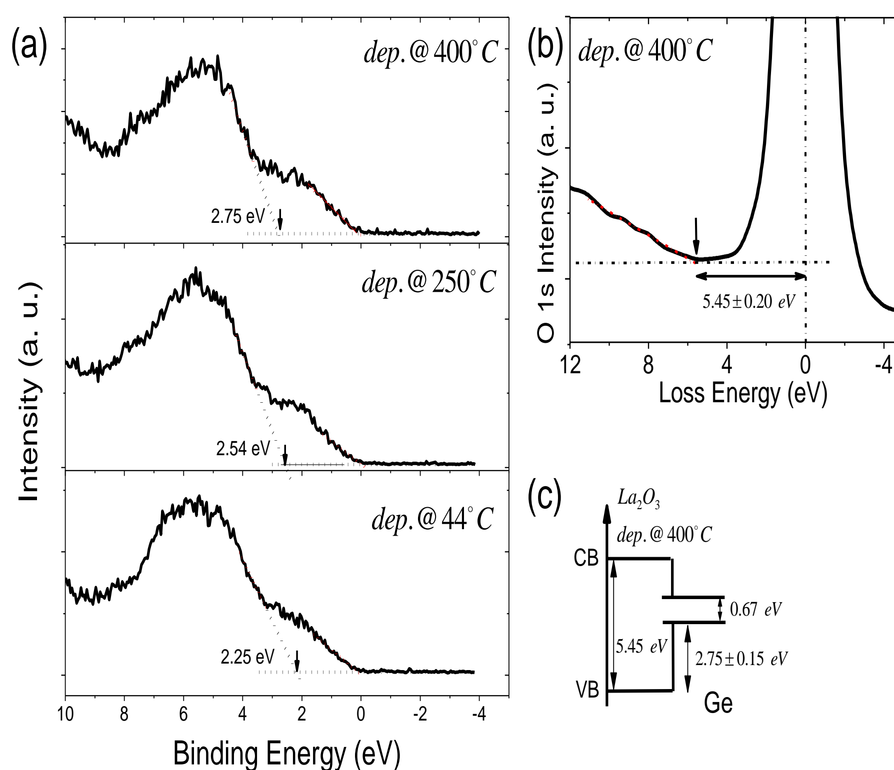

Fig. 4.4 (a) High resolution valence band spectra for La_2O_3/Ge stacks deposited at 44°C, 250°C and 400°C. (b) O 1s XPS energy loss spectrum for the stack deposited at 400°C showing the band gap value of ~ 5.4 eV. (c) The schematic of the band diagram for La_2O_3/Ge deposited at 400°C.

The band diagram of the La_2O_3/Ge stack deposited at 400°C was derived using the valence [81, 82] and O1s energy loss XPS spectra [83, 84] and is shown in Fig. 4.4. The high resolution valence band (VB) spectra for the three La_2O_3/Ge stacks are plotted in Fig. 4.4(a). Although the accuracy in the determination of the Ge VB maximum is quite limited, we measure a VBO value of 2.75 ± 0.15 eV for 400°C deposited sample, in reasonable agreement with the theoretically predicted value of 3.0 eV for La_2GeO_5 and $La_2Ge_2O_7$ compounds[57]. The band

gap is usually obtained from the inelastic energy loss features observed on the high binding energy side of the core level photoemission peaks [79, 82, 84]. The band gap equals the energy distance between the photoemission peak centroid and the onset of the features due to single particle excitations [83]. Fig. 4.4(b) shows the energy loss features of the O 1s peak for the 400°C deposited sample. The band gap of the $LaGeO_x$ film was determined to be 5.45 ± 0.2 eV. By taking into account the band gap of Ge of 0.67 eV, the calculated CBO for $LaGeO_x$/Ge is ~ 2.1 eV (Fig. 4.4(c)). This is in agreement with the IPE study on ZrO_2/La_2O_3/Ge film which indicates CBO of interfacial $LaGeO_x$ film of > 2.0 eV [50]. It is worth noting that the valence band edge of La_2O_3 films reduces by about 0.5 eV as the deposition temperature decreases from 400°C to 44°C as can be seen from Fig. 4.4 (a). This observation might indicate structurally different multi-layer stacks; in particular for the 44°C sample, where the MEIS results point to predominantly La_2O_3 layer on top. For the latter, this implies a VBO of 2.25 ± 0.15 eV and hence conduction band offset value for La_2O_3 on Ge of ~ 2.6 eV from our work, in close agreement with theoretically predicted CBO value of 2.56 eV [52, 53]. It has been observed that La_2O_3 reacts strongly with Ge substrate to form spontaneously a nearly uniform $LaGeO_x$ compound across the entire film thickness during deposition [47-49]. It is evident from the XPS Ge 3d core level spectra in Fig. 4.2 that $LaGeO_x$ is indeed formed at all deposition temperatures in this study, however, our results do not show a uniform layer across the whole thickness of the gate stack. This is particularly evident at lower temperatures. Furthermore, the noticeable shift in the valence band offset in Fig. 4.4(a) cannot be explained by the formation of a structurally different germanate layer formed at a different deposition temperature. Theoretical work points to the band gap and band offsets of the La germinates to be relatively independent of Ge content because the valence band top is formed of O 2p states and the conduction band bottom is formed of La 4d states, which do not change with composition [51]. The theoretically predicted values of band gap and band offsets are 5.0 eV and 3.0 eV respectively for both $La_2Ge_2O_7$ and La_2GeO_5 [51]. However, the observed band line-up substantiates the structural observation from MEIS on transition from a bi-layer La_2O_3/$LaGeO_x$ at 44°C to $LaGeO_x$/Ge gate stack at 400°C. A further argument which underpins our band line-up results, is the observation from electrical measurements [44] that the stack with the best passivation efficiency, that is the lowest D_{it}< 9 x10^{11} $eV^{-1}cm^{-2}$, has been obtained at the highest deposition temperature (360°C); however with higher leakage current and lower scalability in comparison to the La_2O_3/Ge deposited at lower temperatures (44 - 225°C). Interface state density D_{it} ($eV^{-1}cm^{-2}$) for as-deposited La_2O_3/Ge stacks has been reported to be < 9x10^{11}, 1.4x10^{12}, 3x10^{12} and 4x10^{12} for samples deposited at 360°C, 225°C, 150°C and room temperature (44°C) respectively[44].

In summary of this section, our structural study on MBE-deposited La_2O_3/Ge gate stacks shows that as the deposition temperature increases, the stack converts towards a uniform $LaGeO_x$ layer which is beneficial for passivation of the Ge surface. However, the conduction band offset drops by ~ 0.5 eV causing higher leakage, leads to a permittivity reduction to ~ 12[44] and hence lowers the scalability. Moreover, our study confirms that La_2O_3 reacts strongly with Ge and removes the GeO_2 completely. This could allow an abrupt $LaGeO_x$/Ge interface, introducing remote phonon and Coulomb scattering centers directly on the channel and so reducing carrier mobility [57].

4.3.2. Y_2O_3/Ge and Al_2O_3/Ge gate stacks

This section presents a detailed VUV-VASE study of Y_2O_3/Ge stacks deposited at two different temperatures (225°C and 400°C) with a special emphasis on determining the dielectric function and absorption coefficient spectra, as well as estimating the band gap and sub-band gap absorption features. The interfacial composition, band line-up and crystallinity were ascertained from XPS and XRD measurements. In addition, the effect of Al_2O_3 as a capping layer was studied.

4.3.2.1 Thickness, band gap and sub-band gap absorption

Spectroscopic ellipsometry (SE) is very sensitive to the presence of surface layers in the order of just a fraction of a nanometer. The primary sensitivity comes from changes in phase, i.e. ellipsometric angleΔ. Due to the high energy range of SE measurements in this study, all dielectric films became absorbing. The UV absorption is often modelled using a Tauc-Lorentz dispersion relationship [85]. The overall absorption shape is described by amplitude, broadening, centre energy, and band gap energy. The index of refraction is determined from both the Kramers-Kronig (KK) [86] transformation of imaginary part of dielectric function along with addition of an offset and UV pole to account for absorption that is outside the measurement spectral range. The modelling and fitting procedure in this study constituted of firstly, determining the thickness and optical constants in non-absorbing (transparent) region of spectra from 0.5–6 eV using a Cauchy layer representative of a dielectric film. Then, a Kramers-Kronig consistent B-spline layer [87] was used to extend the optical constants into the higher energy range, up to 8.5 eV. This method is consistent with the point-by-point fit method

[88] used in WVASE32, but with two added advantages: firstly, the layer maintains KK consistency which forces the optical constants to keep a physical shape and secondly, the optical constants remain smooth and continuous over the full spectrum, with a controllable parameter to decide the resolution of points. Additionally, the B-spline layer was replaced with the general oscillator model with a possibility of using Cody-Lorentz and Tauc-Lorentz oscillators to discern possible sub-band gap absorption features in the gate stacks and to determine the band gap.

Optical constants for germanium are available in the literature up to 6 eV. We used this spectral range to fit the surface layer thickness of native GeO_2 for the reference Ge substrate. Initial measurements (upon opening the container in N_2 purged environment) on a Ge substrate gave a GeO_2 native oxide thickness of 2.93 nm. Then the germanium optical constants were fitted using a Kramers-Kronig consistent B-spline layer over the entire spectral range. This sample was used as a reference Ge substrate layer to determine the optical constants of thermally grown GeO_2 as well as Y_2O_3 and Al_2O_3 films. The thickness values of the stacks are summarized in Table I. It can be seen that the thickness of Y_2O_3 films is ~ 6-8 nm and of Al_2O_3 ~ 8-9 nm. The reference thermally grown GeO_2 layers have thicknesses of 4.4 nm (non-capped) and 3.2 and 7.2 nm for Al_2O_3 capped samples. The mean squared error (MSE) between the experimental and theoretical curves was in all cases below 5, consistent with a good quality fit of the data.

The real and imaginary part of dielectric function vs photon energy (E) for the stacks is shown in Figs. 4.5(a) and (b) respectively. A pronounced absorption below the band edge can be observed for the Y_2O_3/Ge sample deposited at 225°C, and this is visible in the energy range from about 4 to 5.5 eV in both real and imaginary parts of the dielectric function spectra (see top graphs in Figs. 4.5(a) and (b)). The band-edge tailing is much less apparent for the Y_2O_3/Ge deposited at higher temperature of 400°C. For comparison of these spectra, in the bottom parts of Figs. 4.5(a) and (b), the real (ε_1) and imaginary (ε_2) parts of dielectric function for GeO_2/Ge samples, both non-capped and Al_2O_3 capped are plotted as a reference. The sub-band gap features are evident for GeO_2/Ge samples and this region correlates with the pronounced absorption for the Y_2O_3/Ge sample deposited at 225°C. For the reference GeO_2/Ge sample in this work, a peak appears at ~ 5 eV, while in Ref. 39, two peaks are visible, at 4.4 eV (due to Ge) and at 5.1 eV. Toriumi et al.[89] have reported a peak at 5.1 eV for the GeO_2/Ge sample, thought to be associated with neutral O vacancies or Ge^{+2} in oxygen deficient GeO_2[90]. The high-level ab-initio calculations [91, 92] have shown that –GeX_3 (E' center @ 5.06 eV) and

X_3Ge-GeX_2 (E'-oxygen vacancy @ 5.16 eV) defects are able to form a broad absorption band near 5 eV [90]. Note that X refers to –OH and -$OGeH_3$ simulating the: Ge < defect [92]. From the data in Fig. 4.5(b) it is evident that the pronounced sub-band gap absorption for Y_2O_3/Ge sample deposited at 225°C compares to the absorption features in the GeO_2/Ge spectra and could indicate a possible defective non-stoichiometric germanium oxide interfacial layer. Such an interfacial layer is not apparent for the sample deposited at 400°C.

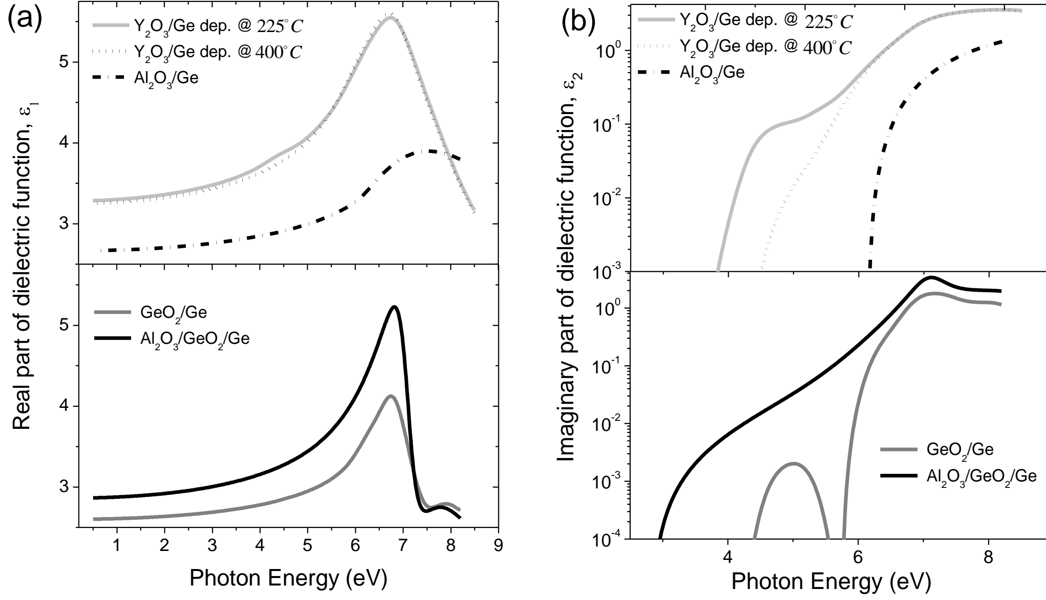

Fig. 4.5 Real (a), and imaginary (b) part of dielectric function vs photon energy for Y_2O_3/Ge stacks deposited at 225°C and 400°C. The dielectric function of GeO_2/Ge with and without capping Al_2O_3 layer is added as a reference.

Following the extraction of the dielectric function ($\tilde{\varepsilon} = \varepsilon_1 + j\varepsilon_2$) for the Y_2O_3, Al_2O_3 and GeO_2 films using the methodology above, the ε_1 and ε_2 parameters are converted into refractive index (n) and extinction coefficient (k) using the KK relations. The absorption coefficient (α) can be found then from the extinction coefficient as

$$\alpha = \frac{4\pi k(E)E}{hc} \tag{4.1}$$

where, h is the Planck's constant, c is the speed of light and E is the photon energy. The band gap in this work is extracted from the Tauc-Lorentz model [85] and α-method, the functional

form of the Tauc-Lorentz model and its simplified expression [93, 94]. The plots of α vs E for Y_2O_3 and Al_2O_3 films are shown in Figs. 4.6(a) and (c) respectively. The associated Tauc-Lorentz plots are depicted in Figs. 4.6(b) and (d). The linear extrapolation of the segments on the curves in the non-absorbing regions gives the band gap values of 5.99 eV for Y_2O_3 layers, and 6.43 eV for Al_2O_3 layer from α-method. The associated band gap values from the Tauc-Lorentz plots are ~ 0.3 eV lower than those derived from the α-method. This result is in agreement with the observations in Ref. [95] that the band gap values obtained from the α-method can be by ~ 0.7 eV larger than the ones determined using the Tauc- or Cody-Lorentz methods. In the insets of Figs. 4.6(b) and (d), the corresponding $(\alpha E)^2$ vs E graphs are added (valid for direct band gap transitions [96]). A summary of the experimental band gap data obtained from this work and literature [39, 56, 66, 97, 102] is shown in Table 4.1. It can be seen that the band gap of Y_2O_3 from the Tauc plots is 5.7 ± 0.1 eV for both deposition temperatures. A similar value has been reported for a radio frequency (rf) sputtered Y_2O_3/Ge stack using SE and XPS measurements [56, 66]. The value reported for Y_2O_3 on Si is 5.6 eV (from SE) [97], on SiO_2 is 6.0 eV (from XPS) [98], and for single crystal 6.1 eV (from SE) [99].

The Tauc coefficient is found to be 1145.4 $eV^{-1/2}cm^{-1/2}$ for both samples. It has been argued that the Tauc plot is related to the degree of order in the structure [104], i.e. disorder generates defects and hence removes states from the bands and generate band tails of localized states. These band tails are generally described by the Urbach exponential [104]

$$\alpha = \alpha_0 \exp(\frac{E}{E_u}), \qquad (4.2)$$

where, α_0 is the constant and E_u is the Urbach energy. In a logarithmic plot of the absorption coefficient, the Urbach tail appears as a linear region at energies below the absorption edge. The logarithmic plot of α vs E, in the sub-band gap energy range (< 6 eV) is shown in the inset of Fig. 4.6(a). An apparent linear region of the plot is visible for the Y_2O_3 sample deposited at 225°C, being indicative of a presence of an Urbach tail. The inverse of this slope gives the Urbach energy of 1.1 eV. The values of E_u = 1.4 eV and the Tauc coefficient of 1344 $eV^{-1/2}cm^{-1/2}$ have been reported for polycrystalline HfO_2 film [103]. A decrease in band tailing for the HfO_2 samples annealed at higher temperatures has been reported and attributed to defect reduction and temperature induced crystallization [105, 106]. The amorphous samples have been proposed to have a continuous and more dense bond network and hence, a lower density of

defects, which is substantiated by the lower trapped charge density [103, 107]. In this work, the sample deposited at higher temperature shows no apparent Urbach tail and has less pronounced sub-band gap absorption region. However, there is no shift of the band edge in comparison to 225°C deposited sample (see Fig. 4. 6(a)), indicating a similar structure. This argument is substantiated by the XRD graphs shown in Fig. 4.7(d), where both films prove to be polycrystalline. The XRD pattern shows polycrystalline phases of Ge (004) plane and Y_2O_3 (631) plane for both samples.

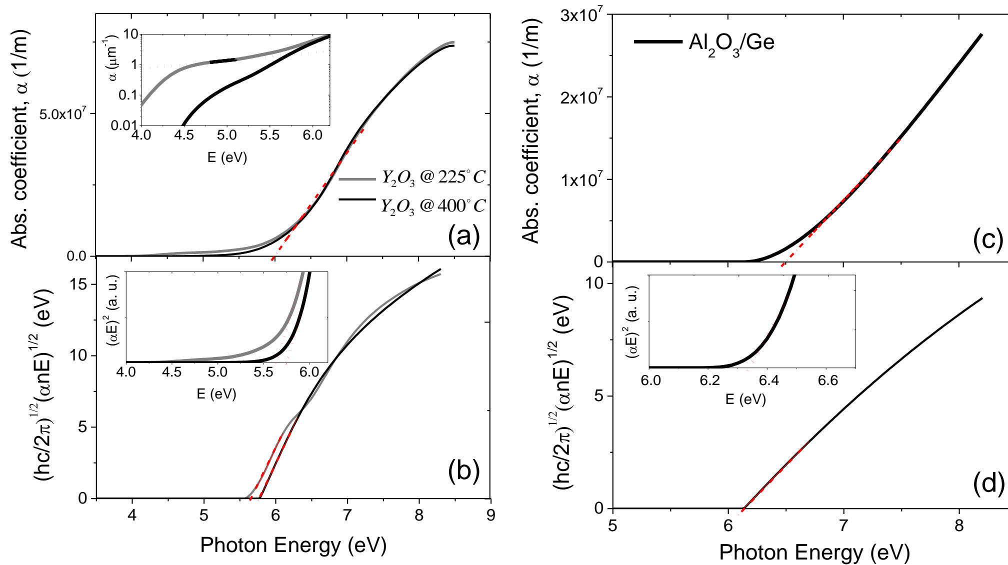

Fig. 4.6 The absorption coefficient (a) and (c), and Tauc $(\alpha nE)^{1/2}$ (b) and (d) vs photon energy plots for Y_2O_3/Ge (deposited at 225°C and 400°C) and Al_2O_3/Ge gate stacks. The inset in (a) shows logarithmic α vs E plots. The insets in (b) and (d) refer to $(\alpha E)^2$ vs E Tauc plots.

4.3.2.2 Interfacial layer study for Y_2O_3/Ge

The Ge 3d XPS core levels can best represent the chemistry at the interface because of their sufficient surface sensitivity and good resolution due to a narrow FWHM [108]. The relevant Ge 3d spectra fitted using a doublet (due to spin-orbit splitting) Voigt functions for each peak are shown in Fig. 4.7(a). The Ge $3d^0$ substrate peak is fitted with a doublet of Ge $3d_{5/2}$ (@29.0 eV) and Ge $3d_{3/2}$ (@ 29.6 eV) with spin-orbit splitting of 0.6 eV and intensity ratio of 2:3 respectively.

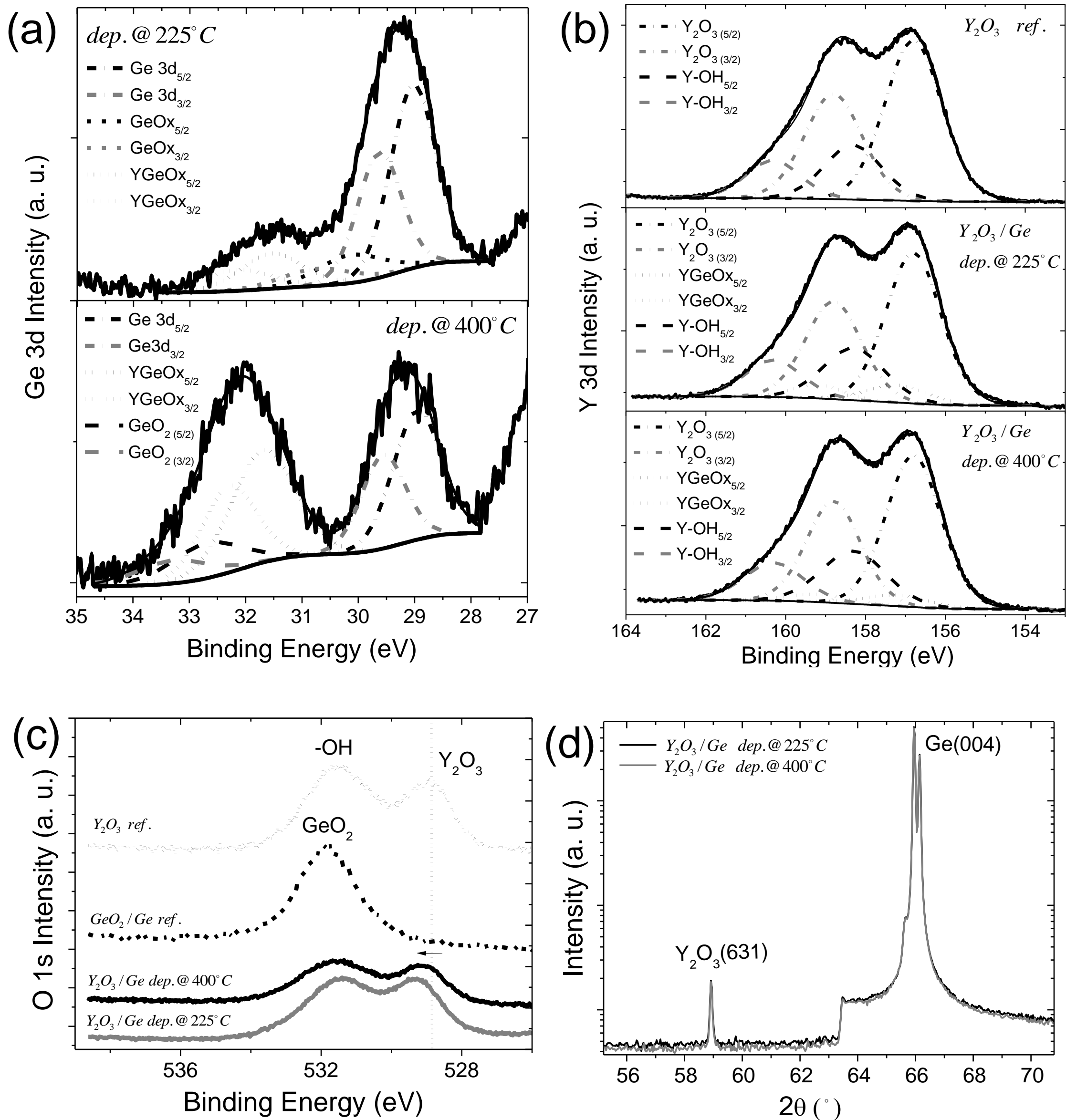

Fig. 4.7 (a) Ge 3d; (b) Y 3d and (c) O 1s XPS core levels for Y_2O_3/Ge deposited at 225°C and 400°C, with GeO_2/Ge and pure Y_2O_3 as reference core level spectra; (d) the referring XRD spectra.

A high BE shoulder to the Ge $3d^0$ substrate peak can be seen for both Y_2O_3 samples, however, with a higher intensity for the layer deposited at 400°C (see Fig. 4.7(a) bottom). Also note that the Ge $3d^0$ is less pronounced for the latter due to the thicker dielectric layer for this sample (see Table 4.1, 7.9 nm for 400°C vs 6.3 nm for 225°C deposited sample). The rising edge at a BE lower than ~ 28 eV originates from Y 4p to O 2s peaks at ~ 25 eV. The formation of the interfacial layer will be reflected in the Ge 3d spectra as positive shifts (with respect to the substrate Ge $3d^0$ peak) when Ge reacts to form $YGeO_x$ layer. It has been reported that the Y-Ge-

O bonding configuration gives rise to a BE shift within the range of + 2.2 to 2.5 eV due to a second nearest-neighbor effect, which is distinctly different from a O-Ge-O type bonding (+3.4 eV shift) [77, 109]. In our spectra in Fig. 4.7(a), the chemical shift for $YGeO_x$ layer is visible at +2.5 to + 2.7 eV from the substrate peak. Note the difference in the interfacial layer between the two samples. The lower temperature deposited Y_2O_3/Ge stack features GeO_x layer at the interface, with a chemical shift of 1.1 eV consistent with +1 Ge oxidation state [78]. The higher temperature deposited stack has sub-oxide fully eliminated, and GeO_2 appears at the interface.

The Y 3d core level spectra were also measured to study the additional bonding and are shown in Fig. 4.7(b). The peak appearing at ~156.95 eV for Y_2O_3/Ge samples represents the co-existence of Y_2O_3at 156.86 eV (see top graph for Y_2O_3 reference in Fig. 4.7(b)) and Ge–O–Y bonding at 157.28 eV (see middle and bottom part of Fig. 4.7(b)). In addition, a positive shift from a reference Y_2O_3 bulk value can be seen from the O 1s spectra shown in Fig. 4.7(c), and this provides firm evidence of charge transfer and formation of $YGeO_x$ at the interface. Also, note that both the Y 3d and O 1s spectra show that Y-OH bond from moisture absorption is present, as in the case of La_2O_3/Ge stacks.

The results imply that Y–O–Y bonding configuration near the surface transforms to a Y–O–Ge configuration near the interface due to the incorporation of Ge atoms into the Y_2O_3 matrix. It has been inferred that Y and Ge atoms intermix more significantly at a higher process temperature [68]. The out-diffusion of Ge signifies the breaking of the strong covalent Ge-Ge bonds even at room temperature. The chemical bonding model proposes possible bond weakening via charge transfer during the formation of chemical bonds [110]. Since the electronegativity difference between Y and Ge (1.22 and 2.01 using Pauling's scale) is large, charge transfer and hence the bond weakening can be significant. Room temperature mixing has also been observed for Si, and the concept of metallic screening of covalent bonds has been used to explain the bond weakening [111,112].

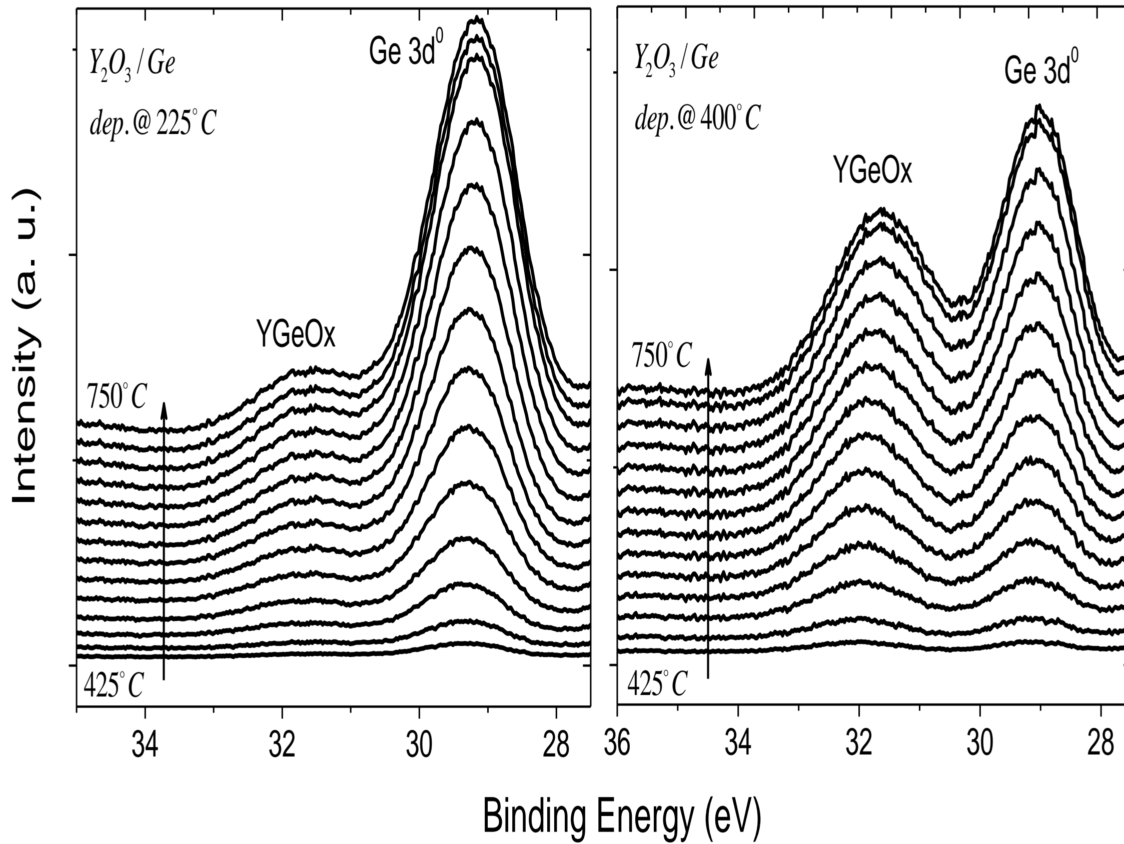

Fig. 4.8 Ge 3d XPS core level for Y_2O_3/Ge deposited at 225°C and 400°C after in-situ anneal from 425°C to 750°C, in steps of 25°C.

In order to study the effect of temperature on the interfacial layer characteristics of Y_2O_3/Ge, XPS in-situ annealing measurements were performed in the temperature range of 425°C to 750°C, with a step of 25°C. The Ge 3d core level spectra as a function of annealing temperature are shown in Fig. 4.8. A stronger formation and more pronounced $YGeO_x$ shoulder is visible for the Y_2O_3/Ge sample deposited at 400°C. The fitting of the Ge 3d core level at different annealing temperature is performed using the same procedure described above. The relevant graphs for the two Y_2O_3/Ge samples are shown in Figs. 4.9(a) and (b).

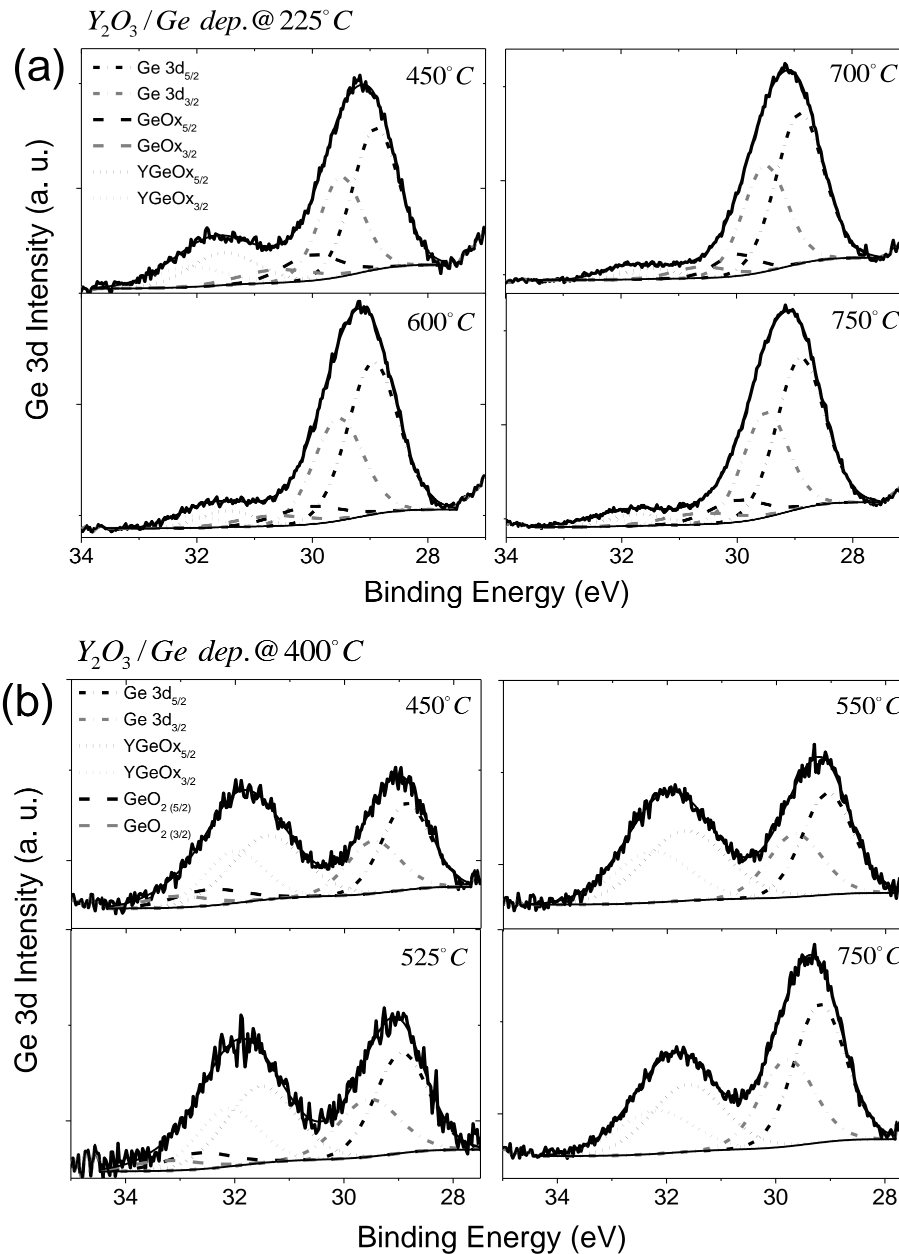

Fig. 4.9 Ge 3d XPS core level fitting after in-situ anneal for two different Y_2O_3/Ge gate stacks deposited at: (a) 225°C, and (b) 400°C.

The Y_2O_3 sample deposited at 225°C shows less pronounced interfacial layer shoulder, with GeO_x present at all annealing temperature as can be seen from Fig. 4.9(a). On the contrary, the 400°C deposited Y_2O_3 sample shows presence of GeO_2 IL layer until the annealing temperature of 525°C. For this gate stack after the 550°C annealing temperature, the interface is pristine $YGeO_x$ layer.

4.3.2.3 Estimation of VBO and derivation of a band diagram for Y_2O_3/Ge

According to Kraut's method [113], the valence band offset value for a Y_2O_3/Ge heterojunction can be determined using the following equation

$$VBO = (E_{Ge3d} - E_V)^{Ge} - (E_{Y3d} - E_V)^{Y_2O_3} + \delta_{CL} \qquad (4.3)$$

where, E_{Ge3d} and E_{Y3d} are the binding energies of the Ge 3d and Y 3d core levels that have been selected as references for Ge substrate and Y_2O_3 respectively. Ev refers to the valence band maximum (VBM) for the Ge substrate and bulk reference Y_2O_3 sample and can be estimated from the valence band spectra using linear interpolation method [114]. The term δ_{CL} is defined as the energy difference between the Ge 3d and Y 3d core levels referring to Ge substrate and Y_2O_3 from the interface Y_2O_3/Ge sample, i.e.

$$\delta_{CL} = E_{Ge3d}^{Ge} - E_{Y3d}^{Y_2O_3}$$

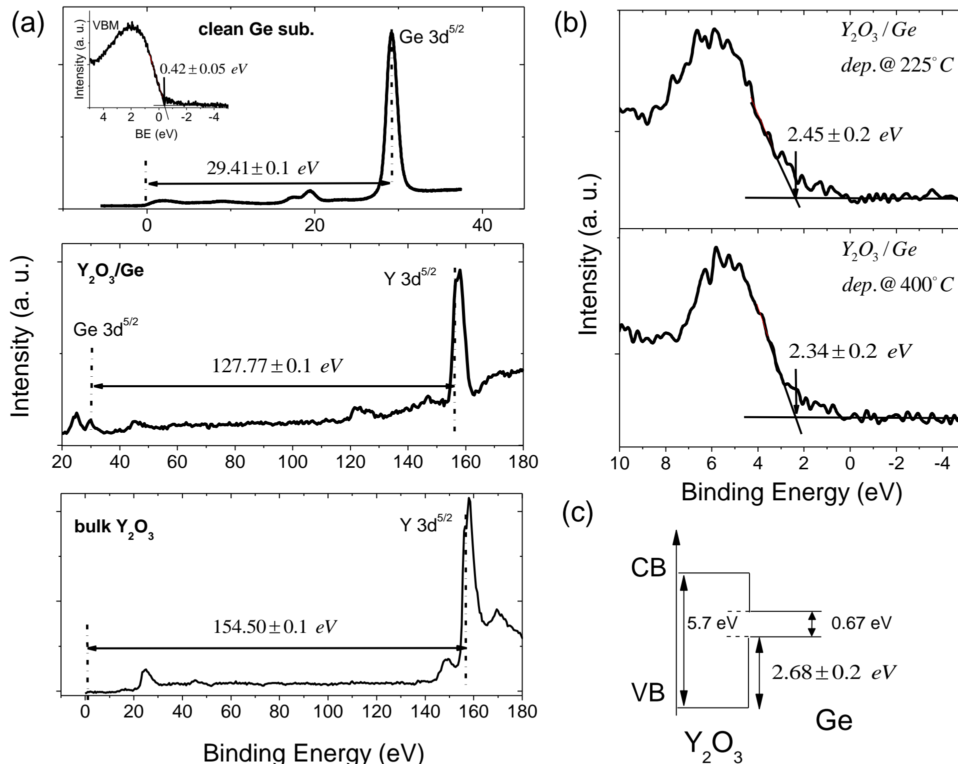

Fig. 4.10 (a) The XPS spectra for the calculation of VBO for Y_2O_3/Ge using Kraut's method. (b) Valence band spectra for Y_2O_3/Ge gate stacks showing VBO of 2.4 ± 0.20 eV and (c) Derived band diagram for the Y_2O_3/Ge stack.

Fig. 4.10(a) shows the selected core levels and valence band spectra for a clean bare n-Ge substrate (top), for interfacial Y_2O_3/Ge (middle) and for a bulk Y_2O_3 (bottom) films. The energy difference between the Ge 3d 5/2 and the VBM in the bare, pre-clean Ge sample (Fig. 4.10(a), top) was measured to be 29.41 ± 0.1 eV. This value compares to the published results of 29.47 ± 0.07 eV [115], 29.40 ± 0.03 eV [116], 29.30 ± 0.1 eV [117], and 29.61 ± 0.1 eV [39]. The value of δ_{CL} is found to be 127.77 ± 0.1 eV for the Y_2O_3/Ge deposited at 225°C (shown in Fig. 4.10(a), middle), and 127.85 ± 0.1 eV for the sample deposited at 400°C. The energy difference for the bulk Y_2O_3 reference sample was estimated to be 154.50 ± 0.1 eV. By inserting the estimated values in Eq. (4.3), the VBO is determined to be 2.68 ± 0.2 eV. The valence band spectra for the two Y_2O_3/Ge stacks are depicted in Fig. 4.10(b). We measure directly from these graphs VBO values of 2.45 eV and 2.34 eV with an error bar of ± 0.2 eV, for 225°C and 400°C deposited samples respectively. It is worth noting that the VBO value is within the tolerance bar of the measurement for both samples. This is in contrast with the La_2O_3/Ge samples, where a more substantial decrease in VBO value with the raise of the deposition temperature was observed (see Fig. 4.4(a)). Note that the spectra shown in Fig. 4.4(a) are obtained from an instrument with higher spectral resolution than once shown in Fig. 4.10(b). It is worth mentioning that we have re-measured the valence band region for the Y_2O_3/Ge samples using a monochromated XPS instrument, and the result of ~ 2.4 ± 0.2 eV was confirmed. The full band diagram of Y_2O_3/Ge is drawn in Fig. 4.10(c) using the Kraut's value of the VBO and the band gap value obtained from the Tauc plots. The conduction band offset (CBO) for Y_2O_3/Ge stack is calculated to be 2.35 eV. The value of the VBO of 2.78 eV has been reported for Y_2O_3/Ge from the Kraut's method [66], however the values of the core level differences in Eq. (4.3) have not been stated, so direct comparison with our data is not possible. The obtained CBO value of 2.35 eV from this work compares to the theoretically predicted value of 2.56 eV [52, 53].

4.3.2.4 Electrical characterization of Y_2O_3/Ge stacks

The high frequency capacitance voltage and leakage current density characteristics for a MOS capacitor from the as-deposited Y_2O_3 films grown at 225°C and 400°C are shown in Figs. 4.11 and 4.12, respectively. The CV curves of the 225°C deposited Y_2O_3 sample (Fig. 4.11(a)) exhibit high frequency dispersion with large bumps in the weak inversion regime. A notable improvement in the CV characteristics is observed as the growth temperature increases from 225°C to 400°C.

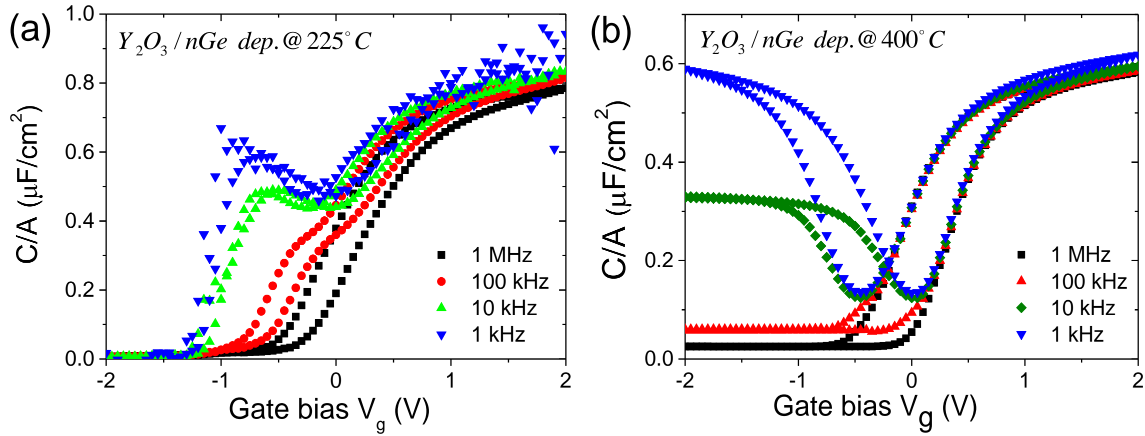

Fig. 4.11 Capacitance voltage characteristics for 10 nm (nominal) Y_2O_3/n-Ge gate stacks deposited at (a) 225°C, and (b) 400°C.

The aforementioned result could be correlated with the Ge 3d XPS spectra presented in Fig. 4.7, where full elimination of GeO_x sub-oxide and enhanced $YGeO_x$ formation have been demonstrated in the case of the 400°C-deposited Y_2O_3/Ge stack.

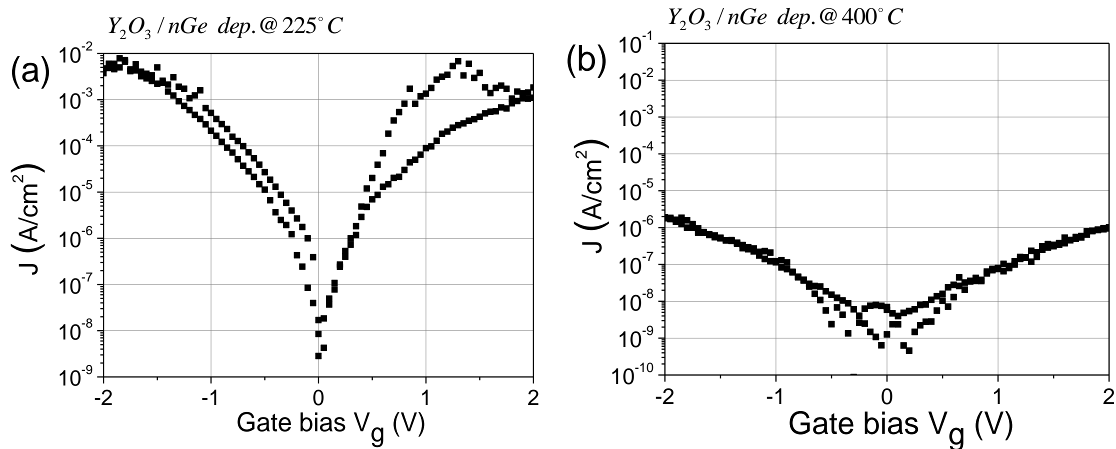

Fig. 4.12 Current density vs voltage characteristics for 10 nm (nominal) Y_2O_3/n-Ge gate stacks deposited at (a) 225°C, and (b) 400°C.

It is evident from Fig. 4.12 that the leakage current of the 400°C-deposited sample is subsequently kept below 10^{-6} A/cm^2 at 1 V, as opposed to La_2O_3 that suffers from high leakage current of ~ 10^{-1} A/cm^2 at 1 V for samples deposited at 360°C (see Ref. 44). This observation is in good agreement with the band diagrams presented in Figs. 4.4 and 4.10, where the Y_2O_3/Ge stack was found to exhibit a higher conduction band offset (> 2.3 eV), than the respective

La_2O_3/Ge (~ 2 eV). Furthermore, this behaviour is in good agreement with the reported VASE and XPS spectra of the as-deposited Ge/Y_2O_3 samples (see Figs. 4.5, 4.7(a) and 4.9), where a reduction of defective GeO_x species has been observed at a growth temperature of 400°C.

4.3.2.5 The effect of an Al_2O_3 capping layer

The band gap value of Al_2O_3 layer is found to be 6.1-6.4 eV from the VUV-VASE results (see Table 4.1 and Fig. 4.6(c)-(d)). The ALD-deposited Al_2O_3 has been reported to have a much lower density (3.1-3.3 g/cm^3) than sapphire, and a lower band gap of ~ 6.2 eV (from photoconductivity measurements) [100, 101] and 6.5 eV (from XPS) [102]; for sapphire the band gap is 8.8 eV[53,118]. No Urbach tail was evident for the Al_2O_3/Ge in this work, suggesting negligible sub-band gap absorption. It has been argued recently that Al_2O_3 is a good oxygen diffusion barrier and therefore blocks the O vacancy diffusion that allows the volatilisation of GeO and the creation of sub-stoichiometric GeO_x interface states [57].

Calculations of electronic structures of interfaces and interface defects and of oxide reactions and considerations of diffusion barrier properties by Robertson's group [57, 119] suggest that a thin Al_2O_3layer in the overall dielectric might be a preferred passivation scheme for Ge channels [34, 35]. Furthermore, the difference in the O density between La_2O_3, Y_2O_3 and Al_2O_3 allows for different behaviour of these oxides on Ge [49]. As discussed in the introduction, both La_2O_3 and Y_2O_3 belong to a group of intimate dielectrics on Ge, i.e. they form stable germanate layers in contact with Ge. On the contrary, Al_2O_3 acts as a barrier on Ge. This has further been associated with the cation radius of the corresponding oxides [49]. In particular the large ionic radius of La^{+3} (117 pm) compared to Al^{+3} (67.5 pm), implies large M–O bond length (M - metal ion), and consequently a less dense O structure.

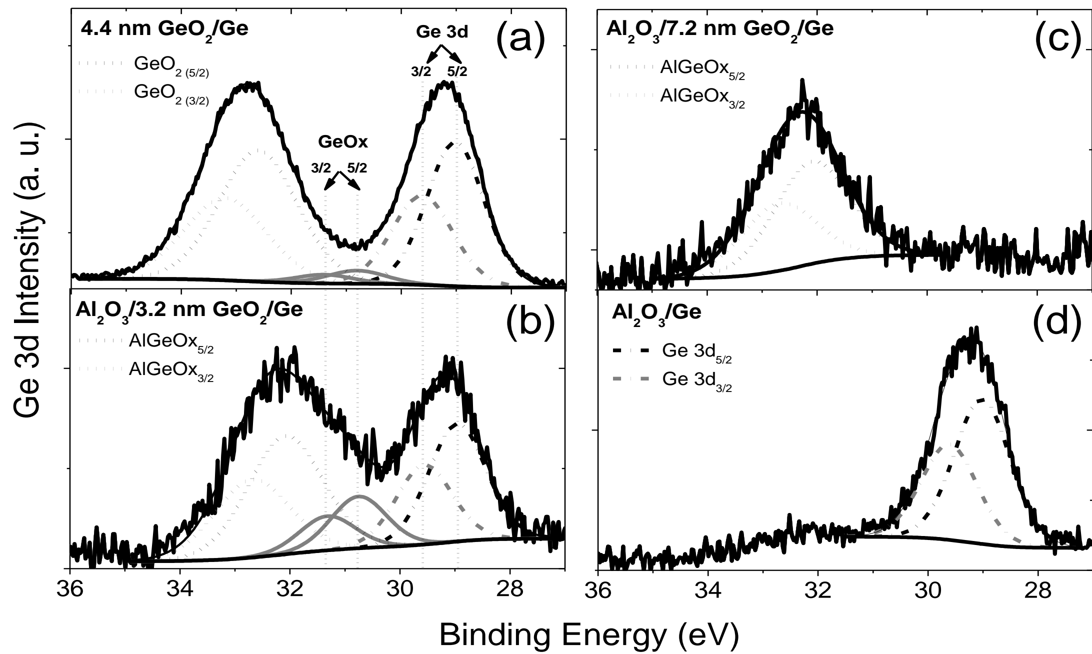

Fig. 4.13 Ge 3d XPS core levels fitting for the (a) GeO_2/Ge, (b) Al_2O_3/3.2 nm GeO_2/Ge, (c) Al_2O_3/7.2 nm GeO_2/Ge and (d) Al_2O_3/Ge.

The interfacial features for the selection of GeO_2/Ge with and without Al_2O_3 capping layers can be found from inspecting the Ge 3d core levels, and are shown in Fig. 4.13. For the non-capped 4.4 nm GeO_2/Ge layer, a strong presence of Ge^{+4} oxidation state is evident from the chemical shift to the Ge $3d^0$ peak of > 3 eV [49, 77,78] (Fig. 4.13(a)). After the Al_2O_3 capping layer deposition on 3.2 nm GeO_2/Ge, the shift to lower energy of the Ge-O peak reveals the impact of Al_2O_3 deposition on the GeO_2 layer. This behaviour suggests the formation of a germanate layer ($AlGeO_x$) at the Al_2O_3/GeO_2 interface. Also, note the presence of GeO_x at the interface for this sample. For the thicker 7.2 nm GeO_2 layer with Al_2O_3 cap, only a sub-peak referring to $AlGeO_x$ can be observed from Fig. 4.13(c). In the case of Al_2O_3/Ge, no high BE shoulder is apparent, rather just a peak referring to the Ge $3d^0$ substrate (Fig. 4.13(d)) suggesting no IL. Further evidence comes from the Al 2p spectra shown in Fig. 4.14, the Al 2pspectrum for Al_2O_3/Ge sample exhibits no clear change, suggesting that there is no detectable chemical reaction in the Al_2O_3 capping layer, and that Al_2O_3 acts indeed as a barrier layer. On the contrary, for the Al_2O_3/GeO_2/Ge structures there is a clear shift for both Al 2p and O 1s peaks towards higher BEs in agreement with $AlGeO_x$ formation discussed above. These observations indicate that the Ge in-diffusion through the GeO_2 into the Al_2O_3 and the intermixing between these different layers lead to a $AlGeO_x$ IL formation, possibly more stable than the GeO_2 interlayer [29]. A

recent theoretical study predicted that the incorporation of Al into the GeO_2 matrix leads only to the formation of Ge–O–Al bonds, with no defect states inside the Ge bandgap [19], indicating that the formation of the $AlGeO_x$ interlayer should not be detrimental to the interface quality[7, 22, 34, 35].

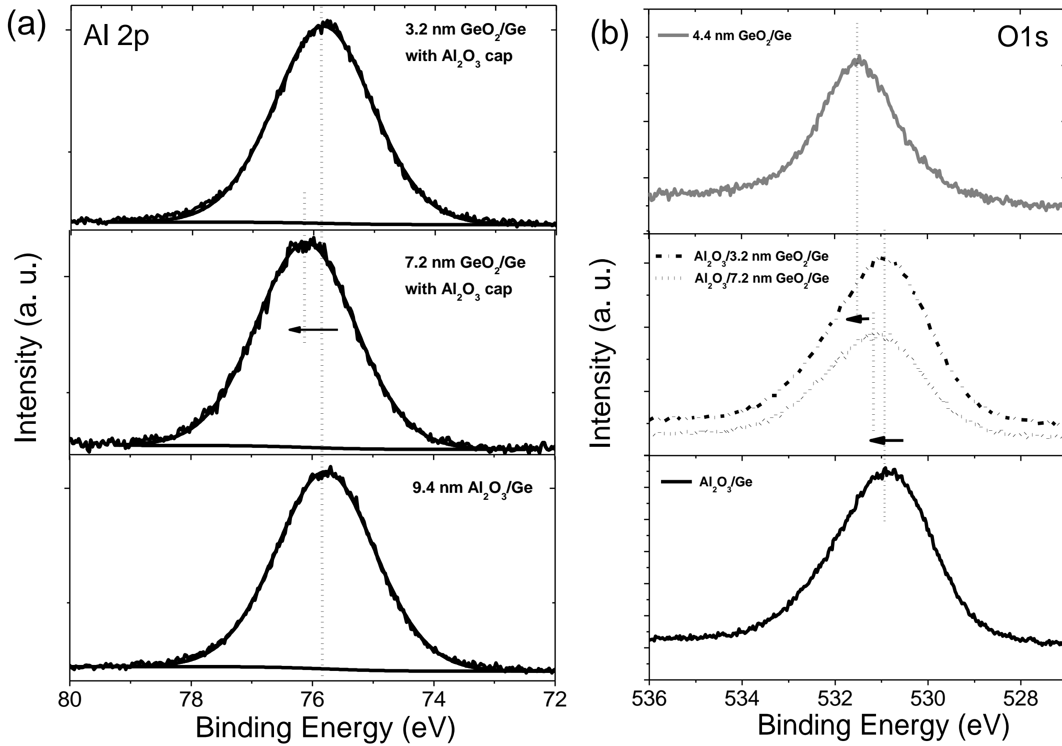

Fig. 4.14 (a) Al 2p and (b) O 1s XPS core level spectra for GeO_2/Ge, with and without Al_2O_3 cap, and Al_2O_3 on Ge.

In summary of this section, there is evidence that Y_2O_3 shows a more moderate reactivity to Ge and shows feasibility for a GeO_2-interfacial layer at the higher deposition temperature of 400°C. The conduction band offset has been derived from the XPS and VUV-VASE data and shows a sufficiently large (~2.3 eV) value to allow for the measured low leakage (< 10^{-6} A/cm^2 @ 1 V). The stack transforms into pristine $YGeO_x$/Ge layer, with no GeO_2 IL, for annealing temperature above 525°C. Our experimental results confirm that Al_2O_3 acts as a barrier on Ge, with no detectable IL, within a resolution of the experimental techniques used.

4.4 Conclusion

A comprehensive study of ultra-thin La_2O_3/Ge and Y_2O_3/Ge gate stacks prepared by molecular beam epitaxy has been conducted in this chapter for consideration as interfacial layers for Ge

surface passivation. In particular, the effect of deposition temperature, ranging from 44-400°C, on interfacial features, band line-up, band gap and sub band-gap absorption and crystallinity has been investigated by MEIS, VUV-VASE, XPS and XRD techniques. Both La_2O_3 and Y_2O_3 show reactivity to germanium. A strong presence of germanate layers was found from the high binding energy shoulders to the Ge 3d substrate XPS core level peak, with a chemical shifts of +2.4-2.6 eV for $LaGeO_x$, and +2.5-2.7 eV for $YGeO_x$. With higher deposition temperature, the higher intensity of the germanate layers formation was evident for both gate stacks. However, the interface structure was found to be somewhat different. In the case of La_2O_3/Ge, there is no GeO_2 present at the interface for all deposition temperatures studied, rather germanium sub-oxide species dominate the interface and even they have been found in the bulk of ultra-thin (2-3 nm) films from angle-resolved XPS data. The high-resolution valence band spectra for the La_2O_3/Ge stacks have shown a noticeable positive (~ 0.5 eV) shift in the valence band edge, as the deposition temperature increased from 44°C to 400°C. This observation underpins previously reported electrical characterization data that the stack with the best passivation efficiency has a uniform $LaGeO_x$ layer, but with higher leakage current and hence low scalability. The band diagram has been derived for $LaGeO_x$/Ge (deposited @ 400°C) from the XPS data and values for valence band offset of 2.75 ± 0.15 eV and band gap of 5.45 ± 0.2 eV, in reasonable agreement with recent theoretical calculations.

A Y_2O_3/Ge gate stack deposited at 225°C shows similar GeO_x interfacial layer. The VUV-VASE data have enabled extraction of dielectric function and absorption coefficient versus photon energy for the $Y2O_3$/Ge stacks. The pronounced sub-band gap absorption region is distinctly evident in the broad region from ~ 4.5-5.5 eV from the ε_2 (imaginary part of dielectric function) and absorption coefficient spectra for the 225°C deposited stack. This absorption range could be attributed to a reported neutral oxygen vacancy coordinated with two Ge ions (at 5.06 eV) and/or a Ge^{+2} coordinated with two oxygen (at 5.16 eV) defects; this result substantiates the existence of sub-stoichiometric GeOx layer. The stack deposited at 400°C has no such absorption region and GeO_2 interfacial layer has been found from the Ge 3d XPS core level spectra. Furthermore, after the annealing above 525°C, this stack has become GeO_2-free, transforming into pristine $YGeO_x$/Ge layer. The band diagram has been derived for the Y_2O_3/Ge using the Kraut's method for the estimation of VBO (2.68 ± 0.2 eV) and Tauc-Lorentz method for the band gap (5.7 ± 0.1 eV). The band gap of Al_2O_3 has been found to be 6.1-6.4 eV from

the Tauc-Lorentz and α-methods. There was no detectable interfacial layer for Al_2O_3/Ge stack, indicating possible barrier role of alumina layer.

A notable improvement in the capacitance voltage and leakage current density characteristics has been observed for the Y_2O_3/Ge stacks as the growth temperature increased from 225°C to 400°C. This result is in agreement with the structural data, as the detrimental effect of GeO_x interfacial layer on electrical properties can be expected for the 225°C deposited stack.

In summary, the results of this study unambiguously point to two important findings: firstly, the optimal deposition temperature is in the higher range, at ~ 400°C, as this allows for more uniform germanate layer at the interface with better passivation properties and secondly, comparing two rare-earth stacks, La_2O_3/Ge with Y_2O_3/Ge, deposited at the optimal temperature (~ 400°C). The latter is seen to have more attractive features for Ge interface engineering: moderate reactivity to Ge, GeO_x-free interface, higher conduction band offset (~ 2.3 eV), larger band gap (~ 5.7 eV), and lower leakage current (< 10^{-6} A/cm^2 at 1 V). As such, Y_2O_3/Ge is a serious contender for interface engineering in future Ge CMOS technology.

4.5 References

[1] Takagi S, Zhang R, Takenaka M. Ge gate stacks based on Ge oxide interfacial layers and the impact on MOS device properties. Microelectronic Engineering. 2013 Sep 30;109:389-95.

[2] Toriumi A, Lee CH, Wang SK, Tabata T, Yoshida M, Zhao DD, Nishimura T, Kita K, Nagashio K. Material potential and scalability challenges of germanium CMOS. InElectron Devices Meeting (IEDM), 2011 IEEE International 2011 Dec 5 (pp. 28-4). IEEE.

[3] Caymax M, Eneman G, Bellenger F, Merckling C, Delabie A, Wang G, Loo R, Simoen E, Mitard J, De Jaeger B, Hellings G. Germanium for advanced CMOS anno 2009: a SWOT analysis. InProceedings of the IEEE International Electron Devices Meeting-IEDM 2009 (pp. 461-464).

[4] McIntyre P, Chi D, Chui CO, Kim H, Seo KI, Saraswat K, Sreenivasan R, Sugawara T, Aguirre-Testado FS, Wallace RM. Interface Layers for High-k/Ge Gate Stacks: Are They Necessary?. ECS Transactions. 2006 Oct 20;3(7):519-30.

[5] Caymax M, Van Elshocht S, Houssa M, Delabie A, Conard T, Meuris M, Heyns MM, Dimoulas A, Spiga S, Fanciulli M, Seo JW. HfO 2 as gate dielectric on Ge: Interfaces and deposition techniques. Materials Science and Engineering: B. 2006 Dec 15;135(3):256-60.

[6] Toriumi A, Tabata T, Lee CH, Nishimura T, Kita K, Nagashio K. Opportunities and challenges for Ge CMOS–Control of interfacing field on Ge is a key. Microelectronic Engineering. 2009 Sep 30;86(7):1571-6.

[7] Xie Q, Deng S, Schaekers M, Lin D, Caymax M, Delabie A, Qu XP, Jiang YL, Deduytsche D, Detavernier C. Germanium surface passivation and atomic layer deposition of high-k dielectrics—a tutorial review on Ge-based MOS capacitors. Semiconductor Science and Technology. 2012 Jul 11;27(7):074012.

[8] Nishimura T, Lee CH, Wang SK, Tabata T, Kita K, Nagashio K, Toriumi A. Electron mobility in high-k Ge-MISFETs goes up to higher. InVLSI Technology (VLSIT), 2010 Symposium on 2010 Jun 15 (pp. 209-210). IEEE.

[9] Lee CH, Nishimura T, Tabata T, Wang SK, Nagashio K, Kita K, Toriumi A. Ge MOSFETs performance: Impact of Ge interface passivation. InElectron Devices Meeting (IEDM), 2010 IEEE International 2010 Dec 6 (pp. 18-1). IEEE.

[10] Lee CH, Nishimura T, Saido N, Nagashio K, Kita K, Toriumi A. Record-high electron mobility in Ge n-MOSFETs exceeding Si universality. InElectron Devices Meeting (IEDM), 2009 IEEE International 2009 Dec 7 (pp. 457-460). IEEE.

[11] Lee CH, Nishimura T, Nagashio K, Kita K, Toriumi A. High-Electron-Mobility n-MOSFETs With Two-Step Oxidation. Electron Devices, IEEE Transactions on. 2011 May;58(5):1295-301.

[12] Delabie A, Bellenger F, Houssa M, Conard T, Van Elshocht S, Caymax M, Heyns M, Meuris M. Effective electrical passivation of Ge (100) for high-k gate dielectric layers using germanium oxide. Applied Physics Letters. 2007 Aug;91(8):2904.

[13] Matsubara H, Sasada T, Takenaka M, Takagi S. Evidence of low interface trap density in GeO2/Ge metal-oxide-semiconductor structures fabricated by thermal oxidation. Applied Physics Letters. 2008 Jul;93(3):2104.

[14] Nakakita Y, Nakane R, Sasada T, Matsubara H, Takenaka M, Takagi S. Interface-controlled self-align source/drain Ge pMOSFETs using thermally-oxidized GeO 2 interfacial layers. InElectron Devices Meeting, 2008. IEDM 2008. IEEE International 2008 Dec 15 (pp. 877). IEEE.

[15] Xie R, Phung TH, He W, Sun Z, Yu M, Cheng Z, Zhu C. High mobility high-k/Ge pMOSFETs with 1 nm EOT-New concept on interface engineering and interface characterization. InElectron Devices Meeting, 2008. IEDM 2008. IEEE International 2008 Dec 15 (pp. 393). IEEE.

[16] Yu HY, Ishibashi M, Park JH, Kobayashi M, Saraswat KC. p-Channel Ge MOSFET by selectively heteroepitaxially grown Ge on Si. Electron Device Letters, IEEE. 2009 Jun;30(6):675-7.

[17] Molle A, Bhuiyan MN, Tallarida G, Fanciulli M. In situ chemical and structural investigations of the oxidation of Ge (001) substrates by atomic oxygen. Applied physics letters. 2006 Aug 21;89(8):083504.

[18] Kuzum D, Park JH, Krishnamohan T, Wong HS, Saraswat KC. The effect of donor/acceptor nature of interface traps on Ge MOSFET characteristics. Electron Devices, IEEE Transactions on. 2011 Apr;58(4):1015-22.

[19] Houssa M, Pourtois G, Caymax M, Meuris M, Heyns MM. First-principles study of the structural and electronic properties of (100) Ge/Ge (M) O2 interfaces (M= Al, La, or Hf). Applied Physics Letters. 2008 Jun;92(24):2101.

[20] Prabhakaran K, Maeda F, Watanabe Y, Ogino T. Distinctly different thermal decomposition pathways of ultrathin oxide layer on Ge and Si surfaces. Applied Physics Letters. 2000 Apr 17;76(16):2244-6.

[21] Takahashi T, Nishimura T, Chen L, Sakata S, Kita K, Toriumi A. Proof of Ge-interfacing concepts for metal/high-k/Ge CMOS-Ge-intimate material selection and interface conscious process flow. InElectron Devices Meeting, 2007. IEDM 2007. IEEE International 2007 Dec 10 (pp. 697-700). IEEE.

[22] Lee CH, Tabata T, Nishimura T, Nagashio K, Kita K, Toriumi A. Ge/GeO2 Interface Control with High-Pressure Oxidation for Improving Electrical Characteristics. Applied Physics Express. 2009 Jul 1;2(7):071404.

[23] Fukuda Y, Ueno T, Hirono S, Hashimoto S. Electrical characterization of germanium oxide/germanium interface prepared by electron-cyclotron-resonance plasma irradiation. Japanese journal of applied physics. 2005 Sep 1;44(9S):6981.

[24] Bellenger F, De Jaeger B, Merckling C, Houssa M, Penaud J, Nyns L, Vrancken E, Caymax M, Meuris M, Hoffmann T, De Meyer K. High FET Performance for a Future CMOS-Based Technology. Electron Device Letters, IEEE. 2010 May;31(5):402-4.

[25] Xie Q, Deduytsche D, Schaekers M, Caymax M, Delabie A, Qu XP, Detavernier C. Effective electrical passivation of Ge (100) for HfO2 gate dielectric layers using O2 plasma. Electrochemical and Solid-State Letters. 2011 May 1;14(5):G20-2.

[26] Fukuda Y, Yazaki Y, Otani Y, Sato T, Toyota H, Ono T. Low-Temperature Formation of High-Quality Interlayer for High-Gate Dielectrics/Ge by Electron-Cyclotron-Resonance Plasma Techniques. Electron Devices, IEEE Transactions on. 2010 Jan;57(1):282-7.

[27] Kita SK, Wang MY. K. Nagashio, T. Nishimura, and A. Toriumi. Tech. Dig.-Int. Electron Devices Meet. 2009;693.

[28] Shannon RD. Dielectric polarizabilities of ions in oxides and fluorides. Journal of Applied Physics. 1993 Jan 1;73(1):348-66.

[29] Dimoulas A, Brunco DP, Ferrari S, Seo JW, Panayiotatos Y, Sotiropoulos A, Conard T, Caymax M, Spiga S, Fanciulli M, Dieker C. Interface engineering for Ge metal-oxide–semiconductor devices. Thin Solid Films. 2007 Jun 4;515(16):6337-43.

[30] Tabata T, Lee CH, Kita K, Toriumi A. Impact of High Pressure O2 Annealing on Amorphous LaLuO3/Ge MIS Capacitors. ECS Transactions. 2008 Oct 3;16(5):479-86.

[31] Gu JJ, Liu YQ, Xu M, Celler GK, Gordon RG, Ye PD. High performance atomic-layer-deposited LaLuO3/Ge-on-insulator p-channel metal-oxide-semiconductor field-effect

transistor with thermally grown GeO2 as interfacial passivation layer. Applied Physics Letters. 2010 Jul 5;97(1):012106.

[32] Kita K, Kyuno K, Toriumi A. Growth mechanism difference of sputtered HfO {sub 2} on Ge and on Si. Applied physics letters. 2004 Jul 5;85(1).

[33] Zhang R, Iwasaki T, Taoka N, Takenaka M, Takagi S. High mobility Ge pMOSFETs with~ 1nm thin EOT using Al 2 O 3/GeO x/Ge gate stacks fabricated by plasma post oxidation. InVLSI Technology (VLSIT), 2011 Symposium on 2011 Jun 14 (pp. 56-57). IEEE.

[34] Zhang R, Huang PC, Lin JC, Takenaka M, Takagi S. Physical mechanism determining Ge p-and n-MOSFETs mobility in high N s region and mobility improvement by atomically flat GeO x/Ge interfaces. InElectron Devices Meeting (IEDM), 2012 IEEE International 2012 Dec 10 (pp. 16-1). IEEE.

[35] Zhang R, Iwasaki T, Taoka N, Takenaka M, Takagi S. High-Mobility Ge pMOSFET With 1-nm EOT Gate Stack Fabricated by Plasma Post Oxidation. Electron Devices, IEEE Transactions on. 2012 Feb;59(2):335-41.

[36] Zhang R, Iwasaki T, Taoka N, Takenaka M, Takagi S. Al {sub 2} O {sub 3}/GeO {sub x}/Ge gate stacks with low interface trap density fabricated by electron cyclotron resonance plasma postoxidation. Applied Physics Letters. 2011 Mar 14;98(11).

[37] Zhang R, Huang PC, Taoka N, Takenaka M, Takagi S. High mobility Ge pMOSFETs with 0.7 nm ultrathin EOT using HfO 2/Al 2 O 3/GeO x/Ge gate stacks fabricated by plasma post oxidation. InVLSI Technology (VLSIT), 2012 Symposium on 2012 Jun 12 (pp. 161-162). IEEE.

[38] Dentoni Litta E, Hellstrom PE, Henkel C, Ostling M. Thulium silicate interfacial layer for scalable high-k/metal gate stacks. Electron Devices, IEEE Transactions on. 2013 Oct;60(10):3271-6.

[39] Mitrovic IZ, Althobaiti M, Weerakkody AD, Sedghi N, Hall S, Dhanak VR, Chalker PR, Henkel C, Litta ED, Hellström PE, Östling M. Interface engineering of Ge using thulium oxide: Band line-up study. Microelectronic Engineering. 2013 Sep 30;109:204-7.

[40] Kita K, Takahashi T, Nomura H, Suzuki S, Nishimura T, Toriumi A. Control of high-k/germanium interface properties through selection of high-k materials and suppression of GeO volatilization. Applied Surface Science. 2008 Jul 30;254(19):6100-5.

[41] Song J, Kakushima K, Ahmet P, Tsutsui KA, Sugii N, Hattori T, Iwai H. Improvement of interfacial properties with interfacial layer in La 2 O 3/Ge structure. Microelectronic engineering. 2007 Oct 31;84(9):2336-9.

[42] Song J, Kakushima K, Ahmet P, Tsutsui K, Sugii N, Hattori T, Iwai H. Characteristics of ultrathin lanthanum oxide films on germanium substrate: Comparison with those on silicon substrate. Japanese journal of applied physics. 2007 Apr 1;46(4L):L376.

[43] Mavrou G, Galata SF, Sotiropoulos A, Tsipas P, Panayiotatos Y, Dimoulas A, Evangelou EK, Seo JW, Dieker C. Germanium metal-insulator-semiconductor capacitors with rare earth La 2 O 3 gate dielectric. Microelectronic engineering. 2007 Oct 31;84(9):2324-7.

[44] Mavrou G, Galata S, Tsipas P, Sotiropoulos A, Panayiotatos Y, Dimoulas A, Evangelou EK, Seo JW, Dieker C. Electrical properties of La2O3 and HfO2/La2O3 gate dielectrics for germanium metal-oxide-semiconductor devices. Journal of Applied Physics. 2008 Jan;103(1):4506.

[45] Rossel C, Dimoulas A, Tapponnier A, Caimi D, Webb DJ, Andersson C, Sousa M, Marchiori C, Siegwart H, Fompeyrine J, Germann R. Ge p-channel MOSFETS with La 2 O 3 and Al 2 O 3 gate dielectrics. InSolid-State Device Research Conference, 2008. ESSDERC 2008. 38th European 2008 Sep 15 (pp. 79-82). IEEE.

[46] Song J, Kakushima K, Ahmet P, Tsutsui KA, Sugii N, Hattori T, Iwai H. Post metallization annealing study in La 2 O 3/Ge MOS structure. Microelectronic Engineering. 2009 Sep 30;86(7):1638-41.

[47] Mavrou G, Tsipas P, Sotiropoulos A, Galata S, Panayiotatos Y, Dimoulas A, Marchiori C, Fompeyrine J. Very high-kappa ZrO2 with La2O3 (LaGeOx) passivating interfacial layers on germanium substrates. Applied Physics Letters. 2008 Nov;93(21):2904.

[48] Tsoutsou D, Panayiotatos Y, Sotiropoulos A, Mavrou G, Golias E, Galata SF, Dimoulas A. Chemical stability of lanthanum germanate passivating layer on Ge upon high-k deposition: A photoemission study on the role of La in the interface chemistry. Journal of Applied Physics. 2010 Sep 15;108(6):064115.

[49] Dimoulas A, Tsoutsou D, Panayiotatos Y, Sotiropoulos A, Mavrou G, Galata SF, Golias E. The role of La surface chemistry in the passivation of Ge. Applied Physics Letters. 2010 Jan 4;96(1):012902.

[50] Afanas' ev VV, Stesmans A, Mavrou G, Dimoulas A. Beneficial effect of La on band offsets in Ge/high-kappa insulator structures with GeO2 and La2O3 interlayers. Applied Physics Letters. 2008 Sep;93(10):2115.

[51] Li H, Lin L, Robertson J. Identifying a suitable passivation route for Ge interfaces. Applied Physics Letters. 2012 Jul 30;101(5):052903.

[52] [Robertson J, Falabretti B. Band offsets of high K gate oxides on high mobility semiconductors. Materials Science and Engineering: B. 2006 Dec 15;135(3):267-71.

[53] Robertson J, Falabretti B. Band offsets of high K gate oxides on III-V semiconductors. Journal of Applied Physics. 2006 Jul;100(1):4111.

[54] Andersson C, Rossel C, Sousa M, Webb DJ, Marchiori C, Caimi D, Siegwart H, Panayiotatos Y, Dimoulas A, Fompeyrine J. Lanthanum germanate as dielectric for scaled Germanium metal–oxide–semiconductor devices. Microelectronic Engineering. 2009 Sep 30;86(7):1635-7.

[55] Leskelä M, Ritala M. Rare-earth oxide thin films as gate oxides in MOSFET transistors. Journal of Solid State Chemistry. 2003 Mar 1;171(1):170-4.

[56] Zhao Y, Kita K, Kyuno K, Toriumi A. Band gap enhancement and electrical properties of La2O3 films doped with Y2O3 as high-k gate insulators. Applied Physics Letters. 2009 Jan;94(4):2901.

[57] Li H, Lin L, Robertson J. Identifying a suitable passivation route for Ge interfaces. Applied Physics Letters. 2012 Jul 30;101(5):052903.

[58] Zhao X, Vanderbilt D. Phonons and lattice dielectric properties of zirconia. Physical Review B. 2002 Jan 18;65(7):075105.

[59] Abermann S, Bethge O, Henkel C, Bertagnolli E. Atomic layer deposition of ZrO2/La2O3 high-k dielectrics on germanium reaching 0.5 nm equivalent oxide thickness. Applied Physics Letters. 2009 Jun;94(26):2904.

[60] Henkel C, Abermann S, Bethge O, Pozzovivo G, Klang P, Reiche M, Bertagnolli E. Ge p-MOSFETs With Scaled ALD Gate Dielectrics. Electron Devices, IEEE Transactions on. 2010 Dec;57(12):3295-302.

[61] Li CX, Lai PT. Wide-bandgap high-k Y2 O3 as passivating interlayer for enhancing the electrical properties and high-field reliability of n-Ge metal-oxide-semiconductor capacitors with high-k HfTiO gate dielectric. Applied Physics Letters. 2009;95(2).

[62] Wu YH, Wu ML, Lyu RJ, Wu JR, Chen LL, Lin CC. Crystalline ZrO2-gated Ge metal-oxide-semiconductor capacitors fabricated on Si substrate with Y2O3 as passivation layer. Applied Physics Letters. 2011 May;98(20):3502.

[63] Liu ZQ, Chim WK, Chiam SY, Pan JS, Ng CM. Formation of the yttrium/germanium interface: Fermi-level pinning and intermixing at room temperature. Applied Physics Letters. 2012 Feb 27;100(9):092110.

[64] Chu LK, Lee WC, Huang ML, Chang YH, Tung LT, Chang CC, Lee YJ, Kwo J, Hong M. Metal-oxide-semiconductor devices with molecular beam epitaxy-grown Y 2 O 3 on

Ge. Journal of Crystal Growth. 2009 Mar 15;311(7):2195-8.

[65] Liu ZQ, Chiam SY, Chim WK, Pan JS, Ng CM. Thermal stability improvement of the lanthanum aluminate/silicon interface using a thin yttrium interlayer. Journal of The Electrochemical Society. 2010 Dec 1;157(12):G250-7.

[66] Chiam SY, Chim WK, Pi C, Huan AC, Wang SJ, Pan JS, Turner S, Zhang J. Band alignment of yttrium oxide on various relaxed and strained semiconductor substrates. Journal of Applied Physics. 2008 Apr;103(8):3702.

[67] Suñé J, Tous S, Miranda E. Gate stack insulator breakdown when the interface layer thickness is scaled toward zero. Applied Physics Letters. 2010 Nov 22;97(21):213503.

[68] Wu ML, Wu YH, Lyu RJ, Chao CY, Wu CY, Lin CC, Chen LL. High quality Ge surface passivation layer formed by thermal oxidation of Y/Ge structure. Microelectronic Engineering. 2013 Sep 30;109:216-9.

[69] Chroneos A, Dimoulas A. Defect configurations of high-k cations in germanium. Journal of Applied Physics. 2012 Jan 15;111(2):023714.

[70] Beamson G, Briggs D, Davies SF, Fletcher IW, Clark DT, Howard J, Gelius U, Wannberg B, Balzer P. Performance and application of the Scienta ESCA300 spectrometer. Surface and Interface Analysis. 1990 Sep 1;15(9):541-9.

[71] Vickerman JC. Surface analysis: the principal techniques.

[72] Shirley DA. High-resolution X-ray photoemission spectrum of the valence bands of gold. Physical Review B. 1972 Jun 15;5(12):4709.

[73] Bersch E, Di M, Consiglio S, Clark RD, Leusink GJ, Diebold AC. Complete band offset characterization of the HfO2/SiO2/Si stack using charge corrected X-ray photoelectron spectroscopy. Journal of Applied Physics. 2010 Feb 15;107(4):043702.

[74] Perego M, Seguini G. Charging phenomena in dielectric/semiconductor heterostructures during x-ray photoelectron spectroscopy measurements. Journal of Applied Physics. 2011 Sep 1;110(5):053711.

[75] Zhang WF, Nishimula T, Nagashio K, Kita K, Toriumi A. Conduction band offset at GeO2/Ge interface determined by internal photoemission and charge-corrected x-ray photoelectron spectroscopies. Applied Physics Letters. 2013 Mar 11;102(10):102106.

[76] Baldovino S, Molle A, Fanciulli M. Evidence of dangling bond electrical activity at the Ge/oxide interface. Applied Physics Letters. 2008 Dec 15;93(24):242105.

[77] Schmeisser D, Schnell RD, Bogen A, Himpsel FJ, Rieger D, Landgren G, Morar JF. Surface oxidation states of germanium. Surface science. 1986 Jul 1;172(2):455-65.

[78] Sasada T, Nakakita Y, Takenaka M, Takagi S. Surface orientation dependence of interface properties of GeO2/Ge metal-oxide-semiconductor structures fabricated by thermal oxidation. Journal of Applied Physics. 2009 Oct;106(7):3716.

[79] Mitrovic IZ, Hall S, Sedghi N, Simutis G, Dhanak VR, Bailey P, Noakes TC, Alexandrou I, Engstrom O, Lopes JM, Schubert J. On the nature of the interfacial layer in ultra-thin TiN/LaLuO3 gate stacks. Journal of Applied Physics. 2012 Aug 15;112(4):044102.

[80] Lopes JM, Roeckerath M, Heeg T, Schubert J, Littmark U, Mantl S, Besmehn A, Myllymaki P, Niinistö L, Adamo C, Schlom DG. Amorphous lanthanum lutetium oxide thin films as an alternative high-k material. ECS Transactions. 2007 Sep 28;11(4):311-8.

[81] Schmeißer D, Henkel K, Bergholz M, Tallarida M. The band gap and band offset in ultrathin oxide–semiconductor heterostructures. Superlattices and Microstructures. 2010 Mar 31;47(3):369-76.

[82] Perego M, Scarel G, Fanciulli M, Fedushkin IL, Skatova AA. Fabrication of GeO2 layers using a divalent Ge precursor. Applied physics letters. 2007 Apr;90(16):2115.

[83] Bell FG, Ley L. Photoemission study of SiO x (0≤ x≤ 2) alloys. Physical Review B. 1988 May 15;37(14):8383.

[84] Ohta A, Nakagawa H, Murakami H, Higashi S, Miyazaki S. Photoemission study of ultrathin GeO2/Ge heterostructures formed by UV-O3 oxidation. e-Journal of Surface Science and Nanotechnology. 2006;4:174-9.

[85] Jellison Jr GE, Modine FA. Erratum:‘‘Parameterization of the optical functions of amorphous materials in the interband region’’[Appl. Phys. Lett. 69, 371 (1996)]. Applied Physics Letters. 1996 Sep 30;69(14):2137-.

[86] Tompkins H, Irene EA. Handbook of ellipsometry. William Andrew; 2005 Jan 6.:870.

[87] Johs B, Hale JS. Dielectric function representation by B-splines. physica status solidi (a). 2008 Apr 1;205(4):715-9.

[88] Price J, Lysaght PS, Song SC, Li HJ, Diebold AC. Identification of sub-band-gap absorption features at the HfO2/Si (100) interface via spectroscopic ellipsometry. Applied Physics Letters. 2007 Aug;91(6):1925.

[89] Toriumi A, Wang S, Lee CH, Yoshida M, Kita K, Nishimura T, Nagashio K. (Invited) Oxidation, Diffusion and Desorption in a Ge/GeO2 System. ECS Transactions. 2010 Apr 16;28(2):171-80.

[90] Hosono H, Abe Y, Kinser DL, Weeks RA, Muta K, Kawazoe H. Nature and origin of the 5-eV band in SiO 2: GeO 2 glasses. Physical Review B. 1992 Nov 1;46(18):11445.

[91] Zyubin AS, Mebel AM, Lin SH. Photoluminescence of oxygen-containing surface defects in germanium oxides: A theoretical study. The Journal of chemical physics. 2005 Jul 22;123(4):044701.

[92] Zyubin AS, Mebel AM, Lin SH. Photoluminescence of oxygen-deficient defects in germanium oxides: A quantum chemical study. The Journal of chemical physics. 2006 Aug 14;125(6):064701.

[93] Nguyen NV, Davydov AV, Chandler-Horowitz D, Frank MM. Sub-bandgap defect states in polycrystalline hafnium oxide and their suppression by admixture of silicon. Applied Physics Letters. 2005 Nov 7;87(19):192903.

[94] Nguyen NV, Sayan S, Levin I, Ehrstein JR, Baumvol IJ, Driemeier C, Krug C, Wielunski L, Hung PY, Diebold A. Optical band gaps and composition dependence of hafnium–aluminate thin films grown by atomic layer chemical vapor deposition. Journal of Vacuum Science & Technology A. 2005 Nov 1;23(6):1706-13.

[95] Di M, Bersch E, Diebold AC, Consiglio S, Clark RD, Leusink GJ, Kaack T. Comparison of methods to determine bandgaps of ultrathin HfO2 films using spectroscopic ellipsometry. Journal of Vacuum Science & Technology A. 2011 Jul 1;29(4):041001.

[96] Robertson J, Peacock PW. Atomic structure, interfaces and defects of high dielectric constant gate oxides. InMaterials Fundamentals of Gate Dielectrics 2005 Jan 1 (pp. 179-214). Springer Netherlands.

[97] Zhang S, Xiao R. Yttrium oxide films prepared by pulsed laser deposition. Journal of applied physics. 1998 Apr;83:3842-8.

[98] Ohta A, Yamaoka M, Miyazaki S. Photoelectron spectroscopy of ultrathin yttrium oxide films on Si (100). Microelectronic engineering. 2004 Apr 30;72(1):154-9.

[99] Tomiki T, Tamashiro J, Tanahara Y, Yamada A, Fukutani H, Miyahara T, Kato H, Shin S, Ishigame M. Optical spectra of Y2O3 single crystals in VUV. Journal of the Physical Society of Japan. 1986 Dec;55(12):4543-9.

[100] Afanas' ev VV, Houssa M, Stesmans A, Heyns MM. Band alignments in metal-oxide-silicon structures with atomic-layer deposited Al2O3 and ZrO2. Journal of applied physics. 2002 Mar;91:3079-84.

[101] Afanas'ev VV, Stesmans A. Internal photoemission at interfaces of high-κ insulators with semiconductors and metals. Journal of applied physics. 2007 Oct 15;102(8):081301.

[102] Yu HY, Li MF, Cho BJ, Yeo CC, Joo MS, Kwong DL, Pan JS, Ang CH, Zheng JZ, Ramanathan S. Energy gap and band alignment for (HfO2) x (Al2O3) 1-x on (100) Si.

Applied physics letters. 2002 Jul 8;81(2):376-8.

[103] Martinez FL, Toledano-Luque M, Gandia JJ, Cárabe J, Bohne W, Röhrich J, Strub E, Mártil I. Optical properties and structure of HfO2 thin films grown by high pressure reactive sputtering. Journal of Physics D: Applied Physics. 2007 Sep 7;40(17):5256.

[104] Urbach F. The long-wavelength edge of photographic sensitivity and of the electronic absorption of solids. Physical Review. 1953 Dec 1;92(5):1324.

[105] Cho YJ, Nguyen NV, Richter CA, Ehrstein JR, Lee BH, Lee JC. Spectroscopic ellipsometry characterization of high-k dielectric HfO2 thin films and the high-temperature annealing effects on their optical properties. Applied physics letters. 2002 Feb 18;80(7):1249-51.

[106] Takeuchi H, Ha D, King TJ. Observation of bulk HfO2 defects by spectroscopic ellipsometry. Journal of Vacuum Science & Technology A. 2004 Jul 1;22(4):1337-41.

[107] Robertson J. Defects and hydrogen in amorphous silicon nitride. Philosophical Magazine B. 1994 Feb 1;69(2):307-26.

[108] Liu ZQ, Chim WK, Chiam SY, Pan JS, Ng CM. Ambiguity in the magnitude and direction of the derived interface dipole in lanthanum aluminate heterostructures: Implications and proposed solution. Journal of Applied Physics. 2011 May 1;109(9):093701.

[109] Opila RL, Wilk GD, Alam MA, Van Dover RB, Busch BW. Photoemission study of Zr-and Hf-silicates for use as high-κ oxides: Role of second nearest neighbors and interface charge. Applied physics letters. 2002 Sep 2;81(10):1788-90.

[110] Nakayama T, Itaya S, Murayama D. Nano-scale view of atom intermixing at metal/semiconductor interfaces. InJournal of Physics: Conference Series 2006 May 10 (Vol. 38, No. 1, p. 216). IOP Publishing.

[111] Chiam SY, Chim WK, Huan AC, Pan JS, Zhang J. Investigation of silicon diffusion into yttrium using x-ray photoelectron spectroscopy. Applied physics letters. 2006 Jan 2;88(1):011904.

[112] Liu ZQ, Chim WK, Chiam SY, Pan JS, Chun SR, Liu Q, Ng CM. Interfacial-layer-free growth of yttrium oxide on germanium by understanding initial surface reactions. Surface Science. 2012 Nov 30;606(21):1638-42.

[113] Kraut EA, Grant RW, Waldrop JR, Kowalczyk SP. Precise determination of the valence-band edge in x-ray photoemission spectra: Application to measurement of semiconductor interface potentials. Physical Review Letters. 1980 Jun 16;44(24):1620.

[114] Chambers SA, Droubay T, Kaspar TC, Gutowski M. Experimental determination of valence band maxima for SrTiO3, TiO2, and SrO and the associated valence band offsets with Si (001). Journal of Vacuum Science & Technology B. 2004 Jul 1;22(4):2205-15.

[115] Perego M, Scarel G, Fanciulli M, Fedushkin IL, Skatova AA. Fabrication of GeO2 layers using a divalent Ge precursor. Applied physics letters. 2007 Apr;90(16):2115.

[116] Yang M, Wu RQ, Chen Q, Deng WS, Feng YP, Chai JW, Pan JS, Wang SJ. Impact of oxide defects on band offset at GeO2/Ge interface. Applied Physics Letters. 2009 Apr;94(14):2903.

[117] Zhang WF, Nishimula T, Nagashio K, Kita K, Toriumi A. Conduction band offset at GeO2/Ge interface determined by internal photoemission and charge-corrected x-ray photoelectron spectroscopies. Applied Physics Letters. 2013 Mar 11;102(10):102106.

[118] Norton DP. Synthesis and properties of epitaxial electronic oxide thin-film materials. Materials Science and Engineering: R: Reports. 2004 Mar 15;43(5):139-247.

[119] Li H, Robertson J. Defects at Ge: GeO 2 and Ge: MeOx interfaces. Microelectronic Engineering. 2013 Sep 30;109:244-9.

Chapter 5

Atomic-layer deposited thulium oxide as a passivation layer on germanium

5.1 Introduction

Interface engineering plays a pivotal role in new high-κ/metal gate technology advancement [1, 2, 3 , 4 , 5].Rare-earth thulium oxide (Tm_2O_3) has been considered as the main high-k dielectric [6, 7, 8] and as a capping layer for La_2O_3-based gate stacks [9], but only on Si. A low reactivity of Tm_2O_3 with the Si substrate has been observed [10]. There have been theoretical prediction and some recent estimations of the band gap (~5 eV [11] ~6.5 eV [12], and 5.76 eV [13] respectively) on Tm_2O_3/Si structures. Atomic-layer deposition (ALD) has become one of the preferred methods for thin film deposition in several fields due to the excellent thickness control, uniformity and conformality. A novel process for atomic-layer deposition of thulium oxide has been recently developed [14]. A TmSiO IL layer with EOT of ~0.25 nm has been achieved, which indicates a strong potential for its integration in sub-10 nm technology nodes [15]. Conversely, there have been no reports on Tm_2O_3 as a passivation layer on Ge, apart from our earlier work [16].

A reliable measurement method to determine the band offsets is essential for modelling the carrier transport properties. The offsets reported at the GeO_2/Ge interface show large scattering in the range of about 1 eV for data obtained by x-ray photoelectron spectroscopy (XPS) and internal photoemission (IPE) (see Ref. 17 and references therein). Detailed mechanism responsible for such discrepancy is not clear. There are assumptions made that this is due to different GeO_2 growth methods [5, 18, 23]. Furthermore, it has come recently to focus that the XPS requires careful attention to charging effects as a result of electron emission from the insulator [24, 26]; while the IPE data demand careful interpretation [27]. A clear understanding of the physical phenomena behind the charge accumulation and neutralization in dielectric/semiconductor heterojunction during XPS measurements seems still to be elusive. A recent XPS study on HfO_2/Ge heterostructures [28] suggests that the role of germanium is not negligible in the neutralization mechanisms beyond the differential charging effect. Charging can occur in an XPS experiment when the holes that are created by the ejection of photoelectrons accumulate in a sample. This build-up of charge results in an increase in the binding energy (BE) of spectral features. Bersch et al. [26] have shown that not correcting for charging results in overestimation of valence band offset (VBO) by ~ 0.5 eV on average. It is common practice for the VBO to be determined from XPS measurements by Kraut's method using the valence band (VB) and core-level (CL) photoemission from bulk-like samples of the two constituent materials and a thin interfacial sample forming the interface of interest [29]. The

overlayer of this heterojunction sample must be sufficiently thin (usually < 5 nm) to allow XPS core-levels from the underlying material to be probed due to the finite escape depth of the photoelectrons. The binding energy values are referenced to the valence band maximum (VBM) of each sample, determined by extrapolating a linear fit of the leading edge of the VB photoemission to the baseline in order to account for broadening of the photoemission spectra.[30] Then, the VBO for oxide/semiconductor substrate sample can be determined as

$$VBO = \delta_{SUB} + \delta_{INT} - \delta_{OXIDE} \qquad (5.1)$$

where, δ_{SUB}, and δ_{OXIDE} are the energy differences between chosen reference core-levels in substrate and bulk oxide samples and their respective VBMs, while δ_{INT} refers to the BE difference for the former two core-levels for the interfacial sample.

This chapter conveys three important findings: (i) the valence band offset for Tm_2O_3/Ge of 3.05 ± 0.2 eV, determined by Kraut's method [29, 30] using a single sample consequently sputtered with core-level spectra taken at different sputtering times, shows consistency within experimental error with the offset result obtained using three distinctive samples (bulk, interfacial and substrate) [16]; (ii) the VBO for thermal GeO_2/Ge is in agreement with the most recent report from Toriumi's group [17] substantiating a conduction band offset (CBO) higher than 1 eV and the appropriateness of GeO_2 use in passivation of Ge; (iii) Tm_2O_3 shows even lower reactivity on Ge than on Si, with an atomically sharp interface indicating possible barrier properties.

5.2 Experimental

The 10 nm (nominal) thick Tm_2O_3 samples were prepared by ALD on 35 nm p-Ge epitaxial layer/Si (100), and on Si (100). The reference samples of GeO_2 (5 and 10 nm nominal thicknesses) were grown on 35 nm n-Ge epi/Si(100) by thermal oxidation at 525°C under 1 atm O_2. Prior to the gate oxide deposition, epi Ge/Si (100) samples were cleaned in a HF 0.5%/Isopropanol 1% /H_2O mixture to remove (minimize) the native Ge oxide layer. The Tm_2O_3 layers were deposited using Tris(cyclopentadienyl)thulium, heated to 140°C, and water vapor as precursor gases. An ultra-high vacuum (UHV) system operating at 4×10^{-8} Pa base pressure and equipped with a VG Al Kα monochromatized x-ray source and a CLAM2 hemispherical analyzer was used for XPS data acquisition at normal emission. The electron analyser was set at constant 20 eV pass energy mode and calibrated [31]. The total energy

resolution is found to be < 0.7 eV from the fitting of the Fermi edge of a clean Au sample. The binding energy is referred to the position of the Fermi level measured on a clean Ta strip in good electrical contact with the sample. In order to reach the Tm_2O_3/Ge interface, the samples were mildly sputtered with 0.5 keV Ar ion energy (0.25 nm/min). The XPS spectra for GeO_2/n-Ge samples were recorded on a separate UHV system consisting of an Al Kα X-ray (hν = 1486.6 eV) source and a PSP Vacuum Technology electron energy analyzer. This spectrometer was calibrated so the Ag $3d_{5/2}$ photoelectron line had a BE of 368.35 eV, a full width at half maximum (FWHM) of 0.8 eV being the spectral resolution for this study, and a 10 eV pass energy. Charge compensation was achieved using a VG Scienta FG300 low energy electron flood gun with the gun settings adjusted for optimal spectral resolution. The electron BEs were then corrected by setting the C 1s peak in the spectra (due to stray carbon impurities) at 284.6 eV for all samples [32]. The error bar (±0.2 eV) we defined in this chapter is due to valence band maximum (VBM) determination through the linear interpolation method [30].The CL binding energy determination by fitting a Voigt curve to a measured peak introduces typically much smaller (± 0.05 eV) error. A Shirley-type background [33] is used during the fitting of all spectra. The vacuum ultra-violet variable angle spectroscopic ellipsometry (VUV-VASE) measurements were performed using a spectral range from 0.5 - 8 eV, and the angles of incidence of 55-75°, by 10° as a step, to maximize the accuracy. The atomic structure and elemental analysis were investigated with high-resolution transmission electron microscopy (HRTEM) and electron energy-loss spectroscopy (EELS) performed on a field emission image-corrected FEI Tecnai™ F20 microscope operating at 200 kV. For local EELS studies, the microscope was also equipped with a scanning stage (STEM), allowing a focused one nanometer-sized probe to be scanned over the sample area of interest (in our case, a line crossing the Tm_2O_3/Ge interface), and an imaging filter (Gatan GIF TRIDIEM) used as a spectrometer.

5.3 Results and Discussion

5.3.1 Valence band offset and band gap estimation for Tm_2O_3/Ge

The valence band offset (VBO) was estimated using Kraut's method [34], where Ge $3d^0$ and Tm 4d were selected as reference core levels. The energy difference between these core levels and the corresponding valence band maxima (VBM, or E_V) were determined in bulk Ge and in thick Tm_2O_3 films. Then, by measuring the energy difference ($E_{Ge3d} - E_{Tm4d}$) in a thin Tm_2O_3/Ge, the VBO can be determined as:

$$VBO = (E_{Ge3d} - E_V^{Ge})_{Ge} - (E_{Tm4d} - E_V^{Tm2O3})_{Tm2O3} + (E_{Ge3d} - E_{Tm4d})_{Tm2O3/Ge}.$$

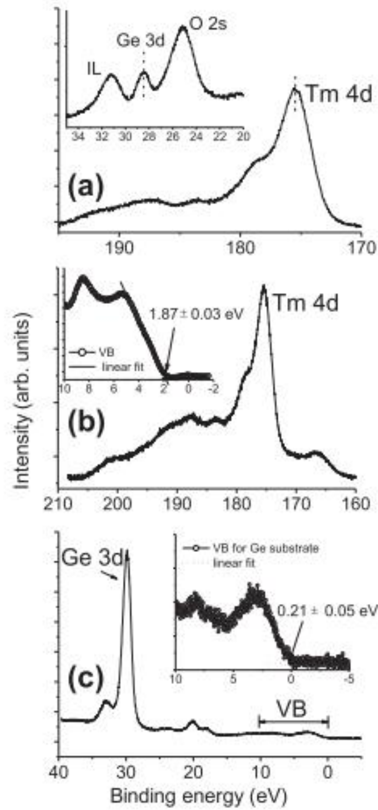

Fig. 5.1 Core level and valence band spectra for: (a) a 5 nm Tm_2O_3/Ge; (b) a 10 nm Tm_2O_3/Ge, and (c) Ge substrate. The insets in (b) and (c) show scans of the valence band regions of the 10 nm Tm_2O_3/Ge sample and bare Ge, respectively.

The XPS spectra for a 5 nm Tm_2O_3/Ge (a), a 10 nm thick Tm_2O_3 film on Ge (b), and Ge substrate (c), are shown in Fig. 5.1. The position of the VBM is determined using the so-called linear method [35] and shown in the insets (b) and (c). The core level positions are defined as the full width at half maximum (FWHM) by fitting a Voigt curve to the measured peaks and determined to within 0.05 eV. A Shirley background function was used to correct for the effect of inelastic photoelectron scattering [36]. From Figs. 5.1(a)-(c), the calculated value for VBO is 29.61 – 173.49 + 146.83 = 2.95 eV, with an error bar of ± 0.08 eV. This large VBO can provide a barrier to holes.

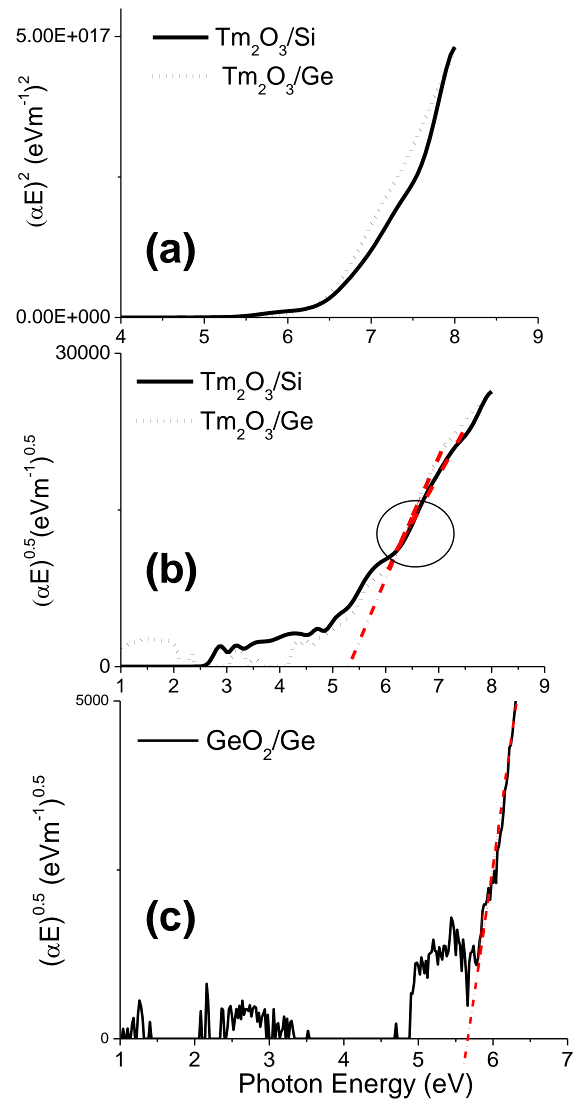

Fig. 5.2 (a) Dependence of $(\alpha E)^2$ on photon energy and (b)-(c) Tauc plots for the 10 nm (nominal) Tm_2O_3/Si, Tm_2O_3/Ge and 5 nm (nominal) GeO_2/Ge samples. The plots were derived from VUV-VASE experimental data. The referring linear fits are shown.

In order to obtain the conduction band offset (CBO), the band gap of Tm_2O_3 was determined by VUV-VASE on a 10 nm Tm_2O_3/Ge. This was accomplished by first determining the thickness in the non-absorbing (transparent) region of the spectra. The dielectric function of the Ge film (31.9 nm) with the native oxide as Cauchy layer (1.4 nm) was measured first. Then, another Cauchy layer was added and fitted for the thickness of Tm_2O_3 film (10.4 nm), and the optical constants (real and imaginary part of dielectric function) extracted. The Tm_2O_3 film was modelled with Cauchy layer at long wavelengths and extended into VUV with the B-spline and then converted to a general oscillator layer. The dielectric function is converted to refractive index and extinction coefficient (k) using the Kramers-Kroning relations. The absorption

coefficient (α) is calculated from the extinction coefficient as $\alpha=4\pi\kappa/\lambda$. Plots of absorption coefficient vs photon energy (E) are shown in Fig. 5.2, using $(\alpha E)^2$ (direct band gap law) and ($(\alpha E)^{1/2}$ (indirect band gap, Tauc law)) [37]. Comparing Figs. 5.2(a) and (b), it is apparent that most of the absorption region fits to a Tauc law (Fig. 5.2(b)). The linear parts in the $(\alpha E)^2$ versus E plot (Fig. 5.2a) show diverging slopes for two samples of Tm_2O_3 on Si and Ge, and without any common data points as is the case in Fig. 5.2(b) (see circled area). Thus, we infer the indirect band gap nature of Tm_2O_3, with value 5.3±0.1 eV. This value is in close agreement with the theoretical prediction of Iwai [38]. A value of 5.76 eV has been reported recently using optical absorbance [39]; however the authors have used the direct band gap law. Fig. 5.2(c) depicts a Tauc plot for GeO_2/Ge, from which the band gap of GeO_2 is found to be 5.65±0.1 eV.

5.3.2 Sub-band gap absorption features, interface and EOT for Tm_2O_3/Ge

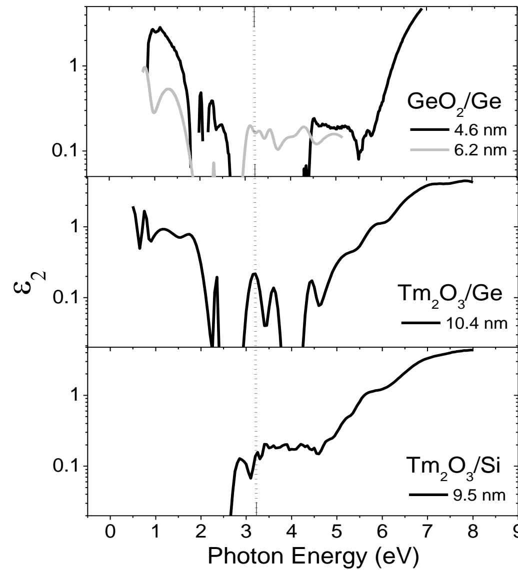

Fig. 5.3 Log scale plot of ε_2 for Tm_2O_3 deposited on Si and Ge, with two samples of GeO_2/Ge as reference spectra.

The parameterized optical models, such as the Tauc-Lorentz or the Cauchy model cannot account for the localized absorption sites below the band gap. Hence, the point-by-point extraction method for the dielectric function available in the J.A. Woollam software was used. The imaginary part of the dielectric function for GeO_2/Ge, Tm_2O_3/Ge and Tm2O3/Si is plotted in Fig. 5.3 on a log scale to accentuate the sub-band gap absorption features. Several absorption peaks are noticeable for Tm_2O_3/Si below the band gap at 2.9, 3.2, 3.4 and 4.25 eV. The latter two refer to the critical points of Si. The absorption at 2.9 eV has been found as intrinsic to interface and refers to optical transitions associated with negatively charged oxygen

vacancies in the interfacial SiO_2 layer [40, 41]. The peak at 3.2 eV can be seen for both Tm_2O_3 on Si and on Ge (see the vertical dotted line), and is likely to be related to the bulk of this oxide. The dominant peaks of Ge at 2.4, 3.6 and 4.4 eV are visible for both GeO_2 and Tm_2O_3 on Ge. Furthermore, GeO_2/Ge has mutual peak energies with Tm_2O_3/Ge stretching from 0.8 to 2.3 eV, likely related to interfacial GeOx species. Note that no absorption features were observed in the energy region of 3 to 4 eV for 4.6 nm GeO_2/Ge sample. An additional measurement, in the range 0.7 to 5.2 eV, on a thicker (6.2 nm) GeO_2/Ge show three distinct absorption peaks at 3.1, 3.3 and 3.6 eV (see Fig. 5.3, top). It is likely that the variation in $\varepsilon_2(E)$ relates to a different sub-oxide species present in two GeO_2 layers prepared using two different thermal oxidation processes. The GeO_2 films of two nominal thicknesses were prepared by ex-situ furnace anneal at 450°C for 5 min and 60 minutes respectively.

The angle-resolved XPS spectra of Ge3d and O1s core levels for 5 nm Tm_2O_3/Ge stack are shown in Figs. 5.4(a) and (b), respectively. The de-convolution of the spectra indicates dominance of Ge 2+ and Ge 4+ oxidation states at the interface, with binding energy shifts of 2.0-2.2 and ~3.5 eV respectively, in agreement with literature values [42, 43]. It has been argued that in cases where multiple sub-oxides are present, 2+ is the most stable [44]. No significant variation was observed when decreasing the TOA to 15°, which means that GeO_2 and GeO are at the Tm_2O_3/Ge interface. The binding energy of O1s for Tm_2O_3 was found to be at 528.9 eV, with the strong presence of –OH species at 531.4 eV; similar was observed for reference oxidized Tm foil (Fig. 5.4(b)). Note an increase of –OH when changing from 30° to 15° TOA, indicating its presence in the bulk and on the surface. This is in agreement with the observation that surface and even bulk hydration takes place for all binary lanthanide oxides [45].

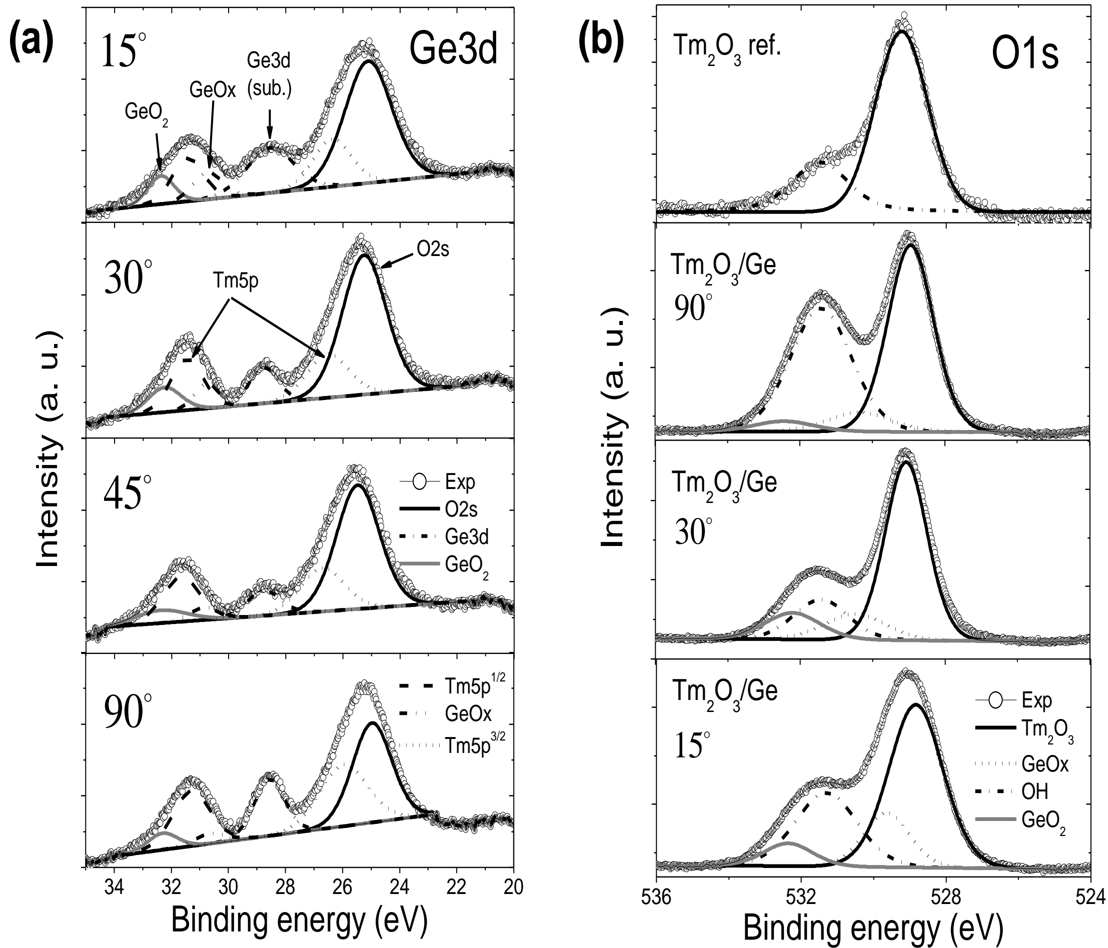

Fig. 5.4 De-convolution of the Ge3d (a) and O1s (b) XPS core levels for 5 nm (nominal) Tm_2O_3/Ge structure providing direct evidence of Ge +2 and +4 oxidation states at the interface. Note that in (a) apart from Ge3d, there is a strong presence of neighbouring O2s and Tm5p doublet (1/2 and 3/2). The top graph in (b) refers to oxidised Tm foil, as a reference Tm_2O_3

Fig. 5.5(a) shows a typical CV plot for the 5 nm Tm_2O_3/Ge sample; from the slope of the EOT versus the physical oxide thickness, the permittivity of the Tm_2O_3 film was estimated to be 14-15. Similar results were obtained for Si substrates [46]. The EOT was extracted by a fit of the experimental CV curves in accumulation using the CVC simulation software [26]. For the as-deposited 5 nm Tm_2O_3/Ge the obtained EOT amounts to 1.28-1.43 nm. No significant effects on the electrical properties are observed regarding the chosen PDA temperatures and atmosphere of O_2 or N_2/H_2. In summary, Fig. 5.5 (b) shows the band diagram for the Tm_2O_3/Ge derived from this work.

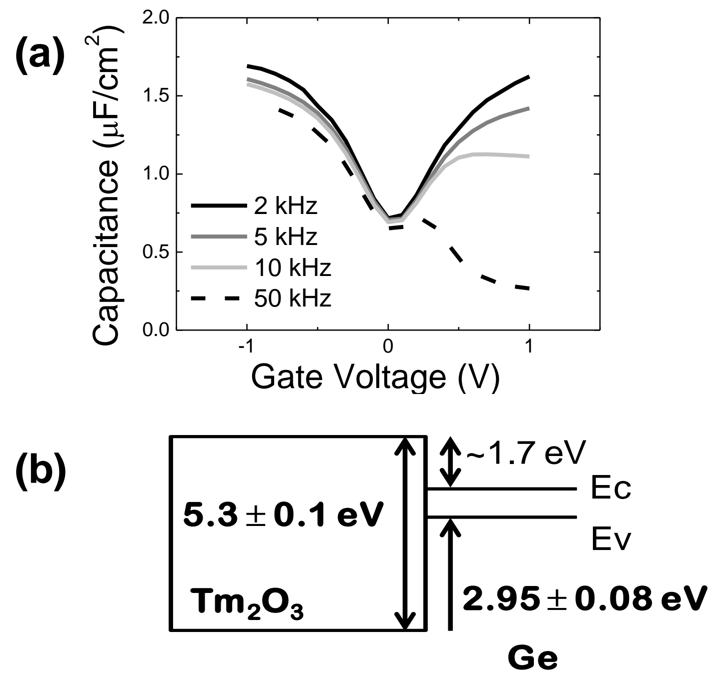

Fig. 5.5 (a) Capacitance voltage plot for 5 nm (nominal) Tm_2O_3/Ge, and (b) band diagram of Tm_2O_3/Ge derived from this work.

5.3.3 Estimation of VBO for Tm_2O_3/Ge gate stack

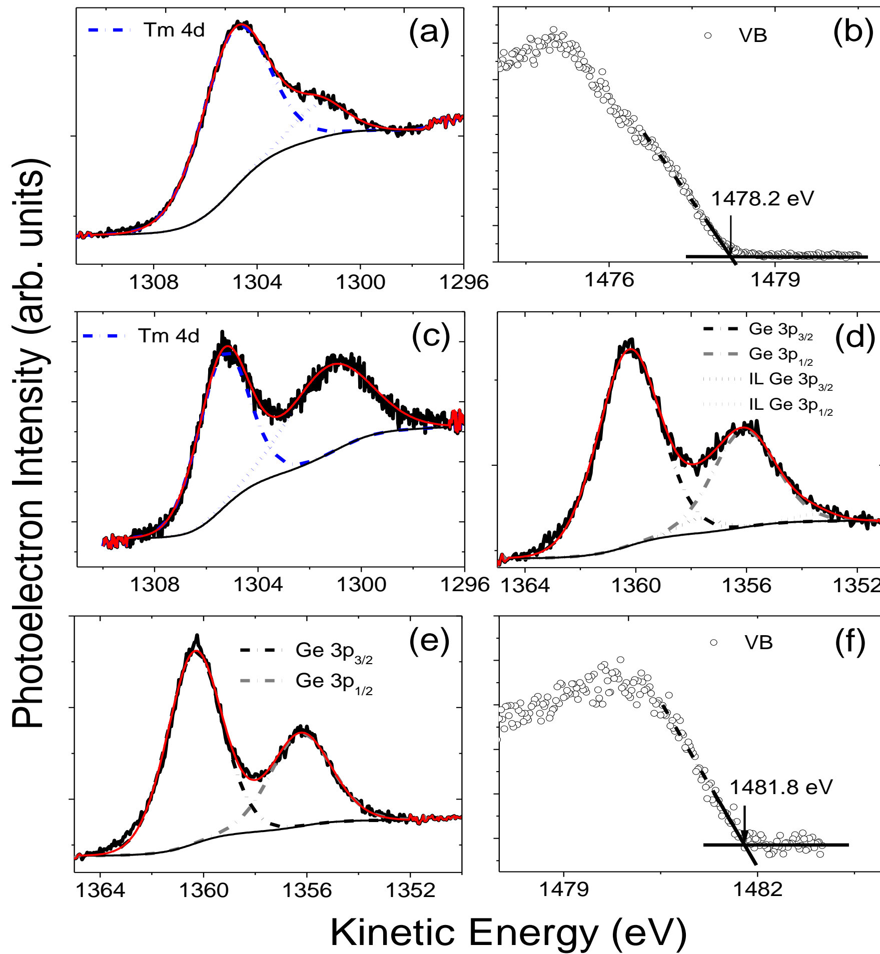

Fig. 5.6 Shallow core-levels and VB spectra for a bulk Tm_2O_3/Ge (a)-(b), an interfacial Tm_2O_3/Ge (c)-(d), and Ge substrate (e)-(f), recorded after sputtering for 210 s, 1470 s and 2190 s respectively. There is an additional peak (with spin-orbit splitting) for Ge 3p fitting in (d) due to IL contribution.

The VBO determination of the Tm_2O_3/Ge system is addressed first. Fig. 5.6 shows high-resolution Tm 4d, valence band and Ge 3p XPS spectra taken at three different sputtering times referring to bulk Tm_2O_3 (Figs. 5.6(a)-(b)), interface (Figs. 5.6(c)-(d)) and Ge substrate (Figs.5.6 (e)-(f)). Since for Ge 3d, a strong presence of neighboring O 2s and Tm 5p doublet complicates

the interpretation of the spectra [16], in this work, Ge $3p_{3/2}$ and the centroid value of Tm 4d core-levels were used for VBO estimation.

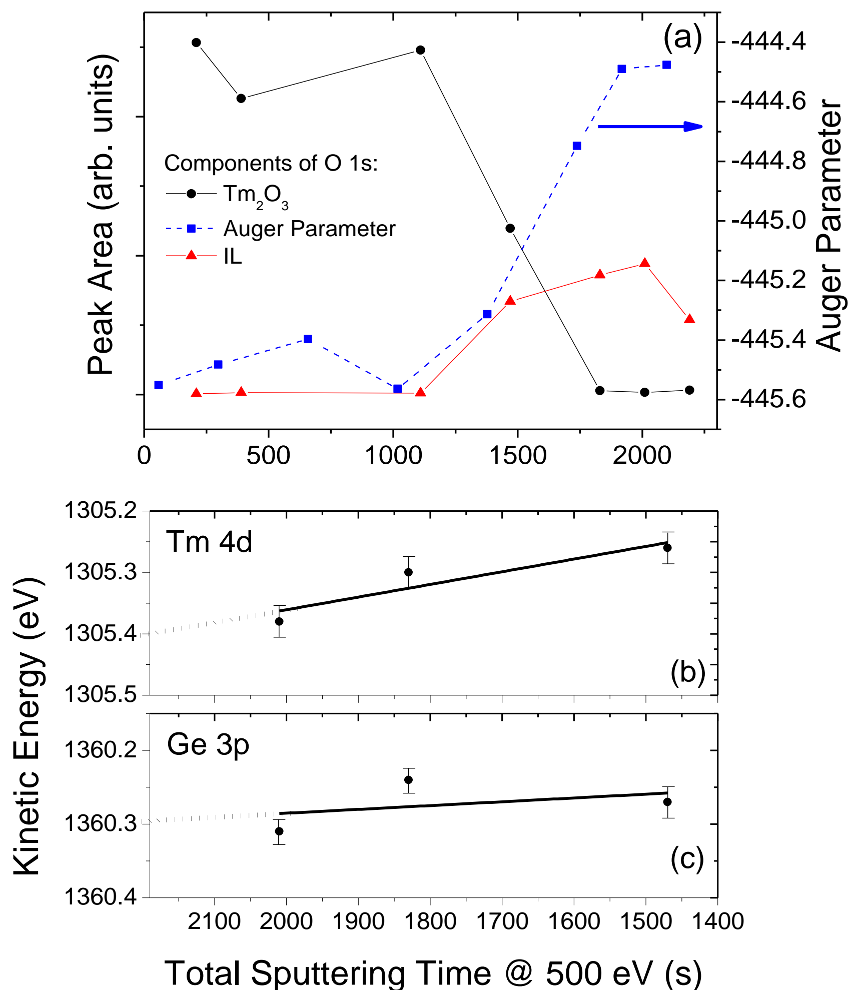

Fig. 5.7 (a) The peak area of the components of O 1s XPS core-level (left) and Auger parameter (right) as a function of total sputtering time. (b)-(c) The extrapolation of charge-corrected kinetic energies of Tm 4d and Ge $3p_{3/2}$ core-levels.

Fig. 5.7(a) shows the peak areas of two components of O 1s core-level: from the main Tm_2O_3 (circle symbol) and from IL (triangle symbol). Each symbol point on the graphs refers to a single sputtering time, when the spectrum was taken. At first the signal is dominated by the thulium contribution (until ~1100 s), however as the sputtering through the film continues, the IL becomes more prominent until only interfacial layer species are left (at ~ 2000 s). These changes

are further reflected in the plot of the Auger parameter, also shown in Fig. 5.7(a). The Auger parameter was calculated using the centroid values of the O 1s peak and from the O KLL Auger peak [47]. Note that in interfacial Tm_2O_3/Ge heterostructures, the Tm 4d core-levels exhibit a monotonically decreasing shift towards lower BEs of ~ 0.12 eV when sputtering Tm_2O_3 film (Figs. 5.6(c) and 2(b)), thus providing clear fingerprints of charging phenomenon [25,26]. On the contrary, a very small variation (~ 0.05 eV) of the Ge 3p BEs was observed (Figs. 5.6(d) and 2(c)). To account for the effect of differential charging, the positions of Tm 4d and Ge 3p peaks were estimated by extrapolating the measured BEs to zero Tm_2O_3 thickness (i.e. to the highest value of sputtering time in our experiment, see Fig. 5.7(a)) and hence ideally to zero charge [25]. The difference of Tm 4d and O 1s peaks was found to be 354.29 ± 0.03 eV, being indicative of the same stoichiometry of the films sputtered < 2000 s. The value Tm 4d – Ge $3p_{3/2} = \delta_{INT} =$ 54.89 eV was extracted from the extrapolated values in Figs. 5.7(b)-(c). Comparing the Ge $3p_{3/2}$ peak of the Ge substrate and the same peak with Tm_2O_3 on top, an energy shift towards higher BEs of 0.06 eV is observed. This is a signature of a small downward band bending, which agrees with the presence of p-type Ge [48]. The result suggests negligible bending of Ge core-levels despite the charging of the Tm_2O_3 film during x-ray exposure; a converse scenario has been observed for HfO_2/n-Ge [28]. The BE differences between Tm 4d centroid and VBM for bulk Tm_2O_3 (δ_{OXIDE}), and Ge $3p_{3/2}$ and VBM for the Ge substrate (δ_{SUB}) measured from Figs. 5.6 (a)-(b) and Figs. 5.6 (e)-(f) respectively. By inserting δ_{OXIDE}, δ_{INT}, δ_{SUB} values in Kraut's equation (5.1), the VBO = $\delta_{SUB} + \delta_{INT} - \delta_{OXIDE}$ = 3.05 ± 0.2 eV is calculated for Tm_2O_3/Ge. The result is in agreement with our previously reported value of 2.95 ± 0.08 eV [16] from the XPS measurements were taken on three distinctive samples.

5.3.4 Estimation of VBO for GeO_2/Ge gate stack

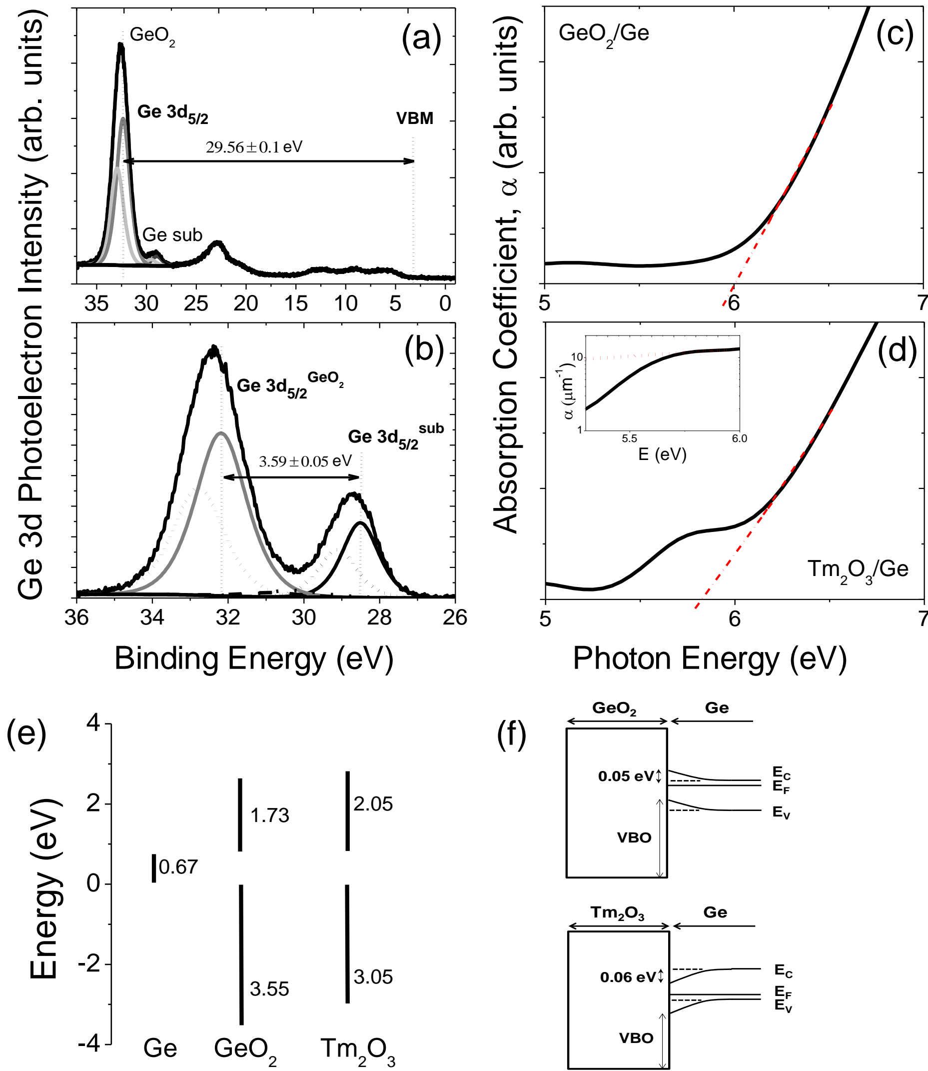

Fig. 5.8 The experimental and fitted Ge 3d XPS core-levels for (a) a thick 10 nm GeO_2/Ge, and (b) a thin 5 nm GeO_2/Ge. VBM refers to valence band maximum. Absorption coefficient vs photon energy extracted from VUV-VASE data for: (c) GeO_2/Ge and (d) Tm_2O_3/Ge. (e) The schematic of measured band gaps and hole barrier heights, where electron barrier heights i.e. CBO is calculated using CBO = $E_{g(OXIDE)}$ – VBO – $E_{g(Ge)}$, where E_g refers to the band gap. (f) The schematic of experimentally observed band bending for GeO_2/n-Ge and Tm_2O_3/p-Ge in this work.

Further, VBO for the reference GeO_2/Ge system is estimated. Figs. 5.8(a)-(b) show high-resolution Ge 3d core-levels taken for bulk and interfacial GeO_2/Ge after prolonged (at least an hour) x-ray exposure, until the point when constant BEs are reached [17, 25, 26]. The GeO_2 film shows two main peaks, fitted to doublets of Voigt functions with spin orbit splitting of 0.6 eV and branching ratio (1/2). The difference between Ge $3d_{5/2}$ of the substrate (28.95 eV) and GeO_2 (32.34 eV) for the bulk sample is 3.4 eV, showing a stoichiometric GeO_2 and negligible differential charging [17, 49]. Comparing the Ge $3d_{5/2}$ peak of the bare Ge (not shown) and the same peak from Ge with GeO_2 on top (Fig. 5.8(a)), an energy shift of 0.05 eV towards lower BEs is observed. The shift is consistent with n-Ge [20] and implies a 0.05 eV upward band bending at the GeO_2/n-Ge interface, in agreement with the formation of a superficial p-inversion layer in the n-type Ge substrates [50]. The measured BE differences, δ_{OXIDE}, δ_{INT}, δ_{SUB}, for GeO_2/Ge are shown in fig 5.8 and the literature values [17, 20, 28, 51] are also inserted for comparison. Applying Kraut's equation (1), yields a VBO = $\delta_{SUB} + \delta_{INT} - \delta_{OXIDE} = 3.55 \pm 0.2$ eV, consistent with a value of 3.6 ± 0.2 eV reported by XPS [17] and by synchrotron radiation photoemission spectroscopy [5].

5.3.5 Band gap evaluation and nature of Tm_2O_3/Ge interface

The band gaps of Tm_2O_3 and GeO_2 were determined by VUV-VASE. This was accomplished by first determining the thickness in the non-absorbing (transparent) region of the spectra. The dielectric function of the Ge film (31.9 nm) with the native oxide as Cauchy layer (1.4 nm) was modelled first. Then, another Cauchy layer was added and fitted for the thickness of Tm_2O_3 film (10.4 nm), or GeO_2 (4.6 nm). Subsequently, the optical constants (real and imaginary part of dielectric function) were extracted. The Tm_2O_3 (GeO_2) film was modelled with Cauchy layer at long wavelengths and extended into VUV with the B-spline and then converted to a general oscillator layer. The dielectric function converts to refractive index and extinction coefficient (k) using Kramers-Kroning relations. The absorption coefficient (α) is calculated from the extinction coefficient as $\alpha=4\pi k/\lambda$, where λ is wavelength. The absorption coefficient vs photon energy plots for GeO_2/Ge and Tm_2O_3/Ge stacks are shown in Figs. 5.8 (c)-(d) respectively. The band gap can be estimated by linear extrapolation of the segments on the curves in the non-absorbing

regions, and is found to be 5.95 eV for GeO_2 and 5.77 eV for Tm_2O_3. The schematics of derived band line-ups for GeO_2/Ge and Tm_2O_3/Ge are depicted in Figs. 5.8(e)-(f). Note that both band gap values are slightly higher than those reported using the Tauc-Lorentz method [16], in agreement with the finding of Di *et al* [52]. The band gap value for GeO_2 compares to Lange *et al*. [53] where the optical band gap has been measured from an increase of the absorption edge and found to vary from 5.21 eV to 5.95 eV depending on O_2 flow rate during reactive DC magnetron sputtering deposition. The band gap of 5.95 eV refers to highest O_2 flow and polycrystalline films of GeO_2. The band gap of GeO_2 of ~ 6.0 eV has been reported from SE measurements from absorption edge [54]. The band gap value of Tm_2O_3 compares to 5.76 eV reported from optical reflectance on Tm_2O_3/Si stack [13]. It is worth noting the pronounced absorption (at ~ 5.3 eV) below the band edge for the Tm_2O_3/Ge, and an Urbach tail (see inset in Fig. 5.8(d)) as a signature of the poly-crystalline nature [55] of the thulium oxide film.

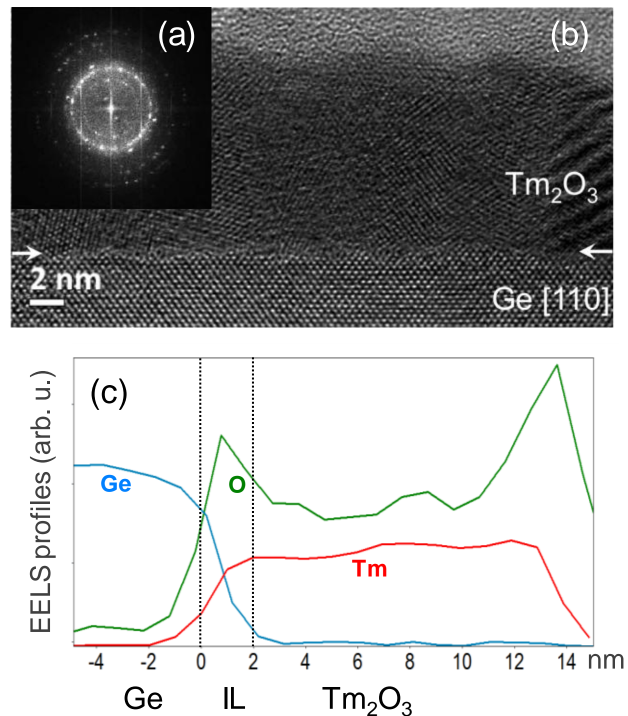

Fig. 5.9 Electron diffraction pattern (a), HRTEM image (b), and derived EELS elemental profiles across the interface (c), for 10 nm (nominal) Tm_2O_3 on Ge (white arrows in (b) help to locate the interface).

The polycrystalline nature of the Tm_2O_3 deposited on Ge is directly seen from the HRTEM image and the electron diffraction pattern of Figs. 5.9 (a) and (b), from which the cubic Tm_2O_3 structure has been identified. The HRTEM image is the direct and sharp interface between the Ge epi-layer and the Tm_2O_3 film (see white arrows in Fig. 5.9(b)), which is not the case for Tm_2O_3 deposited on Si where a thin amorphous interfacial layer is observed (not shown). This feature is common to RE oxide or RE oxide-based films [56, 58]. From the chemical point of view, there is a transition region between the Ge substrate and the Tm_2O_3 film where the three elements Tm, O and Ge are present, as can be observed from calculated EELS elemental profiles in Fig. 5.9(c). This may point to a chemically modified interface, below 1 nm, of possible germanate nature (Tm-O-Ge).

5.4 Conclusion

In summary, we have investigated the band line-up, sub-band gap absorbance features and nature of the interface of Tm_2O_3/Ge gate stacks deposited by atomic layer deposition using X-ray photoelectron spectroscopy and VUV-variable angle spectroscopic ellipsometry. A dielectric constant of 14 to 15 and the band gap of 5.3±0.1 eV has been determined from capacitance voltage and ellipsometric measurements respectively. There is a presence of GeO and GeO_2 at the Tm_2O_3/Ge interface, confirmed from absorbance features and chemical shifts of de-convoluted Ge3d and O1s core levels. An absorbance at 3.2 eV has been designated to thulium oxide bulk since it is clearly distinguished from the Si and Ge critical points. A large valence band offset (~2.95 eV) and conduction band offset (~1.7 eV) can provide a sufficient barrier to holes and electrons for improved Ge MOSFET performance. Also, a consistent valence band offset value of ~ 3 eV has been obtained for atomic-layer deposited Tm_2O_3/Ge from core-level and valence band XPS spectra measured at different sputtering times from a single bulk oxide layer. This method allows for more authentic probing of the interface, as there is no variation introduced when fabricating three separate samples for the XPS measurements. Furthermore, this study points unambiguously to both Tm_2O_3/Ge and GeO_2/Ge exhibiting sufficient conduction band offsets (> 1.5 eV) to adequately suppress leakage current in real applications. The barrier

role of Tm_2O_3 interlayer could suppress the growth of unstable GeO_x and bring effective passivation route in future Ge-based scaled CMOS devices.

5.5 References

[1] Choi K, Ando T, Cartier EA, Kerber A, Paruchuri V, Iacoponi J, Narayanan V. (Invited) The Past, Present and Future of High-k/Metal Gates. ECS Transactions. 2013 May 3;53(3):17-26.

[2] Takagi S, Zhang R, Takenaka M. Ge gate stacks based on Ge oxide interfacial layers and the impact on MOS device properties. Microelectronic Engineering. 2013 Sep 30;109:389-95.

[3] Zhang R, Chern WT, Yu X, Takenaka M, Hoyt JL, Takagi S. High mobility strained-Ge pMOSFETs with 0.7-nm ultrathin EOT using plasma post oxidation HfO 2/Al 2 O 3/GeO x gate stacks and strain modulation. InElectron Devices Meeting (IEDM), 2013 IEEE International 2013 Dec 9 (pp. 26-1). IEEE.

[4] Prabhakaran K, Ogino T. Oxidation of Ge (100) and Ge (111) surfaces: an UPS and XPS study. Surface Science. 1995 Mar 1;325(3):263-71.

[5] Kobayashi M, Thareja G, Ishibashi M, Sun Y, Griffin P, McVittie J, Pianetta P, Saraswat K, Nishi Y. Radical oxidation of germanium for interface gate dielectric GeO2 formation in metal-insulator-semiconductor gate stack. Journal of Applied Physics. 2009 Nov;106(10):4117.

[6] Lee CH, Lu C, Tabata T, Zhang WF, Nishimura T, Nagashio K, Toriumi A. Oxygen potential engineering of interfacial layer for deep sub-nm EOT high-k gate stacks on Ge. Electron Devices Meeting (IEDM), 2013 IEEE International 2013 Dec 9 (pp. 2-5). IEEE.

[7] Sioncke S, Lin HC, Delabie A, Conard T, Struyf H, De Gendt S, Caymax M. Scaling the Ge Gate Stack: Toward Sub 1 nm EOT. ECS Journal of Solid State Science and Technology. 2012 Jan 1;1(3):P127-32.

[8] Kouda M, Kawanago T, Ahmet P, Natori KE, Hattori T, Iwai H, Kakushima K, Nishiyama A, Sugii N, Tsutsui K. Interface and electrical properties of Tm2O3 gate dielectrics for gate oxide scaling in MOS devices. Journal of Vacuum Science &

Technology B. 2011 Nov 1;29(6):062202.
[9] Kouda M, Kakushima K, Ahmet P, Tsutsui K, Nishiyama A, Sugii N, Natori K, Hattori T, Iwai H. Rare earth oxide capping effect on La2O3 gate dielectrics for equivalent oxide thickness scaling toward 0.5 nm. Japanese Journal of Applied Physics. 2011 Oct 1;50(10S):10PA04.
[10] Ji T, Cui J, Fang ZB, Nie TX, Fan YL, Li XL, He Q, Jiang ZM. Single crystalline Tm 2 O 3 films grown on Si (001) by atomic oxygen assisted molecular beam epitaxy. Journal of Crystal Growth. 2011 Apr 15;321(1):171-5.
[11] Iwai H, Ohmi S, Akama S, Ohshima C, Kikuchi A, Kashiwagi I, Taguchi J, Yamamoto H, Tonotani J, Kim Y, Ueda I. Advanced gate dielectric materials for sub-100 nm CMOS. InElectron Devices Meeting, 2002. IEDM'02. International 2002 Dec 8 (pp. 625-628). IEEE.
[12] Wang JJ, Fang ZB, Ji T, Ren WY, Zhu YY, He G. Band offsets of epitaxial Tm 2 O 3 high-k dielectric films on Si substrates by X-ray photoelectron spectroscopy. Applied Surface Science. 2012 Jun 1;258(16):6107-10.
[13] Jianjun WA, Ting JI, Yanyan ZH, Zebo FA, Weiyi RE. Band gap and structure characterization of Tm 2 O 3 films. Journal of Rare Earths. 2012 Mar 31;30(3):233-5.
[14] Litta ED, Hellström PE, Henkel C, Valerio S, Hallén A, Östling M. High-deposition-rate atomic layer deposition of thulium oxide from TmCp3 and H2O. Journal of The Electrochemical Society. 2013 Jan 1;160(11):D538-42.
[15] Dentoni Litta E, Hellstrom PE, Henkel C, Ostling M. Thulium silicate interfacial layer for scalable high-k/metal gate stacks. Electron Devices, IEEE Transactions on. 2013 Oct;60(10):3271-6.
[16] Mitrovic IZ, Althobaiti M, Weerakkody AD, Sedghi N, Hall S, Dhanak VR, Chalker PR, Henkel C, Litta ED, Hellström PE, Östling M. Interface engineering of Ge using thulium oxide: Band line-up study. Microelectronic Engineering. 2013 Sep 30;109:204-7.
[17] Zhang WF, Nishimula T, Nagashio K, Kita K, Toriumi A. Conduction band offset at GeO2/Ge interface determined by internal photoemission and charge-corrected x-ray photoelectron spectroscopies. Applied Physics Letters. 2013 Mar 11;102(10):102106.
[18] Lin L, Xiong K, Robertson J. Atomic structure, electronic structure, and band offsets at Ge: GeO: GeO2 interfaces. Applied Physics Letters. 2010 Dec;97(24):2902.

[19] Yang M, Wu RQ, Chen Q, Deng WS, Feng YP, Chai JW, Pan JS, Wang SJ. Impact of oxide defects on band offset at GeO2/Ge interface. Applied Physics Letters. 2009 Apr;94(14):2903.

[20] Perego M, Scarel G, Fanciulli M, Fedushkin IL, Skatova AA. Fabrication of GeO2 layers using a divalent Ge precursor. Applied physics letters. 2007 Apr;90(16):2115.

[21] Fukuda Y, Yazaki Y, Otani Y, Sato T, Toyota H, Ono T. Low-Temperature Formation of High-Quality Interlayer for High-Gate Dielectrics/Ge by Electron-Cyclotron-Resonance Plasma Techniques. Electron Devices, IEEE Transactions on. 2010 Jan;57(1):282-7.

[22] Broqvist P, Binder JF, Pasquarello A. Erratum:"Band offsets at the Ge/GeO2 interface through hybrid density functionals"[Appl. Phys. Lett. 94, 141911 (2009)]. Applied Physics Letters. 2011 Mar 21;98(12):129901.

[23] Broqvist P, Binder JF, Pasquarello A. Band offsets at Ge/GeO 2 interfaces: Effect of different interfacial bonding patterns. Microelectronic Engineering. 2011 Jul 31;88(7):1467-70.

[24] Puthenkovilakam R, Chang JP. An accurate determination of barrier heights at the HfO2⁄ Si interfaces. Journal of applied physics. 2004 Sep 1;96(5):2701-7.

[25] Perego M, Seguini G. Charging phenomena in dielectric/semiconductor heterostructures during x-ray photoelectron spectroscopy measurements. Journal of Applied Physics. 2011 Sep 1;110(5):053711.

[26] Bersch E, Di M, Consiglio S, Clark RD, Leusink GJ, Diebold AC. Complete band offset characterization of the HfO2/SiO2/Si stack using charge corrected X-ray photoelectron spectroscopy. Journal of Applied Physics. 2010 Feb 15;107(4):043702.

[27] Engström O. A model for internal photoemission at high-k oxide/silicon energy barriers. Journal of Applied Physics. 2012 Sep 15;112(6):064115..

[28] Perego M, Molle A, Seguini G. Electronic properties at the oxide interface with silicon and germanium through x-ray induced oxide charging. Applied Physics Letters. 2012 Nov 19;101(21):211606.

[29] Kraut EA, Grant RW, Waldrop JR, Kowalczyk SP. Precise determination of the valence-band edge in x-ray photoemission spectra: Application to measurement of semiconductor interface potentials. Physical Review Letters. 1980 Jun 16;44(24):1620.

[30] Chambers SA, Droubay T, Kaspar TC, Gutowski M. Experimental determination of

valence band maxima for SrTiO3, TiO2, and SrO and the associated valence band offsets with Si (001). Journal of Vacuum Science & Technology B. 2004 Jul 1;22(4):2205-15.

[31] M.T. Anthony in Appendix 1. Spectrometer calibration; Practical Surface Analysis by Auger and X-ray Photoelectron Spectroscopy, (New York: Wiley, Eds. D. Briggs and M.P. Seah) 1988:429.

[32] Vickerman JC. Surface analysis: the principal techniques.

[33] Shirley DA. High-resolution X-ray photoemission spectrum of the valence bands of gold. Physical Review B. 1972 Jun 15;5(12):4709.

[34] Kraut EA, Grant RW, Waldrop JR, Kowalczyk SP. Precise determination of the valence-band edge in x-ray photoemission spectra: Application to measurement of semiconductor interface potentials. Physical Review Letters. 1980 Jun 16;44(24):1620.

[35] Chambers SA, Droubay T, Kaspar TC, Gutowski M. Experimental determination of valence band maxima for SrTiO3, TiO2, and SrO and the associated valence band offsets with Si (001). Journal of Vacuum Science & Technology B. 2004 Jul 1;22(4):2205-15.

[36] Perego M, Seguini G. Charging phenomena in dielectric/semiconductor heterostructures during x-ray photoelectron spectroscopy measurements. Journal of Applied Physics. 2011 Sep 1;110(5):053711.

[37] Martinez FL, Toledano-Luque M, Gandia JJ, Cárabe J, Bohne W, Röhrich J, Strub E, Mártil I. Optical properties and structure of HfO2 thin films grown by high pressure reactive sputtering. Journal of Physics D: Applied Physics. 2007 Sep 7;40(17):5256.

[38] Iwai H, Ohmi S, Akama S, Ohshima C, Kikuchi A, Kashiwagi I, Taguchi J, Yamamoto H, Tonotani J, Kim Y, Ueda I. Advanced gate dielectric materials for sub-100 nm CMOS. InElectron Devices Meeting, 2002. IEDM'02. International 2002 Dec 8 (pp. 625-628). IEEE.

[39] Jianjun WA, Ting JI, Yanyan ZH, Zebo FA, Weiyi RE. Band gap and structure characterization of Tm 2 O 3 films. Journal of Rare Earths. 2012 Mar 31;30(3):233-5.

[40] Price J, Lysaght PS, Song SC, Li HJ, Diebold AC. Identification of sub-band-gap absorption features at the HfO2/Si (100) interface via spectroscopic ellipsometry. Applied Physics Letters. 2007 Aug;91(6):1925.

[41] Price J, Bersuker G, Lysaght PS. Identification of interfacial defects in high-k gate stack films by spectroscopic ellipsometry. Journal of Vacuum Science & Technology B.

2009;27(1):310-2.

[42] Zhang XJ, Xue G, Agarwal A, Tsu R, Hasan MA, Greene JE, Rockett A. Thermal desorption of ultraviolet–ozone oxidized Ge (001) for substrate cleaning. Journal of Vacuum Science & Technology A. 1993 Sep 1;11(5):2553-61.

[43] I.Z. Mitrovic, S. Hall, N. Sedghi, I. McLeod, P. Spencer, D. Hesp, V.R. Dhanak, P. Bailey, T.C.Q. Noakes, P.R. Chalker, A. Dimoulas, and D. Tsoutsou, Systematic investigation of Ge surface passivation with LaGeOx, IEEE SISC, 2011.

[44] Brunco DP, Dimoulas A, Boukos N, Houssa M, Conard T, Martens K, Zhao C, Bellenger F, Caymax M, Meuris M, Heyns MM. Materials and electrical characterization of molecular beam deposited CeO2 and CeO2/HfO2 bilayers on germanium. Journal of Applied Physics. 2007 Jul;102(2):4104.

[45] Lopes JM, Roeckerath M, Heeg T, Schubert J, Littmark U, Mantl S, Besmehn A, Myllymaki P, Niinistö L, Adamo C, Schlom DG. Amorphous lanthanum lutetium oxide thin films as an alternative high-k material. ECS Transactions. 2007 Sep 28;11(4):311-8.

[46] E. Dentoni Litta, P.-E. Hellström, C. Henkel, S. Valerio, A. Hallén and M. Östling, Chemistry of Materials 2013 .

[47] Cole RJ, Gregory DA, Weightman P. Analysis of Auger-parameter and XPS shifts: Application of potential models. Physical Review B. 1994 Feb 15;49(8):5657.

[48] Hovis JS, Hamers RJ, Greenlief CM. Preparation of clean and atomically flat germanium (001) surfaces. Surface science. 1999 Oct 1;440(1):L815-9.

[49] Sasada T, Nakakita Y, Takenaka M, Takagi S. Surface orientation dependence of interface properties of GeO2/Ge metal-oxide-semiconductor structures fabricated by thermal oxidation. Journal of Applied Physics. 2009 Oct;106(7):3716.

[50] Dimoulas A, Tsipas P, Sotiropoulos A, Evangelou EK. Fermi-level pinning and charge neutrality level in germanium. Applied physics letters. 2006 Dec 3;89(25):252110-.

[51] Hudait MK, Zhu Y, Maurya D, Priya S, Patra PK, Ma AW, Aphale A, Macwan I. Structural and band alignment properties of Al2O3 on epitaxial Ge grown on (100),(110), and (111) A GaAs substrates by molecular beam epitaxy. Journal of Applied Physics. 2013 Apr 7;113(13):134311.

[52] Di M, Bersch E, Diebold AC, Consiglio S, Clark RD, Leusink GJ, Kaack T. Comparison of methods to determine bandgaps of ultrathin HfO2 films using spectroscopic

ellipsometry. Journal of Vacuum Science & Technology A. 2011 Jul 1;29(4):041001.

[53] Lange T, Njoroge W, Weis H, Beckers M, Wuttig M. Physical properties of thin GeO 2 films produced by reactive DC magnetron sputtering. Thin Solid Films. 2000 Apr 3;365(1):82-9.

[54] Lee CH, Tabata T, Nishimura T, Nagashio K, Kita K, Toriumi A. Ge/GeO2 interface control with high pressure oxidation for improving electrical characteristics. ECS Transactions. 2009 May 15;19(1):165-73.

[55] Martinez FL, Toledano-Luque M, Gandia JJ, Cárabe J, Bohne W, Röhrich J, Strub E, Mártil I. Optical properties and structure of HfO2 thin films grown by high pressure reactive sputtering. Journal of Physics D: Applied Physics. 2007 Sep 7;40(17):5256.

[56] Lamagna L, Wiemer C, Perego M, Volkos SN, Baldovino S, Tsoutsou D, Schamm-Chardon S, Coulon PE, Fanciulli M. O3-based atomic layer deposition of hexagonal La2O3 films on Si (100) and Ge (100) substrates. Journal of Applied Physics. 2010 Oct 15;108(8):084108.

[57] Schamm-Chardon S, Coulon PE, Lamagna L, Wiemer C, Baldovino S, Fanciulli M. Combining HRTEM–EELS nano-analysis with capacitance–voltage measurements to evaluate high-κ thin films deposited on Si and Ge as candidate for future gate dielectrics. Microelectronic Engineering. 2011 Apr 30;88(4):419-22.

[58] Schamm-Chardon S. Interdiffusion and Chemical Reaction at Interfaces by TEM/EELS. Transmission Electron Microscopy in Micro-Nanoelectronics.:135-64.

Chapter 6

Low EOT $GeO_2/Al_2O_3/HfO_2$ on Ge Substrate Using Ultrathin Al Deposition

6.1 Introduction

This chapter investigates HfO_2/Ge gate stacks with ultra-thin Al_2O_3 layer as a barrier interface. Direct deposition of HfO_2 onto Ge leads to high interface state density (Dit) [1] and a thin native oxide, GeO_2 interfacial layer (IL) has been shown to be effective for reducing Dit. However, Ge suffers from desorption of volatile GeO to the surface, which causes device instability, high Dit and mobility degradation [2]. A variety of methods have been used for capping the IL to prevent desorption of GeO. Recently alumina (Al_2O_3) has been proposed as an interlayer between Ge and HfO_2 to act as a diffusion barrier [3, 4] and stabilize a very thin GeO_2 layer on the Ge channel to achieve a low Dit. One approach to form the Al_2O_3 interlayer is to deposit a thin layer of Al metal by molecular beam epitaxy (MBE) and subsequently oxidize it to form an Al_2O_3/GeO_2/Ge structure [5]. This chapter shows the use of such a passivation scheme, combined with HfO2 as a high-j layer, to achieve an EOT as low as 1.3 nm with an acceptable leakage current of less than 10^{-7} A/cm^{-2} at ±1 V.

6.2 Sample preparation

Ge (100) wafers (n- and p-type) were cleaned in ultra high vacuum (<10^{-6} mbar) at 500 ºC and 600 ºC for 10 min to evaporate any native oxide and so achieve an oxide free surface. Subsequently, wafers were exposed to an Al flux for a range of times to deposit ultrathin Al layers. The samples were then oxidized at ambient temperatures in the MBE load lock to produce Al_2O_3 layers. The samples were transferred within 1 min to an Oxford Instruments OpAL reactor and thin films of HfO2 were deposited on the Al_2O_3 using atomic layer deposition (ALD). The HfO_2 depositions used a [(CpMe)2HfOMeMe] precursor coupled with an O_2 plasma as the oxidizing species. Between 30 and 130 ALD cycles were used to grow HfO_2 thicknesses from 1.6 to 7 nm at 250 ºC. For electrical measurements, circular gold contacts of area 1.96 x10^3 cm^2 were deposited onto the films to form MOS gate electrodes and Al was deposited on the back of the Ge wafers to provide an ohmic contact. After preliminary measurements, the samples were annealed in forming gas (FGA) at 350 ºC for 30 min. The oxide leakage current was measured using a Keithley 230B voltage source and Keithley 617B electrometer. The HP 4192A low

frequency (LF) impedance analyzer at small signal frequencies between 100 Hz to 1 MHz was used to perform high frequency capacitance–voltage (HF CV) measurements.

6.3 Results and Discussion

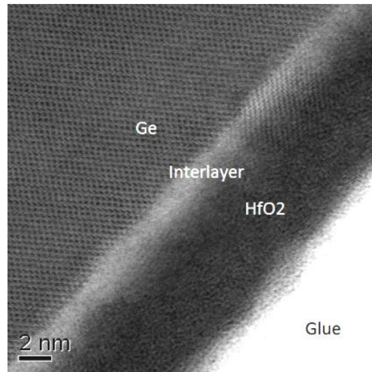

Fig. 6.1 TEM image showing a 2 nm thick HfO_2/Al_2O_3 layer with HfO_2 on top.

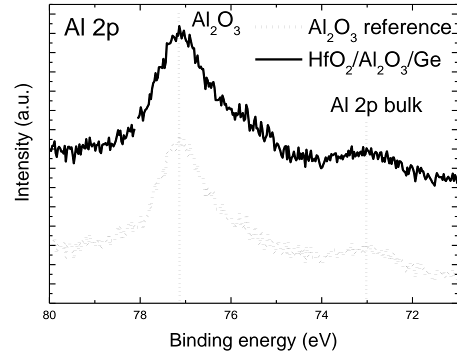

Fig. 6.2 XPS spectra for Al 2p from 10 s Al MBE exposure and 30 ALD cycles of HfO_2.

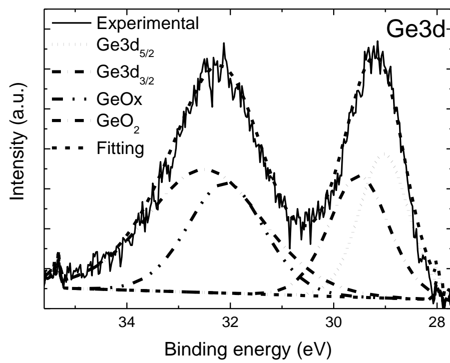

Fig. 6.3 XPS spectra for Ge 3d from 10 s Al MBE exposure and 30 ALD cycles of HfO_2.

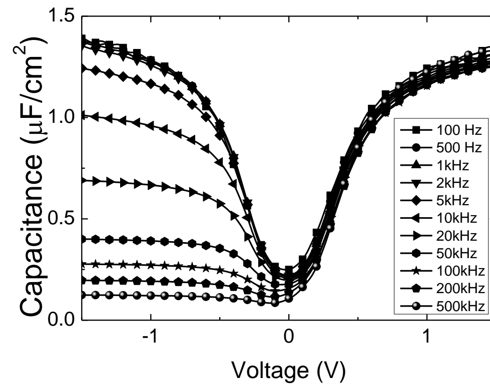

Fig. 6.4 HF CV characteristics of sample with 5 s exposure to Al MBE source followed by 65 ALD cycles of HfO_2 deposition.

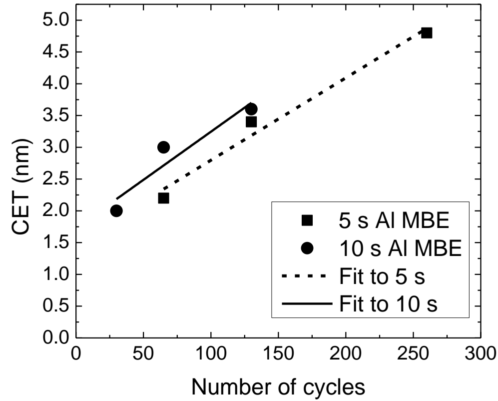

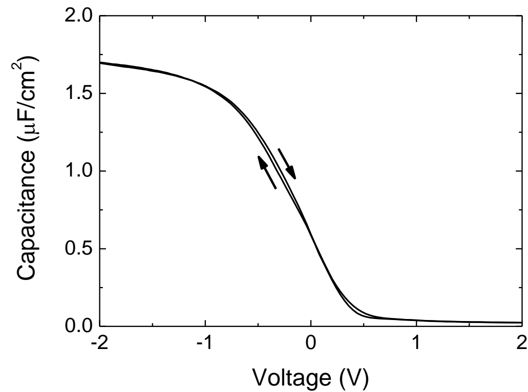

Fig. 6.5 CET against number of ALD cycles for different MBE exposure times of Al for as-deposited samples.

Fig. 6.6 CV plots showing the hysteresis of circa 10 mV measured at 1 MHz of HfO_2/ Al_2O_3/Ge.

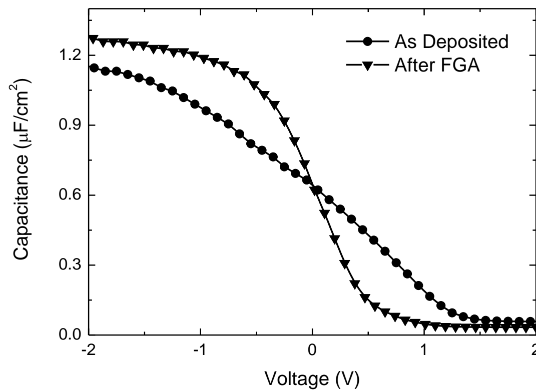

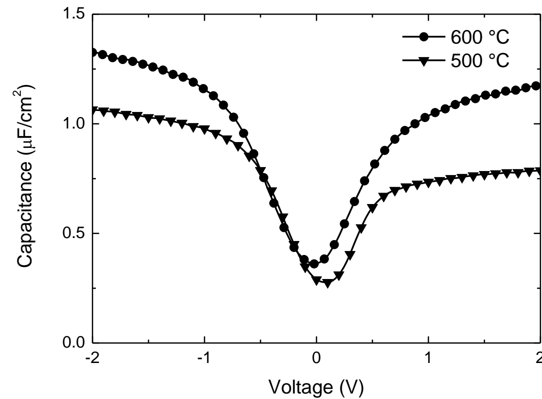

Fig. 6.7 CV plots before and after FGA of HfO_2/ Al_2O_3/Ge measured at 1 MHz

Fig. 6.8 CV plots of HfO_2/ Al_2O_3/Ge cleaned at 500 °C and 600 °C measured at 1 MHz

Fig. 6.1 shows an HRTEM image of a sample with 10 s exposure to the MBE Al source with 130 ALD cycles to deposit HfO_2, obtained with a JEOL 2100F TEM operating in STEM mode with an operating voltage of 200 kV. The image indicates a 2 nm thick layer of GeO_2/Al_2O_3 with a 7 nm layer of HfO_2 on top. X-ray Photoelectron spectroscopy (XPS) was carried out to investigate the chemical bonding present in the films. Fig. 6.2 shows XPS Al (2p) spectra confirming that Al_2O_3 is formed when compared to a reference Al foil. The small peak at 73 eV is attributed to differential charging across the thin alumina layer. The XPS Ge (3d) data of Fig.6.3 shows that a layer of GeO_2 is present at the Ge surface. Typical CV plots measured in the range 100 Hz - 500 kHz are shown in Fig. 6.4 The plots indicate very low frequency dispersion in the accumulation

region and well-behaved variation of inversion capacitance with frequency at negative voltages Fig. 6.5 shows the relationship between the capacitance equivalent thickness (CET) and the physical thickness of high-j layers calculated from the number of ALD cycles on a sample cleaned at 500 ºC for two different Al deposition times. The CET of GeO_2/Al_2O_3 layer can be found from the linear interpolation of these data, from which the thickness of the alumina layer was estimated by extrapolating the CET at zero HfO_2 thickness for 5 s and 10 s Al deposition with the difference being attributed to increasing alumina thickness. The alumina thickness was found to be 0.6 nm per 5 s and the thickness of GeO_2 was calculated to be 1.6 nm by using k values of 9 and 5 for alumina and GeO_2 respectively. For the sample cleaned at 600 ºC the thickness of GeO_2 was reduced to 1 nm (EOT of 0.65 nm). The CV plots show very small hysteresis of ca. 10 mV, as shown in Fig. 6.6. To estimate the IL thickness, samples with various thickness of HfO_2 were fabricated. The CV plots of a sample with 10 s Al MBE exposure and 30 ALD cycles of HfO_2 before and after FGA are shown in Fig. 6.7, which shows a steeper slope and larger accumulation after FGA. The steeper slope is assumed to be due to a reduction of interface states by the FGA. In the presence of interface states, the CV plot is broadened and cannot saturate to the oxide thickness in the accumulation region in the swept voltage range. This can explain the difference in oxide capacitance before and after FGA, corresponding to reduction of EOT of the gate stack from 1.7 nm to 1.3 nm by FGA. The hysteresis was slightly improved on some samples with FGA but degraded slightly on others. This observation is under investigation. The CV plots shown in Fig. 6.8 are for samples with thermal clean at 500 ºC and 600 ºC with 130 cycles of HfO_2 at small frequency of 1 kHz. The sample cleaned at 600 ºC shows about 30% higher oxide capacitance which gives the EOT value of 2.3 nm, compared to the value of 3 nm for the sample cleaned at 500 ºC. The reduction of EOT for the sample cleaned at higher temperature is an indication of lower thickness of GeO_2.

6.4 Conclusion

ALD hafnia high-kdielectric gate stack was fabricated on Ge with alumina as the barrier level using combined MBE and ALD technique and have been characterised by physical and electrical techniques. The devices show low EOT down to 1.3nm, low leak- age current of less than10^{7} A cm^{2} at ±1V, and CV hysteresis of ca. 10mV. The thicknesses of GeO_2 interfacial layer and alumina barrier layer were estimated by comparing samples with different high-k thickness. The forming gas anneal indicates an improvement in the shape of CV plots due to reduction of interface states. Thermal cleaning at higher temperature reduces the thickness of GeO_2 resulting in an improved EOT.

6.5 References

[1] Dimoulas A, Brunco DP, Ferrari S, Seo JW, Panayiotatos Y, Sotiropoulos A, Conard T, Caymax M, Spiga S, Fanciulli M, Dieker C. Interface engineering for Ge metal-oxide–semiconductor devices. Thin Solid Films. 2007 Jun 4;515(16):6337-43.

[2] Wang SK, Kita K, Lee CH, Tabata T, Nishimura T, Nagashio K, Toriumi A. Desorption kinetics of GeO from GeO2/Ge structure. Journal of applied physics. 2010 Sep 1;108(5):054104.

[3] Zhang R, Iwasaki T, Taoka N, Takenaka M, Takagi S. Al {sub 2} O {sub 3}/GeO {sub x}/Ge gate stacks with low interface trap density fabricated by electron cyclotron resonance plasma postoxidation. Applied Physics Letters. 2011 Mar 14;98(11).

[4] Li H, Lin L, Robertson J. Identifying a suitable passivation route for Ge interfaces. Applied Physics Letters. 2012 Jul 30;101(5):052903.

[5] Hideshima I, Hosoi T, Shimura T, Watanabe H. Al 2 O 3/GeO 2 stacked gate dielectrics formed by post-deposition oxidation of ultrathin metal Al layer directly grown on Ge substrates. Current Applied Physics. 2012 Dec 31;12:S75-8.

Chapter 7

Hafnia and Alumina on Sulphur Passivated Germanium

7.1 Introduction

A number of alternative methods have been suggested to passivate the Ge surface, such as nitridation, rare-earth buffer oxide layer [1, 2, 3], and Al_2O_3 or sulphur passivation [4, 5]. The introduction of S in the GeO_x can result in superior Ge gate stack [6]. It has been shown for Al_2O_3/Ge stacks that depending on the oxidant precursor (H_2O or O_3) of the Atomic Layer Deposition (ALD) of Al_2O_3, the gate stack can be tuned for p-MOS (Metal Oxide Semiconductor) or nMOS applications [7]. In effect, with Al_2O_3 deposition with H_2O, no GeO_x was detected at the interface and a low density of interface states (D_{it}) has been measured at the valence band edge making this gate stack suitable for pMOS application. On the contrary, Al_2O_3 with O_3 deposition has resulted in a thin Ge-suboxide and low D_{it} at the conduction band edge making this gate stack suitable for nMOS application [7]. In this chapter, HfO_2/Ge and Al_2O_3/Ge gate stacks have been deposited by ALD using O-plasma and H_2O. Both O-plasma and O_3 as the co-reagents in ALD avoid the potential incorporation of hydrogen that is possible if using H_2O vapour. The hydroxyl incorporation has been reported for H_2O-based ALD [8]. Oxygen-plasma and O_3 have more effective pumping speeds facilitating shorter purge times than H_2O. O_3 is effectively more reactive than O-plasma, which can lead to thicker interfacial oxides at the growth temperatures of 250°C used in this chapter, and also can lead to more carbon incorporation from the metal precursor ligands. Therefore, O-plasma and H_2O were used as oxidants during ALD and an assessment of their effect on the S passivated germanium is the main new contribution of this work.

7.2 Experimental

Ge (100) n- wafers of the resistivity 0.3-3 Ωcm were degreased by ultrasonic bath in acetone and then given a cyclic HF/water rinse in order to remove the native oxide layer, followed by sulphur deposition by dipping the samples in a 20% ammonium sulphide, $(NH_4)_2S$, solution in water for 10 minutes and then dried under an argon flow. The samples were then immediately transferred into an Oxford Instruments OpAL ALD reactor, where 65, 130 and 250 cycles were used to

deposit 3, 7 and 20 nm HfO_2 layers using [(CpMe)2HfOMeMe] precursor coupled with remote oxygen plasma or water. The 3 nm Al_2O_3 layers were deposited in the same ALD reactor using trimethilaluminium (TMA) precursor with both O-plasma and water, as above. Note that we have also fabricated HfO_2 layers on alumina S-passivated Ge using O-plasma. For this process, S-treated samples were exposed to an Al flux for a range of times to deposit ultra-thin Al layers. The samples were then oxidized at ambient temperatures in the Molecular Beam Epitaxy (MBE) load lock to produce sub-nm (~ 0.3 nm) Al_2O_3 layers. Then, the samples were transferred to the ALD reactor, where 7 nm HfO_2 films were deposited using 130 ALD cycles using the same HfO_2 precursor and O-plasma as oxidant. As reference samples to the latter batch, 7 nm HfO_2 on S-passivated Ge were fabricated using O-plasma. The thickness of deposited HfO_2 and Al_2O_3 films was obtained using in-situ single wavelength spectroscopic ellipsometer. The Transmission Electron Microscopy (TEM) measurements were performed on 20 nm HfO_2/Ge sample prepared by focussed ion beam milling. The final thinning of the sample was carried out at 100 pA using gallium ions at 30 kV.

X-ray Photoelectron Spectroscopy (XPS) measurements were carried out on thin 3 nm HfO_2/S/Ge and Al_2O_3/S/Ge stacks to ascertain the effect of S and particularly ALD oxidant on the interfacial layer (IL). The XPS core-levels (CLs) were acquired using an ultra high vacuum (UHV) system consisting of Al Kα X-ray (1486.6 eV) source and a PSP Vacuum systems 5-channel HSA electron energy analyser. The reference samples for this study comprise of clean Ge, native GeO_2/Ge, S-treated Ge, 3 nm HfO_2/Ge and 3 nm Al_2O_3/Ge. The clean Ge sample was obtained by sputtering and in-situ annealing of a Ge (100) surface in UHV and was considered clean when no oxygen or carbon was detected by XPS. The electron binding energies (BEs) were calibrated using the Ag 3d peaks from a clean silver foil or by setting the C 1s peak in the spectra (due to stray carbon impurities in the as-received samples from the ALD reactor) at 284.6 eV for all samples [9]. The CL spectra were fitted using Gaussian-Lorentzian line shapes with a Shirley-type background [10].

For electrical measurements, gold contacts were deposited on 7 nm HfO_2 films to form MOS gate electrodes, while Al was deposited on the back of the Ge wafers to provide an Ohmic contact. The capacitance voltage (CV) measurements in the frequency range of 1-400

kHz were performed to estimate the effect of different passivation methods on the interfacial layer.

7.3 Results and Discussion

7.3.1 Interfacial Features of Hafnia on Sulphur Passivated Germanium

Fig. 7.1 shows a comparison of the Ge 3d line shape measured from several samples. The XPS Ge 3d CL spectrum for a sample of clean Ge is shown in Fig. 7.1(a). The experimental curve is fitted with two sub-peaks corresponding to Ge $3d_{5/2}$ at 29.42 eV and Ge $3d_{3/2}$ at 30.37 eV, corresponding to the spin-orbit doublet. Compared to the spectrum of clean Ge sample, the S-treated Ge sample in Fig. 7.1(b) shows an additional feature, which is also fitted with a doublet. This feature is at ~ 0.9 eV chemical shift from Ge 3d substrate peak and can be attributed to GeS species in agreement with the literature [4].

Fig. 7.1(c) shows the spectrum of native GeO_2/Ge. The peak fitted at 33.03 eV is attributed to the +4 Ge oxidation state (i.e. GeO_2), while a small peak centred around 1.7 eV above the Ge $3d^0$ (indicated on the Fig. with arrows) is related to +2 Ge oxidation state (i.e. GeO) [11]. Comparing with the sulphur treated sample, it is apparent that the addition of sulphur is very effective in passivating the sample, as evidenced by the absence of the GeO_2 peak in Fig. 7.1(b).

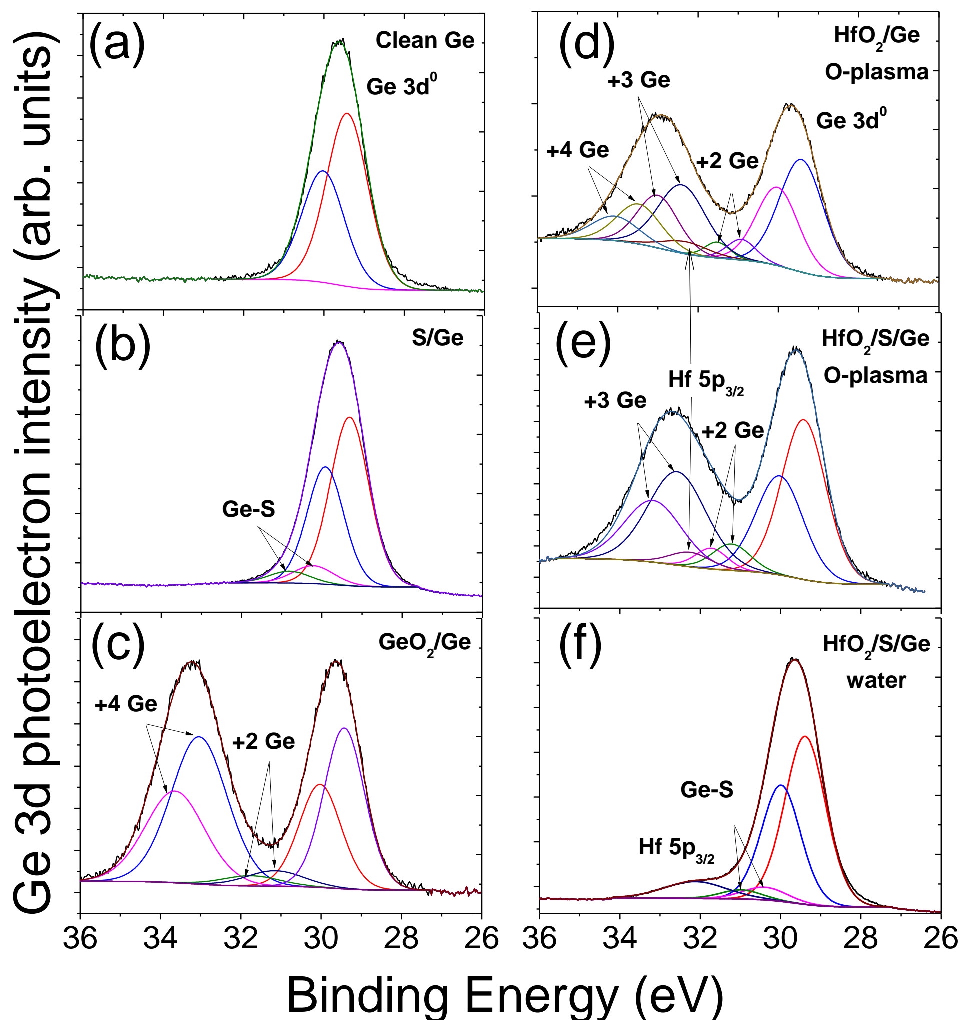

Fig. 7.1 Ge 3d XPS core level line shape for: (a) clean Ge, (b) S-passivated Ge, (c) native GeO_2/Ge, (d) HfO_2/Ge, (e) HfO_2/S/Ge using oxygen plasma as oxidant, and (f) HfO_2/S/Ge using water as oxidant during ALD deposition. The thickness of all oxide layers is ~ 3 nm.

Fig. 7.1(d) and 7.1(e) show the Ge 3d line shape from hafnia grown using oxygen plasma without and with S-pretreatment respectively. The effect of O-plasma is increased presence of GeO_x, in particular +2 Ge, as indicated by the increased intensity in the region between the two main peaks, at ~ 31 eV. This is evident when comparing with Fig. 7.1(c) where the sample had predominantly the GeO_2 layer on Ge. Binding energy differences lower than 3.4 eV in Figs. 7.1(d)-(e) indicate either HfGeO or the occurrence of Ge in oxidation states lower than +4 [12]. The former has been excluded

since the chemical shift observed (~3 eV) is larger than reported for HfGeO (2.45 eV) [13]. Furthermore, there is no appreciable shift of Hf 4f peaks for both samples in Figs. 7.1(d)-(e) [14]. The chemical shift value is close to reported 2.9 eV for +3 Ge oxidation states [4]. It can be seen that the overall line shape due to the GeO_2 peak (see Figs. 7.1(d)-(e) in comparison to Fig. 7.1(c)) is broadened, together with the presence of Hf $5p_{3/2}$ peak from HfO_2 at ~ 32 eV as indicated by the arrows. Also, note the slight narrowing of IL sub-peak and dominance of +3 Ge species for O-plasma HfO_2/S/Ge in comparison to HfO_2/Ge. Fig. 7.1(f) shows the Ge 3d XPS spectrum for HfO_2 taken from sample made on S-passivated Ge using water as the oxidant. It is apparent that the GeO_2 and GeO_x peaks are significantly suppressed for the latter sample. Thus, it is possible to conclude that hafnia deposited on S-passivated samples using water does not induce a reaction with germanium to produce significant amounts of GeO_x. On the other hand, despite S-passivation, oxygen plasma seems more aggressive during hafnia growth and induces significant GeO_x (+2 Ge and +3 Ge) formation. The HfO_2 layers on Ge deposited using O-plasma were found to be amorphous. Fig. 7.2 shows a typical TEM image of a 20 nm HfO_2 on Ge. The image shows the crystalline nature of the Ge substrate and the amorphous HfO_2 and IL.

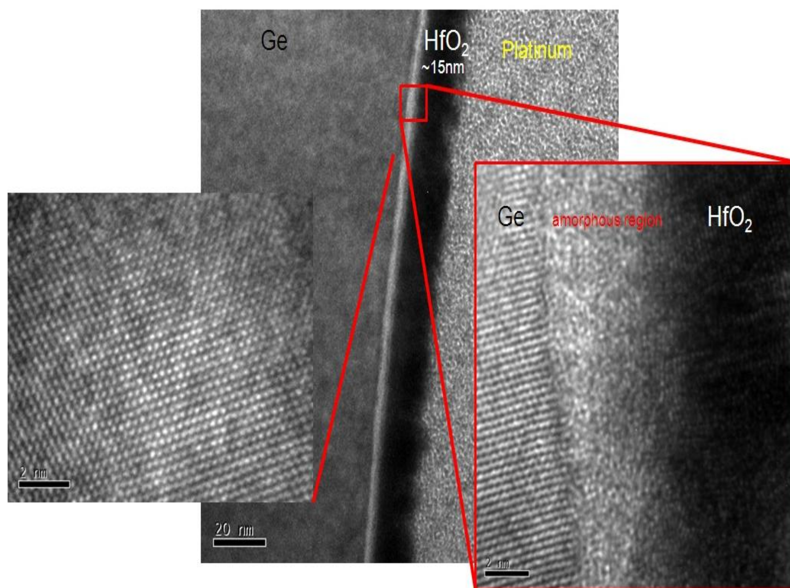

Fig. 7.2 The cross-section TEM image of 20 nm HfO_2/Ge deposited by ALD using O-plasma oxidant.

7.3.2 Interfacial Features of Al_2O_3 on Sulphur Passivated Germanium

Fig. 7.3 shows the Ge 3d XPS spectra for 3 nm Al_2O_3/Ge stacks deposited with and without sulphur passivation.

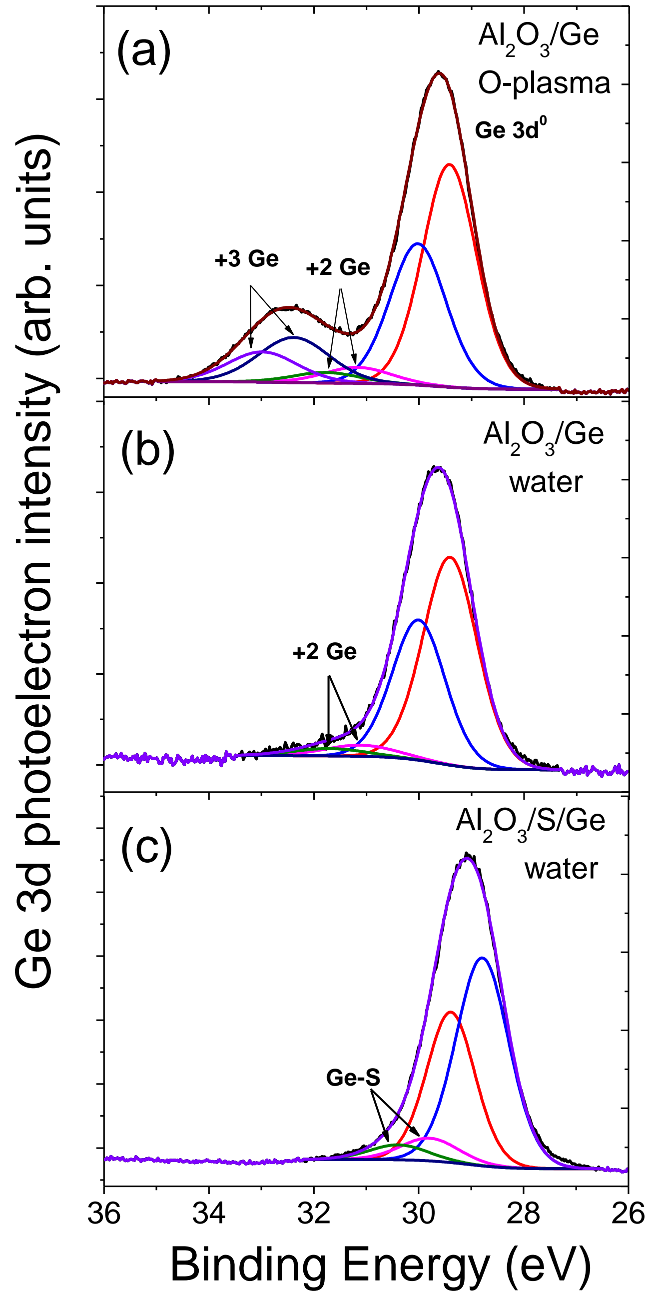

Fig. 7.3 Ge 3d XPS core level for (a) Al_2O_3/Ge using O-plasma, (b) Al_2O_3/Ge using water, and (c) Al_2O_3/S/Ge using water as oxidants during ALD.

The experimental curve fitting procedure was the same as for that shown in Fig. 7.1. Figs. 7.3(a) and 7.3(b) show the Ge 3d core levels from Al_2O_3 grown on Ge substrate using oxygen plasma and using water as oxidants respectively, both without S-pretreatment. Note narrower IL sub-peak for Al_2O_3/Ge stack in Fig. 7.1(a) than for the same thickness HfO_2/Ge stack in Fig. 7.1(d). This is in agreement with experimentally [1] and theoretically [15] observed lower reactivity of alumina on Ge than hafnia on Ge. It can be seen in Fig. 7.3(a) that the effect of the oxygen plasma is a significant presence of both +3 Ge (at ~ 3 eV chemical shift) and +2 Ge (at 1.7 eV), compared to the sample grown using water as the oxidant in Fig. 7.3(b). It is evident from Fig. 7.3(c) that S-pretreatment in combination with depositing alumina with water prevents the formation of GeO_x. There isa clear Ge-S doublet peak at ~ 0.9 eV chemical shift in agreement with the observation in Fig. 1(f), as a fingerprint of Ge-S bond at the interface. The results from Fig. 7.3 suggest that samples prepared by ALD using H_2O have much reduced GeO_x species, and this improves further if the Ge is pretreated with S.

7.3.3 The Effect of S and S/sub-nm Al_2O_3 passivation on CV characteristics of HfO_2/Ge stacks

The capacitance voltage characteristics for 7 nm HfO_2/Ge stacks deposited by ALD using O-plasma are shown in Fig. 7.4. Two types of passivation treatments on Ge, namely S (open square symbol in Fig. 7.4) and S/0.3 nm Al_2O_3 (triangle symbol curve in Fig. 7.4) were compared to the CV results from HfO_2/Ge sample without any passivation (open circle symbol curve in Fig. 7.4). The CV results were plotted for two frequencies that are 50 and 100 kHz. There is evidence of the frequency dependence of the distortion in the CV, around 0.5 V for the HfO_2/Ge sample and ~ -0.5 V for HfO_2/0.3 nm Al_2O_3/S/Ge sample indicated by the arrows in Fig. 7.4. There is a slight shift of these humps to lower voltages with decreasing measuring frequency to 50 kHz. This behaviour is consistent with the response of interfacial defects located in the energy gap at the insulator/semiconductor interface [16, 17]. Note that such behaviour is not evident for S-passivated Ge stack (see open square curves in Fig. 7.4). The electrical quality of the interface has been found to strongly depend on the Ge oxidation states [18, 19]. Houssa et al. [20] have

found from the first principle calculations that the formation of Ge–O bonds or Hf–O–Ge bonds at or near the HfO_2/Ge interface does not result in the presence of surface states in the Ge energy band gap. However, the formation of a metallic Ge–Hf bond at the interface, likely present if Hf is located in the sub-oxide interfacial layer (GeO_x with $x < 2$), has been shown to result in the formation of a defect level in the upper part of the Ge energy band gap, hampering the electrical properties of MOS devices. Referring to our XPS results in Figs. 7.1 (d) and 1(e), there is no evidence of +1 Ge oxidation species and even for HfO_2/S/Ge stacks, the presence of both +2 Ge and +3 Ge species at the interface has no detrimental effect on the CV characteristic shown in Fig. 7.4, where the curve is near ideal without any distortions around flat band region.

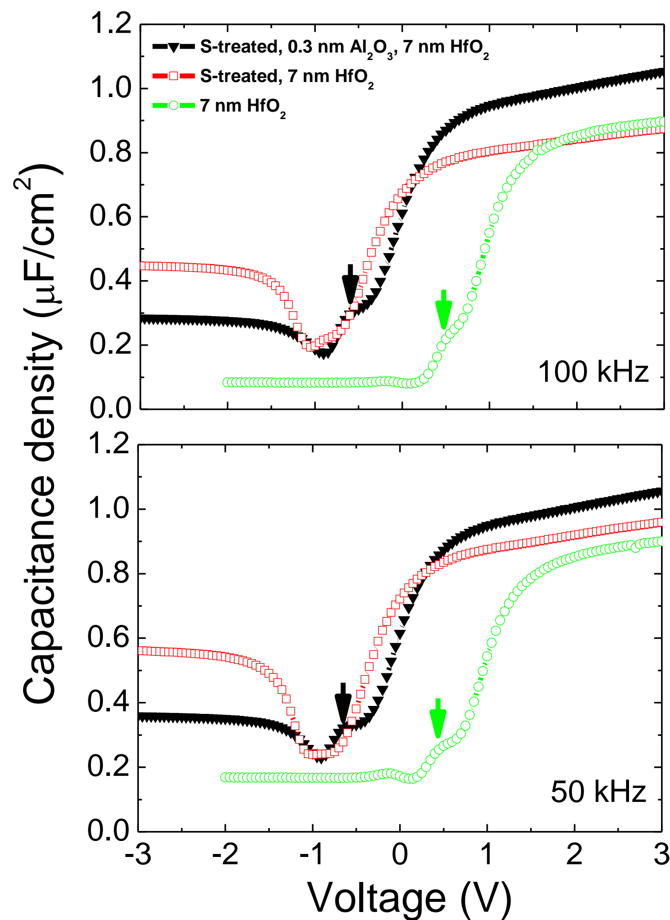

Fig. 7.4 The CV plots at 50 and 100 kHz of 7 nm HfO_2/Ge gate stacks deposited by ALD using O-plasma as oxidant on two differently passivated Ge surfaces: S/Ge, and 0.3 nm Al_2O_3/S/Ge. The reference sample is HfO_2/Ge without any passivation. The arrows point to the CV distortions around flat band regions.

Hence, it seems plausible that the observation of the CV distortion in HfO_2/Ge simple (see Figs. 7.4 and 7.1(d)) does not relate to Hf-Ge bonds, but could rather originate from extrinsic defects. For the sample with HfO_2/0.3 nm Al_2O_3/S/Ge the CV distortion is less pronounced. Note also that the latter gate stack is the most scalable, as it shows the highest value of accumulation capacitance.

From the CV characteristics for HfO_2/S/Ge sample in Fig. 7.4, the capacitance equivalent thickness (CET) of 2.7 nm can be calculated from the maximum (accumulation) capacitance. Assuming permittivity of 21.3 for HfO_2, estimated previously from the variation of CET as a function of HfO_2 thickness [21], the equivalent oxide thickness (EOT) of IL for HfO_2/S/Ge stacks is estimated to be 1 nm. The electrical results in Fig 7.4 strongly support the case for sulphur passivation of the interface where there is no distortions around flat band region.

7.3.4 Determination of Band Gap of HfO2 on Ge

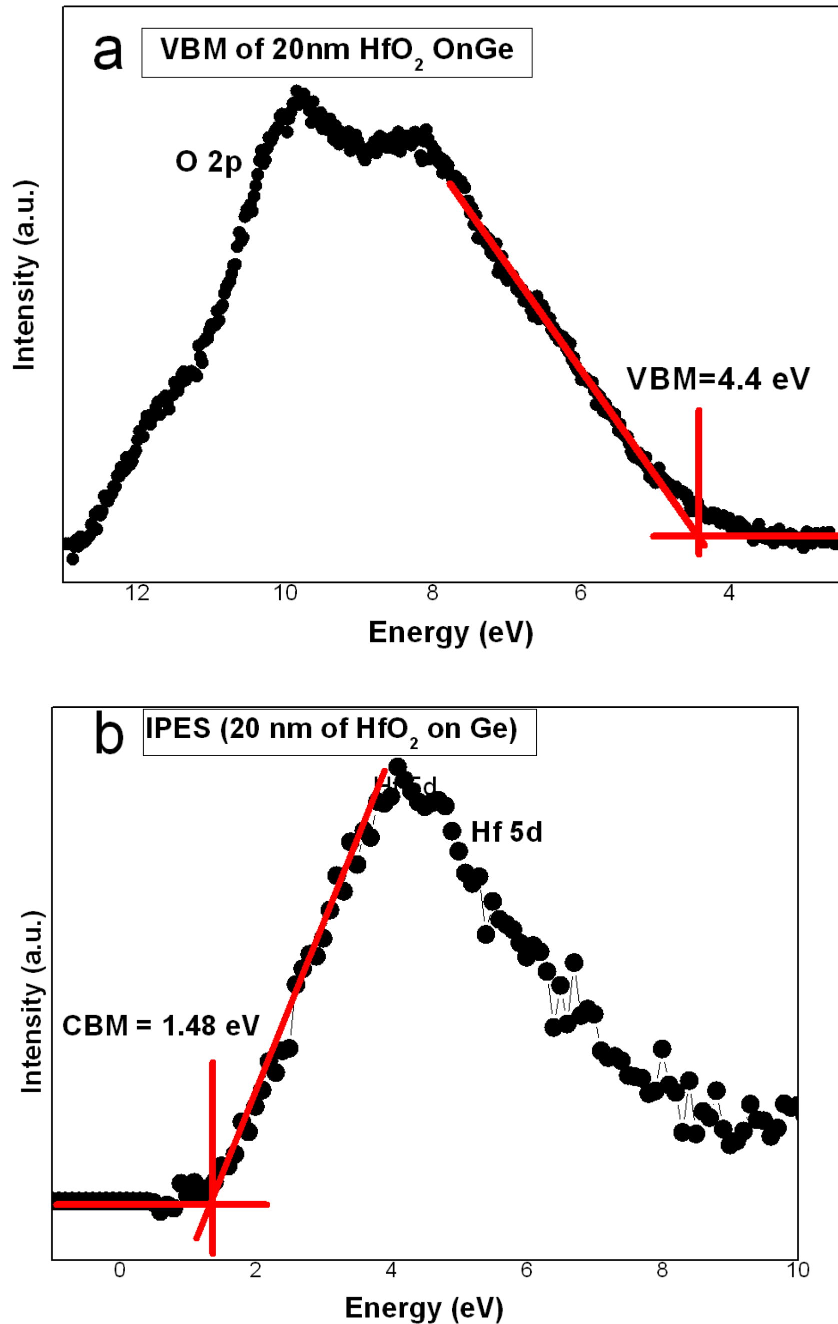

Fig.7.5 Photoemission (a) and Inverse photoemission (b) spectra of 20 nm HfO_2 on Ge.

In Fig. 7.5 the valance band maximum and the conduction band minimum were determined to be 4.4 and 1.48 eV, respectively. The peak at about 10 eV binding energy in the valence band is

attributed to O2p states. The empty Hf5d states are indicated in the IPES spectrum. The band gap was determined to be 5.88 eV.

7.4. Conclusion

In this chapter, HfO_2/Ge and Al_2O_3/Ge gate stacks have been deposited by atomic layer deposition using O-plasma and H_2O as oxidants. Detailed X-ray photoelectron spectroscopy results show that sulphur passivation of germanium is very effective in preventing the formation of the GeO_x at the interface, in particular if the ALD oxidant is water when depositing either 3 nm HfO_2 or Al_2O_3 films. Furthermore, the interfacial +3 Ge and +2 Ge species evident for HfO_2/S/Ge stack deposited using O-plasma, have been found to have no deleterious effect on the electrical quality of the interface. The results suggest the efficient passivation of Ge by sulphur, when a well controlled oxidation process is performed.

7.5 References

[1] Takagi S, Zhang R, Takenaka M. Ge gate stacks based on Ge oxide interfacial layers and the impact on MOS device properties. Microelectronic Engineering. 2013 Sep 30;109:389-95.

[2] Oshima Y, Shandalov M, Sun Y, Pianetta P, McIntyre PC. Hafnium oxide/germanium oxynitride gate stacks on germanium: Capacitance scaling and interface state density. Applied Physics Letters. 2009 May;94(18):3102.

[3] Chen JJ, Bojarezuk N, Shang H, Copel M, Hannon JB, Karasinski J, Preisler E, Banerjee SK, Guha S. Ultrathin Al 2 O 3 and HfO 2 gate dielectrics on surface-nitrided Ge. Electron Devices, IEEE Transactions on. 2004 Sep;51(9):1441-7.

[4] Chellappan RK, Gajula DR, McNeill D, Hughes G. High temperature thermal stability of the HfO 2/Ge (100) interface as a function of surface preparation studied by synchrotron radiation core level photoemission. Applied Surface Science. 2014 Feb 15;292:345-9.

[5] Chellappan RK, Gajula DR, McNeill D, Hughes G. Soft x-ray photoemission study of the thermal stability of the Al2O3/Ge (100) interface as a function of surface preparation. Journal of Applied Physics. 2013 Aug 28;114(8):084312..

[6] Sioncke S, Ceuppens J, Lin D, Nyns L, Delabie A, Struyf H, De Gendt S, Müller M, Beckhoff B, Caymax M. Atomic layer deposition of Al 2 O 3 on S-passivated Ge. Microelectronic Engineering. 2011 Jul 31;88(7):1553-6.

[7] Sioncke S, Lin HC, Nyns L, Brammertz G, Delabie A, Conard T, Franquet A, Rip J, Struyf H, De Gendt S, Müller M. S-passivation of the Ge gate stack: Tuning the gate stack properties by changing the atomic layer deposition oxidant precursor. Journal of Applied Physics. 2011 Oct 15;110(8):084907.

[8] Afanas' ev VV, Stesmans A, Delabie A, Bellenger F, Houssa M, Meuris M. Electronic structure of GeO2-passivated interfaces of (100) Ge with Al2O3 and HfO2. Applied Physics Letters. 2008 Jan;92(2):2109.

[9] Vickerman JC. Surface analysis: the principal techniques.

[10] Shirley DA. High-resolution X-ray photoemission spectrum of the valence bands of gold. Physical Review B. 1972 Jun 15;5(12):4709.

[11] Sasada T, Nakakita Y, Takenaka M, Takagi S. Surface orientation dependence of interface properties of GeO2/Ge metal-oxide-semiconductor structures fabricated by thermal oxidation. Journal of Applied Physics. 2009 Oct;106(7):3716.

[12] Delabie A, Alian A, Bellenger F, Caymax M, Conard T, Franquet A, Sioncke S, Van Elshocht S, Heyns MM, Meuris M. H2O-and O3-Based Atomic Layer Deposition of High-κ Dielectric Films on GeO2 Passivation Layers. Journal of The Electrochemical Society. 2009 Oct 1;156(10):G163-7.

[13] Renault O, Fourdrinier L, Martinez E, Clavelier L, Leroyer C, Barrett N, Crotti C. High-resolution photoelectron spectroscopy of Ge-based HfO2 gate stacks. Applied physics letters. 2007 Jan;90(5):2112.

[14] Van Elshocht S, Caymax M, Conard T, De Gendt S, Hoflijk I, Houssa M, De Jaeger B, Van Steenbergen J, Heyns M, Meuris M. Effect of hafnium germanate formation on the interface of HfO2/germanium metal oxide semiconductor devices. Applied physics letters. 2006 Apr;88(14):1904.

[15] Li H, Lin L, Robertson J. Identifying a suitable passivation route for Ge interfaces. Applied Physics Letters. 2012 Jul 30;101(5):052903.

[16] O'sullivan BJ, Hurley PK, Leveugle C, Das JH. Si (100)-SiO2 interface properties following rapid thermal processing. Journal of Applied Physics. 2001 Apr;89:3811-20..

[17] Hurley PK, Cherkaoui K, O’connor E, Lemme MC, Gottlob HD, Schmidt M, Hall S, Lu Y, Buiu O, Raeissi B, Piscator J. Interface Defects in HfO2, LaSiO x, and Gd2O3 High-k/Metal–Gate Structures on Silicon. Journal of The Electrochemical Society. 2008 Feb 1;155(2):G13-20.

[18] Kuzum D, Krishnamohan T, Pethe AJ, Okyay AK, Oshima Y, Sun Y, McVittie JP, Pianetta PA, McIntyre PC, Saraswat KC. Ge-interface engineering with ozone oxidation for low interface-state density. Electron Device Letters, IEEE. 2008 Apr;29(4):328-30.

[19] Grassman TJ, Bishop SR, Kummel AC. An atomic view of Fermi level pinning of Ge (100) by O 2. Surface Science. 2008 Jul 15;602(14):2373-81.

[20] Houssa M, Pourtois G, Caymax M, Meuris M, Heyns MM. Electronic properties of (100) Ge/Ge (Hf) O 2 interfaces: A first-principles study. Surface Science. 2008 Feb 15;602(4):L25-8.

[21] Mitrovic IZ, Althobaiti M, Weerakkody AD, Sedghi N, Hall S, Dhanak VR, Mather S, Chalker PR, Tsoutsou D, Dimoulas A, Henkel C. (Invited) Interface Engineering Routes for a Future CMOS Ge-Based Technology. ECS Transactions. 2014 Mar 24;61(2):73-88.

[22] Mather S, Sedghi N, Althobaiti M, Mitrovic IZ, Dhanak V, Chalker PR, Hall S. Low EOT GeO 2/Al 2 O 3/HfO 2 on Ge substrate using ultrathin Al deposition. Microelectronic Engineering. 2013 Sep 30;109:126-8.

Chapter 8

Electrical property and interfacial study of $Hf_xTi_{1-x}O_2$ high permittivity gate insulators deposited on germanium substrates

8.1 Introduction

Due to the lack of stable native oxide of germanium, it was difficult to fabricate a Ge MOSFET and a variety of dielectric materials were attempted. Among the various candidates, hafnium-based gate stacks such as HfO_2 [1, 2, 3, 4], HfON and $LaHfO_x$ were proved to be possible solutions to Ge MOS devices and transistors with relative good reliability and high performance were achieved [5, 6, 7]. However, the reported dielectric constants of hafnium-based gate stacks varied from 11.5 to 21, which limited the further scale into sub-nanometer regime [8, 9, 10, 11]. In order to overcome this problem, a number of trials were carried out to further increase the permittivity of dielectrics. One approach was to add a smaller amount of rare earth materials to the oxides to stabilize the crystal phase with higher relative dielectric constant, such as lanthanum doped zirconium oxide [12, 13]. The similar trials were performed on the hafnium oxide deposited on a silicon substrate. However, the increase of the dielectric constant was not significant [14, 15]. Another possible solution was to mix hafnium oxide with other dielectric materials with higher permittivity, such as titanium oxide (with k ~ 50-80). The high dielectric constant of the titanium oxide was benefited from the soft phonons of titanium. The increase of the overall dielectric constant of gate oxides after mixing HfO_2 and TiO_2 was achieved [16, 17]. Although, the addition of TiO_2 increased the dielectric constant of an HfO_2-based material, the small energy band gap of TiO_2, which would result in a large leakage current, was an issue to be considered [17]. Thus, the influence of different amount of the titanium oxide on the property of the HfO_2-based material was of great interest to be studied. In addition, the deterioration of the interface due to the oxidation source borne by the high-k materials was observed and the effective passivation of the germanium surface was still an open question [3]. In order to minimize deterioration of interface and suppress of the growth of unstable native oxide of germanium, a number of methods have been conceived to passivate the germanium surface, such as NH_3 and sulphur treatment [19, 20], or inserting an interfacial layer, such as aluminium oxide [21], between the high-k thin film and germanium substrate.

In this chapter, a 0.3 nm Al_2O_3 interfacial layer was deposited on the germanium substrate to passivate the surface. Then, the thin films with different content of the TiO_2 in HfO_2 were deposited by atomic layer deposition (ALD). The effect of TiO_2 content in hafnium oxide was explored in terms of physical and electrical properties. Furthermore, the interface quality and

chemical structure between the oxides and substrate was investigated. The results provided a reference for the properties and the performance of TiO_2-HfO_2 thin films, which would be presented and discussed in the chapter.

8.2 Experimental Section

Before the mix HfO_2 with TiO_2 to form $Ti_xHf_{1-x}O_2$, the growth rates of TiO_2 and HfO_2were tested individually. Titanium isopropoxide and methoxymethyl hafnium working at 40 °C and 100 °C, respectively, were used as the ALD precursors. Deionized water used as oxygen source and argon was employed as carrier gas in the experiment. All the deposition was performed at the substrate temperature of 300 °C. The sequence for ALD deposition was precursor pulse/purge/water pulse/purge. For both precursors, the precursor pulse duration of 3 seconds was followed by a purge time of 6 seconds. Water pulse time of 0.01 second was followed by 3 seconds purge time. The thickness of thin films with different ALD cycles was measured by an ellipsometer. The relationship between thin film thicknesses and corresponding ALD cycles were concluded in Fig. 8.1. The x- and y-axis represented the ALD cycles and thickness of thin films, respectively. From the slopes of the fitting straight lines, it was found that the deposition rates for TiO_2 and HfO_2 were approximately 0.203 Å/cycle and 0.166 Å/cycle, respectively. Based upon the growth rates, the cycle ratio of the titanium oxide to the hafnium oxide was evaluated to obtain the dielectric oxides with the ratio of TiO_2 to HfO_2 being 1:3 and 9:1 ($Ti_{0.25}Hf_{0.75}O_2$ and $Ti_{0.9}Hf_{0.1}O_2$), respectively, in terms of thickness. For example, for $Ti_{0.25}Hf_{0.75}O_2$, two TiO_2 cycles (0.4 Å) were followed by seven HfO_2 cycles (1.2 Å). The content of TiO_2, 25%, is equal to 0.4/(0.4+1.2) . According to the cycle ratio and deposition rates, the total cycles for each oxide were designed to produce the required thickness of the thin films. The p-type germanium wafers were used as the substrate of ALD $Ti_xHf_{1-x}O_2$ thin films. The Ge wafer was cleaned by ultrasonic in acetone ambient followed by O_2 plasma treatment. Then, the germanium oxide on the surface was removed by cyclic rinsing between deionized water (DI water) and diluted 2% HF. The clean wafers were transferred to the ALD chamber (Oxford Instruments OpAL^{TM}, UK) immediately to deposit an Al_2O_3 passivation layer (~0.3 nm) using trimethylaluminum (TMA) as precursor. Then, the TiO_2, $Ti_{0.9}Hf_{0.1}O_2$, $Ti_{0.25}Hf_{0.75}O_2$ and HfO_2 thin films with nominal thickness were deposited, respectively, afterwards. After the completion of deposition, X-ray Photoelectron Spectroscopy (XPS) was performed to analyze the interface quality and chemical

structure of the Ge/high-*k* stack. Grazing Incident X-ray diffraction (GIXRD) was carried out using Bruker diffractometer (Bruker, Germany) with $Cu_{K\alpha}$ radiation source (40 kV, 40 mA), spanning a 2θ range from 20° to 50° at a scan rate of 1°/second for all measurements. Surface morphology and roughness of the thin films was analyzed using atomic force microscope (AFM) (Bruker, Germany). The thickness of each thin film was measured by an ELLIP-SR-1 ellipsometer with the incident angle of 65°and wavelength from 300 nm to 900 nm with the step of 20 nm. The electrode contacts with a diameter of 0.3 mm and thickness of 350 nm were deposited by E-beam evaporation (TEMD-600, China). The backside was deposited with aluminium as well to form ohmic contact. Agilent 4284A precision LCR meter and Keithley 487 picoammeter were employed to investigate the electrical property of the samples. All the electrical measurements were performed in the dark at room temperature with the Faraday Cage surrounding the prober station.

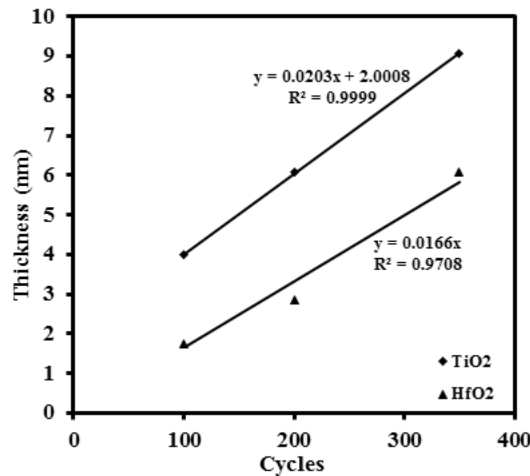

Fig. 8.1 The thin film thicknesses versus ALD cycles for titanium oxide and hafnium oxide, respectively. The slopes of the two fitting straight lines (y=0.0203x+2.0008 and y=0.0166x) represent the corresponding deposition rates and R^2 is the coefficient of determination. The deposition rates for TiO_2 and HfO_2 are approximately 0.203 Å/cycle and 0.166 Å/cycle, respectively.

8.3 Results and Discussion

XPS was used to characterize the quality of the interface and thin films in the stacks. Firstly, the XPS was performed on the 5 nm and 10 nm HfO_2 thin films to find out the chemical structure of the HfO_2 samples in depth direction. XPS is a surface sensitive technique so the interface was probed by using a 5 nm nominal thickness film on the germanium substrate. As shown in Fig. 8.2 (a) and (b), the Hf 4*f* line-shape is typically composed of $4f_{5/2}$ and $4f_{7/2}$ spin orbit doublet [22]. With respect to the Hf 4*f* peak positions, there is a clear difference between the two thin films with different thickness. The sample with thickness of 10 nm has the lower binding energy (BE) peak at the position of 16.5 eV, which is tentatively assigned to stoichiometric HfO_2. For the sample with thickness of 5 nm, the binding energy of the peak is centered at 17.3 eV, a difference of 0.8 eV with respect to the 10 nm one. This shift is indicative of the greater interaction between the HfO_2 and Ge and suggests stoichiometric and chemical changes at the interface. This is in accord with previous research, which has reported that the binding energy of Hf 4*f* peak in $HfSi_xO_y$ was 1 eV higher than that from HfO_2 with binding energy in the range of 16.5–17 eV [23, 24]. Similar results have also been found for the Ge MOS device, which stated that there existed about 0.5 eV shift of binding energy for Hf 4*f* peak from $HfGeO_x$ compared with that from HfO_2 [25, 26]. We can thus tentatively assign the shift in the Hf4f binding energy to the formation of a germanate $HfGeO_x$. In contrast, the XPS results in Fig. 8.2(c, d) for TiO_2 samples in this experiment show that the binding energy of the Ti 3*p* peaks for the 5 nm and 10 nm thickness samples are centered at the same position at 36.9 eV, suggesting that no chemical structure change occurs for the TiO_2 samples in depth direction. Based upon the above analysis, it is clear that HfO_2 interacts strongly with the Ge atoms at the interface without an effective passivation of the substrate. Formation of $HfGeO_x$ at the interface deteriorates the interface and possibly increases the leakage current in the stack [26].

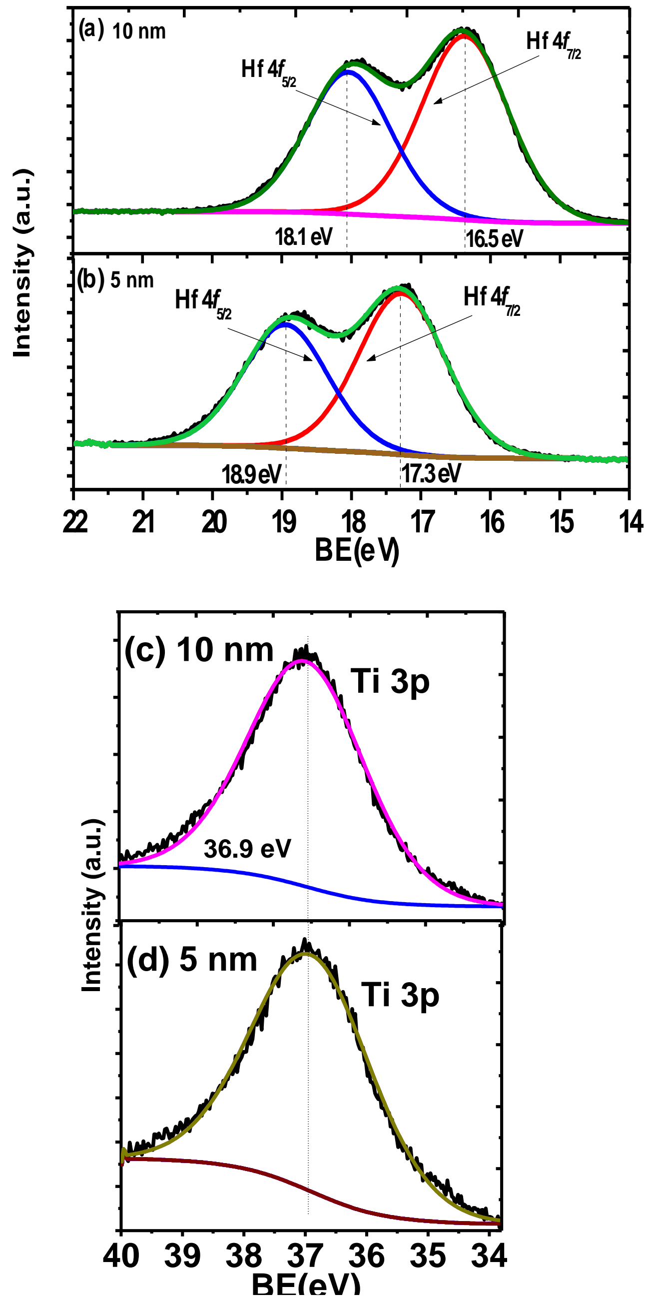

Fig. 8.2 The XPS line shape of (a, b) Hf4f and (c, d) Ti3p from 10nm and 5 nm thick films of HfO_2 and TiO_2, respectively, on Ge

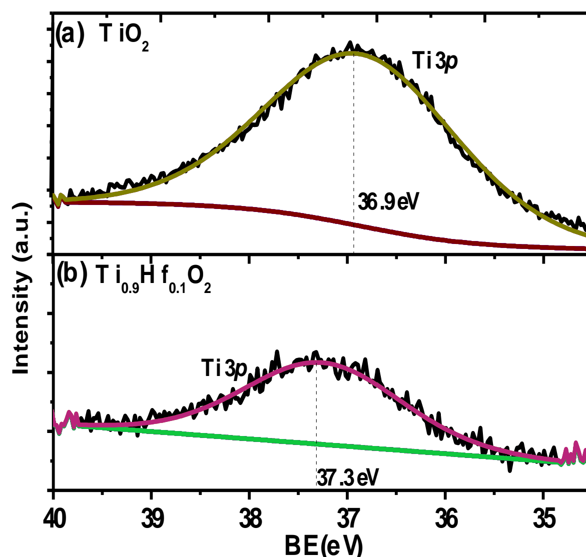

Fig. 8.3 The Ti 3*p* spectra from (a) TiO_2 and (b) $Ti_{0.9}Hf_{0.1}O_2$ thin films with a thickness of 5 nm.

Fig. 8.3(b) compares the Ti3p spectrum from the $Ti_{0.9}Hf_{0.1}O_2$ sample with the Ti3p from a pure TiO_2 film on germanium while Fig. 8.4 shows the Hf $4f_{7/2}$spectra from the same 5 nm thick $Ti_{0.9}Hf_{0.1}O_2$ sample and compares it to Hf $4f_{7/2}$ from a pure HfO2 film. It is clear that the Hf $4f_{7/2}$ binding energy from $Ti_{0.9}Hf_{0.1}O_2$, 17 eV, has a small difference compared with that from pure HfO_2 at 17.3 eV ($Ti_{0.25}Hf_{0.75}O_2$ has the same Hf $4f_{7/2}$ binding energy as $Ti_{0.9}Hf_{0.1}O_2$, not shown here). In addition, Fig. 8.3 (a) and (b) shows that there is also a difference of 0.4 eV to higher binding energy of Ti 3*p* spectra between TiO_2 (36.9 eV) and $Ti_{0.9}Hf_{0.1}O_2$ (37.3 eV). For the $Ti_{0.25}Hf_{0.75}O_2$ sample, the Ti3p spectrum was found shifted to higher binding energy by about 0.2 eV. The shift of the Hf $4f_{7/2}$ peak in the $Ti_xHf_{1-x}O_2$ samples to lower binding energy and of Ti3p to higher binding energy suggests a charge transfer from the Ti to Hf as a result of chemical mixing between TiO_2 and HfO_2.

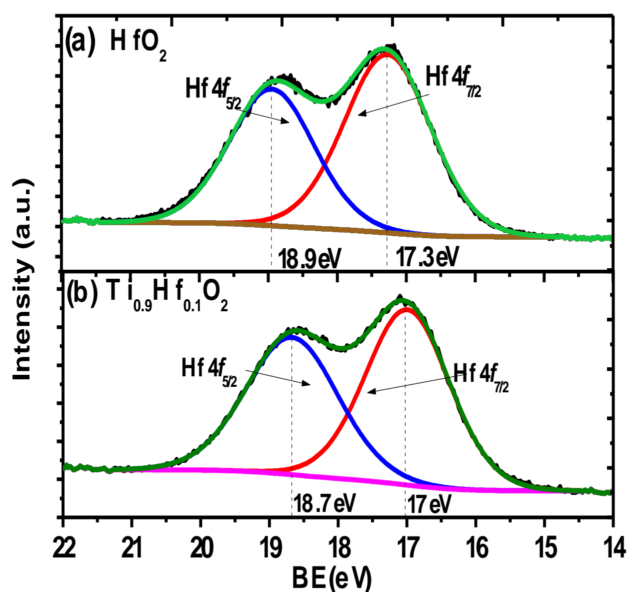

Fig. 8.4 The Hf 4*f* spectra from 5 nm thick films of (a) HfO_2 and (b) $Ti_{0.9}Hf_{0.1}O_2$ on Ge.

	Ge^{+2}	**Ge^{+3}**	**Ge^{+4}**
TiO_2 on Ge	**0.06**	**0.12**	**-**
$Ti_{0.9}Hf_{0.1}O_2$	**0.06**	**0.24**	**0.14**
$Ti_{0.25}Hf_{0.75}O_2$	**0.17**	**0.24**	**0.41**
HfO_2 on Ge	**0.13**	**0.45**	**0.75**

Table 8.1 Compositions extracted from the line fits shown in fig. 4, relative to the bulk substrate Ge^0 peak for the four samples.

In addition, from the analysis of Ge 3*d* spectra from the four samples with thickness of 5 nm, shown in Fig. 8.5 more information about the Ge surface can be deduced. The corresponding O1s spectra from the four samples are shown in Fig. 8.6. The peaks corresponding to Ge from elemental Ge and GeO_x are labeled in the Fig 8.5. The presence of Ge^{+2}, Ge^{+3} and Ge^{+4} is due to oxidation of the germanium substrate at the interfacial region as well as possible germanate formation. Table 8.1 shows the compositions extracted from the line fits, relative to the bulk substrate Ge^0 peak, of the various components at the interface for the four samples. It is clear that the oxidation is much less in the samples with TiO_2 (Fig. 8.5 (a)) compared with the other

samples, while oxidation of the substrate in the case of HfO_2 is much greater (Fig. 8.5 (d)). The fitting of the spectra shows an absence of Ge^{+4} in the TiO_2 sample while an incremental increase of the GeO_x intensity, especially Ge^{+4} is observed with increasing HfO_2 content. This suggests that increasing the amount of HfO_2 in the dielectric films provide an oxidation source at the interface [27]. This has also been supported by other research, which stated that Ge atoms were oxidized by the oxygen atoms provided by the HfO_2 layer [3]. Furthermore, the Hf $4f_{7/2}$ binding energy difference for the HfO_2 samples with different thicknesses, shown in Figs. 8.2 (a) and (b) and discussed above, also supports this finding. Therefore, the HfO_2 is considered to be a factor in the oxidation and deteriorating effect on the interface.

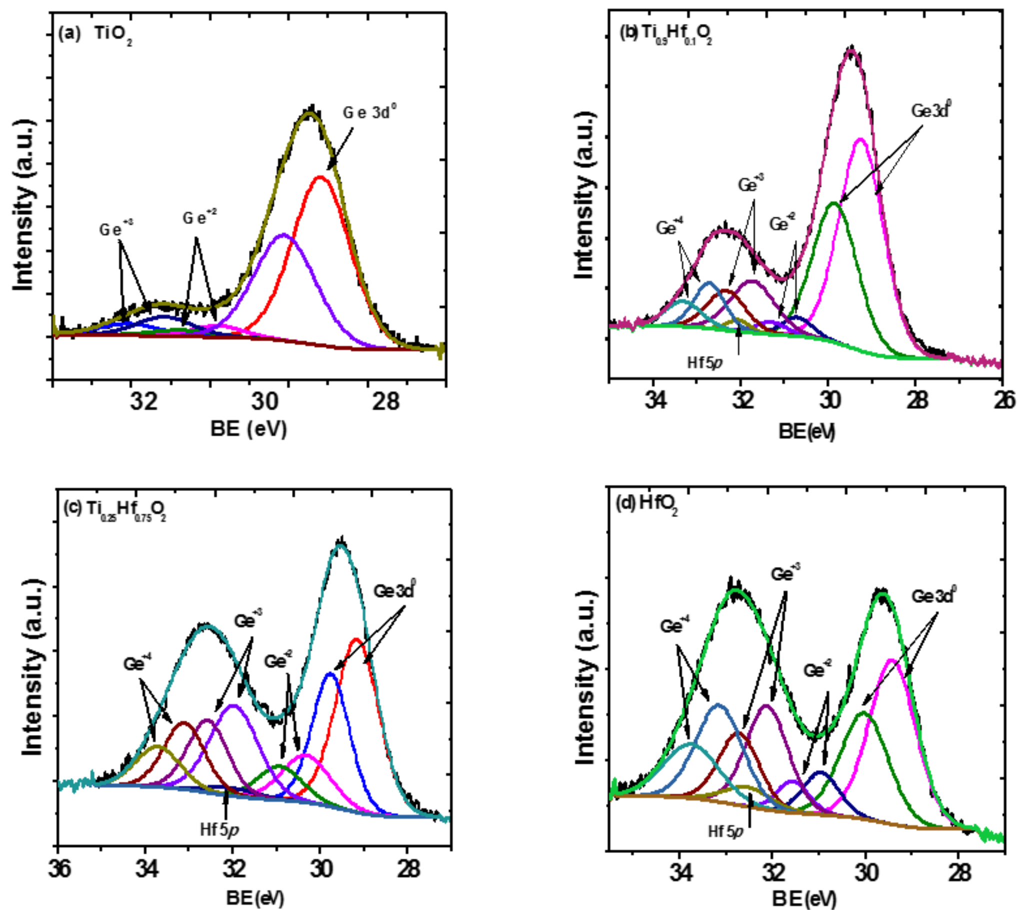

Fig. 8.5 Ge3*d* spectra from 5 nm films of (a) TiO_2, (b) $Ti_{0.9}Hf_{0.1}O_2$, (c) $Ti_{0.25}Hf_{0.75}O_2$, and (d) HfO_2.

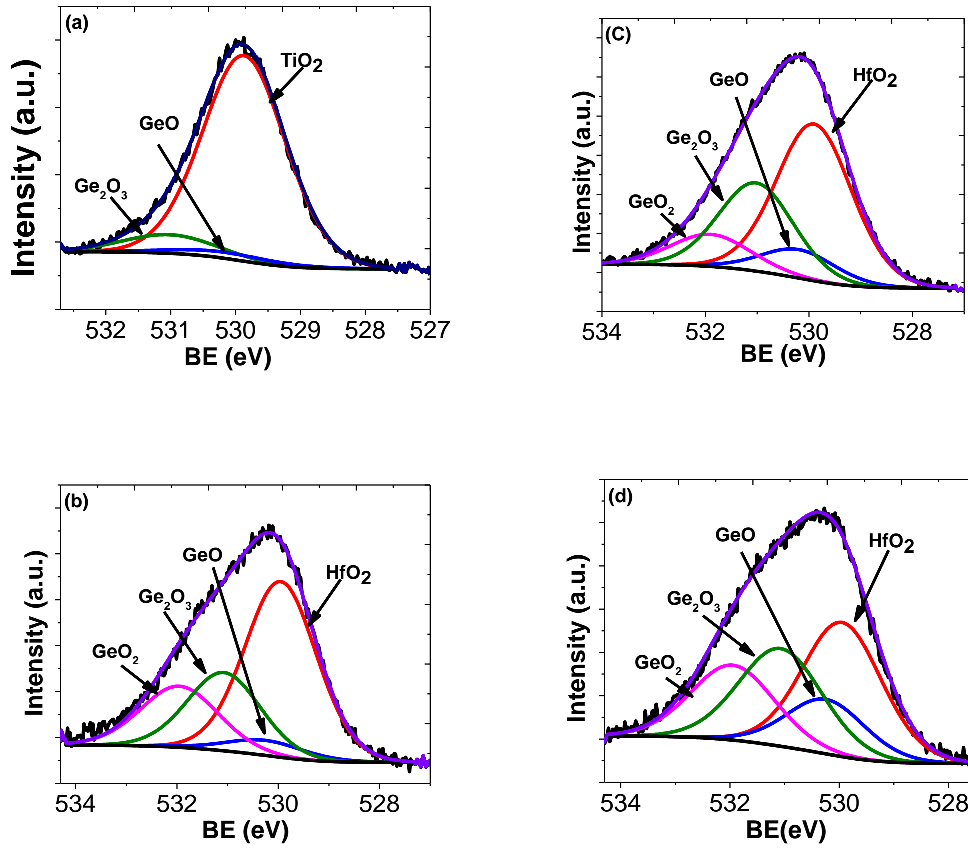

Fig. 8.6 O 1s spectra from 5 nm films of (a) TiO_2 , (b) $Ti_{0.9}Hf_{0.1}O_{2,}$ (c) $Ti_{0.25}Hf_{0.75}O_{2,}$ and (d) $HfO_{2.}$

AFM was used to examine the surface roughness of the samples and the results for a scan area of 100 nm ×100 nm are presented in Fig. 8.7. The surface roughness of the samples is quantitatively determined by the root-mean-squared roughness (R_{rms}), defined as

$$R_{rms} = \sqrt{\frac{\sum_{n=1}^{N}(z_n - \bar{z})^2}{N - 1}} \qquad (1)$$

where z_n is the measured height, $\bar{z}$ is the average height of the sample and N is the number of measurements.

As can be seen, all the samples exhibit good surface morphology with a roughness R_{rms} of 0.325 nm, 0.431 nm, 0.425 nm and 0.202 nm for TiO_2, $Ti_{0.9}Hf_{0.1}O_2$, $Ti_{0.25}Hf_{0.75}O_2$ and HfO_2 respectively. The relatively large roughness measured for the $Ti_{0.25}Hf_{0.75}O_2$ and $Ti_{0.9}Hf_{0.1}O_2$ samples is possibly due to reaction of TiO_2 and HfO_2.

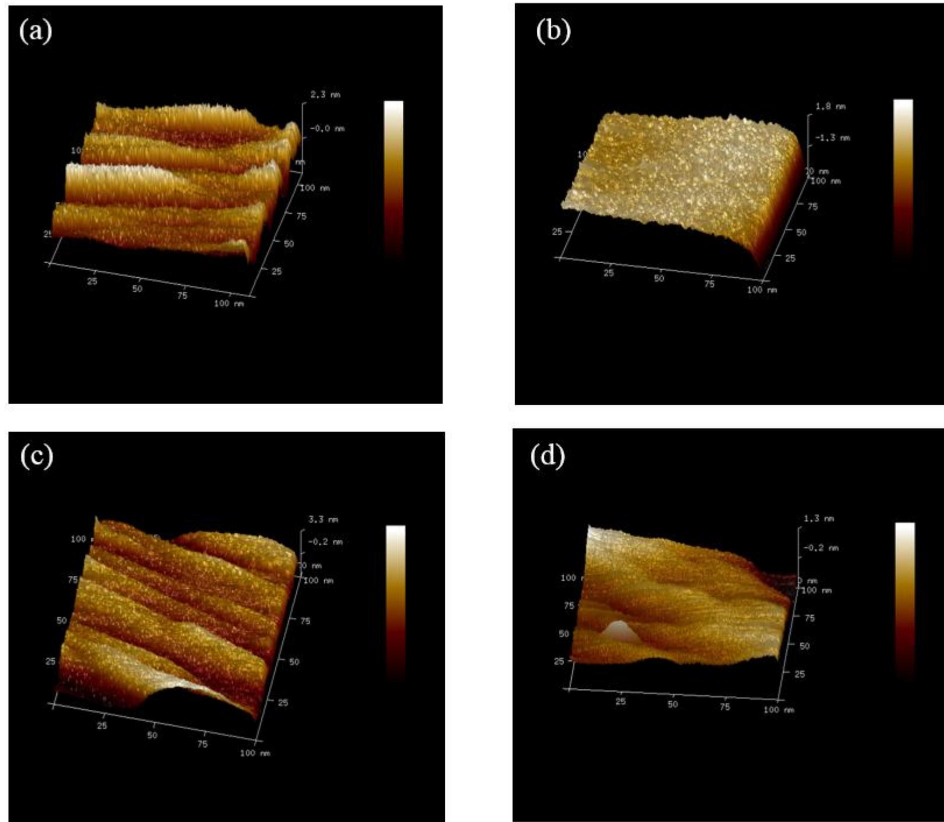

Fig. 8.7 AFM images of the samples (a) TiO2, (b) Ti0.9Hf0.1O2, (c) Ti0.25Hf0.75O2 and (d) HfO2.

Fig. 8.8 shows the XRD patterns for the four samples with different composition of TiO_2 and HfO_2. The measurement was performed on the samples with a nominal thickness of 10 nm (The actual thickness was in the range 8 to 11 nm determined by ellipsometer). For the four samples, no noticeable diffraction peaks are observed excepted for the one coming from the substrate centered at around 31.5 degree. This behavior indicates that all the thin films remained as amorphous under these deposition conditions, although we note that the samples were only 10 nm in thickness and the sensitivity of the instrument maybe a limiting factor.

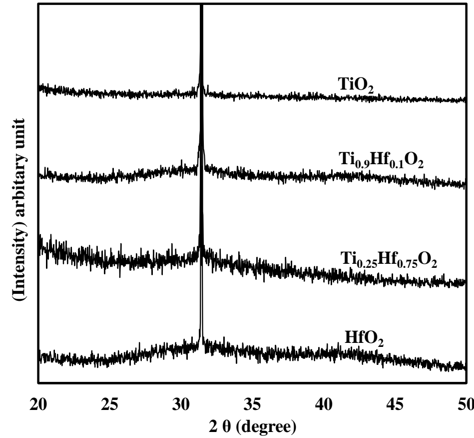

Fig. 8.8 XRD patterns for the 10 nm HfO_2, $Ti_{0.25}Hf_{0.75}O_2$, $Ti_{0.9}Hf_{0.1}O_2$ and TiO_2 thin films deposited on germanium substrate.

The Capacitance-Voltage (CV) curves were obtained by sweeping the gate voltage from -1 V to 0.5V in both directions (ramp up and ramp down) at the frequency of 1 MHz using Agilent 4284A LCR meter. Due to an unacceptable distortion of the CV characteristics caused by a large leakage current for the TiO_2 sample, reported below, only the CV curves from HfO_2, $Ti_{0.25}Hf_{0.75}O_2$ and $Ti_{0.9}Hf_{0.1}O_2$ samples are presented in Fig. 8.9. The high frequency CV measurements on the three as-grown thin films show that the samples have low trap densities because there is almost no hysteresis between ramp up and ramp down of the CV curves. The vertical change in the CV measurements observed for all the samples is characteristic of dielectric relaxation [28]. Regarding the CV characteristics of the $Ti_{0.25}Hf_{0.75}O_2$ sample, it is noted that saturation in the accumulation region is not obtained, regardless of the bias voltage. This behavior is attributed to the large leakage current for this sample, which is possibly partially related to the deterioration of the interface as discussed above in the section for XPS analysis. Further comments regarding the leakage current are made in the following section.

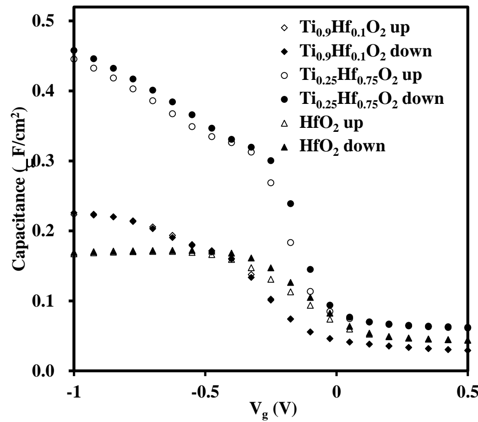

Fig. 8.9 CV characteristics for the 5 nm thin films of $Ti_{0.9}Hf_{0.1}O_2$, $Ti_{0.25}Hf_{0.75}O_2$ and HfO_2.

Fig. 8.10 illustrates the relationship between gate leakage current density (J_g) and bias voltage (V_g) of the samples. The maximum current limit on our instrument was set at 2 mA. From observation of Fig. 8.10, it is apparent that the titanium oxide has the highest leakage current level followed by hafnium oxide and $Ti_{0.25}Hf_{0.75}O_2$ thin films, both with similar leakage current levels. The $Ti_{0.9}Hf_{0.1}O_2$ sample has the lowest leakage current, with less than 1 mA/cm^2 at the bias voltage of 0.5 V. The large leakage current for the TiO_2 sample is attributed to the small band gap of TiO_2 as shown in Fig. 8.10 (a) and discussed further below. For HfO_2 and $Ti_{0.25}Hf_{0.75}O_2$, it is clear that the leakage current increases with increasing amount of HfO_2. Previous research has also reported a large leakage current caused by the formation of $HfGeO_x$ at the interface between HfO_2 and Ge, and the leakage current improved if a germanium nitride barrier layer was first introduced, preventing the formation of $HfGeO_x$ [3]. High leakage current behavior, therefore, is probably due to the deterioration of the interfacial layer caused by the interaction of HfO_2 and Ge, which is consistent with the results shown in Fig. 8.5. Thus, the increase of leakage current clearly correlates with the hafnium oxide rich samples. For the TiO_2 doped samples, the TiO_2 would react with HfO_2 to form $HfTiO_x$, consuming the HfO_2 which would otherwise have reacted with the Ge at the interface. It is also possible that other mechanisms may also exist to suppress the leakage current as has been observed for titanium doped tantalum oxide. Titanium doping was found to suppress the oxygen vacancies in tantalum oxide capacitors, which resulted in a significant reduction in leakage current [29]. For HfO_2

capacitors, there are also a considerable number of oxygen vacancies [30-33], which are possibly suppressed when titanium is doped in the HfO_2.

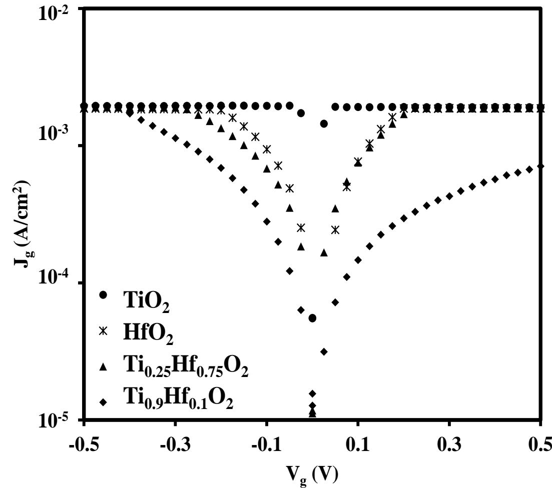

Fig. 8.10 Gate leakage current density (J_g) versus gate voltage (V_g) for 5 nm films of HfO_2, $Ti_{0.25}Hf_{0.75}O_2$, $Ti_{0.9}Hf_{0.1}O_2$ and TiO_2.

Although the titanium incorporation seems to suppress the leakage current, the current is still relatively large. The energy band diagram [18, 19] in Fig. 8.11 attempts to provide a possible explanation in conjunction with the XPS results discussed above. From the energy band diagram in Fig. 8.11 (a), titanium oxide has a relatively small band gap (3.2 eV) and the conduction band minimum is at 4.21 eV, while the band gap and conduction band minimum for germanium are 0.66 eV and at 4.13 eV, respectively. The thin aluminum oxide with the thickness of about 0.3 nm is used to passivate the germanium surface and it has almost no contribution to suppressing the leakage current. If a voltage was applied at the gate on the stack TiO_2/Al_2O_3, dramatic leakage current should be induced from considering the energy band diagram in Fig. 8.11 (a). For the energy band diagram of hafnium oxide shown in Fig. 8.11 (b), the band gap is wider and the conduction band minimum is higher than that of TiO_2. Thus, the HfO_2 sample has a higher potential barrier across the oxide. Therefore, the leakage current of HfO_2 is 5 times smaller than that of TiO_2 regardless of the deterioration of the interface caused by the oxidation of the substrate at the interface. When TiO_2 is doped in HfO_2, the reaction of TiO_2 and HfO_2 should adjust the energy band diagram as shown in Fig. 8.10 (c) and the leakage current should be the range of between that of TiO_2 and HfO_2 from the point view of energy band diagram. However,

as mentioned above, HfO_2 is considered to be the oxidation source and contributing to the interface deterioration, which enhances the leakage current for the HfO_2 rich samples. Fortunately, the formation of $HfTiO_x$ inTiO_2 doped HfO_2 reduces the reaction between HfO_2 and germanium and suppresses the deterioration of interface, which results in the significant reduction of leakage current. Therefore, in our case, the $Ti_{0.25}Hf_{0.75}O_2$ dielectric sample has almost the same leakage current as HfO_2 sample while the $Ti_{0.9}Hf_{0.1}O_2$ sample with much less HfO_2 has the smallest leakage current among them.

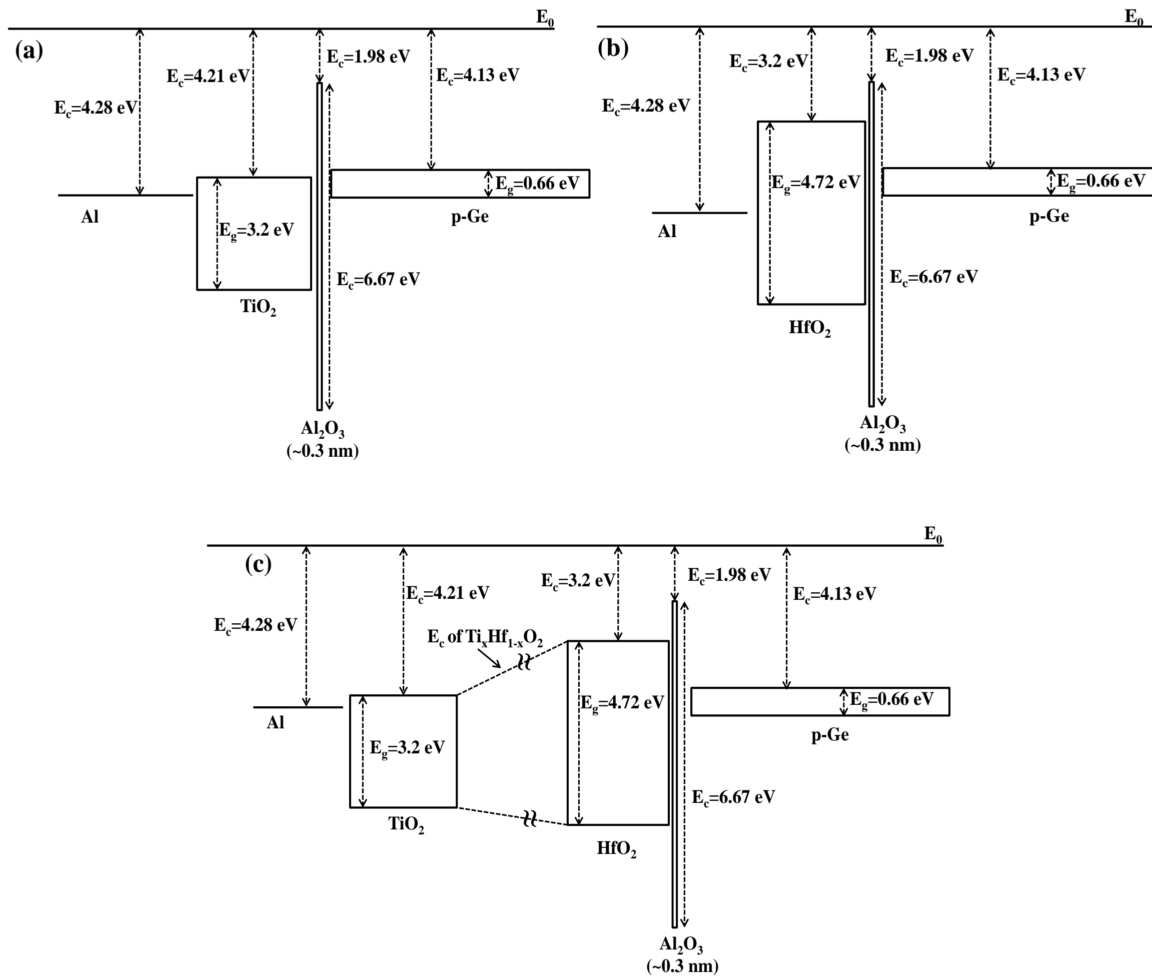

Fig. 8.11 Energy band diagrams for (a) titanium oxide, (b) hafnium oxide and (c) titanium doped hafnium oxide.

8.4 Conclusion

Hafnium titanate oxide thin films, $Ti_xHf_{1-x}O_2$, with a titanium content of x = 0, x = 0.25, x = 0.9 and x = 1 were deposited on germanium substrate. XPS was employed to analyze the interface quality and chemical structure. It showed that the HfO_2 would react with germanium at the interfacial region, which deteriorated the interface quality and enhanced the leakage current for the samples. The surface roughness was analyzed by atomic force microscope and all the samples exhibited relative good surface morphology with the roughness RMS of 0.202 nm, 0.425 nm, 0.431 nm and 0.325 nm respectively for HfO_2, $Ti_{0.25}Hf_{0.75}O_2$, $Ti_{0.9}Hf_{0.1}O_2$ and TiO_2, respectively. XRD analysis found that the four samples remained as amorphous at this deposition condition. The electrical characterization yielded that the samples had low trap density because there was almost no hysteresis between ramp up and ramp down of the CV curves. The relatively large leakage current was observed, with the lowest leakage current of about 1 mA/cm^2 at the bias of 0.5 V for $Ti_{0.9}Hf_{0.1}O_2$ sample among the four samples. The large leakage current was probably attributed to the deterioration of the interface caused by the oxidation source borne by HfO_2 and the small band gap of the dielectric materials.

8.5 References

[1] Heyns M, Bellenger F, Brammertz G, Caymax M, De Gendt S, De Jaeger B, Delabie A, Eneman G, Groeseneken G, Houssa M, Leonelli D. High mobility channel materials and novel devices for scaling of nanoelectronics beyond the Si roadmap. InMRS Proceedings 2009 Jan 1 (Vol. 1194, pp. 1194-A07). Cambridge University Press.

[2] Saraswat K, Chui CO, Krishnamohan T, Kim D, Nayfeh A, Pethe A. High performance germanium MOSFETs. Materials Science and Engineering: B. 2006 Dec 15;135(3):242-9.

[3] Kamata Y. High-k/Ge MOSFETs for future nanoelectronics. Materials today. 2008 Feb 29;11(1):30-8.

[4] Shang H, Okorn-Schmidt H, Chan KK, Copel M, Ott J, Kozlowski PM, Steen SE, Cordes SA, Wong HS, Jones EC, Haensch WE. High mobility p-channel germanium MOSFETs with a thin Ge oxynitride gate dielectric. InElectron Devices Meeting, 2002. IEDM'02. International 2002 Dec 8 (pp. 441-444). IEEE.

[5] Goley PS, Hudait MK. Germanium based field-effect transistors: challenges and opportunities. Materials. 2014 Mar 19;7(3):2301-39.

[6] Wu D, Lindgren AC, Persson S, Sjoblom G, von Haartman M, Seger J, Hellström PE, Olsson J, Blom HO, Zhang SL, Ostling M. A novel strained Si/sub 0.7/Ge/sub 0.3/surface-channel pMOSFET with an ALD TiN/Al/sub 2/O/sub 3//HfAlO/sub x//Al/sub 2/O 3 gate stack. Electron Device Letters, IEEE. 2003 Mar;24(3):171-3.

[7] Houssa M, De Jaeger B, Delabie A, Van Elshocht S, Afanas’ev VV, Autran JL, Stesmans A, Meuris M, Heyns MM. Electrical characteristics of Ge/GeO x (N)/HfO 2 gate stacks. Journal of non-crystalline solids. 2005 Jul 15;351(21):1902-5.

[8] Zhao Y. Design of higher-k and more stable rare earth oxides as gate dielectrics for advanced CMOS devices. Materials. 2012 Aug 17;5(8):1413-38.

[9] Wu N, Zhang QC, Zhu CX, Chan DS, Li MF, Balasubramanian N, Chin A, Kwong DL. Alternative surface passivation on germanium for metal-oxide-semiconductor applications with high-k gate dielectric. Applied physics letters. 2004 Nov 1;85(18):4127-9.

[10] Chen JJ, Bojarezuk N, Shang H, Copel M, Hannon JB, Karasinski J, Preisler E, Banerjee SK, Guha S. Ultrathin Al 2 O 3 and HfO 2 gate dielectrics on surface-nitrided Ge. Electron Devices, IEEE Transactions on. 2004 Sep;51(9):1441-7.

[11] Li XF, Liu XJ, Zhang WQ, Fu YY, Li AD, Li H, Wu D. Comparison of the interfacial and electrical properties of HfAlO films on Ge with S and GeO2 passivation. Applied Physics Letters. 2011 Apr;98(16):2903.

[12] Zhao CZ, Taylor S, Werner M, Chalker PR, Murray RT, Gaskell JM, Jones AC. Dielectric relaxation of lanthanum doped zirconium oxide. Journal of Applied Physics. 2009 Feb;105(4):4102.

[13] Lu Q, Zhao C, Mu Y, Zhao CZ, Taylor S, Chalker PR. Hysteresis in lanthanide zirconium oxides observed using a pulse CV technique and including the effect of high temperature annealing. Materials. 2015 Jul 29;8(8):4829-42.

[14] Huang LY, Li AD, Zhang WQ, Li H, Xia YD, Wu D. Fabrication and characterization of La-doped HfO 2 gate dielectrics by metal-organic chemical vapor deposition. Applied Surface Science. 2010 Feb 1;256(8):2496-9.

[15] Wang T, Ekerdt JG. Atomic layer deposition of lanthanum stabilized amorphous hafnium oxide thin films. Chemistry of Materials. 2009 Jun 29;21(14):3096-101.

[16] Chen F, Bin X, Hella C, Shi X, Gladfelter WL, Campbell SA. A study of mixtures of HfO 2 and TiO 2 as high-k gate dielectrics. Microelectronic Engineering. 2004 Apr 30;72(1):263-6.

[17] Werner M, King PJ, Hindley S, Romani S, Mather S, Chalker PR, Williams PA, van den Berg JA. Atomic layer deposition of Ti-HfO2 dielectrics. Journal of Vacuum Science & Technology A. 2013 Jan 1;31(1):01A102.

[18] Xu Y, Schoonen MA. The absolute energy positions of conduction and valence bands of selected semiconducting minerals. American Mineralogist. 2000 Apr 1;85(4):543-56.

[19] Van Elshocht S, Brijs B, Caymax M, Conard T, Chiarella T, De Gendt S, De Jaeger B, Kubicek S, Meuris M, Onsia B, Richard O. Deposition of HfO2 on germanium and the impact of surface pretreatments. Applied physics letters. 2004 Oct;85:3824.

[20] Xie R, Zhu C. Effects of sulfur passivation on germanium MOS capacitors with HfON gate dielectric. Electron Device Letters, IEEE. 2007 Nov;28(11):976-9.

[21] Kato R, Kyogoku S, Sakashita M, Kondo H, Zaima S. Effects of Atomic Layer Deposition-Al2O3 Interface Layers on Interfacial Properties of Ge Metal–Oxide–Semiconductor Capacitors. Japanese Journal of Applied Physics. 2009 May 1;48(5S1):05DA04.

[22] Sahin D, Yildiz I, Gencer AI, Aygun G, Slaoui A, Turan R. Evolution of SiO 2/Ge/HfO 2 (Ge) multilayer structure during high temperature annealing. Thin Solid Films. 2010 Feb

26;518(9):2365-9.

[23] Cho MH, Roh YS, Whang CN, Jeong K, Nahm SW, Ko DH, Lee JH, Lee NI, Fujihara K. Thermal stability and structural characteristics of HfO2 films on Si (100) grown by atomic-layer deposition. Applied physics letters. 2002 Jul;81:472-4.

[24] Opila RL, Wilk GD, Alam MA, Van Dover RB, Busch BW. Photoemission study of Zr-and Hf-silicates for use as high-κ oxides: Role of second nearest neighbors and interface charge. Applied physics letters. 2002 Sep 2;81(10):1788-90.

[25] Van Elshocht S, Caymax M, Conard T, De Gendt S, Hoflijk I, Houssa M, De Jaeger B, Van Steenbergen J, Heyns M, Meuris M. Effect of hafnium germanate formation on the interface of HfO2/germanium metal oxide semiconductor devices. Applied physics letters. 2006 Apr;88(14):1904.

[26] Xie Q, Deng S, Schaekers M, Lin D, Caymax M, Delabie A, Qu XP, Jiang YL, Deduytsche D, Detavernier C. Germanium surface passivation and atomic layer deposition of high-k dielectrics—a tutorial review on Ge-based MOS capacitors. Semiconductor Science and Technology. 2012 Jul 11;27(7):074012.

[27] Curreem KK, Lee PF, Wong KS, Dai J, Zhou MJ, Wang J, Li Q. Comparison of interfacial and electrical characteristics of $HfO_2$and HfAlO high-k dielectrics on compressively strained Si [sub 1− x] Ge [sub x]. Applied physics letters. 2006 May 1;88(18):1-3.

[28] Tao J, Zhao CZ, Zhao C, Taechakumput P, Werner M, Taylor S, Chalker PR. Extrinsic and intrinsic frequency dispersion of high-k materials in capacitance-voltage measurements. Materials. 2012 Jun 1;5(6):1005-32.

[29] Lau WS, Tan TS, Babu P, Sandler NP. Mechanism of leakage current reduction of tantalum oxide capacitors by titanium doping. Applied physics letters. 2007 Mar 12;90(11):112903.

[30] Chen YY. Electrical Characteristics of the Uniaxial-Strained nMOSFET with a Fluorinated HfO2/SiON Gate Stack. Materials. 2014 Mar 20;7(3):2370-81.

[31] Ji M, Wang L, Du J. Preparation and characterization of Gd2O3-doped HfO2 high-k gate dielectric thin films by RF sputtering. InJournal of Physics: Conference Series 2009 Mar 1 (Vol. 152, No. 1, p. 012005). IOP Publishing.

[32] Guha S, Narayanan V. Oxygen vacancies in high dielectric constant oxide-semiconductor films. Physical review letters. 2007 May 8;98(19):196101..

[33] Miyata N. Study of direct-contact HfO2/Si interfaces. Materials. 2012 Mar 19;5(3):512-27.

Chapter 9

Band Alignment of Ta_2O_5 on Sulphur Passivated Germanium by X-ray Photoelectron Spectroscopy

9.1 Introduction

Among the major issues related to Ge channels is the quality of interfacial layer. As a low quality interfacial layer leads to substantial current degradation, a higher quality interfacial layer is highly desirable [1, 2]. In order to obtain a high quality interfacial layers of Ge, a variety of materials and processes have been employed, including high-k dielectrics, different materials for metal gates, methods of deposition and post deposition annealing procedures, and lastly but necessarily the passivation of the Ge surface [3,4]. Several reports in literature revealed that the above steps significantly affect the performance of metal-oxide-semiconductor (MOS) [5]. Ta_2O_5 on Ge-rich silicon has been introduced as an excellent alternative to the thin layers of high-K material [6]. For the amorphous films of Ta_2O_5, about 4.5 eV band gap was calculated, whereas a 1.5 eV of conduction band offset for Ta_2O_5. The dielectric constant of Ta_2O_5 is about 25, which is quite enough to achieve a lower EOT (effective oxide thickness) [6]. In this chapter, we have characterised high-k gate dielectric films of Ta_2O_5 deposited on Ge substrates, which were either untreated or sulphur-passivated prior to deposition of the films. X-ray photoelectron spectroscopy (XPS) was used to analyze the chemical states and composition of the thin films of Ta_2O_5, and determine the valance band offsets VBO with respect to Ge.

9.2 Experimental

The Ta_2O_5 films were deposited on p-type Ge (100) wafers. Both, S-passivated and unpassivated surfaces were used. In sulphur passivation, the few monolayers of S are incorporated on the surface of Ge, with the aim of reducing dangling bonds. In our work, this was done by dipping the as-received Ge wafers in a 20% ammonium sulphide solution in water for 10 minutes and then dried under a nitrogen flow. The substrates were then immediately transferred into the ALD reactor chamber.Ta_2O_5 films were deposited at 250^oC on the substrates by thermal ALD using an Oxford Instruments OpAL reactor. During each step of the ALD cycle, the overall gas flow was maintained at 200 ccm to keep the pressure constant at approximately 200 mTorr. Pentakis(dimethylamino)tantalum (PDMAT, supplied by SAFC-Hitech) was dosed into the reactor as a tantalum source using a conventional heated bubbler held at 75^oC with 100sccm of argon (BOC zero grade 99.998%) bubbled through the precursor. Water vapour was used as a

co-reactant and was delivered by vapour draw from a room temperature source. Between 40 and 260 ALD cycles were used to grow Ta_2O_5 of thicknesses from 3 nm to 20 nm. XPS measurements were carried out in a UHV system consisting of Al Kα X-ray (1486.6eV) source and a PSP Vacuum systems 5-channel HSA electron energy analyser. The C1s peak in the spectra at 284.6 eV, due to impurity carbon in the samples, was used to correct for any charging effects during measurements. The thickness of the Ta_2O_5 films was obtained by using spectroscopic ellipsometry.

9.3 Results and Discussion

The Kraut method [7] was used for the estimation of valence band offset (VBO) for Ta_2O_5 on Ge with and without Sulfur passivation, using $Ta4f_{7/2}$ and Ge3d core levels as reference. The Ge3d from the clean substrate and $Ta4f_{7/2}$ from the thick films of Ta_2O_5 were used to determine the difference between the energy of the core levels and the analogous valence band maxima (VBM). Finally, by measuring the difference between thick and thinTa_2O_5/Ge, the valence band offset was determined by using the following equation:

$$VBO = [E_{Ge3d} - E_{Ta4f}]_{Ta2O5/Ge} + ([E_{Ge3d} - E_{VGe}]_{Ge} - [E_{Ta4f} - E_{VTa2O5}]_{Ta2O5}) \quad (9.1)$$

where, the first term is the difference in energy between the Ge3d and Ta4f levels at the interface, the second term is the difference between the Ge3d and the VBM of the substrate, and the final term is the difference between Ta4f and VBM of a thick film of Ta_2O_5.

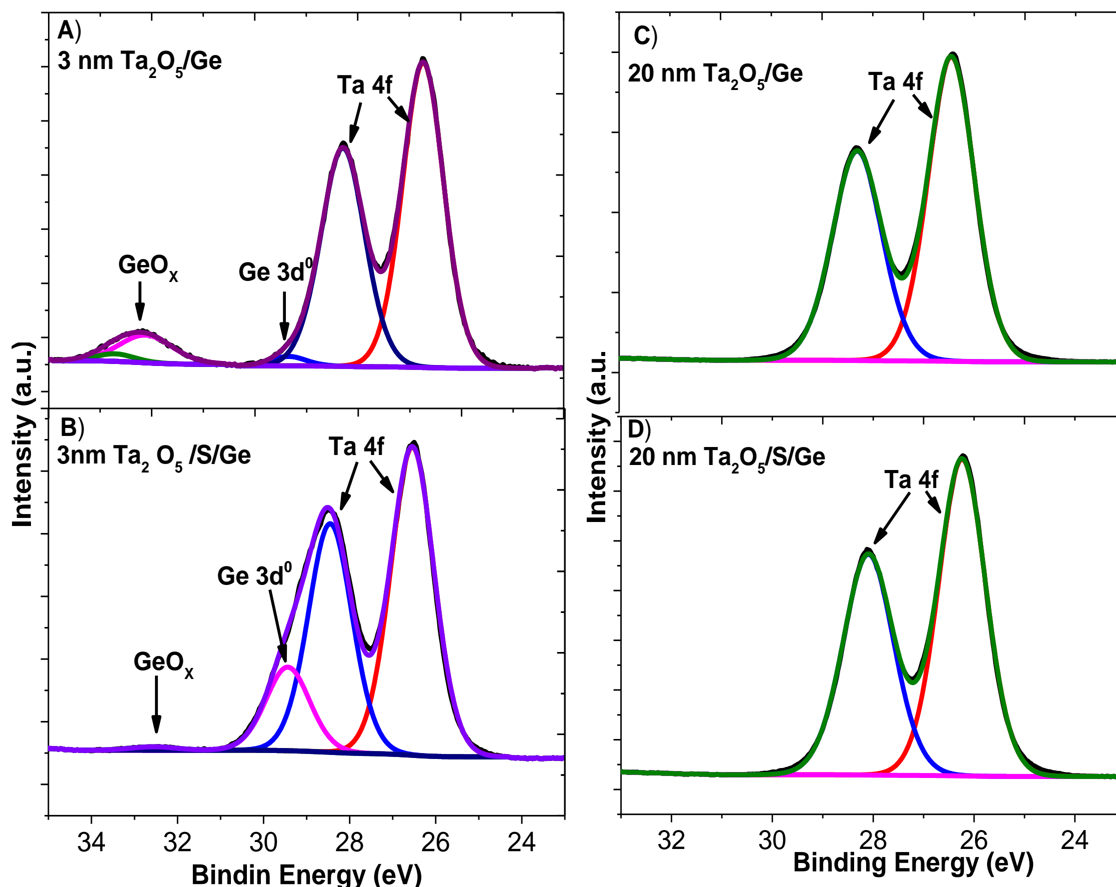

Fig. 9.1 Ge 3d XPS core level line shape for: (a) 3nm Ta_2O_5 on Ge, (b) 3nm Ta_2O_5/S/Ge, (c) 20nm Ta_2O_5 on Ge, and (d) 20 nmTa_2O_5/S/Ge.

Fig. 9.1 shows the XPS spectra from a 3 nm and 20 nm films on S-treated (Fig. 9.1(c), (d)) and untreated substrates (Fig 9.1 (a), (b)). The Ta 4f peak is clearly visible. The experimental curves were fitted, using CASA XPS, with two sub peaks. These correspond to Ta $4f_{7/2}$ and Ta $4f_{5/2}$. A spin-orbit splitting of 1.91 eV and a branching ratio of 0.75 eV were used. From Figs. 9.1(a) and 9.1(b), it is clearly seen that for the untreated substrates, the growth of Ta_2O_5 also results in significant amount of interfacial GeO_x at32.3eV. It is apparent that the addition of sulphur is very effective in preventing the appearance of interfacial oxides.

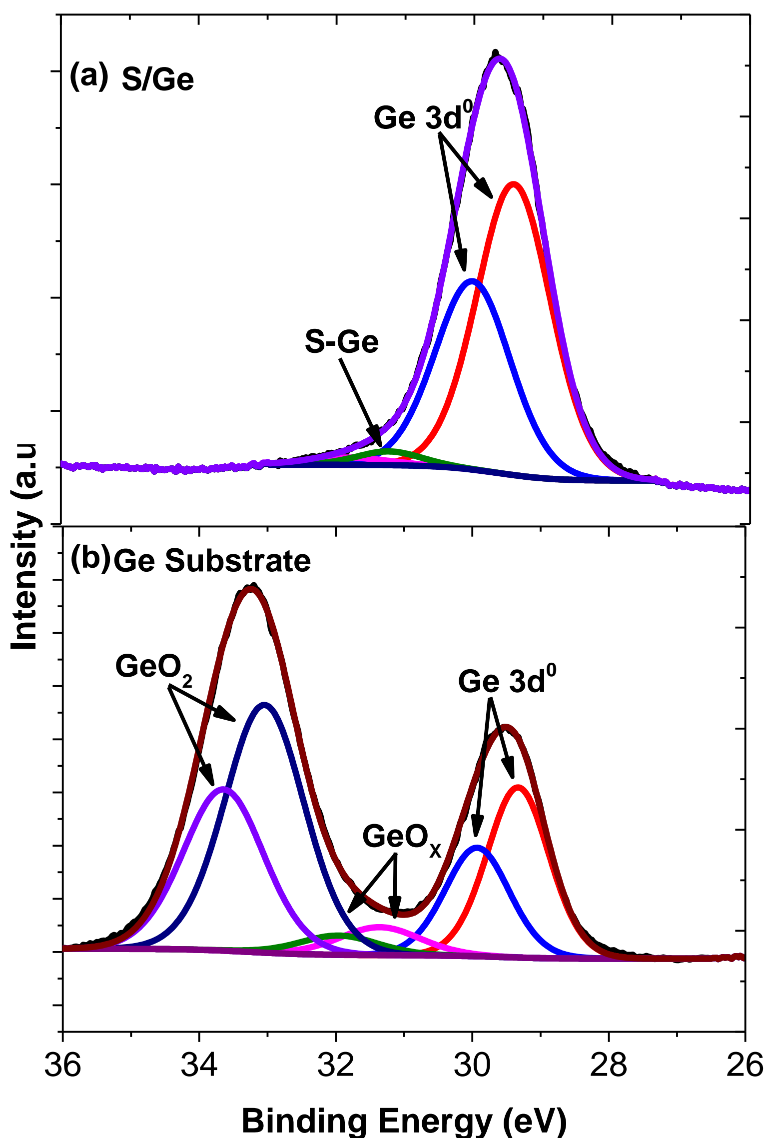

Fig. 9.2 Ge 3d XPS core level line shape for: (a) Sulphur passivated on Ge, (b) Ge Substrate. The fitting was performed using the Ge3d spin-orbit doublets for all species and a single peak for the GeS.

The effectiveness of sulphur passivation is clearly seen in Fig. 9.2, where the XPS spectra near the Ge3d region is presented for as-received and S-treated Ge wafers. The untreated surface shows a characteristic dominant peak at33.04 eV binding energy due to GeO_2 as well as a peak at about 1.7 eV below the bulk Ge3d level, ascribed to GeO_x

species. In the spectrum in Fig. 9.2(b) there is an additional feature at about 1 eV below with respect to the Ge bulk 3d peak, ascribed to GeS.

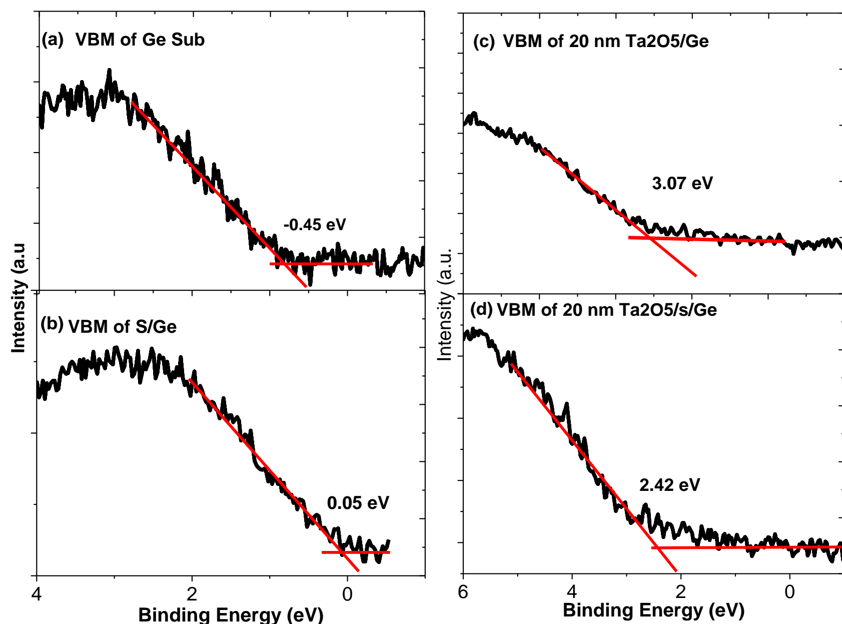

Fig. 9.3 Determination of the valance band maxima (VBM) for: (a) Ge Substrate, (b) Sulphur passivated on Ge, (c) 20nm Ta_2O_5 on Ge, and (d) 20 nm Ta_2O_5/S/Ge.

To determine the VBM position, a linear fit together with a Shirley background correction was applied as shown in Fig. 9.3. The value of VBO of Ta_2O_5/S/Ge was calculated by using the above equation from Kraut and found to be 2.7 ± 0.09 eV. In contrast, the VBO for Ta_2O_5 /Ge on the untreated Ge was found to be 2.84 ± 0.07 eV. The large value for the VBO suggests that it can offer barrier to the holes.

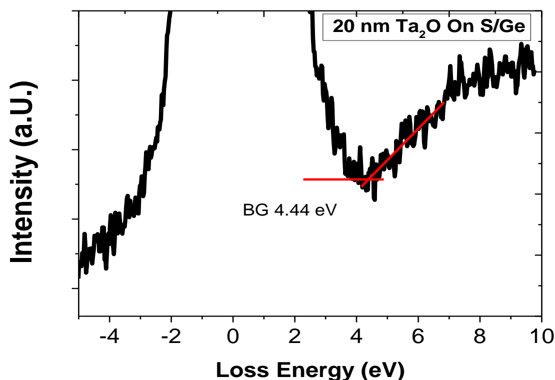

Fig. 9.4 O1s energy loss spectrum of a 20 nm Ta_2O_5 thin film.

In order to determine the conduction band offset, the band gap of Ta_2O_5 was estimated by using the O1s electron energy loss spectrum, as shown in Fig. 9.4. The band gap value for the 20 nm Ta_2O_5 film on the S-treated Ge was extracted to be 4.44 eV. Finally, Fig. 9.5 shows the band diagram for Ta_2O_5 on the S-treated Ge.

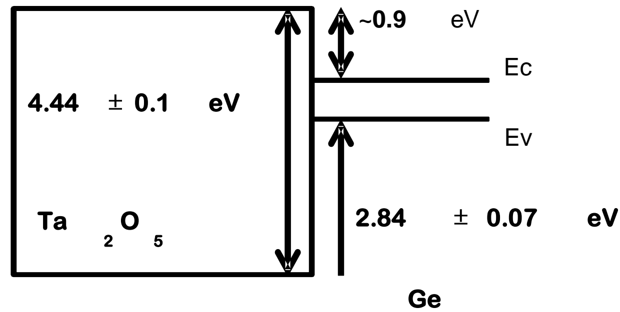

Fig. 9.5 Band diagram of Ta_2O_5/Ge derived from this work.

9.4 Conclusion

In conclusion, the band line-up, band gap, and interfacial nature of Ta_2O_5/Ge gate stacks deposited via atomic layer deposition method were investigated using XPS. The O 1s energy loss spectrum was used to calculate the electron energy band gap of Ta_2O_5 films. XPS results show that sulphur passivation of germanium is very effective in preventing the formation of the GeO_x at the interface. The results show that valence band offset with respect to the S-treated Ge is 2.67 eV and the conduction band offset is ~1.77 eV, which acts as a barrier to holes and electrons, respectively.

9.5 References

[1] Takagi S, Zhang R, Takenaka M. Ge gate stacks based on Ge oxide interfacial layers and the impact on MOS device properties. Microelectronic Engineering. 2013 Sep 30;109:389-95.

[2] Oshima Y, Shandalov M, Sun Y, Pianetta P, McIntyre PC. Hafnium oxide/germanium oxynitride gate stacks on germanium: Capacitance scaling and interface state density. Applied Physics Letters. 2009 May;94(18):3102.

[3] Kwon KW, Kang CS, Park SO, Kang HK, Ahn ST. Thermally robust Ta 2 O 5 capacitor for the 256-Mbit DRAM. Electron Devices, IEEE Transactions on. 1996 Jun;43(6):919-23.

[4] Murawala PA, Sawai M, Tatsuta T, Tsuji O, Fujita S, Fujita S. Structural and Electrical Properties of Ta2O5 grown by the plasma-enhanced liquid source CVD using penta ethoxy tantalum source. Japanese journal of applied physics. 1993 Jan 1;32(1S):368.

[5] Kim I, Ahn SD, Cho BW, Ahn ST, Lee JY, Chun JS, Lee WJ. Microstructure and electrical properties of tantalum oxide thin film prepared by electron cyclotron resonance plasma-enhanced chemical vapor deposition. Japanese journal of applied physics. 1994 Dec 1;33(12R):6691.

[6] Das R, Saha S. Electrical and Chemical Characteristics of Ta2O5 Gate Dielectrics on Ge-rich SiGe Heterolayers. Journal of Physical Sciences. 2012;16:177-84.

[7] Kraut EA, Grant RW, Waldrop JR, Kowalczyk SP. Precise determination of the valence-band edge in x-ray photoemission spectra: Application to measurement of semiconductor interface potentials. Physical Review Letters. 1980 Jun 16;44(24):1620.

Chapter 10

Conclusion

The aim of this thesis has been to investigate the interface of high k oxides and Ge substrates and to extract the band alignments of high k oxides. Various High k oxides have been characterized for different properties related to interface stability. The research in this thesis has made contribution in selection of suitable candidate for future Ge CMOS technology. A further contribution of this research is to improve interface properties such as GeOx free interface and achieve low leakage current of Ge devices.

Various high-κ dielectric gate stacks such as La_2O_3/Ge, Y_2O_3/Ge, Al_2O_3/Ge and Tm_2O_3/Ge are studied as interfacial layers for Ge surface passivation. It is observed that both La_2O_3 and Y_2O_3 are reactive to germanium but have different interface structure. In comparison to La_2O_3 , Y_2O_3 was observed to be better in terms of moderate reactivity to Ge, GeOx- free interface, higher conduction band offset, larger band gap and lower leakage current which makes it good candidate for Ge interface engineering.

Various properties were also determined by different techniques such as band gaps for Y_2O_3, Al_2O_3 and Tm_2O_3 films were determined by VUV-VASE data and band line-ups for La_2O_3/Ge, Y_2O_3/Ge, Tm_2O_3/Ge and GeO_2/Ge were derived from XPS and VUV-VASE data. Also, after using combined MBE and ALD techniques for fabricating ALD hafnia high-k dielectric gate stacks on Ge with alumina as the barrier layer, after the forming gas anneal, low EOT down to 1.3 nm was observed. It is also concluded from the study that the S-passivated samples show improved interfacial layer thickness. By XPS and HRTEM study, Al_2O_3 and Tm_2O_3 barrier properties on Ge were inferred which concluded that Tm_2O_3 can also act as an interfacial barrier layer, in similar way to an ultra-thin Al_2O_3 layer used in high-performance Ge CMOS gate stacks.

The $La_2O_3$and Y_2O_3films were deposited on the Ge substrate using molecular beam epitaxy. The film deposition was carried out at different temperature ranging 40-400°C. Higher temperature leads to more oxidation of Ge at the interface, which was also observed during the characterization by XPS. However both samples have different germinate composition. The germanate layer was strongly present with a XPS chemical shift of +2.4-2.6 eV for $LaGeO_x$, and +2.5-2.7 eV for $YGeO_x$. It was observed from the band diagram (derived using XPS) of $LaGeO_x$/Ge (deposited @ 400°C) that the values for valence band offset of 2.75 ± 0.15 eV and band gap of 5.45 ± 0.2 eV are in reasonable agreement with recent earlier work. However,

similar interface was visible in the case of Y_2O_3 at lower temperature of 225°C. Pronounced absorption regions were found for Y_2O_3/Ge stack at 225°C, which were not present in stack prepared at 400°C making the Y_2O_3/Ge a favorable candidate between the two. It was observed that the conduction band offset (2.3 eV) and band gap (Tauc-Lorentz method, 5.7 ± 0.1 eV) were greater for Y_2O_3 film deposited at 400 °C. Y_2O_3 also provided the GeO_2 free interface and lower leakage current (< 10^{-6} A/cm^2 at 1 V). XPS results also suggest the use of Al_2O_3. The band gap for the Al_2O_3 film was found to be 6.1 - 6.4 eV, justifying its role as a barrier layer. Hence considering the comparison between these two films, 400°C being the optimal temperature for both, Y_2O_3 is a better candidate for interface engineering for future Ge based CMOS devices.

Moving to the next material, Tm_2O_3, the valence band offset for 10 nm (nominal) thick Tm_2O_3 samples prepared using ALD was calculated using two different approaches. The first approach was core-level and valence band XPS spectra analysis at different sputtering times and the second was using XPS, three separate samples (bulk oxide, bulk Ge and oxide/Ge). The first method ensures the authenticity of the measurement as there is no variation introduced during the sample preparation. It is also concluded from this method that Tm_2O_3/Ge and GeO_2/Ge both show sufficient conduction band offsets (> 1.5 eV), to suppress leakage current in practical device applications. The energy bandgap was calculated to be 5.3 ±0.1 eV, dielectric constant estimated 14 to 15 and VBO 2.95 eV for Tm_2O_3 film. VBO value is close to the value calculated by first method (~3.0 eV). Tm_2O_3 interlayer also works as a barrier layer enabling the possibilities of using Tm_2O_3 dielectric as a reliable passivation route in future Ge-based scaled CMOS devices. Reliable barrier role was again confirmed by the large conduction band offset estimated by first method (1.5eV) as well as second method (1.7 eV). Large conduction band offset helps to provide a sufficient barrier to holes and electrons for improved Ge MOSFET performance.

Ta_2O_5 film, for their use on germanium surface was characterized and two types of Ge samples were prepared; one sulphur passivated and the other un-passivated. Ta_2O_5 was deposited using ALD technique at a temperature of 250°C. Ge samples were passivated by sulphur using 20% ammonium sulphide solution. Sulphur passivation helps to reduce the dangling bonds on the surface of Ge. Pentakis(dimethylamino)tantalum (PDMAT) as tantalum source and water vapour as oxygen source were pulsed into the ALD chamber. It was observed that it took about 40 to

260 cycles for growing a film thickness of 3 nm to 20 nm which was verified by thickness measurement using the spectroscopy ellipsometry. XPS analysis of the deposited film was carried out to analyze the band line-up, band gap, and the interfacial nature of Ta_2O_5/Ge gate stacks. The electron energy band gap of Ta_2O_5 films was calculated using the O 1s energy loss spectrum. It was observed from XPS that the sulphur passivation is advantageous as it prevents the formation of the GeO_x at the Ge / Ta_2O_5 interface. The valence band offset with respect to the S-treated Ge was found to be 2.67 eV and the conduction band offset was observed to be ~1.77 eV. This acts as a barrier to holes and electrons, respectively.

It is known that HfO_2/Ge interface shows oxidation at the interface. Hence, the leakage current of such devices is high. This oxidation at interface was confirmed by XPS characterization. Hafnium titanate is one alternative to HfO_2 which solves this problem and offers a better interface, which was confirmed by an experiment where hafnium titanate oxide thin films, $Ti_xHf_{1-x}O_2$, with a titanium content of x = 0, 0.25, 0.9 and 1 were prepared on alumina passivated germanium substrates. The samples were first characterized for surface properties such as morphology and roughness. It was observed that the film roughness values were very low. HfO_2 film was less rough (0.202nm) than $Ti_{0.25}Hf_{0.75}O_2$ film (0.425 nm) and $Ti_{0.9}Hf_{0.1}O_2$ (0.431 nm) film, whereas when the samples were characterized for electrical properties such as leakage current it was observed that the hafnium titanate ($Ti_{0.9}Hf_{0.1}O_2$) gave the lowest leakage current of about 1 mA/cm^2 at the bias of 0.5 V. It can conclude that the $Ti_{0.9}Hf_{0.1}O_2$ has good interface quality and lowest interface trap densities.

Furthermore, the advantages of sulphur passivation were witnessed by obtaining a GeO_X free interface, which was confirmed by the XPS measurement. The surface is also passivated further using Al_2O_3 (depositing Al and oxidizing the sample using molecular beam epitaxy). Various thicknesses of HfO_2 film were produced such as 3, 7 and 20 nm using 65, 130 and 250 respective cycles. [(CpMe)2HfOMeMe] precursor coupled with remote oxygen plasma or water was used for HfO_2 deposition by ALD. Sulphur passivation was found to be very effective in all the cases, even when the oxygen source is water vapour in the ALD. The film thickness monitoring was done using the spectroscopy ellipsometry. It can also be concluded that the interfacial +3 Ge and +2 Ge species evident for HfO_2/S/Ge stack deposited using O-plasma have been observed to have negligible effect on the interface quality, especially electrical quality. Sulphur passivation

along with being useful to improve leakage current also provides a way to obtain reliable passivation during the oxidation process. All these experiments were performed using the properly degreased n-type Ge wafers with resistivity 0.3-3 Ω-cm.

This work concludes that among the studied gate oxides Y_2O_3 proves to be the best gate oxide whereas the properties of Al_2O_3 are also good in terms of its application as a barrier layer with a bandgap of ~6.1 eV. Sulphur passivation provides the leakage improvement in Ge based devices. The estimated bandgap of Y_2O_3 is ~5.7 eV, which seems to be maximum out the studied oxides making it more favorable for its use as gate oxide layer. Y2O3 gate oxide provides good electrical isolation with a very low leakage current (< 10-6 A/cm^2 at 1 V). Based on this research it is concluded that sulphur passivated Ge wafers with Y_2O_3 as gate oxide provides the best interface properties as no GeO_x is found at the interface and hence giving a reliable Ge MOSFET technology.

Future work

Further characterization of the defect between the oxides and germanium substrate will be carried out by Electron Spin Resonance (ESR) and photoluminescence studies. More leakage studies will be performed for characterizing the interface quality. Advanced characterization of oxides interfaces with germanium by High-Resolution Photoemission using synchrotron radiation will be carried out. Future work also includes the extraction of CBM of oxides by Inverse Photoemission (IPES) and photoabsorption in synchrotron studies. Basic MOS devices will be fabricated with Y_2O_3/Ge (sulphur passivated) stack and interface properties and MOS characteristics will be analyzed.